Study of the effect of Ge and Y additions on the microstructure, phase stability and environmental degradation of Nb silicide alloys

Andrew Tweddle

Supervisor: Professor Panos Tsakiropoulos

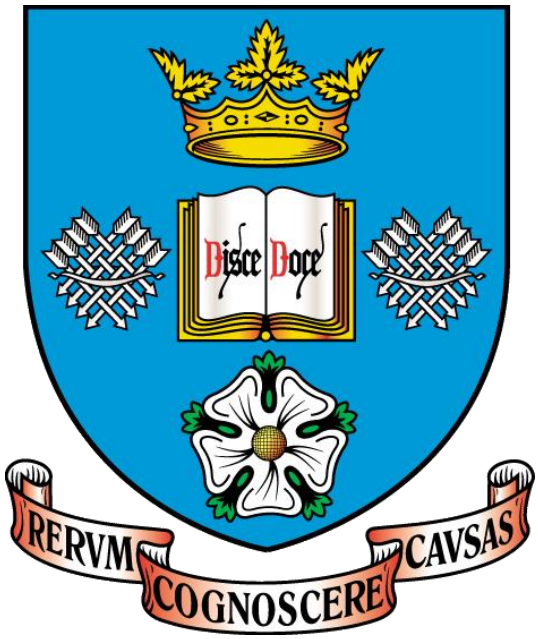

Thesis submitted for the Degree of Doctor of Philosophy

The Department of Materials Science and Engineering,

University of Sheffield

January 2015

Abstract

Niobium based silicide alloys are candidate materials to replace current single crystal Ni superalloys in next generation gas turbines. As turbine entry temperatures increase to gain better fuel efficiency, new materials are required to withstand the increased temperatures. It is seen throughout the literature that whilst the mechanical properties of Nb silicide alloys are sufficient, their resistance to environmental degradation requires greater improvement before being used in structural applications. This thesis discusses the current body of research in the literature, identifying gaps in knowledge that this body of work aims to fill. Results are reported for several iterations of alloying element levels and the effects they bring about on microstructure and oxidation properties. Results show that additions of Ge and Y along with high levels of Ti can promote the formation of hexagonal crystal structured phases, γNb_5Si_3, which could be detrimental for mechanical properties. The results also show that additions of Y inhibit the formation of Cr_2Nb Laves phase in the microstructure and still can provide a beneficial effect on the oxidation resistance within the 'pest' range (750 – 900 ^oC). Additions of Y provided no beneficial effect on the oxidation resistance at high temperatures (1200 ^oC) and no improvement in oxide scale adherence to the substrate material. This thesis confirms that the intermetallic phases are not immune to the oxidation process, showing both external and internal formation of oxides. A mechanism for oxidation at high temperatures (1200 ^oC) is proposed including the results of the present work.

Acknowledgements

Thanks go to Professor Panos Tsakiropoulos for his supervision and guidance during this research. His encouragement and willingness for discussion have been vital to the completion of this thesis. Also thanks go to the rest of my research group for the many discussions and understandings about some of the difficulties of conducting this research.

Thanks to the technical/research staff at the University of Sheffield and Dr. Chris Hayward, Research Fellow at the School of Geosciences, University of Edinburgh for use and guidance collecting data on the microprobe.

Thank you to Dr. Howard Stone from the Department of Materials Science and Metallurgy, University of Cambridge for the use of the arc melting facilities in order to make the alloys.

Finally, thank you to Neil Jones of Rolls-Royce Plc, UK for arranging use of Rolls-Royce microscope facilities; Rolls-Royce Plc and the Engineering and Physical Sciences Research Council (EPSRC) for funding of this research.

Contents

Chapter 1

Literature Review: Phase equilibria

1.1 Introduction

With the ever increasing demand for reducing carbon emissions to stave off global warming, research has favoured materials that can work at very high temperatures. This is especially true for gas turbines used in transport and energy industry sectors. If gas turbines were able to operate at higher temperatures than they currently function, this could lead to improvements in efficiency, which means better fuel consumption and lower NO_x and CO_x emissions. New high temperature materials should not only improve operating temperature but also reduce weight, which can benefit thrust to weight ratio, and extend the life of the turbine keeping costs down.

In the most advanced gas turbines today, metal surface temperatures have reached ~1150 ^{o}C which is essentially the limit for single crystal, Ni-base superalloys. Further increase in their temperature capability is unlikely due to the liquidus temperature of the most advanced Ni base superalloy being ~1350 ^{o}C, and can also be jeopardised by incipient melting at ~1250 ^{o}C (Jackson et al., 1996, Bewlay et al., 2003). New materials are therefore required for any potential increase in turbine entry temperature (TET).

Niobium silicide based *in-situ* composites have been shown to possess great potential as a possible material to one day replace Ni base superalloys in the high temperature zones of next generation gas turbines. These materials possess superior properties to Ni base superalloys with low densities (6.6 – 7.2 g/cm^3), high melting points (>1700 ^{o}C) and excellent mechanical properties at high temperatures (Bewlay and Jackson, 2000). However, these materials suffer from poor room temperature fracture toughness and oxidation resistance which has hindered the use of these materials thus far in structural applications. Therefore, research needs to address these issues and achieve a good balance of properties including creep, room temperature fracture toughness and oxidation resistance, in order for these

materials to be used in structural applications. A set of targets have been laid out that need to be met.

In this study we aim to develop multi-component Nb-silicide base *in-situ* composites for use in high temperature applications. The objectives of this research are:

- Design and develop oxidation resistant alloys with acceptable mechanical properties.
- Understand phase selection and microstructural stability in these alloys.
- Assess oxidation and mechanical properties.
- Provide relevant data for the determination of phase equilibria data for ternary and higher order systems.

This thesis begins with a thorough review of the current literature dealing with Nb-silicide base *in-situ* composites. Evaluation of phase equilibria data for binary and ternary systems forms the main focus of the literature review, using the data in order to understand the effect of alloying elements on the phases present in the microstructure.

1.2 Nb-Si binary

Niobium silicide alloys are based on the Nb-Si binary system and Figure 1.1 shows the accepted phase diagram of the Nb-Si binary system.

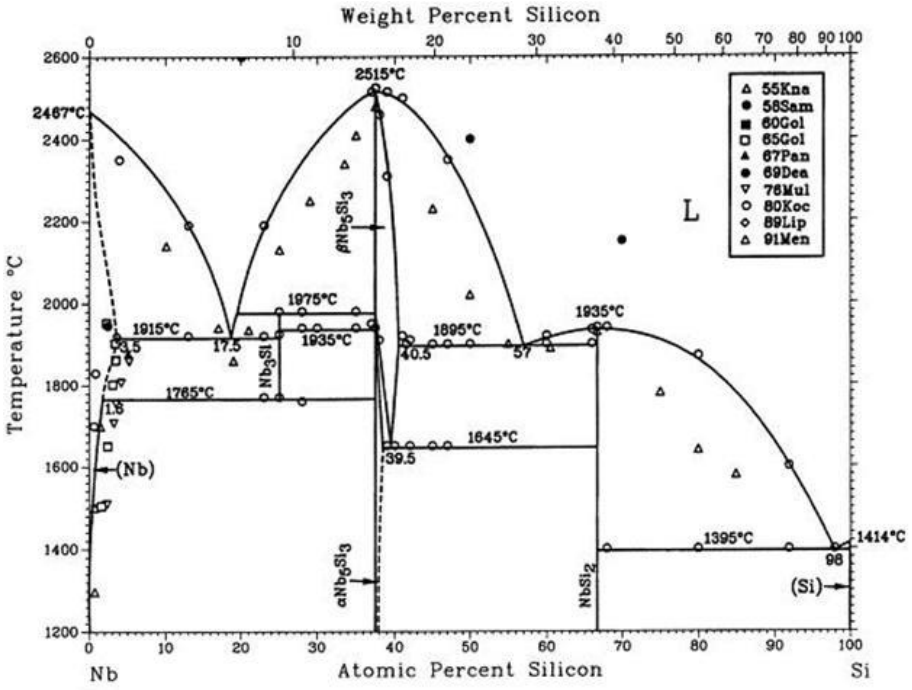

Figure 1.1 : Phase diagram of the Nb-Si binary system (Schlesinger et al., 1993).[1]

The Nb silicide alloys are designed to sit in the region between 0-37 at.% Si. Here, there is a wide two-phase region with the Nb_{ss} and Nb_5Si_3 phases in thermodynamic equilibrium from 1765 ^oC down to room temperature. This, coupled with a eutectic phase transformation of $L \rightarrow Nb_{ss} + Nb_3Si$ at 1915 ^oC at 17.5 at.% Si, a eutectoid transformation of $Nb_3Si \rightarrow Nb_{ss} + \alpha Nb_5Si_3$ at 1765 ^oC at ~26 at.% Si and a peritectic transformation of $L + \beta Nb_5Si_3 \rightarrow Nb_3Si$, can allow for a wide range of volume fractions and microstructure morphologies to be produced for these alloys (Dimiduk et al., 1995). The presence of a eutectic transformation could allow these alloys to be directionally solidified as eutectics. Although the equilibrium phases are Nb_{ss} and αNb_5Si_3, it is common for these alloys to solidify with the Nb_{ss} and βNb_5Si_3,

[1] Springer and the Journal of Phase Equilibria, 14, 1993, 502-509, The Nb-Si (Niobium-Silicon) system, Schlesinger, M, Okamoto, H, figure 1, copyright 2014) is given to the publication in which the material was originally published, with kind permission from Springer Science and Business Media

and even Nb_3Si, present in the microstructure. This is due to the solid state transformations being very sluggish in this system with transformations requiring heat treatments of 1500 ^oC for 100 h (Mendiratta and Dimiduk, 1991). The microstructure can be thought of as a brittle, intermetallic phase, providing high temperature strength, reinforced with a ductile, metallic phase, for room temperature toughness and ductility. Table 1.1 and Table 1.2 summarise the rest of the important features of the Nb-Si binary system.

Table 1.1 Crystal structures of phases present within the Nb-Si binary system.

Phase	Composition (at.% Si)	Pearson Symbol	Space Group	Strukturbericht designation	Structure type	Lattice Parameter (Å)		
						a	*b*	*c*
Nb	0 -35	cI2	Im3m	A2	W	3.3		
Nb_3Si	25	tP32	$P4_2/n$	--	Ti_3P	10.224	-	5.189
αNb_5Si_3	36.7 - 39.8	tI32	I4/mcm	$D8_1$	Cr_5B_3	6.579	-	1.1884
βNb_5Si_3	37.5 - 40.5	tI32	I4/mcm	$D8_m$	W_5Si_3	10.026	-	5.0717
γNb_5Si_3	37.5	hP16	$P6_3/mcm$	$D8_8$	Mn_5Si_3	7.463	-	5.132
$NbSi_2$	64.9 - 68.8	hP9	$P6_222$	C40	$CrSi_2$	4.819	-	6.592
Si	100	cF8	Fd3m	A4	C $_{(diamond)}$	5.4286	-	-

Table 1.2 Phase transformations present within the Nb-Si binary system.

Reaction	Compositions of phases (at.% Si)			Temperature, (^oC)	Reaction type
$L \leftrightarrow (Nb)$		0		2467	Melting
$L \leftrightarrow (Nb) + Nb_3Si$	17.5	3.5	25	1915	Eutectic
$L + \beta Nb_5Si_3 \leftrightarrow Nb_3Si$	19.5	37.5	25	1975	Peritectic
$Nb_3Si \leftrightarrow (Nb) + \alpha Nb_5Si_3$	25	1.6	35.5	1765	Eutectoid
$L \leftrightarrow \beta Nb_5Si_3$		37.5		2515	Melting
$Nb_3Si + \beta Nb_5Si_3 \leftrightarrow \alpha Nb_5Si_3$	25	37.5	37.5	1935	Peritectoid
$\beta Nb_5Si_3 \leftrightarrow \alpha Nb_5Si_3 + NbSi_2$	39.5	38.5	66.7	1645	Eutectoid
$L \leftrightarrow \beta Nb_5Si_3 + NbSi_2$	57	40.5	66.7	1895	Eutectic
$L \leftrightarrow NbSi_2$		66.7		1935	Melting
$L \leftrightarrow NbSi_2 + Si$	98	68.8	100	1395	Eutectic
$L \leftrightarrow Si$		100		1414	Melting

Abbaschian and Lipschutz (1997) and Bendersky et al., (1987) looked at rapid solidification of Nb-Si alloys using arc melting and melt spinning for creation of the alloys. Both showed that under rapid solidification conditions, the stable eutectic of Nb_{ss} and Nb_3Si is no longer present; instead a metastable eutectic of Nb_{ss} and Nb_5Si_3 exists, as shown in Figure 1.2. This new eutectic point is located at 18.6 at.% (Abbaschian and Lipschutz, 1997) and 20 at.% (Bendersky et al., 1987) rather than 17.5 at.%, as shown in Figure 1.1. There is also evidence to suggest that under rapid solidification conditions, both regular and anomalous eutectic formation is possible (Li and Kuribayashi, 2003, Kurz and Fisher, 1979, Wei et al., 1993).

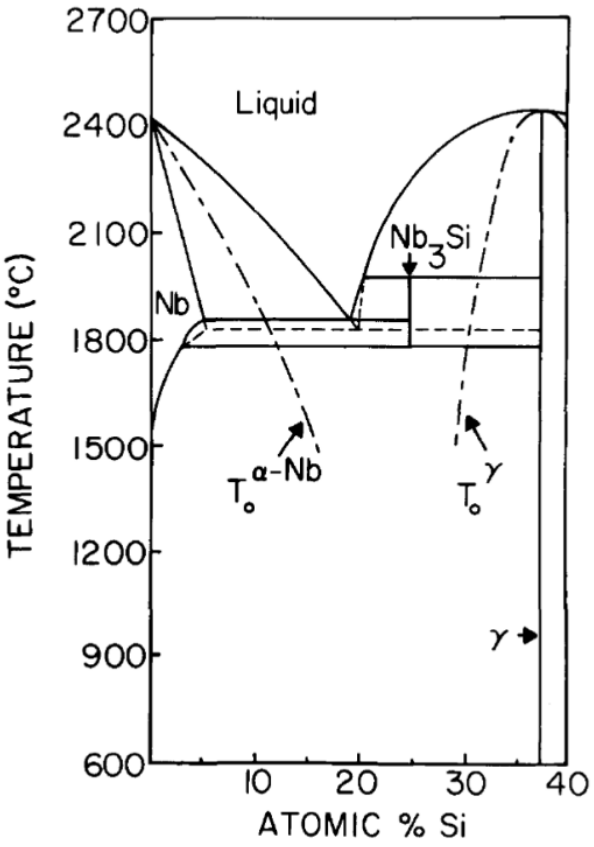

Figure 1.2 Phase diagram showing the metastable eutectic of Nb_{ss} and βNb_5Si_3 (Bendersky et al., 1987).[2]

[2] Reprinted from Materials Science and Engineering, 89, Bendersky, L., Biancaniello, F. S., Boettinger, W. J. Perepezko, J. H, Microstructural characterization of rapidly solidified Nb-Si alloys, 151-159., Copyright (2014), with permission from Elsevier.

1.2.1 Nb_5Si_3

Figure 1.3 shows the crystal structures of the three allotropes of α, β and γNb_5Si_3. There are 32 atoms in both the unit cells of α and βNb_5Si_3 and 16 in γNb_5Si_3. Each of these structures can be orientated to show similar stacking patterns of atom planes. The unit cell of αNb_5Si_3 possesses stacking patterns of *MLLLMLLL* (M and L refer to the more closely packed and less closely packed layers) whereas β and γNb_5Si_3 possess stacking patterns of alternate *M* and *L* layers. From these stacking patterns it can be determined that there are two types of Nb atom (Nb(I) and Nb(II)) and two types of Si atom (Si(I) and Si(II)) in both α and β Nb_5Si_3, whereas in γNb_5Si_3 there are still two Nb atoms but all the Si atoms are equivalent. In this thesis, Nb(I) and Si(I) are those atoms on the less closely packed planes and Nb(II) and Si(II) are those located on the more closely packed plane.

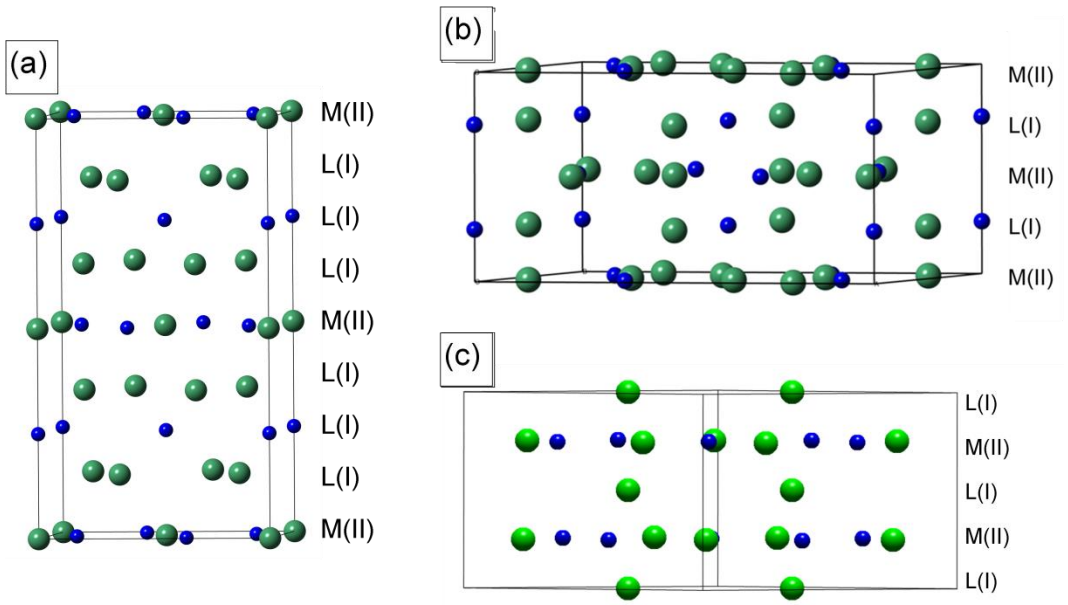

Figure 1.3 Crystal structures of (a) α, (b) β and (c) γNb_5Si_3. Large spheres represent Nb atoms, small spheres represent Si atoms.

There are a few papers in the literature that report on the effects of site substitution of a variety of elements into these structures (Chen et al., 2011, Chen et al., 2007b, Chen et al., 2007a, Kang et al., 2009) using a modelling approach, many of them using the Cambridge serial total energy package (CASTEP) (It is worth noting that the nomenclature of the sites is opposite to these studies, hence Nb(I) in this thesis is Nb(II) in those papers). In these studies the elements added included Ti, Cr, V, W, Zr, Mo, Hf, and Ta. It was found in these studies that elements do have a preference of which site to occupy when substituting onto the crystal structure, all of the elements in these studies substituted on the Nb sites. It was found that elements with smaller atomic radii than Nb (Ti, Cr, V, Mo and W) preferred to substitute onto the Nb sites on the more closed packed plane *Nb(II)* in αNb_5Si_3, but prefer the Nb sites on less closely packed planes *Nb(I)* in β and γNb_5Si_3. Atoms with larger atomic radii than Nb showed opposite behaviour.

These results are only based on calculations of formation energies and only considered substituting one atom at a time. This work aims to show, through a structural refinement using the x-ray diffraction patterns, whether similar behaviour exists when several atoms are substituting onto the crystal structure.

1.2.2 Summary

Whilst pure Nb-Si binary alloys are attractive materials, they do not possess all the properties required to be used in high temperature structural applications. In order to improve some of the inherent negative properties of these alloys, alloying investigations have taken place throughout the world attempting to find the correct combination of alloying elements to give the best balance of properties.

The rest of this chapter will look at other binary and ternary systems that are needed in order to predict the phases present in the microstructure of more complex alloys.

1.3 Nb-Ge binary and Nb-Ge-Si ternary

The Nb-Ge binary phase diagram is shown in Figure 1.4 and data about the phases present, compositions and structure types are show in Table 1.3. This phase diagram was drawn based on the work by (Pan et al., 1995) and (Jorda et al., 1978). In this version there are five phases present, BCC Nb_{ss}, cubic Nb_3Ge, tetragonal Nb_5Ge_3, hexagonal $NbGe_2$ and the cubic Ge. The solubility of Ge in Nb is ~11 at.% at 1900 ^oC and there are several phase transformations present including a peritectic reaction $L + Nb_{ss} \rightarrow Nb_3Ge$ at 1900 ^oC and a eutectic reaction of $L \rightarrow Nb_3Ge + Nb_5Ge_3$. There is no eutectic reaction of $L \rightarrow Nb_{ss} + Nb_3Ge$.

Recently, however, the Nb-Ge binary system was thermodynamically assessed using CALPHAD and that binary phase diagram includes the Nb_3Ge_2 phase ($P6_3/mcm$, Mn_5Si_3 $D8_8$) and this new phase diagram is shown in Figure 1.5 (Geng et al., 2011).

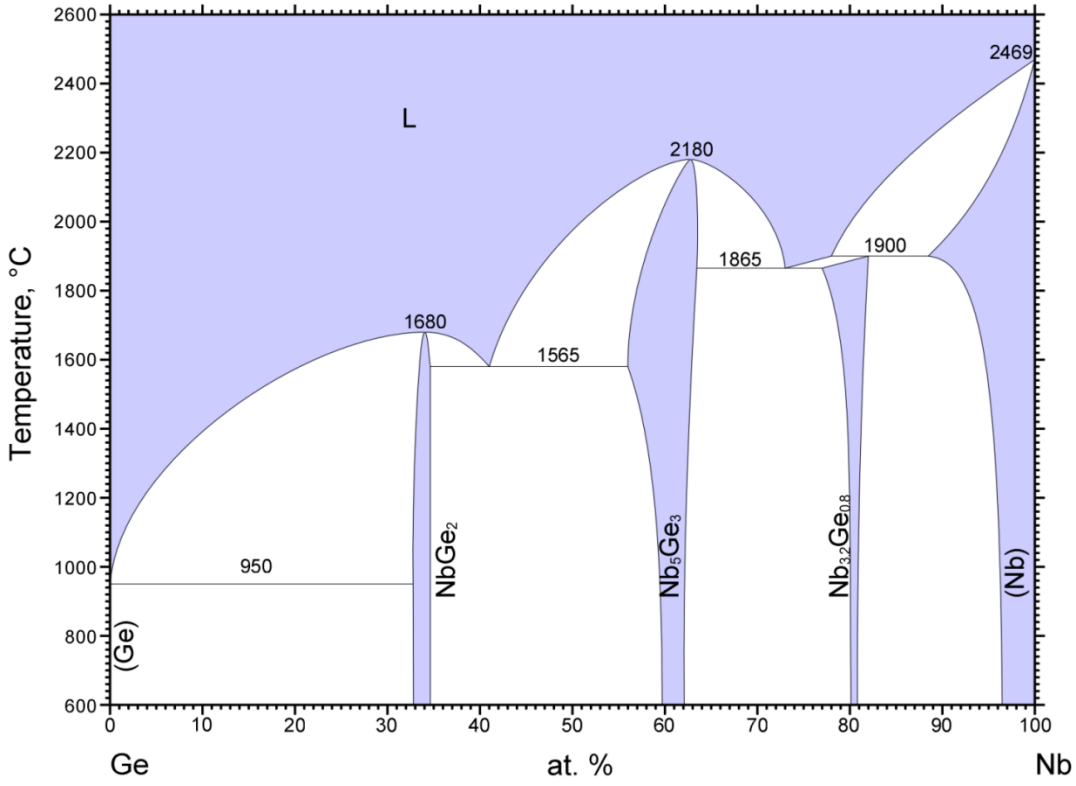

Figure 1.4 The Nb-Ge binary phase diagram (Okamoto, 1990a).

Table 1.3 Crystal structures of phases present within the Nb-Ge binary system.

Phase	Composition (at.% Ge)	Pearson Symbol	Space Group	Lattice Parameter (Å)		
				a	*b*	*c*
Nb	0 - 11	cI2	Im3m	3.2942	-	-
$Nb_{3.2}Ge_{0.8}$	19-20	cP8	Pm3n	5.1692	-	-
Nb_5Ge_3	38-41	tI32	I4/mcm	10.146	-	5.136
$NbGe_2$	65-68	hP9	$P6_222$	4.967	-	6.783
Ge	100	cF8	Fd3m	5.6579	-	-

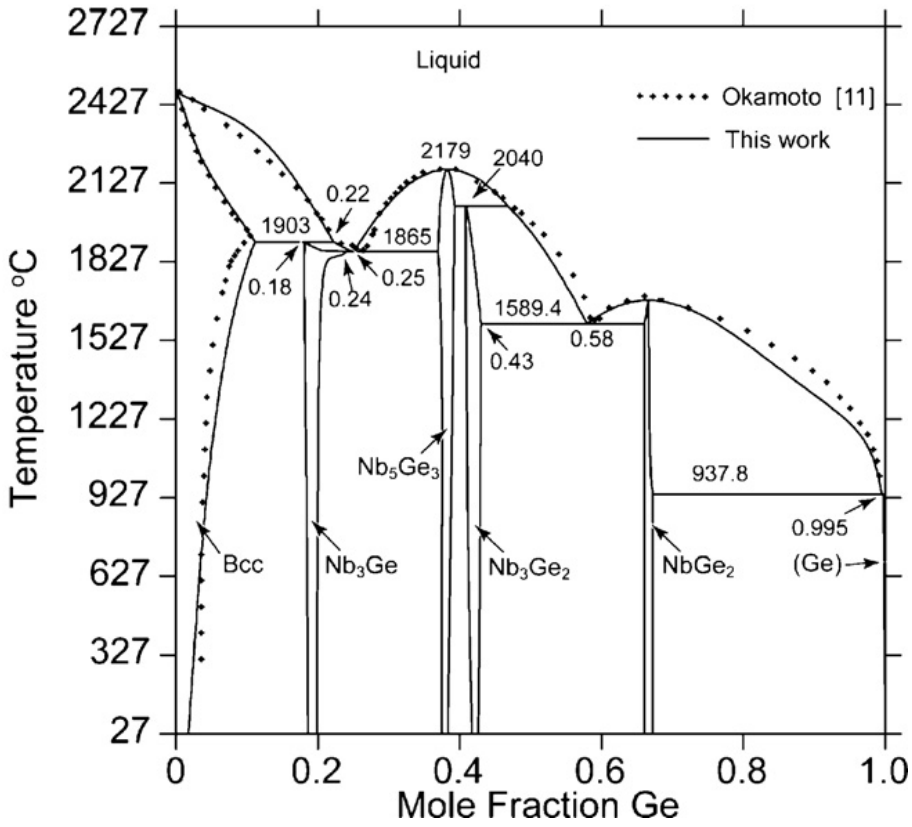

Figure 1.5 Phase diagram of the Nb-Ge binary system produced from thermodynamics (Geng et al., 2011).[3]

[3] Reprinted from Journal of Alloys and Compounds, 509, Geng, T., Li, C., Du, Z., Guo, C., Zhao, X. and Xu, H, Thermodynamic assessment of the Nb–Ge system, 3080-3088., Copyright (2014), with permission from Elsevier.

Care must be taken when looking into the literature of the Nb-Ge phase diagram. The hexagonal Nb_3Ge_2 phase was previously reported as a metastable phase (Jorda et al., 1978) and has also been labelled as hexagonal Nb_5Ge_3, βNb_5Ge_3, $Nb_{10}Ge_7$,$NbGe_{0.67}$ or $Nb_5Ge_{3.5}$. The important point to make from this system is that Nb_5Ge_3 possesses a tetragonal crystal structure so additions of Ge should stabilise the tetragonal Nb_5Si_3. Also, Nb_5Ge_3 has the same structure as the βNb_5Si_3 (W_5Si_3, $D8_m$) and therefore additions of Ge should stabilise the βNb_5Si_3 not the αNb_5Si_3 as others have reported (Zifu and Tsakiropoulos, 2010). With the inclusion of the Nb_3Ge_2 phase possessing a hexagonal crystal structure (same of Ti_5Si_3 and γNb_5Si_3, hP16, Mn_5Si_3, $P6_3/mcm$, $D8_8$), it is possible that additions of Ge with Ti will help stabilise hexagonal crystal structures.

The literature on the Nb-Si-Ge ternary system is very limited. Pan et., al. reported partial isothermal sections at 1820, 1800 and 1780 ^oC and these are shown in Figure 1.6 (Pan et al., 1982).

Figure 1.6 shows that at 1820 ^oC there is the Nb_{ss}, Nb_3Ge, Nb_5Ge_3, Nb_3Si and Nb_5Si_3 with ternary phase fields of Nb + Nb_3Ge + Nb_5Ge_3, Nb_{ss} + Nb_3Si + Nb_5Ge_3 and Nb_3Si + Nb_5Si_3 + Nb_5Ge_3. There is also a two phase field where the Nb_{ss} is in equilibrium with Nb_3Si with minor Ge additions. The solubility of Ge in Nb_3Si is below 2 at.%. With decreasing temperature, the two phase field decreases in size at 1800 ^oC and disappears at 1780 ^oC, and two new ternary phase fields are formed of Nb_{ss} + Nb_3Si + Nb_5Si_3 (at 1800 ^oC, disappears at 1780 ^oC) and Nb_{ss} + Nb_5Si_3 + Nb_5Ge_3. Below 1780 ^oC, Nb_3Si does not exist; hence additions of Ge have very little effect on stabilising the Nb_3Si to lower temperatures.

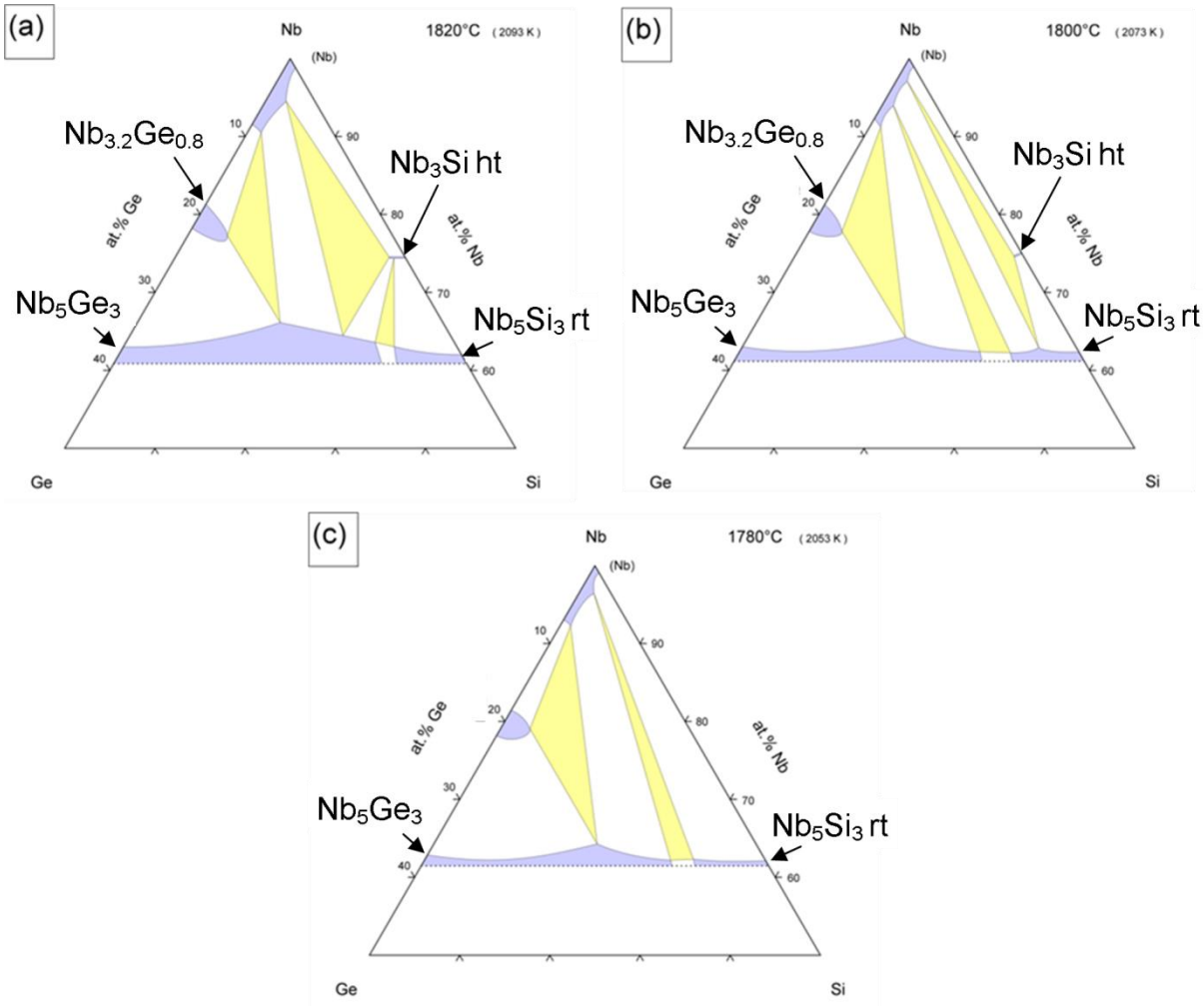

Figure 1.6 Partial Isothermal sections of the Nb-Ge-Si ternary system produced at (a) 1820 ^{o}C, (b) 1800 ^{o}C and (c)1780 ^{o}C (Pan, 1982).

1.4 Nb-Ti and Ti-Si binaries and Nb-Ti-Si ternary

Figure 1.7 shows a comprehensive phase diagram of the Ti-Si binary system and Table 1.4 and Table 1.5 give the phases and reaction data. From the phase diagram it is clear to see that there are seven stable phases, the liquid (L), the HCP solid solution (αTi), the bcc solid solution (βTi) in which a maximum of about 4 at.% Si can dissolve, the tetragonal Ti_3Si (Ti_3P), the hexagonal Ti_5Si_3 (Mn_5Si_3) with homogeneity of about 4 at.%, the tetragonal Ti_5Si_4 (Zr_5Si_4), the stoichiometric TiSi, the stoichiometric $TiSi_2$ and the diamond cubic (Si) solid solution. The Ti_3Si phase is

isomorphous with the Nb_3Si phase, both having the *tI*32 crystal structure, and therefore it is reasonable to assume that additions of Ti to the Nb-Si binary system will stabilise Nb_3Si to lower temperatures and this has been confirmed by several studies (Bewlay et al., 1998, Bewlay et al., 1997, Zelenitsas and Tsakiropoulos, 2006b, Zelenitsas and Tsakiropoulos, 2005, Zhao et al., 2004). The Ti_5Si_3 phase and the Nb_5Si_3 phase are not isomorphous and have *hP16* and *tI32* crystal structures respectively. However, the metastable γNb_5Si_3 has the same crystal structure as the Ti_5Si_3. The addition of Ti to these alloys has seen improvements in fracture toughness and density (Bewlay and Jackson, 2000, Davidson and Chan, 1999, Chan, 2002). Due to this, there have been extensive studies on the Nb-Ti-Si ternary system (Geng et al., 2009, Jing et al., 2008, Zhao et al., 2004). Figure 1.8 shows a three dimensional schematic of the Nb-Ti-Si system and an isothermal section at 1200 ^{o}C (Zhao et al., 2004).

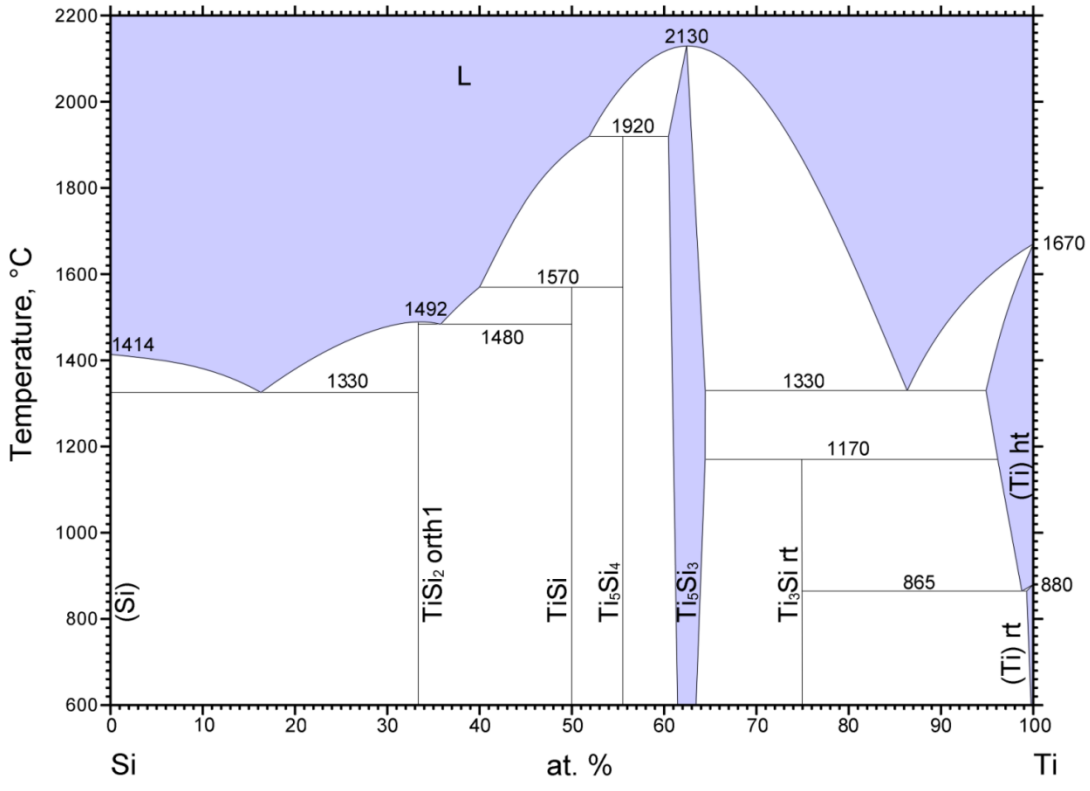

Figure 1.7 The Ti-Si binary phase diagram (Murray, 1990).

Table 1.4 Crystal structures of phases present within the Ti-Si binary system.

Phase	Composition, at% Si	Pearson Symbol	Space group	Strukturbericht designation	Prototype
αTi	0 - 0.5	hP2	$P6_3/mmc$	A3	Mg
βTi	0 - 3.5	cI2	Im3m	A2	W
Si	100	cF8	Fd3m	A4	C
Ti_3Si	25	tP32	$P4_2/n$	-	PTi_3
Ti_5Si_3	35.5 - 39.5	hP16	$P6_3/mcm$	$D8_8$	Mn_5Si_3
Ti_5Si_4	44.4	tP36	$P4_12_12$	-	Si_4Zr_5
TiSi	50	oP8	Pnma	B24	BFe
$TiSi_2$	66.7	oF24	Fddd	C54	Si_2Ti

Table 1.5 Reactions present within the Ti-Si binary system.

Reaction	Compositions of the respective phases, at.% Si			Temperature, ^oC	Reaction type
$\beta Ti_{ss} \leftrightarrow \alpha Ti_{ss} + Ti_3Si$	1.1	0.5	25	865	Eutectoid
$\beta Ti_{ss} + Ti_5Si_3 \leftrightarrow Ti_3Si$	3.5	37.5	25	1170	Peritectoid
$L \leftrightarrow \beta Ti_{ss} + Ti_5Si_3$	13.5	4.7	37.5	1330	Eutectic
$L \leftrightarrow Ti_5Si_3$		37.5		2130	Congruent
$L + Ti_5Si_3 \leftrightarrow Ti_5Si_4$	48.1	37.5	44.4	1920	Peritectic
$L + Ti_5Si_4 \leftrightarrow TiSi$	60	44.4	50	1570	Peritectic
$L \leftrightarrow TiSi + TiSi_2$	64.2	50	66.7	1480	Eutectic
$L \leftrightarrow TiSi_2$		66.7		1500	Congruent
$L \leftrightarrow TiSi_2 + Si_{ss}$	83.8	66.7	100	1330	Eutectic
$L \leftrightarrow \beta Ti_{ss}$		0		1670	Melting
$\beta Ti_{ss} \leftrightarrow \alpha Ti_{ss}$		0		882	Allotropic
$L \leftrightarrow Si_{ss}$		100		1414	Melting

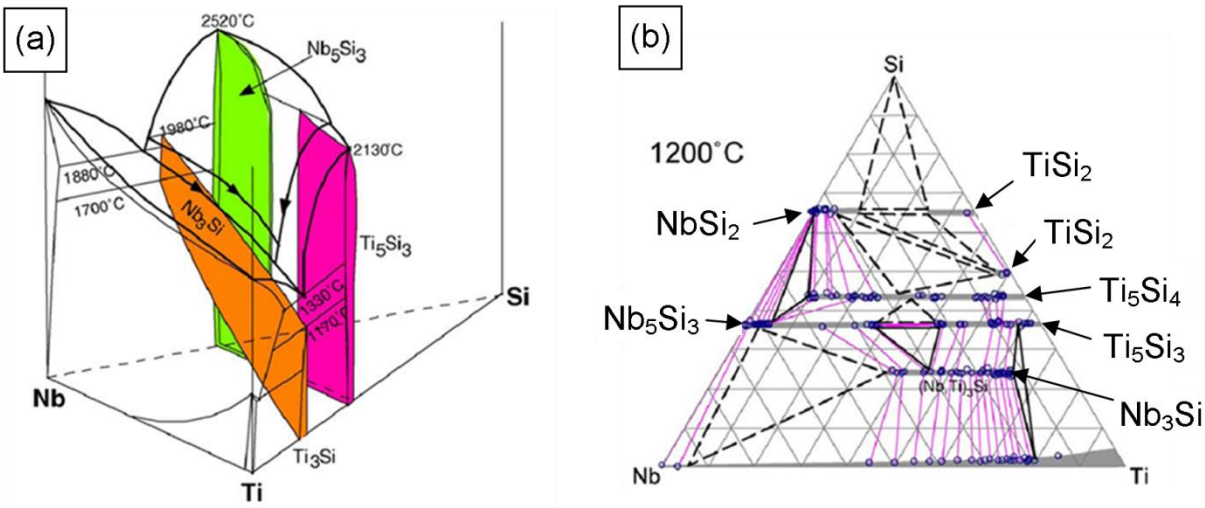

Figure 1.8 Image showing (a) a three dimensional schematic of the Nb-Ti-Si system and (b) an isothermal section at 1200 ^{o}C (Zhao et al., 2004).[4]

The major phases of interest in the three dimensional plot are Nb_{ss}, Nb_3Si, Nb_5Si_3, Ti_3Si and Ti_5Si_3. The main points of interest from the two diagrams above are as follows. The isomorphic nature of Ti_3Si and Nb_3Si is easily seen in Figure 1.8(a), as the Nb_3Si field is extended to lower temperatures as more and more Ti is added. The fact that Nb_5Si_3 and Ti_5Si_3 are not isomorphous is seen in the diagram as well. Titanium can be dissolved in Nb_5Si_3 up to a certain point, as more Ti is added, a two-phase region exists of both Nb_5Si_3 and Ti_5Si_3, and then a region of Ti_5Si_3 exists.

It can be seen, therefore, that Ti can have several effects on the Nb-Si binary system. Titanium can: 1) Stabilise the tetragonal Nb_3Si to lower temperatures; 2) promote the formation of hexagonal Ti_5Si_3 which has been reported to be detrimental for creep strength of these alloys (Bewlay et al., 2002); and 3) reduce the eutectic ($L \rightarrow Nb_{ss} + Nb_3Si$) temperature and therefore the melting temperature of these alloys. Titanium has been seen to have many beneficial effects to these composites such as increasing room temperature fracture

[4] Reprinted from Materials Science and Engineering A, 372, Zhao, J. C., Jackson, M. R. and Peluso, L. A, Mapping of the Nb-Ti-Si phase diagram using diffusion multiples, 21-27, Copyright (2014), with permission from Elsevier.

toughness and improving oxidation resistance (Bewlay et al., 2001a, Bewlay and Jackson, 2000, Bewlay et al., 2002, Chan and Davidson, 1999, Chan, 2005, Zelenitsas and Tsakiropoulos, 2005). It has been reported that the maximum level of Ti added should not exceed 25 at.% so that the detrimental, hexagonal Ti_5Si_3 phase is not formed, and so that the eutectic temperature remains above 1700 ^oC (Chan, 2002).

1.5 Ti-Ge binary

Figure 1.9 shows the Ti-Ge binary phase diagram and Table 1.6 and Table 1.7 show the important crystal structure data and reactions present within the Ti-Ge system.

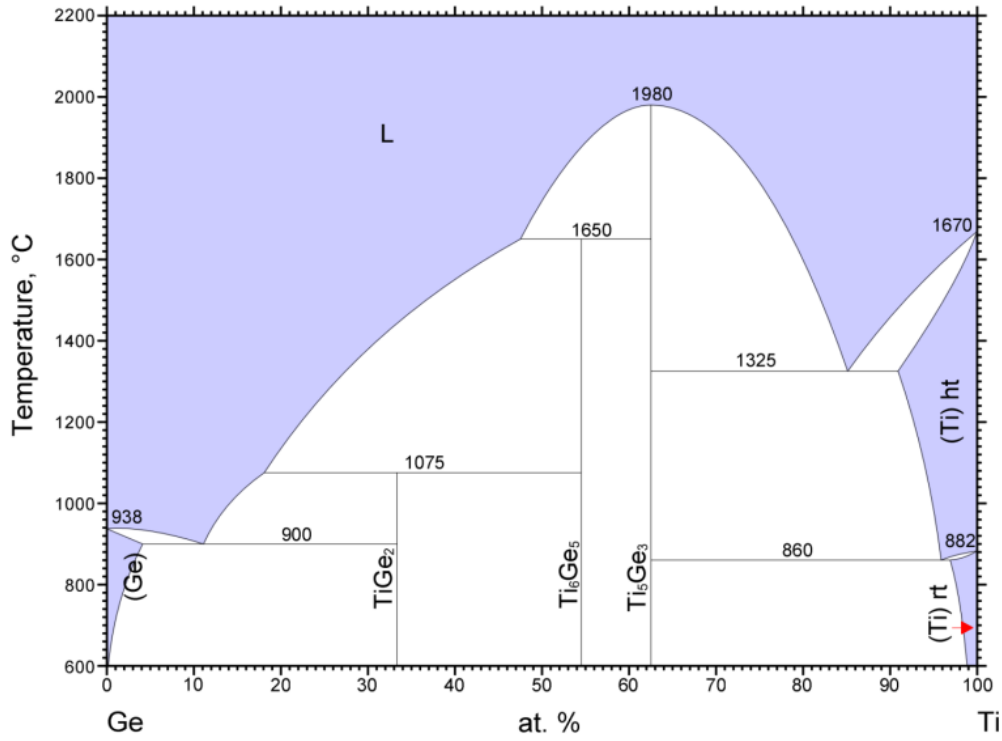

Figure 1.9 Phase diagram of the Ti-Ge binary system (Zarembo, 2000).

Table 1.6 Crystal structures of phases present within the Ti-Ge binary system.

Phase	Composition (at.% Ge)	Pearson Symbol	Space Group	Structure type	Lattice Parameter (Å)		
					a	*b*	*c*
Ge	100	cF8	Fd3m	C	5.6579	-	-
$TiGe_2$	66	oF24	Fddd	$TiSi_2$	5.032	8.588	8.862
Ti_6Ge_5	45	oI44	Ibam	V_6Si_5	7.954	16.92	5.233
Ti_5Ge_3	37	hP16	$P6_3/mcm$	Mn_5Si_3	7.563	-	5.228
Ti	0	cI2	Im3m	W	0.333	-	-

Table 1.7 Reactions present within the Ti-Ge binary system.

Reaction	Compositions of phases (at.% Ge)			Temperature, (^oC)	Reaction type
$L \rightarrow (Ge) + TiGe_2$	11	4	33.3	900	Eutectic
$L + Ti_6Ge_5 \rightarrow TiGe_2$	18	54.5	33.3	1075	Peritectic
$L + Ti_5Ge_3 \rightarrow Ti_6Ge_5$	47.5	62.5	54.5	1650	Peritectic
$L \rightarrow Ti_5Ge_3$		62.5		1980	Congruent
$L \rightarrow Ti_5Ge_3 + (Ti)$ ht	85.1	62.5	91	1325	Eutectic
(Ti) ht $\rightarrow Ti_5Ge_3 + (Ti)$ rt	96	62.5	97	860	Eutectoid

Of the five phases present within the Ti-Ge binary system, the main focus for this report is the presence of Ti_5Ge_3. Table 1.6 shows Ti_5Ge_3 possesses the hexagonal Mn_5Si_3 type crystal structure (*hP16*, $P6_3/mcm$), which is isomorphous with the hexagonal γNb_5Si_3. In section 1.3, it was commented that Ge additions would stabilise the βNb_5Si_3 and Ti_5Si_3 phase, however now it is entirely possible that additions of Ge would stabilise the hexagonal γNb_5Si_3, or even promote the formation of Ti_5Si_3 phase when Ti is present.

1.6 Nb-Cr and Cr-Si binaries and Nb-Cr-Si ternary

The accepted Nb-Cr binary phase diagram is shown in Figure 1.10 reported by Thoma and Perepezko (Thoma and Perepezko, 1992). This diagram was modified from a previous diagram determined by Venkatraman and Neumann

(Venkatraman and Neumann, 1986). There are five stable phases in the Nb-Cr diagram: the BCC Nb_{ss}, a low temperature $NbCr_2$ Laves (C15) phase, a high temperature $NbCr_2$ (C14) Laves phase, the BCC Cr_{ss} and the liquid. There are two eutectic transformations within this phase diagram; the first between Nb_{ss} and $NbCr_2$ at ~ 50.5 at.% Cr, and the second between $NbCr_2$ and Cr_{ss} at ~81.5 at.% Cr.

For the $NbCr_2$ phase, there are two different crystal structures at different temperatures. The C15 $NbCr_2$ phase has a cubic crystal structure and the high temperature C14 $NbCr_2$ phase has a hexagonal crystal structure.

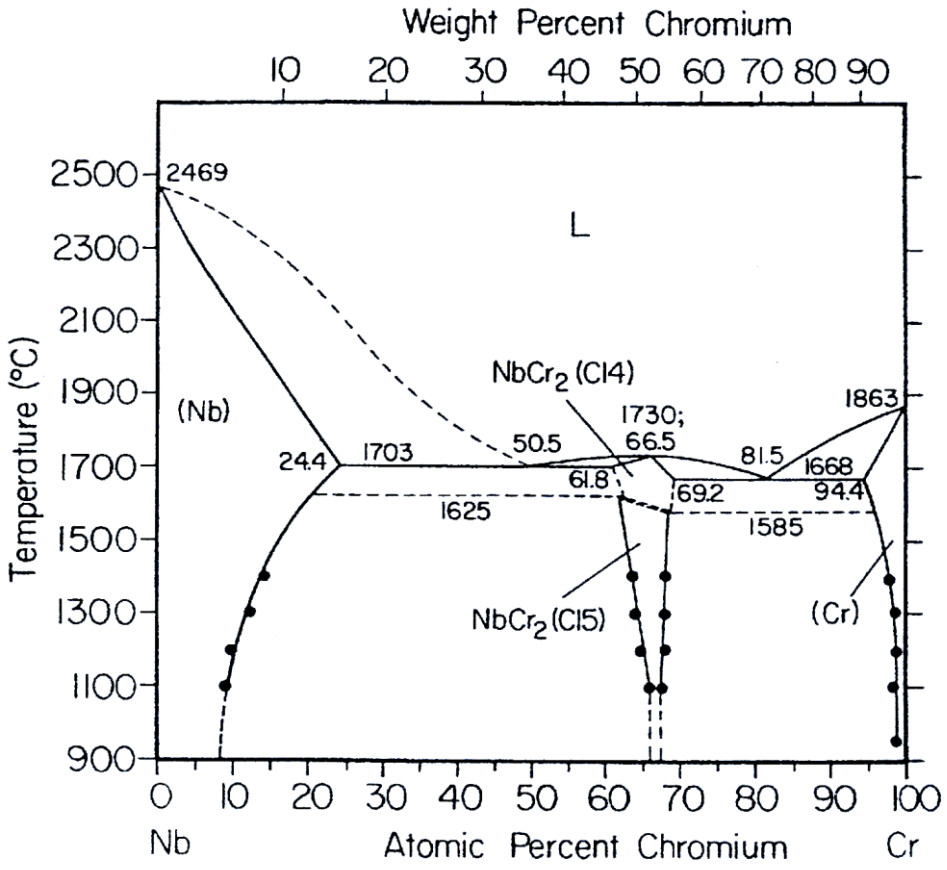

Figure 1.10 Phase diagram of the Nb-Cr binary system

(Thoma and Perepezko, 1992).[5]

[5] Reprinted from Materials Science and Engineering A,179-180, Thoma, D. J., Perepezko, J. H., Plantz, D. H. and Schwarz, R. B, Metastable b.c.c. phase formation in the Nb-Cr system, 176-180, Copyright (2014), with permission from Elsevier.

Figure 1.11 shows an assessed Cr-Si phase diagram and there are seven stable phases present in the binary system, (1) the bcc terminal solid solution (Cr_{ss}) with a maximum solubility of 9.5 at% Si at 1705 ^{o}C, (2) the cubic Cr_3Si which has a melting temperature of 1770 ^{o}C, (3) the tetragonal Cr_5Si_3 which undergoes an allotropic transformation at 1505 ^{o}C (α ↔ β), (4) the cubic CrSi which undergoes a peritectic reaction at 1413 ^{o}C, (5) the hexagonal $CrSi_2$ which has a melting temperature of 1490 ^{o}C, (6) the cubic terminal solid solution (Si_{ss}) and (7) the liquid. When the Cr-Si binary is compared to the Nb-Si binary phase diagram, there are similarities and differences. There is a cubic CrSi (cP8) phase in the Cr-Si system but no NbSi in the Nb-Si system. The βCr_5Si_3 and the γNb_5Si_3 have the same crystal structure (*hP16*), αCr_5Si_3 and βNb_5Si_3 are isomorphous, both with the *tI32* crystal structure, and Cr_3Si and Nb_3Si have different crystal structures, *cP8* and *tP32* respectively (Table 1.9). Hence, the addition of Cr to the Nb-Si system would be expected to stabilise γNb_5Si_3 and βNb_5Si_3 to lower temperatures and to destabilise Nb_3Si.

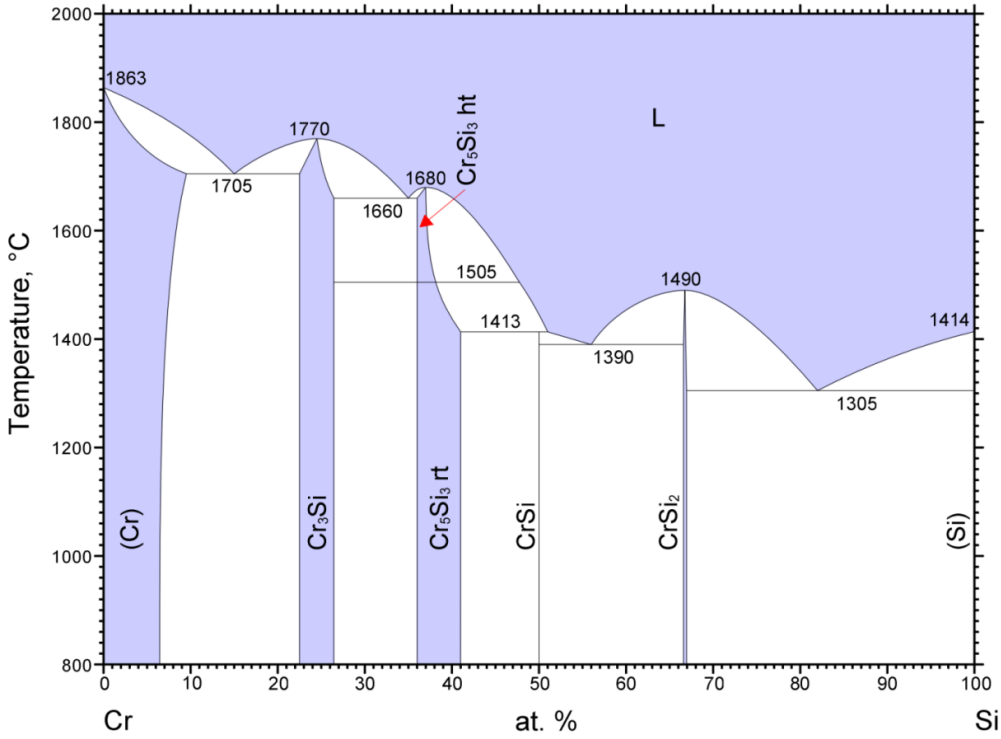

Figure 1.11 Phase diagram of the Cr-Si binary system (Gokhale, 1990a).

It has, however, been widely accepted that there is no high temperature βCr_5Si_3 and that a more appropriate phase diagram to describe the Cr-Si binary system is shown in Figure 1.12. This then suggests Cr additions will stabilise βNb_5Si_3 only.

Table 1.8 Crystal structures of phases present within Cr-Si binary system.

Phase	Composition at.% Si	Pearson Symbol	Space Group	Strukturbericht designation	Prototype
Cr	0 - 9.5	cI2	Im3m	A2	W
Cr_3Si	22.5 - 26.4	cP8	Pm3m	A15	Cr_3Si
αCr_5Si_3	36 - 41	tI38	I4/mcm	$D8_m$	W_5Si_3
(βCr_5Si_3)*	*37.5*	*hP16*	*$P6_3/mcm$*	*$D8_8$*	*Mn_5Si_2)*
CrSi	50	cP8	$P2_13$	B20	FeSi
$CrSi_2$	66.67 - 66.99	hP9	$P6_222$	C40	CrSi
Si	~100	cF8	Fd3m	A4	C (Diamond)

*Not widely accepted

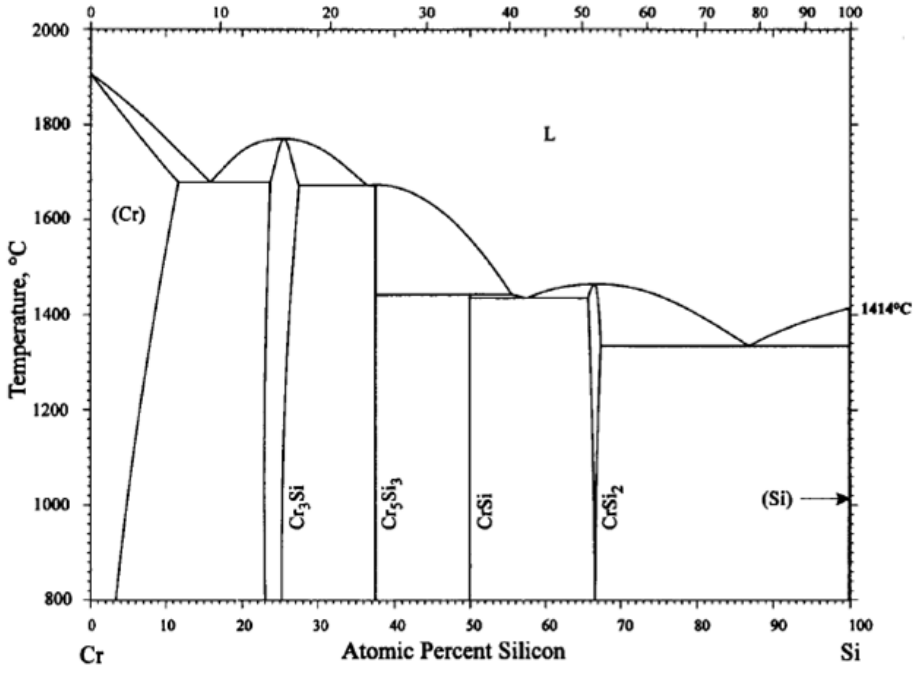

Figure 1.12 More widely accepted phase diagram of the Cr-Si binary system (Okamoto, 1997).[6]

[6] Springer and the Journal of Phase Equilibria, 18, 1997, 222-222, Cr-Si (Chromium-Silicon), Okamoto, H., figure 1, copyright 2014) is given to the publication in which the material was originally published, with kind permission from Springer Science and Business Media

Table 1.9 Reactions present within Cr-Si binary system. Information taken from ASM Alloy phase diagram database under licence 2012.

Reaction	Compositions of the respective phases, at.% Si			Temperature, ^{o}C	Reaction type
$L \leftrightarrow (Cr) + Cr_3Si$	9.5	22.5	15	1705 ± 5	Eutectic
$L \leftrightarrow Cr_3Si$		25		1770 ± 10	Congruent
$L \leftrightarrow Cr_3Si + Cr_5Si_3$	26.4	36	35	1660 ± 10	Eutectic
$L \leftrightarrow Cr_5Si_3$		37.5		1680 ± 20	Congruent
$Cr_5Si_3(\alpha) \leftrightarrow Cr_5Si_3(\beta)$		*36 - 41*		*1505 ± 20*	*Allotropic*
$Cr_5Si_3 + L \leftrightarrow CrSi$	41	51	50	1413 ± 5	Peritectic
$L \leftrightarrow CrSi + CrSi_2$	50	66.67	56	1390 ± 10	Eutectic
$L \leftrightarrow CrSi_2$		66.67		1490 ± 20	Congruent
$L \leftrightarrow CrSi_2 + (Si)$	66.99	8 x 10-6	87	1305 ± 10	Eutectic
$L \leftrightarrow Cr$		0		1860 ± 20	Melting
$L \leftrightarrow Si$		100		1414 ± 2	Melting

The three binary systems that constitute the Nb-Si-Cr ternary phase diagram (Nb-Si, Nb-Cr, Cr-Si) contain a number of terminal and intermediate phases and therefore, the ternary phase diagram is going to be very complex. Figure 1.13 shows an early isothermal section of the Nb-Si-Cr ternary phase diagram at 1000 ^{o}C reported by Goldschmidt and Brand (1961). As suggested, the ternary phase diagram has a high level of complexity to it. Goldschmidt and Brand reported eleven binary phases (including a metastable Nb_4Si) and five ternary (*ρ, τ, θ, β, ν)* phases that had not been seen before. The focus of the work was based on the so called "pseudo-binary" sections of $CrSi_2 \leftrightarrow NbSi_2$ and $Cr_5Si_3 \leftrightarrow Nb_5Si_3$ and the identification of these ternary phases. As $CrSi_2$ and $NbSi_2$ are isomorphous with a C40 structure (see Table 1.8 and Table 1.1) it was expected that a complete series of solid solutions would be possible, however they discovered only limited inter-solubility existed due to the size difference of Cr and Nb. The atomic radii are Cr = 0.117 nm and Nb = 0.134 nm.

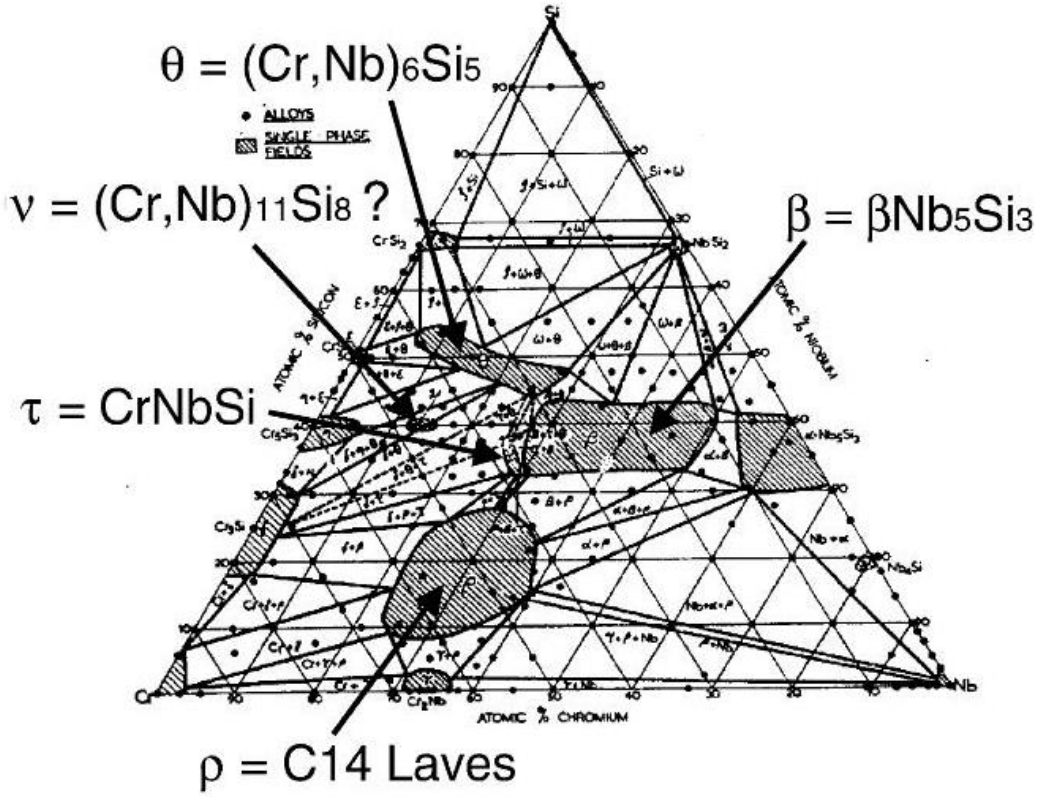

Figure 1.13 Isothermal section (1000 ^{o}C) of the Nb-Si-Cr ternary system (Goldschmidt and Brand, 1961).[7]

The $Cr_5Si_3 \leftrightarrow Nb_5Si_3$ pseudo-binary system provided a more challenging situation. As seen by the data for the Nb-Si system, Nb_5Si_3 exists in two allotropic forms depending on temperature: αNb_5Si_3 is stable below 1935 ^{o}C, and βNb_5Si_3 is stable above 1935 ^{o}C. Both βNb_5Si_3 and αCr_5Si_3 have the same crystal structures (see Table 1.9 and Table 1.1) and therefore, as αCr_5Si_3 is stable to room temperature, it is likely that additions of Cr to Nb-Si will stable the high temperature βNb_5Si_3 to lower temperatures. As this "*β*" phase is present on the 1000 ^{o}C isothermal section in Figure 1.13, additions of Cr can stabilise βNb_5Si_3 to at least 1000 ^{o}C. This "*β*" phase seems to have considerable solubility for Cr ranging from ~8 – 37 at.% Cr.

[7] Reprinted from Acta Materialia, 51, Zhao, J. C., Jackson, M. R. and Peluso, L. A., Determination of the Nb-Cr-Si phase diagram using diffusion multiples, 6395-6405, Copyright (2014), with permission from Elsevier.

Between the β phase field and Cr_5Si_3 there is are two other ternary phase fields. The "*r*" phase has a BCC crystal structure and an approximate composition of $Cr_{37}Nb_{27}Si_{36}$. The "*v*" phase has an appropriate composition of $Cr_{45}Nb_{15}Si_{40}$, however this phase was metastably retained over a certain composition range and therefore, there is some uncertainty in the diagram at this part. At 50 at.% Si, a further ternary phase "*θ*" occurs with a composition range of 6 – 28 at.% Nb, with a representative empirical formula $Cr_7Nb_3Si_{10}$.

The last of the new ternary compounds "*ρ*" is the hexagonal C14 $NbCr_2$ Laves phase. This ternary compound begins to form and replace the cubic C15 Laves phase at ~2.5 at.% Si and is seen to have substantial solubility for all three elements, Nb, Cr and Si. Due to the low 2.5 at.% Si where C14 begins to replace C15 Laves phase, it is clear to see that Si stabilises the hexagonal C14 Laves phase to lower temperatures.

In a more recent study, Zhao et al., (2003a) determined the Nb-Cr-Si phase diagram using a diffusion-multiple approach. They analysed the system using a combination of EPMA and EBSD and produced a set of isothermal sections at 1000 and 1150 ^oC shown in Figure 1.14. They found that the solubility of Cr in Nb_{ss} and Nb_5Si_3 was similar at both temperatures with 3 and 10 at.% respectively in the two phases. They found the hexagonal C14 Laves phase was stabilised to lower temperatures by Si by the Laves phase's presence in both isothermal sections of the ternary system, and that its stability ranged from ~6 – 26 at.% Si and the solubility of Si in the C14 Laves phase was only slightly altered by temperature.

There are many differences in the isothermal sections reported by Goldschmidt and Brand (1961) and by Zhao et al., (2003a) In the latter, $(Cr,Nb)_6Si_5$, $(Cr,Nb)_{11}Si_8$ and the C14 Laves phase are essentially line compounds with a variable Cr/Si ratio, whereas in the former, these phases exhibited larger composition ranges of all three elements. They attributed the differences to the possibility that the alloys used by Goldschmidt and Brand had not fully reached

equilibrium and therefore, the data reported by them does not represent equilibrium conditions. Zhao et al. claimed that the diffusion-multiple approach provided data closer to full equilibrium conditions due to the length of the experiment and heat applied to the system.

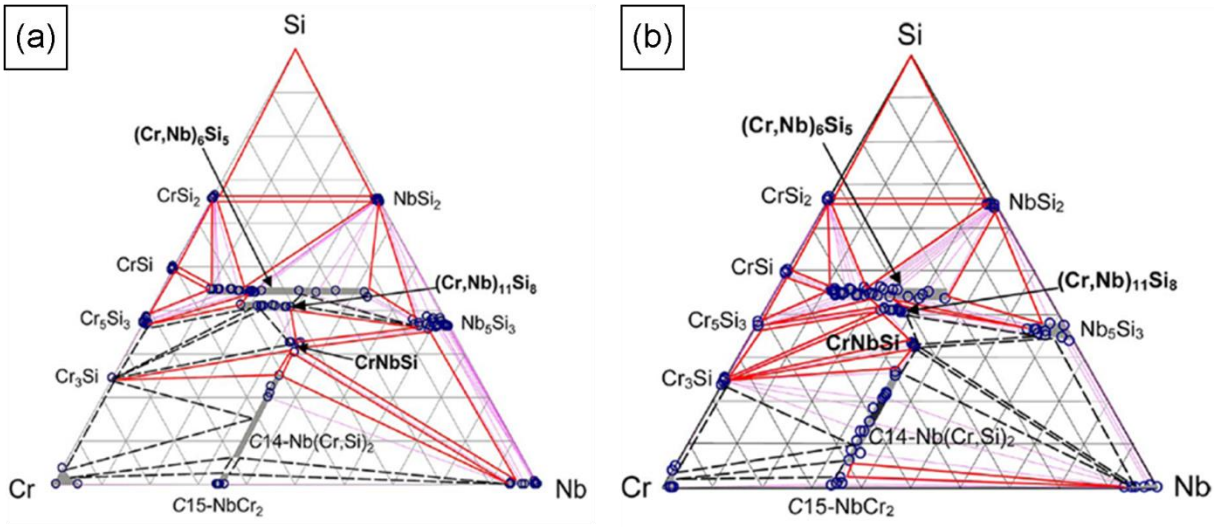

Figure 1.14 Isothermal section of the Nb-Cr-Si ternary system at (a) 1000 ^{o}C and (b) 1150 ^{o}C (Zhao et al., 2003a).[8]

Zhao et al., (2003a) deduced that the crystal structure of the "*θ"* phase (see Figure 1.13) reported by Goldschmidt and Brand (1961) was the same as the crystal structure for $(Cr,Nb)_6Si_5$ and that they too found this phase in equilibrium with $CrSi_2$, $NbSi_2$, CrSi and Cr_5Si_3. They commented on how the primary solidification process may be the cause of why this phase is off the stoichiometric composition of $(Cr,Nb)_6Si_5$. The "*ν", "τ"* and "*ρ*" phases are $(Cr,Nb)_{11}Si_8$, CrNbSi and C14 Laves respectively.

One major difference in the isothermal sections produced by Goldschmidt and Brand and by Zhao et al. is that in the former (Figure 1.13), the Nb_{ss} cannot be in direct equilibrium with the ternary CrNbSi ("*τ*" phase field) giving a three phase

[8] Reprinted from Acta Materialia, 51, Zhao, J. C., Jackson, M. R. and Peluso, L. A., Determination of the Nb-Cr-Si phase diagram using diffusion multiples, 6395-6405, Copyright (2014), with permission from Elsevier.

field of Nb_{ss} + αNb_5Si_3 + C14 Laves phase. In the latter, the Nb_{ss} is in equilibrium with CrNbSi ternary phase giving a three phase region of Nb_{ss} + αNb_5Si_3 + CrNbSi. Later work by Shao, (2005) and Geng et al.,(2006a) showed the three phase region originally reported by Goldschmidt and Brand to be correct.

Even more recently, Bewlay et al., (2009) published work proposing the existence of a new ternary phase $Nb_9(Cr,Si)_5$ and Deal et al., (2007) provided back-up data for its existence separately. This phase was discovered in alloys containing 10 or 12 at.% Si and 25 or 30 at.% Cr. In the alloys containing 18 at.% Si this phase was not seen, therefore any alloy generated with a nominal composition including 18 at.% Si should not have this phase present in the microstructure. The paper by Bewlay et al., (2009) is the only paper where this phase is presented, no other research comments on its presence in any other alloy compositions. Also, the paper claims that the details of the model will be published separately, however to this date, no details have been provided. Whilst the early evidence from both Bewlay et al. and Deal et al. is intriguing, more work is needed to confirm the presence of this phase and details of the thermodynamic model need to be published.

1.7 Nb-Al binary and Nb-Si-Al ternary

The assessed Nb-Al binary phase diagram is shown in Figure 1.15. Shown in the diagram are five stable phases: the FCC Al_{ss} terminal solid solution, the intermediate tetragonal Al_3Nb, the intermediate tetragonal $AlNb_2$, the cubic $AlNb_3$, the BCC Nb terminal solid solution.

From the data in Table 1.10, it should be noted that Nb_3Al has a cubic crystal structure, whereas Nb_3Si has a tetragonal structure (see Table 1.1). As these phases are not isomporhous, additions of Al to the Nb-Si binary system should have the effect of destabilising the Nb_3Al phase, which is an undesirable phase. However,

Nb_3Al and Cr_3Si are isomorphous, both with cP8 structure. This phase is responsible for high temperature strength in Nb-Al based alloys; however it possesses poor fracture toughness and oxidation properties. Therefore, care must be taken when additions of Cr and Al are incorporated into the same alloy to reduce the possibility of forming the brittle Nb_3Al phase. In the literature it has been seen that Al additions are kept below 5 at.% in order to avoid formation of the Nb_3Al phase.

Table 1.10 Reactions present within Nb-Al binary system. Information taken from ASM Alloy phase diagram database under licence 2012.

Phase	Composition, at.% Nb	Pearson Symbol	Space group	Strukturbericht designation	Prototype
(Al)	<0.3	cF8	Fm3m	A1	Cu
Al_3Nb	25	tI8	I4/mmm	$D0_{22}$	Al_3Ti
$AlNb_2$	58.7 - 68	tP30	$P4_2/mnm$	$D8_b$	σCrFe
$AlNb_3$	68 - 82	cP8	Pm3n	A15	Cr_3Si
(Nb)	77 - 100	cI2	Im3m	A2	W

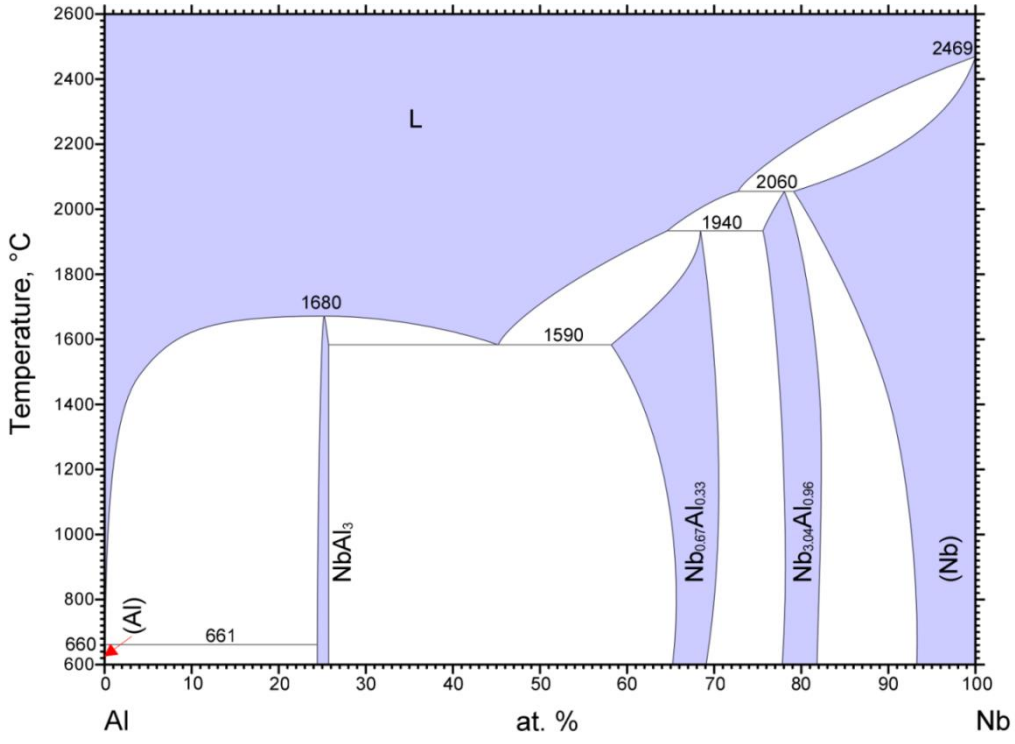

Figure 1.15 Phase diagram of the Nb-Al binary system (Kattner, 1990).

There have been several investigations into the Nb-Si-Al ternary phase diagram, each reporting slight modifications to the phase diagram, contradicting and agreeing with other sections. Brukl et al., (1961) produced the first isothermal section of the Nb-Si-Al ternary phase diagram shown in Figure 1.16(a). The upper part of the isothermal section is for 1400 ^{o}C, and the lower part for 500 ^{o}C. Brukl et al., (1961) determined the presence of two ternary compounds, $Nb_3Si_5Al_2$ and $Nb_{10}Si_3Al_3$ and found them in equilibrium with each other. This determination was not agreed upon by a later study by Pan et al., (1984). They determined that the two ternary compounds were not in equilibrium, but $NbAl_3$ and αNb_5Si_3 were in equilibrium. Pan et al., (1984) also produced an isothermal section of the Nb-Si-Al ternary phase diagram at 1500 ^{o}C, shown in Figure 1.16(b). A more recent study by Murakami et al., (2001) into the Nb-Si-Al ternary system, produced an estimated isothermal section of the Nb-Si-Al ternary system in the temperature range of 1200 – 1600 ^{o}C, shown in Figure 1.16(c). Murakami et al., (2001) looked into the disagreement by Brukl et al. and Pan et al. and discovered similar results to Pan et al. They found Nb_5Si_3 was in equilibrium with $NbAl_3$ and that Pan's diagram is more appropriate around the composition range.

It should be noted from the diagrams Figure 1.16(a-c) that the solubility of Al in αNb_5Si_3 was reported differently by each study. Al solubility in αNb_5Si_3 was reported as near zero by Brukl et al., (1961), ~10 at.% by Pan et al., (1984) and near zero by Murakami et al., (2001)

Zhao et al., (2003b) used the diffusion-multiple approach to investigate the Nb-Si-Al ternary system to help judge the reliability of previously reported data. The isothermal section at 1000 ^{o}C is shown in Figure 1.16(d). Zhao et al. agree with the results of Pan's and Murakami's study that $NbAl_3$ is in equilibrium with αNb_5Si_3. They reported that the solubility of Al in αNb_5Si_3 was ~8 at.% supporting the results of Pan et al. Zhao et al. only observed one ternary compound, $Nb_3Si_5Al_2$, and not the $Nb_{10}Si_3Al_3$. They commented that the latter is actually the binary phase βNb_5Si_3,

based on crystal structure and lattice parameters, stabilised to lower temperatures by the addition of Al.

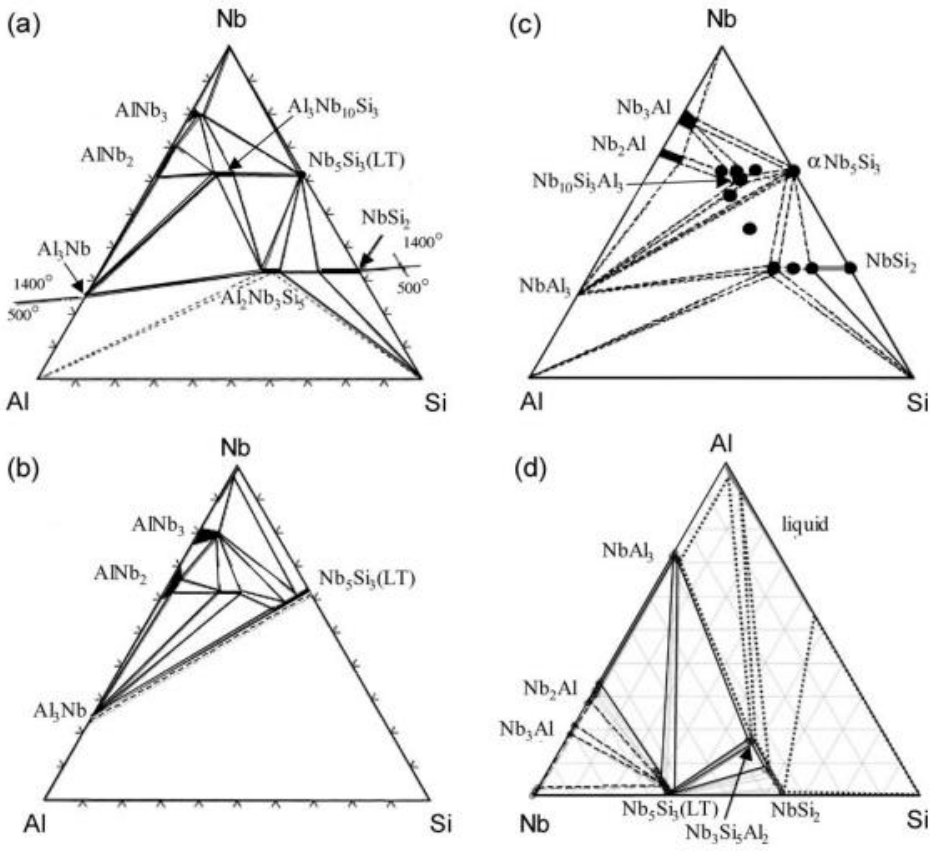

Figure 1.16 Isothermal sections of the Nb-Si-Al ternary system:

(a) the 1400 ^{O}C (upper part) and 500 ^{o}C (lower part) results (Brukl et al., 1961),

(b) the partial isothermal (1500 ^{o}C) reported by (Pan et al., 1984),

(c) tentative isothermal (1200 – 1600 ^{o}C) section reported by (Murakami et al., 2001) and (d) at 1000 ^{o}C for 2000 h (Zhao et al., 2003b).[9]

1.8 Nb-Cr-Al ternary

An isothermal section of the Nb-Cr-Al system at 1000 ^{o}C shown in Figure 1.17 was obtained from the ASM Alloy phase diagram database, but is almost identical to the diagram produced by Hunt and Raman (1968). As can be

[9] Reprinted from Journal of Alloys and Compounds, 360, Zhao, J. C., Peluso, L. A., Jackson, M. R. and Tan, L., Phase diagram of the Nb-Al-Si ternary system, 183-188, Copyright (2014), with permission from Elsevier.

seen, there is a large phase field comprised of the hexagonal C14 Laves phase (labelled in this diagram as NbCrAl). According to the Nb-Cr binary phase diagram (see Figure 1.10), C14 Laves phase is only stable above ~1500 ^{o}C. We have already seen that Si can help stabilise the C14 Laves to lower temperatures, and now by its presence in the isothermal section in Figure 1.17, Al can stabilise the C14 Laves to at least 1000 ^{o}C.

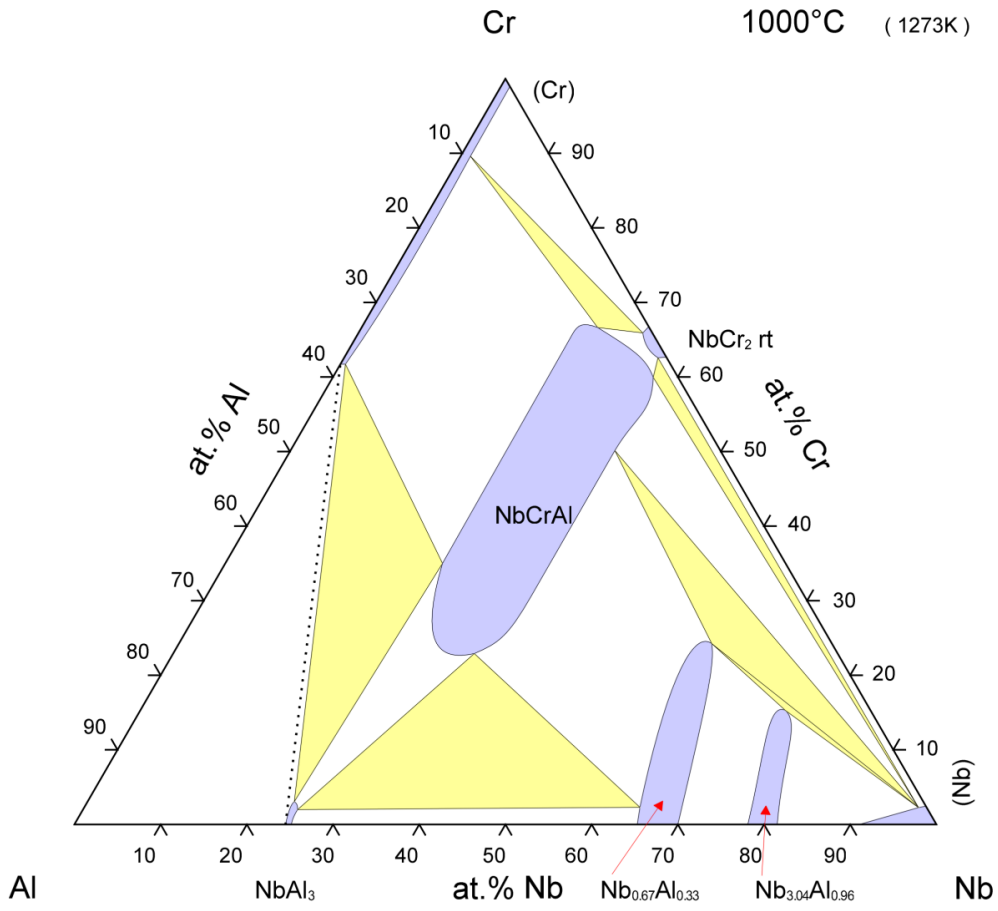

Figure 1.17 Isothermal section (1000 ^{o}C) of the Nb-Cr-Al ternary system phase diagram obtained from (Gramme, 1991).

1.9 Nb-Y, Y-Si and Y-Ge binaries

The addition of Y to Nb-silicide alloy systems has been proposed due to its reported benefits in nickel superalloys and other materials in aiding oxidation resistance (Park, 1989, Smialek, 2000b, Zhao et al., 2010). The addition of Y to the

latter has been seen to improve the adherence of both Cr_2O_3 and Al_2O_3 oxide scales and has been reported to be beneficial in protecting superalloys from attack by sulphur (Smialek, 2000b). Due to its presence Nb-silicide systems, any phase equilbria data dealing with Y and any of Ti, Si, Ge, Cr and Al need to be studied.

Figure 1.18 shows the binary Nb-Y phase diagram clearly showing a lack of any solubility of Nb in Y and vice versa. The two elements do not mix even as liquids. From this is it can be deduced that the majority of the Y present in Nb silicides (if not all) will be present in the last liquid to solidify and will most likely be found between the dendrites of Nb_5Si_3 and Nb_{ss}. This could have an effect on the formation of any Cr_2Nb Laves phase formation. The same behaviour exists for both Y-Ti and Y-Cr binary systems.

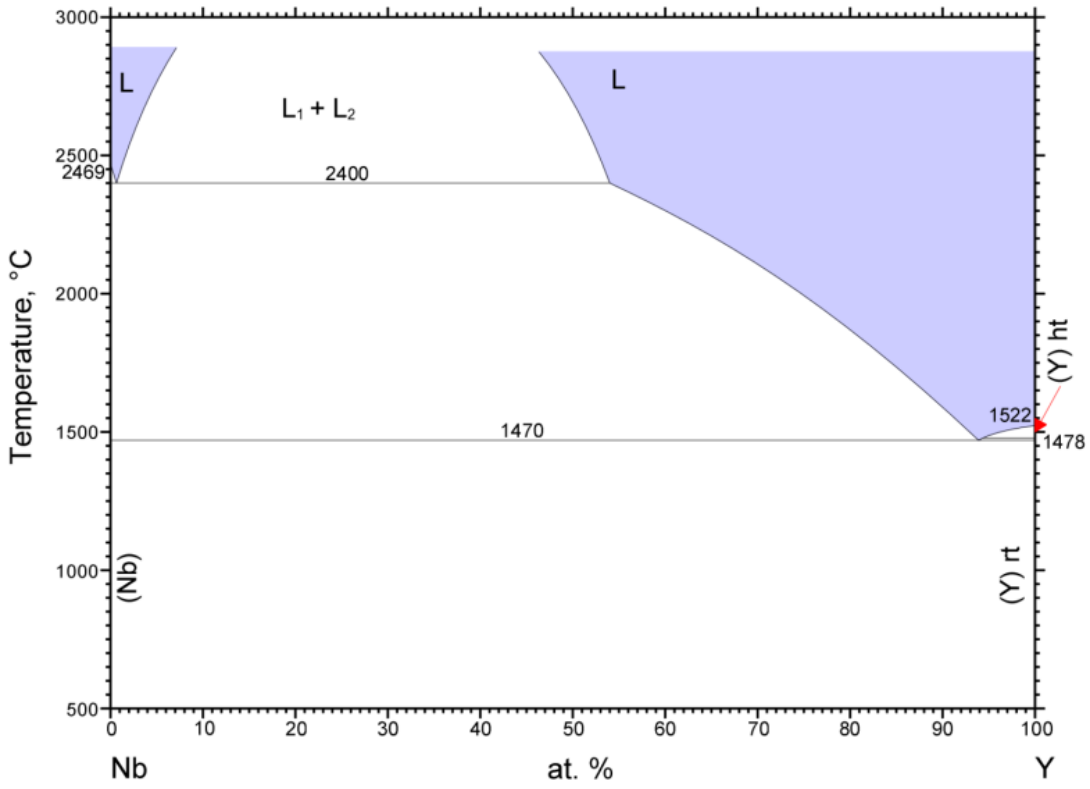

Figure 1.18 Phase diagram of the Nb-Y phase diagram (Palenzona, 1990).

Figure 1.19 shows the phase diagram of the Y-Si binary system and within this system there are several potential phases that can form. Table 1.11 shows there is no presence of a tetragonal Y_3Si, but there is a hexagonal Y_5Si_3 phase. Hence, it is suggested that Y additions will destabilise the formation of Nb_3Si and tetragonal Nb_5Si_3, but will instead promote the formation of γNb_5Si_3 and Ti_5Si_3 (if Ti is present). The binary Y-Ge phase diagram is shown in Figure 1.20 and crystal data and reaction information are presented in Table 1.13 and Table 1.14. Like the Y-Si system, there are several Y-Ge intermetallic phases that form within this system. The most important piece of data from this system is that again, like the Y-Si system, there is no Y_3Ge compound but instead a hexagonal Y_5Ge_3 ($P6_3/mcm$, *hP16*).

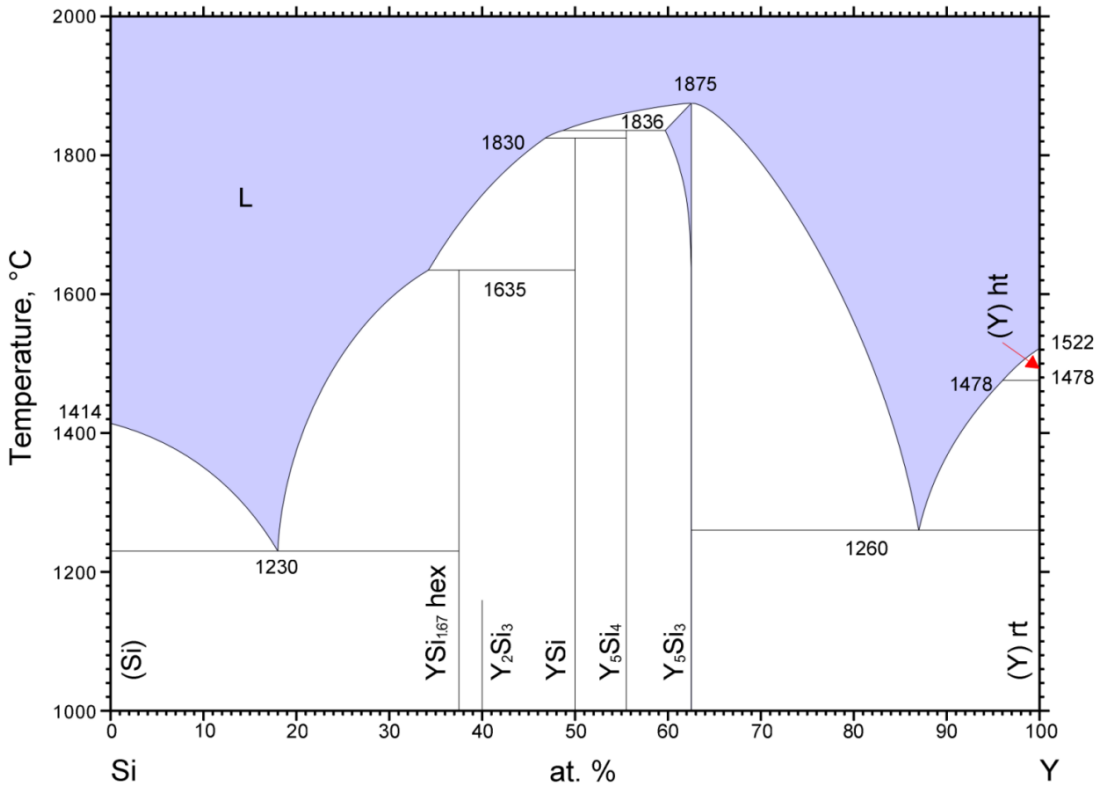

Figure 1.19 Phase diagram of the Si-Y phase diagram (Okamoto, 1991).

Table 1.11 Crystal structures of phases present within Y-Si binary system.

Information taken from ASM Alloy phase diagram database under licence 2012.

Phase	Pearson Symbol	Space Group	Structure type	Lattice Parameter (Å)		
				a	*b*	*c*
(Y) rt	hP2	$P6_3/mmc$	Mg	3.6509	-	5.7388
(Y) ht			***(No data)***			
Y_5Si_3	hP16	$P6_3/mcm$	Mn_5Si_3	8.42	-	6.32
Y_5Si_4	mP36	P121/c1	$Gd_5(Ge_{0.5}Si_{0.5})_4$	14.613	7.6592	7.4722
Y_2Si_3			***(no data)***			
$YSi_{1.67}$	hP3	P6/mmm	AlB2	3.842	-	4.14
YSi	oS8	Cmcm	T I	4.251	10.526	3.826
Si	cF8	Fd3m	C	5.4309	-	-

Table 1.12 Reactions present within Y-Si binary system.

Information taken from ASM Alloy phase diagram database under licence 2012.

Reaction	Compositions of phases (at.% Si)		Temperature, (^oC)	Reaction type
$L \rightarrow (Si) + YSi_{1.67}$ ht	18	0	1230	Eutectic
$L + YSi \rightarrow YSi_{1.67}$ ht	34	50	1635	Peritectic
$L + Y_5Si_4 \rightarrow YSi$	47	55.6	1820	Peritectic
$L + Y_5Si_3 \rightarrow Y_5Si_4$	48.7	60	1836	Peritectic
$L \rightarrow Y_5Si_3$	-	62.5	1875	Congruent
$L \rightarrow Y_5Si_3$ + (Y) rt	87	62.5	1260	Eutectic
L + (Y) ht + (Y) rt	96	100	1478	unknown

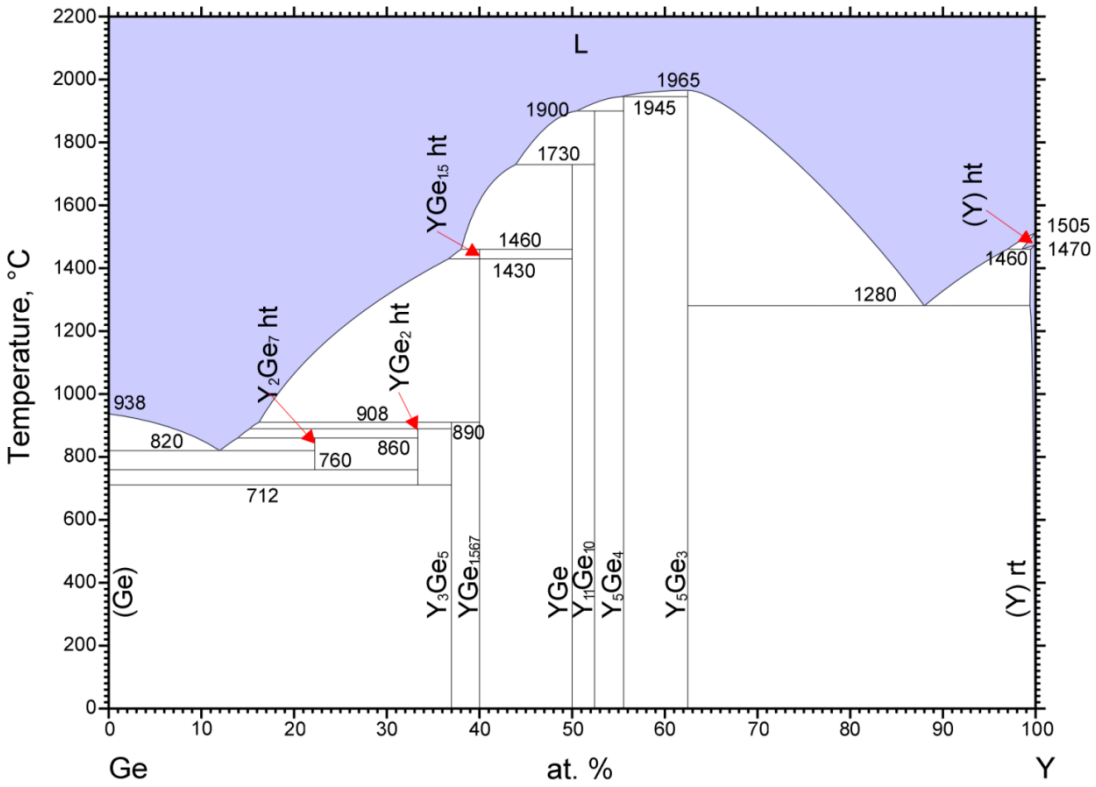

Figure 1.20 Phase diagram of the Ge-Y phase diagram (Gokhale, 1990b).

Table 1.13 Crystal structures of phases present within Y-Ge binary system.

Information taken from ASM Alloy phase diagram database under licence 2012.

Phase	Pearson Symbol	Space Group	Structure type	Lattice Parameter (Å)		
				a	*b*	*c*
(Y) rt	hP2	$P6_3/mmc$	Mg	3.6509	-	5.7388
(Y) ht			***(No data)***			
Y_5Ge_3	hP16	$P6_3/mcm$	Mn_5Si_3	8.42	-	6.36
Y_5Ge_4	oP36	Pnma	Sm_5Ge_4	7.6317	14.695	7.6963
$Y_{11}Ge_{10}$	tI84	I4/mmm	$Ho_{11}Ge_{10}$	10.86	-	16.39
Y_3Ge_5	oF64	Fdd2	Y_3Ge_5	5.746	17.284	13.696
Y_2Ge_7 (ht)	oS72	-	-	4.047	15.636	20.84
YGe_2	oP48	-	-	8	8.2	14.92
$YGe_{1.567}$	-	-	-	3.948	6.802	4.142
$YGe_{1.5}$	hP3	P_6/mmm	AlB_2	3.938	-	4.137
YGe	oS8	Cmcm	T I	4.262	10.694	3.941
Ge	cF8	Fd3m	C	5.6579	-	-

Table 1.14 Reactions present within Y-Ge binary system.

Information taken from ASM Alloy phase diagram database under licence 2012.

Reaction	Compositions of phases (at.% Si)			Temperature, (^{oC})	Reaction type
L → (Ge) + Y_2Ge_7 ht	12	0	22.2	820	Eutectic
L + YGe_2 ht → Y_2Ge_7 ht	14	33.3	22.2	860	Peritectic
Y_2Ge_7 ht →(Ge) + YGe_2 ht	22.2	0	33.3	760	Eutectoid
L + Y_5Ge_3 → YGe_2 ht	15	37.5	33.3	880	Peritectic
YGe_2 ht → (Ge) + Y_3Ge_5	33.3	0	37.5	710	Eutectoid
L + $YGe_{1.567}$ → Y_3Ge_5	16.5	40	37.5	910	Peritectic
L + YGe → $YGe_{1.5}$ ht	38.5	50	40	1460	Peritectic
$YGe_{1.5}$ ht → $YGe_{1.567}$		40		1430	Polymorphic
L + $Y_{11}Ge_{10}$ → YGe	44	52.4	59	1730	Peritectic
L + Y_5Ge_4 → $Y_{11}Ge_{10}$	50	55.6	52.4	1900	Peritectic
L + Y_5Ge_4 + Y_5Ge_3	55.6	55.6	62.5	1945	unknown
L →Y_5Ge_3		62.5		1965	Congruent
L → Y_5Ge_3 + (Y) rt	88	62.5	99.5	1280	Eutectic
(Y) ht → L + (Y) rt	99.5	97.5	99.5	1460	Catatectic

1.10 Summary of important crystal structure data

There are many complex interactions that can occur when attempting to combine many elements into an Nb silicide alloy. Table 1.15 shows a summary of the most important phases, crystal structures and prototype information that needs to be considered with the elements that are present in the alloys generated in this study. The combination of elements used in this study could possibly provide a microstructure containing both tetragonal and hexagonal phases.

Table 1.15 Summary of the crystal structures.

Phase	Pearson Symbol	Space group	Structure Type	
Nb_3Si	***tP32***	***$P4_2/n$***	***--***	***Ti_3P***
Ti_3Si	tP32	$P4_2/n$	-	Ti_3P
Cr_3Si	cP8	Pm3m	A15	Cr_3Si
Nb_3Al	cP8	Pm3n	A15	Cr_3Si
$Nb_{3.2}Ge_{0.8}$	cP8	Pm3n		Cr_3Si
βNb_5Si_3	***tI32***	***I4/mcm***	***$D8_m$***	***W_5Si_3***
$(\alpha)Cr_5Si_3$	tI32	I4/mcm	$D8_m$	W_5Si_3
Nb_5Ge_3	tI32	I4/mcm	$D8_m$	W_5Si_3
γNb_5Si_3	***hP16***	***$P6_3/mcm$***	***$D8_8$***	***Mn_5Si_3***
Ti_5Si_3	hP16	$P6_3/mcm$	$D8_8$	Mn_5Si_3
Ti_5Ge_3	hP16	$P6_3/mcm$	$D8_8$	Mn_5Si_3
Y_5Ge_3	hP16	$P6_3/mcm$	$D8_8$	Mn_5Si_3
Y_5Si_3	hP16	$P6_3/mcm$	$D8_8$	Mn_5Si_3
$(\beta)Cr_5Si_3$	*hP16*	*$P6_3/mcm$*	*$D8_8$*	*Mn_5Si_3*
αNb_5Si_3 rt	***tI32***	***I4/mcm***	***$D8_1$***	***Cr_5B_3***

Chapter 2

Literature review: Processing and Mechanical Properties

2.1 Introduction

An understanding of the mechanical properties of intermetallic alloys is key to the successful implementation of these materials in structural applications, not only to ensure that these materials can survive the operating conditions, but also that they can survive any processing or machining (if necessary) to acquire the final component shape. Fracture toughness, which is crucial for structure critical components, and creep, which is important for materials operating at high temperatures, are both very important final properties of all alloys, not just Nb-based *in-situ* composites, which will be discussed in this chapter.

2.2 Processing

Different processing techniques have been used to produce Nb-silicide based *in-situ* composites including arc melting (AM) and casting, directional solidification (DS), physical vapour deposition (PVD) and powder metallurgy (PM) (Bewlay et al., 1999, Bewlay and Jackson, 2000, Bewlay et al., 2002, Mendiratta and Dimiduk, 1993, Mendiratta et al., 1991, Subramanian et al., 1997, Dicks et al., 2009, Wang et al., 2010a, Wang et al., 2010b, Wang and Zhang, 2010), with each technique providing a different microstructure. There is a problem, however, when using solidification processing to produce these alloys, as it is severely limited by the existing mould materials that cannot withstand the high temperatures required to melt the alloy. Thus, cold crucible methods have been developed in conjunction with arc melting and DS. Directional Solidification techniques that have been employed are optical image float zone processing (OIFZ), Czochralski and Bridgman methods (Bewlay and Jackson, 2000, Bewlay et al., 2002, Bewlay et al., 1999).

2.2.1 Arc Melting

Both consumable and non-consumable electrode arc melting have been extensively employed to produce Nb silicide based alloys as it provides an economical method to produce alloys of high melting points under appropriate inert gases. The alloy is melted using plasma under an Ar atmosphere and the plasma can impose mixing which can be controlled using the current and electrode distance from the melt. After melting, the ingot is left to cool in a water cooled Cu crucible and inverted and re-melted several times to ensure homogeneity. There are several disadvantages of this method for manufacture of Nb silicide alloys. Firstly, loss of low melting point materials can occur and the overall composition of the alloy can be different than intended (Mendiratta and Dimiduk, 1993). Secondly, cracks and pores remain in the ingot, most likely due to thermal stresses arising between the top and bottom of the ingot, and also solidification shrinkage can be present in the centre of the ingot rather than on an outer edge. Thirdly, it is difficult to control the cooling rate and the solidification path using a cold hearth technique and finally, large scale macrosegregation of elements can be present. Levels of macrosegregation and microstructure morphology can depend upon the alloying additions (Geng et al., 2006b, Geng et al., 2007a, Grammenos and Tsakiropoulos, 2010, Li and Tsakiropoulos, 2013, Vellios and Tsakiropoulos, 2007, Zelenitsas and Tsakiropoulos, 2005).

2.2.2 Rapid Solidification

Several studies have looked at the microstructure morphology and phases present during rapid solidification of these alloys using both arc melting and melt spinning (Abbaschian and Lipschutz, 1997, Bendersky et al., 1987, Gokhale et al., 1988). For arc melting, the rapid solidification occurs where the melt is in contact with the water cooled Cu hearth. As mentioned in the previous chapter (section 1.1) under rapid solidification conditions, the eutectic of Nb_{ss} and Nb_3Si is suppressed

and a new, metastable eutectic of Nb_{ss} and βNb_5Si_3 is present at a higher Si content, therefore, care must be taken if these materials are to be directionally solidified as eutectics.

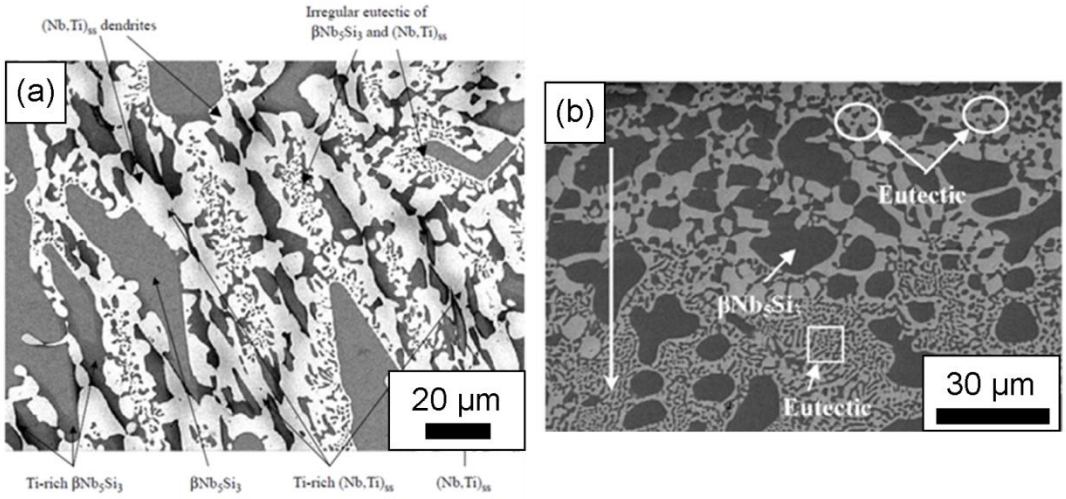

Figure 2.1 SEM images of as cast microstructures of (a) KZ7 (Zelenitsas and Tsakiropoulos, 2005, Zelenitsas and Tsakiropoulos, 2006b) (Image from the centre of ingot)[10] and (b) ZF1 (Zifu and Tsakiropoulos, 2010) (microstructure present at the melt, mould interface)[11]. Arrow shows the directionality of the ingot from melt/mould interface to the bulk.

This issue will be discussed in the next section. The works dealing with rapid solidification of Nb-Si show that transitions can exist between morphologies of the microstructure. Bendersky et al., (1987) showed that with a high enough undercooling even a glass can form. Under the correct conditions, very fine eutectics form in the undercooled melt and transform into primary dendrites and interdendritic eutectic regions further from the chilled surface. Work has also shown that anomalous eutectics can form at the chilled surface, as shown by Figure 2.1(b).

[10] Reprinted from Intermetallics, 14, Zelenitsas, K. and Tsakiropoulos, P., Study of the role of Ta and Cr additions in the microstructure of Nb-Ti-Si-Al in situ composites, 639-659, Copyright (2014), with permission from Elsevier.

[11] Reprinted from Intermetallics, 18, Zifu, L. I. and Tsakiropoulos, P., Study of the effects of Ge addition on the microstructure of Nb-18Si in situ composites, 1072-1078, Copyright (2014), with permission from Elsevier.

This image shows a transition from an anomalous eutectic to a regular eutectic structure and other work has shown the reverse (Li and Kuribayashi, 2003, Li et al., 2002).

2.2.3 Directional Solidification

2.2.3.1 Float Zone processing

A schematic of optical imaging float zone technique (OIFZ) is shown in Figure 2.2. In float zone processing, a small volume of the alloy (in a relatively large rod-type charge) is melted, the molten zone is translated along the rod where solidification takes place. A crucible is not required as the molten zone is retained in position due to surface tension between two rods. The main advantages of this method are that it is clean and capable of working with a range of different materials. However, specimen size is limited and the material must possess a high level of homogeneity (Bewlay et al., 1999). An example of a directionally solidified microstructure is shown in Figure 2.3.

2.2.3.2 Czochralski Method

Directionally solidified ingots have been prepared via Czochralski crystal growth from an induction levitated melt using higher growth rates than those seen for Ni-based superalloys and a schematic of the equipment is shown in Figure 2.4 (Bewlay et al., 2002). The alloys are induction-levitation melted in a segmented, water-cooled Cu crucible. The seed of the alloy to be directionally solidified is lowered into the melt and withdrawn at a constant rate (Bewlay et al., 1999). This method has been used to produce alloys with a range of melting temperatures up to ~2300 ^{o}C (Bewlay et al., 1999) and it is very flexible for producing highly alloyed Nb *in-situ* composites.

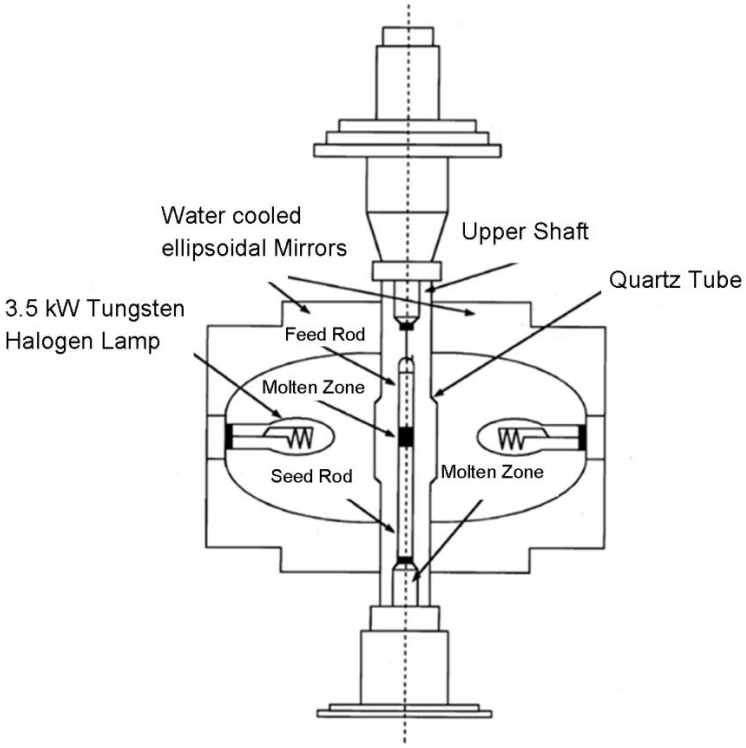

Figure 2.2 Schematic of OIFZ processing (Bewlay et al., 1999).[12]

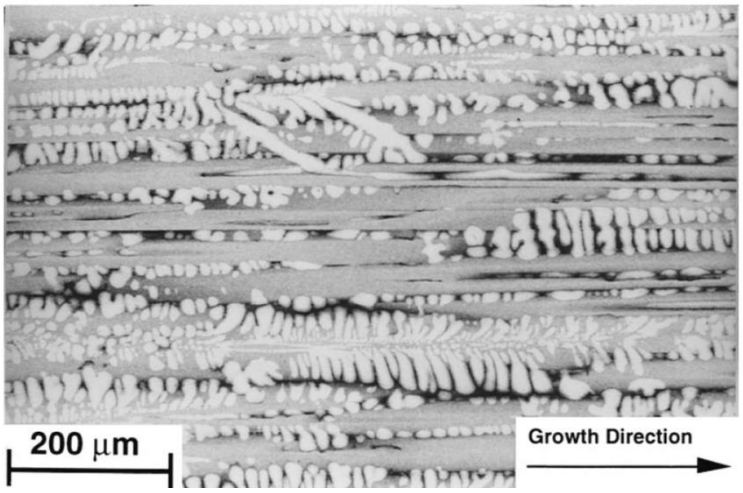

Figure 2.3 Example of DS microstructure (Bewlay et al., 1996)[13].

[12] Permission obtained from Cambridge University Press for MRS Online Proceedings Library, 322, Pope, D. P., Shah, D. M., Romanow, W. and Huntley, M., Directional Solidification of Refractory Intermetallics: Single Crystals and Composites, 1993,Copyright 2014

[13] Springer and the Metallurgical and Materials Transactions A, 27, 1996, 3801-3808, The balance of mechanical and environmental properties of a multielement niobium-niobium silicide-based In Situ composite, Bewlay, B. P., Jackson, M. R. and Lipsitt, H. A., figure 2(a), copyright 2014) is given to the publication in which the material was originally published, with kind permission from Springer Science and Business Media

2.2.3.3 Bridgman Method

The Bridgman method is very similar to the Czochralski method (Figure 2.5), only this time, the water-cooled copper crucible is withdrawn in a controlled manner through the electromagnetic field that is used to melt the alloy by induction levitation (Bewlay and Jackson, 2000).

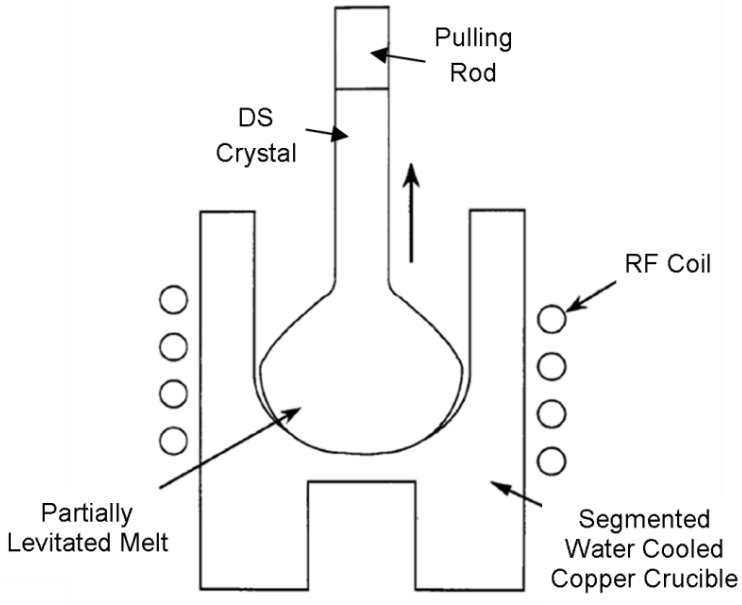

Figure 2.4 Schematic of Czochralski method (Bewlay and Jackson, 2000).[14]

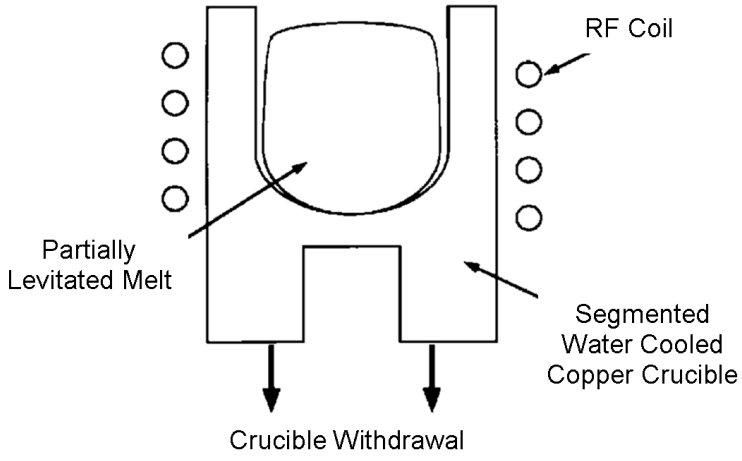

Figure 2.5 Schematic of Bridgman method(Bewlay and Jackson, 2000).[14]

[14] Reprinted from *Comprehensive Composite Materials*, Bewlay, B. P. and Jackson, M. R., High-temperature In Situ Composites: Processing and Properties, 579-615, Copyright (2014), with permission from Elsevier.

2.2.3.4 Mould Materials

Up until now, directional solidification has used either non-mould or cold mould techniques, such as those that have been described previously, however, use of ceramic crucibles could provide an alternative method with high enough melting temperatures to accommodate melting of Nb silicide alloys. One group has researched the possible use of Y_2O_3 as a mould material for DS of Nb silicide alloys (Ma et al., 2012a, Ma et al., 2012b, Ma et al., 2012c), due to its high melting temperature of 2438 ^oC and its previous application to induction melting and investment casting of Ti alloys. They found that during solidification of alloys containing Hf, there was an interaction layer between the mould wall and the melt, comprised of Y_2O_3 and HfO_2 and found $HfO_2 – Y_2O_3$ inclusions both around the solid liquid interface but also in the steady state growth region of the alloy (Figure 2.6). In an alloy containing no Hf, they found no reaction layer at the mould melt interface but found higher levels of Ti at the metal mould interface. If high temperature Y_2O_3 moulds were to be used in a manufacturing process, further machining would be required in order to remove this reaction layer.

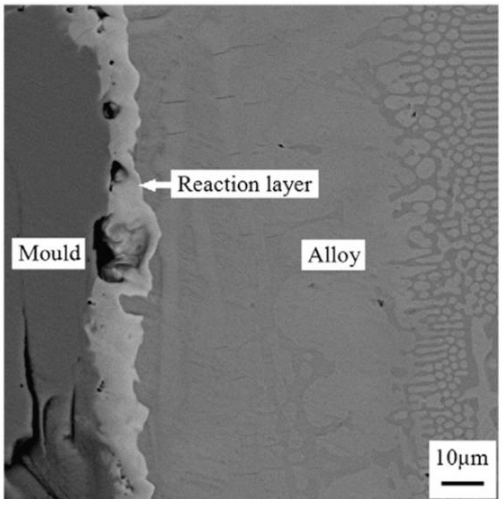

Figure 2.6 Image of the reaction layer between melt and Y_2O_3 mould during DS (Ma et al., 2012c).[15]

[15] Reprinted from International Journal of Refractory Metals and Hard Materials, Ma, L. M., Yuan, S. N., Cui, R. J., Tang, X. X., Li, Y. L., Gao, M. and Zhang, H., M. R., Interactions between Nb-silicide based alloy and yttria mould during directional solidification, 96-101, Copyright (2014), with permission from Elsevier.

2.2.4 Powder Metallurgy

The use of powders as starting materials and mechanical alloying has been employed to produce several Nb-Si alloys (Li and Peng, 2007, Wang et al., 2010a, Wang et al., 2010b, Wang and Zhang, 2010, Jéhanno et al., 2005). The technique involved ball milling of powder for different lengths of time followed by sintering or hot isostatic pressing (HIP). This technique has allowed for a variety of equilibrium and non-equilibrium phases to be produced in the microstructure (example shown in Figure 2.7) by using different powders. Mechanical alloying has the advantage over casting techniques of minimising macrosegregation.

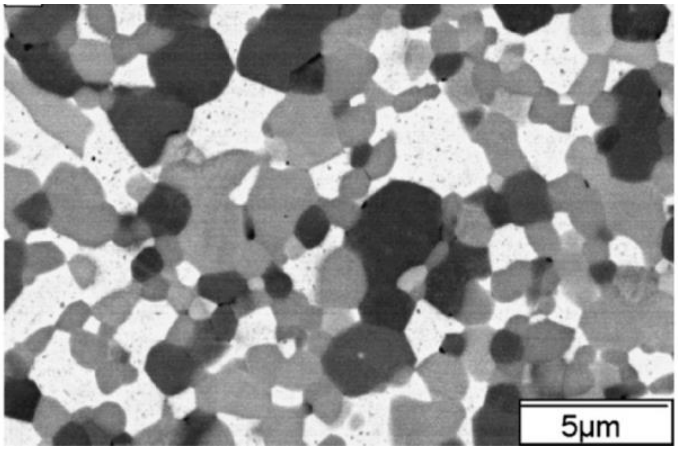

Figure 2.7 Microstructure of mechanically alloyed and HIP(ed) Nb-16Si (Wang and Zhang, 2010).[16]

2.2.5 Extrusion

The microstructures and mechanical properties of several Nb-silicide based *in-situ* composites have been evaluated in the extruded plus heat treated conditions (Mendiratta and Dimiduk, 1993, Mendiratta et al., 1991). Commonly, the grains align themselves in the extrusion direction (Figure 2.8). Mendiratta et al., (1991) reported that the extrusion process rendered the primary, large Nb_{ss} much softer than its

[16] Reprinted from Journal of Alloys and Compounds, 490, Wang, X. L. and Zhang, K. F., Mechanical alloying, microstructure and properties of Nb–16Si alloy, 677-683, Copyright (2014), with permission from Elsevier.

initial condition when just cast and heat treated (Mendiratta et al., 1991). This could prove beneficial in increasing the fracture toughness of these alloys, which is inherently low.

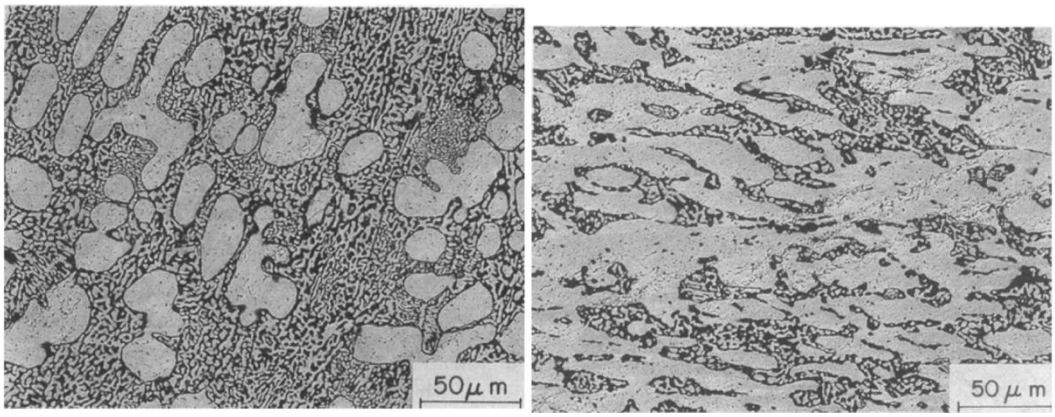

Figure 2.8 Microstructure of a Nb-10Si alloy (a) in heat treated (1500 ^{o}C for 100 h) and (b) extruded conditions (Mendiratta et al., 1991) (extrusion from left to right).[17]

2.2.6 Vapour-phase processing

Vapour phase processing allowed microstructure morphologies to be produced via sputter deposition of alternate layers of metallic and intermetallic phases. With this type of processing, the laminate thickness of each phase can be carefully controlled by altering the time of exposure of a phase and/or the deposition rate (Bewlay et al., 1999). The microstructure can also be graded to generate high vol. % of Nb_{ss} for the core, to provide toughness and low vol. % of Nb_{ss} closer to the surface to reduce metal recession via oxidation (Bewlay et al., 1999). Sputter deposition is very time insensitive and is perfect for the study of a specific composite phase chemistry and composition, but is largely impractical for large scale, economical manufacture of aerospace components (Jackson et al., 1996).

[17] Springer and the Metallurgical and Materials Transactions A, 22, 1991, 1573-1583, Strength and ductile-phase toughening in the two-phase Nb/Nb_5Si_3 alloys, Mendiratta, M., Lewandowski, J. and Dimiduk, D, figure 1(a) and 3(b), copyright 2014) is given to the publication in which the material was originally published, with kind permission from Springer Science and Business Media

2.3 Mechanical properties

Whilst the discussion so far has dealt primarily with microstructure, phases and solidification (which is what this research deals with), it is necessary to discuss the mechanical properties of these alloys that have been investigated by researchers. Whilst Nb-Si alloys have received attention due to the high melting temperature and potential properties associated with incorporating a metallic and intermetallic phase together, it is these properties that will determine whether or not the material is incorporated into any future design.

2.3.1 Brittle to Ductile Transition temperature (BDTT)

The BDTT is very important if Nb silicide alloys are ever to be used in service as structural materials. In order to reduce the risk of a structure critical component failing via brittle fracture, the BDTT needs to be kept low and not go beyond -50 ^{o}C in aerospace materials. When discussing the BDTT, it is that of the Nb_{ss} that needs to be addressed, not necessarily the intermetallic phases. The BDTT for pure Nb is in the region of -200 ^{o}C making it a very attractive material for structural applications (Grill and Gnadenberger, 2006). However, alloying additions can have a dramatic effect on this value. Figure 2.9 shows the effect of interstitials such as O and N on the BDTT and hardness (HV) of pure Nb (Grill and Gnadenberger, 2006). It shows that minimal levels of interstitials can induce a very rapid rise in the BDTT. Due to this, any annealing or heat treatments need to be conducted carefully under an inert atmosphere. Begley (1994) also showed the effect of several different alloying additions on the BDTT (Figure 2.10). The work showed that Ti can have a beneficial effect (or much less detrimental effect) than many other elements on mechanical properties.

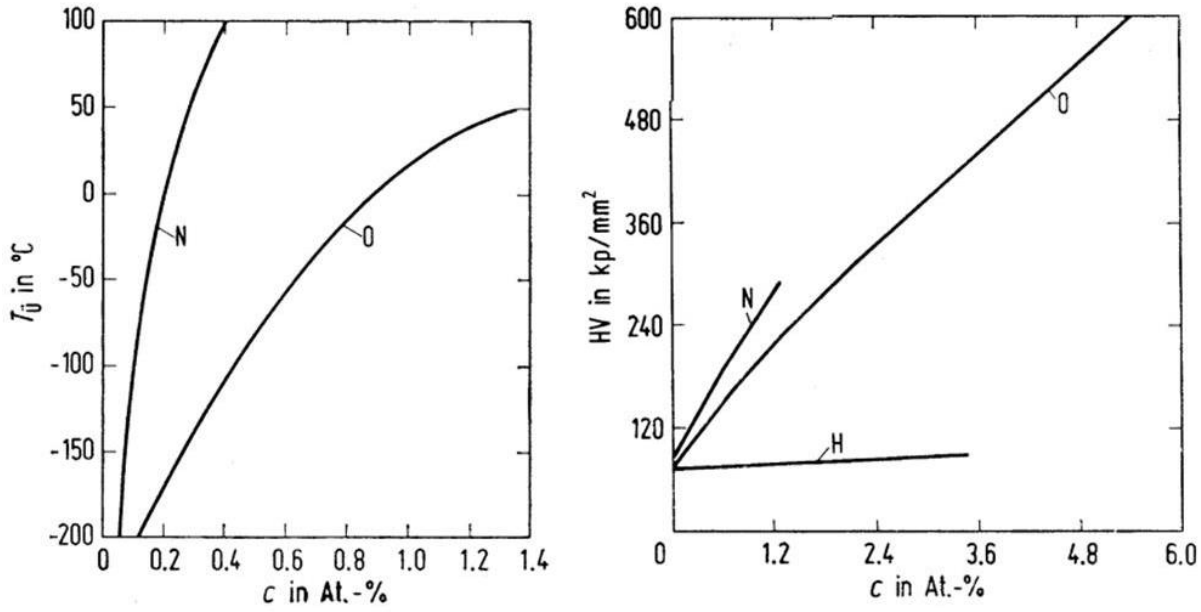

Figure 2.9 The influence of interstitials on (a) the BDTT and (b) the hardness of Nb (Grill and Gnadenberger, 2006).[18]

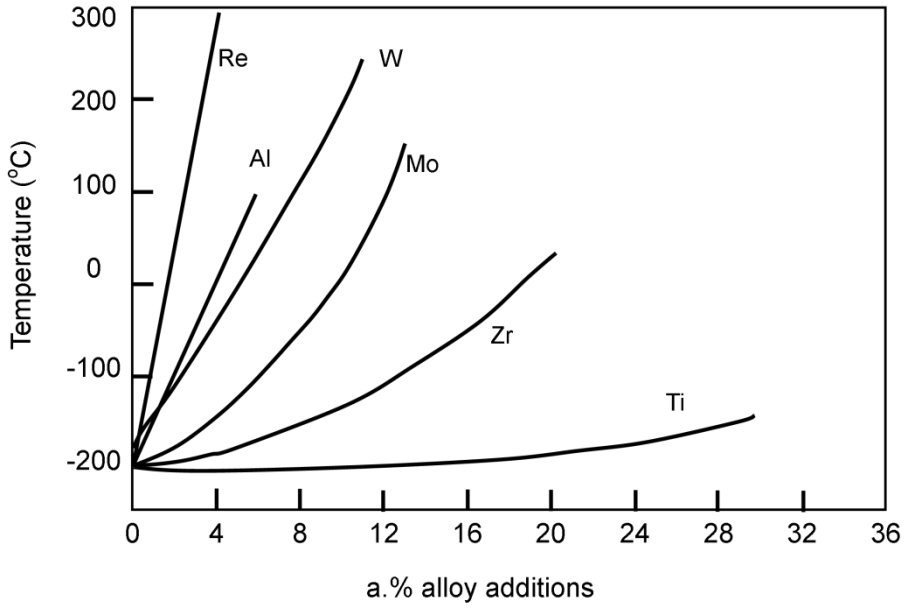

Figure 2.10 Effect of alloying additions on the BDTT. Image adapted from (Begley, 1994).

[18] Reprinted from International Journal of Refractory Metals and Hard Materials, 24, Grill, R. and Gnadenberger, A., Niobium as mint metal: Production-properties-processing, 275-282, Copyright (2014), with permission from Elsevier.

2.3.2 Fracture toughness

A fracture toughness of 20 MPa√m is considered to be the minimum value for structure critical components and achieving this level is now considered to be fairly straight forward (Bewlay et al., 2002).There have been many studies looking at the fracture behaviour of Nb-based *in-situ* composites, looking at the fracture of individual phases (Kim et al., 2001, Chan, 2005, Chan, 2002) and the effects of alloying elements, specifically Ti, on the fracture behaviour of these alloys (Davidson et al., 1996, Chan and Davidson, 1999). Figure 2.11 shows the fracture toughness levels for a series of Nb-based composites (Bewlay and Jackson, 2000).

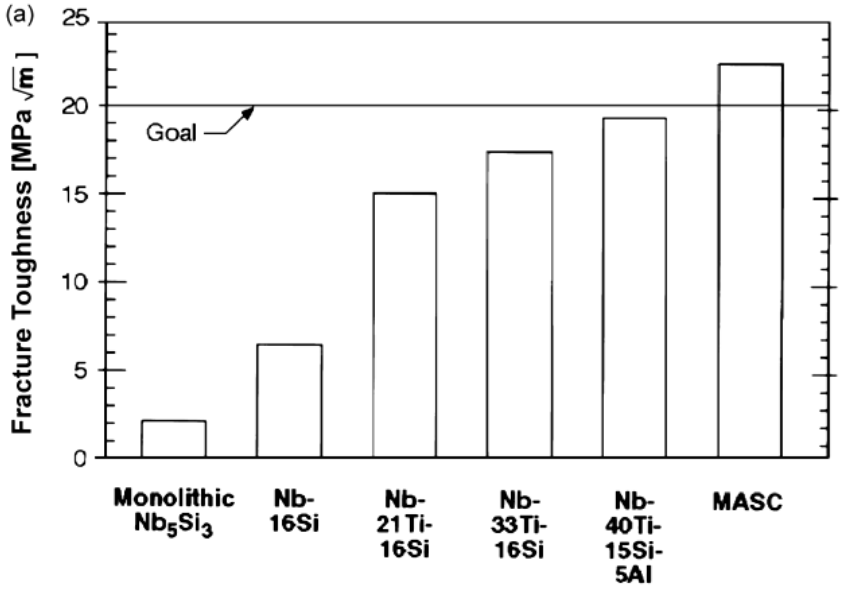

Figure 2.11 Fracture toughness levels of a series of Nb-based composites including binary and ternary alloys (MASC is an Nb-Ti-Hf-Al-Cr-Si composition alloy) (Bewlay and Jackson, 2000).[14]

What should be noted from the diagram is that addition of Ti has a marked beneficial effect on the fracture toughness of these alloys and several studies have looked into how Ti provides this improvement in fracture toughness (Davidson et al., 1996, Chan and Davidson, 1999).

2.3.3 Fracture mechanisms

In order to achieve an acceptable level of fracture toughness for a brittle material, it is widely accepted that the incorporation of a metallic, ductile phase throughout the microstructure can improve the toughness properties. This ductile phase can control the room temperature fracture toughness in a wide variety of composites, including *in-situ* composites. This addition of a ductile phase into a brittle material is known as 'ductile-phase toughening' (Chan and Davidson, 2001, Chan, 2002, Henshall et al., 1995, Mataga, 1989, Mendiratta et al., 1991).

As mentioned earlier, the Nb-Si binary system is of interest due to the wide two phase region with Nb_{ss} and αNb_5Si_3 in thermodynamic equilibrium (see Figure 1.1). This wide region can allow for varying composition and volume fractions of each phase. Also, in the Nb-Si system there are several different reactions taking place to reach the equilibrium phases of Nb_{ss} and αNb_5Si_3. The most important being the eutectic, $L \rightarrow Nb_3Si + Nb_{ss}$, and the eutectoid, $Nb_3Si \rightarrow Nb_{ss} + \alpha Nb_5Si_3$ reactions. Due to these different reactions, different compositions and morphologies of microstructure can be achieved in order to balance out different properties, and in this case, acceptable fracture toughness. The two desirable phases therefore, are the Nb_{ss} and αNb_5Si_3, with a possible addition of C14 Laves phase. The fracture toughness of Nb_5Si_3 has been reported as 3 MPa $\sqrt{m}$ (Mendiratta and Dimiduk, 1993), and has a very complex crystal structure (Figure 1.3(b)). Being able to improve the fracture toughness of Nb_5Si_3 by altering the chemistry of the phase itself is going to prove difficult. Therefore, it is more likely that through the incorporation of the ductile Nb_{ss} phase is a promising way of improving the fracture toughness of these *in-situ* composites. Chan (2002) reported on the fracture process for Nb-based *in-situ* composites. He summarised that the process involves:

(1) cracking of the hard intermetallic Nb_5Si_3 phase (and $NbCr_2$ if present),

(2) blunting of the particle cracks and bridging of the main crack and the microcracks by intact ligaments, and

(3) plastic stretching and failure of the bridging ligaments.

Mendiratta and Dimiduk (1993) investigated the strength and toughness of a near eutectic alloy, Nb-16.5 at.% Si after heat treatment and extrusion processes. They found that at all temperatures, the Nb_5Si_3 phase fractured via a brittle cleavage mode. The large Nb_{ss} particles fractured in a cleavage like mode at low temperatures and in a ductile fashion at higher temperatures (1200 – 1400 ^oC) and small eutectoid Nb_{ss} particles ruptured in a ductile manner at all temperatures. It can be seen therefore that it is the Nb_{ss} particles that control the toughness of Nb-based *in-situ* alloys. The brittle fracture seen at low temperatures for Nb_{ss} particles is caused by high constraint levels imposed by the surrounding matrix. Fracture behaviour of these alloys can be looked at in terms of composition/volume fraction of phases and in terms of processing. First to be discussed will be the compositional effects and the effect of volume fraction of phases, termed the effect of alloying, on fracture toughness followed by any processing effects on toughness.

2.3.3.1 Effect of alloying on fracture toughness of Nb_{ss}

This section will mainly focus on the effect of Ti additions to the Nb-based composites as this has been the most widely studied of alloying elements. Through the addition of Ti to Nb-bases *in-situ* composites, fracture toughness is enhanced (Davidson et al., 1996, Chan and Davidson, 1999). Figure 2.12 shows a plot of fracture toughness versus Ti content in Nb-Cr-Ti solid solution alloys. The fracture toughness of the alloys is seen to increase with increasing Ti content and reaches a maximum at ~ 37 at.% Ti. Both single and multiphase alloy compositions show this trend, albeit the latter shows a much lower increase in toughness. The marked drop

in fracture toughness of the alloy containing 50 at.% Ti is not due to the Ti but to the presence of Al which embrittles the solid solution.

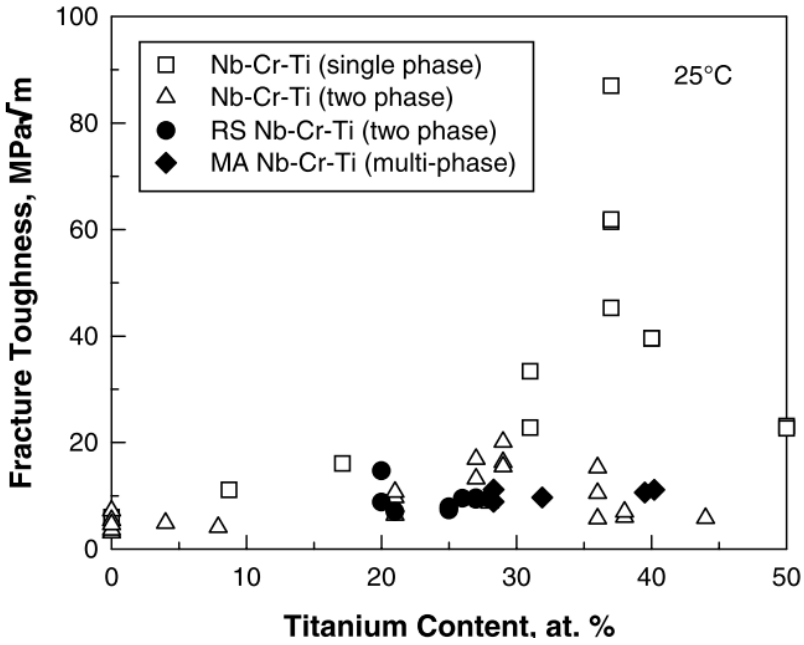

Figure 2.12 Dependence of fracture toughness of Nb-Cr-Ti solid solution alloys and *in-situ* composites on Ti content. The alloys include conventional cast, rapid-solidified (RS) and mechanically-alloyed (MA) materials (Chan and Davidson, 1999).[19]

This improvement in ductility is attributed to the alteration of chemical bonding in the Nb_{ss}. In order for dislocations to move from a low energy position to another, they must overcome the Peierls-Nabarro (P-N) energy barrier, the value of which is determined by the nature of the chemical bonding in the system. For transition metals, bonding involves the interaction of *d* shell electrons. The hybridisation of *s* and *d* shell electrons is what gives the transition metals their metallic behaviour. The number of *s* and *d* electrons is a good indication of bonding and therefore the level of the P-N energy barrier. Figure 2.13 shows a correlation

[19] Springer and the Metallurgical and Materials Transactions A, 30, 1999, 925-939, Effects of Ti addition on cleavage fracture in Nb-Cr-Ti solid-solution alloys, Chan, K. and Davidson, D, figure 1 and 3, copyright 2014) is given to the publication in which the material was originally published, with kind permission from Springer Science and Business Media

between fracture toughness and the number of *s* + *d* electrons (Chan and Davidson, 1999). The trend shows that an increase in the number of *d* + *s* electrons leads to a decrease in fracture toughness. This would be the result if Cr (6 *d* + *s* electrons) was added to Nb_{ss}. When Ti is added, there is a decrease in *s* + *d* electrons, an alteration to the chemical bonding and a lowering of the P-N energy barrier (Chan, 2002). With this lowering of P-N energy barrier, emission of dislocations from the crack tip is promoted and an increase in fracture toughness is seen.

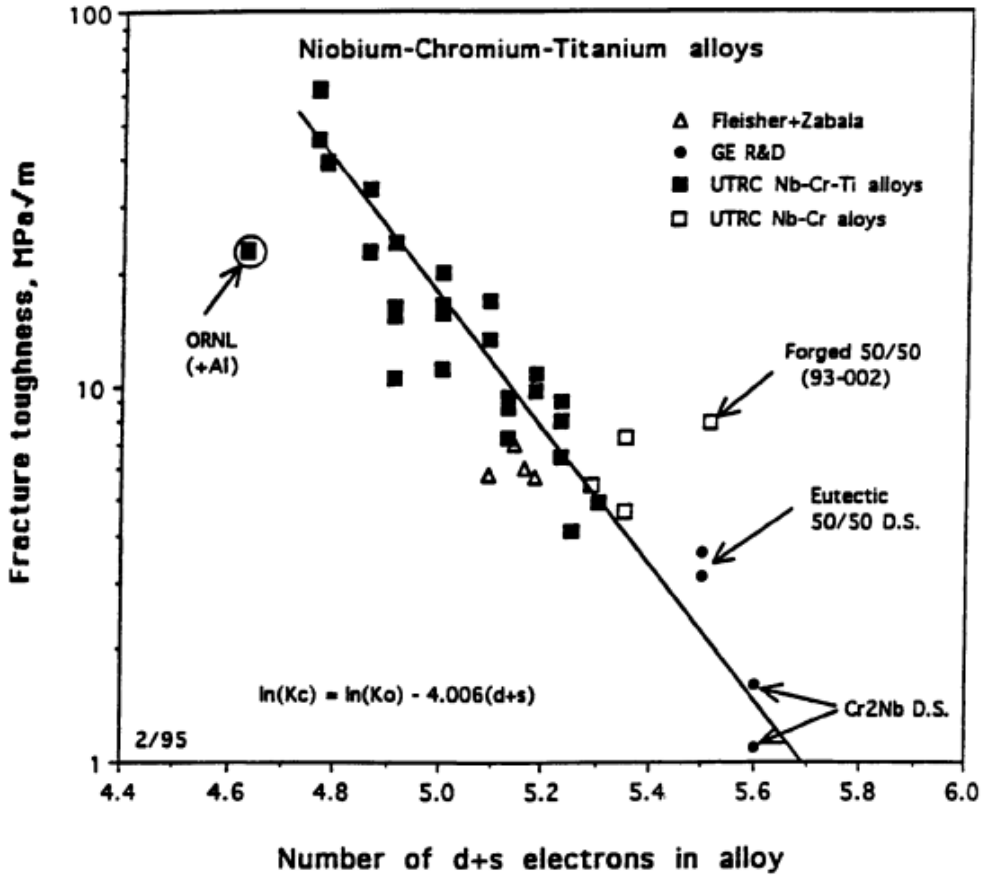

Figure 2.13 Correlation of fracture toughness versus the number of *d* + *s* bonding electrons per atom in Nb-based alloys (Chan and Davidson, 1999).[19]

Kim et al. (2001) studied the effect of Mo addition on the mechanical properties of Nb_{ss}/Nb_5Si_3 *in-situ* composites in order to improve the room temperature fracture toughness of the alloys. They found that for the binary alloys

(Nb-Si), fracture toughness decreased rapidly from 12 – 4 MPa √m with increasing Si content from 10 – 16 at.%. However, fracture toughness was insensitive to Si content between 16 – 22 at.% as shown by Figure 2.14.

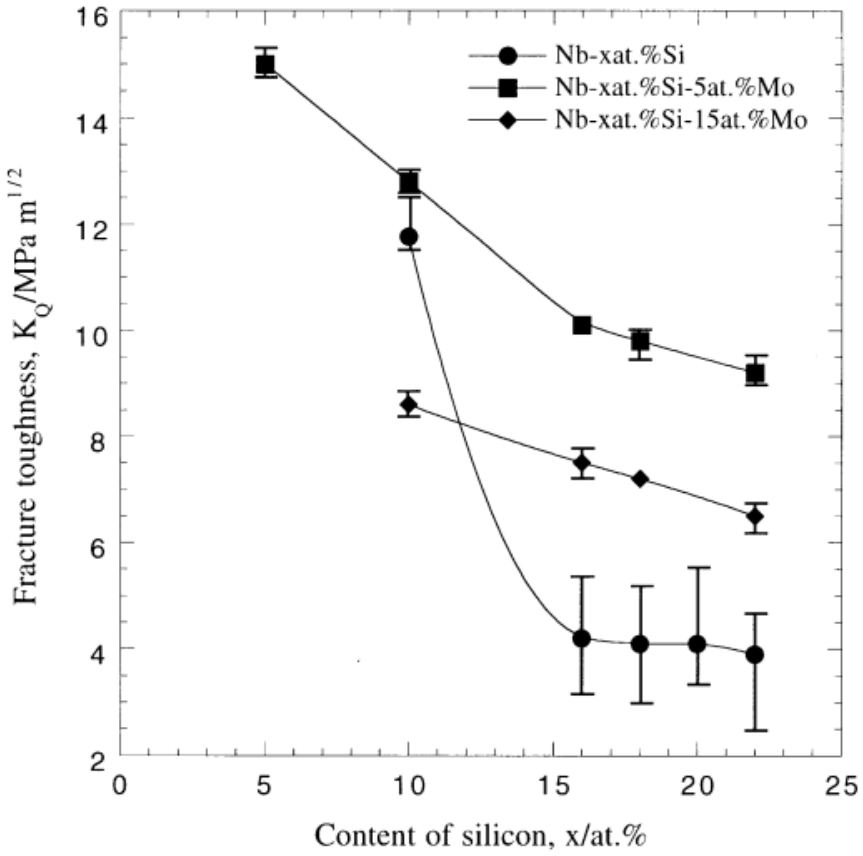

Figure 2.14 Fracture toughness of binary and ternary alloys as a function of Si content (Kim et al., 2001).[20]

What can also be seen from Figure 2.14 is that the fracture toughness of the ternary alloys increases with decreasing Mo content. They attributed this effect to that, during solidification, Mo preferentially partitions to the bcc Nb_{ss}. The ductile phase is therefore strengthened and its ductility lowered, making the phase more brittle. This accounts for the decrease in fracture toughness with the increase in Mo content.

[20] Reprinted from Intermetallics, 9, Kim, W. Y., Tanaka, H., Kasama, A. and Hanada, S. Microstructure and room temperature fracture toughness of Nb_{ss}/Nb_5Si_3 in situ composites, 827-834, Copyright (2014), with permission from Elsevier.

2.3.3.2 Effect of alloying on the fracture toughness of silicide and Laves phase

Chan (2005) wrote a review dealing with the alloying effects on the fracture toughness of Nb-based silicides and Laves phases and commented on a similar effect that Ti has on the fracture toughness of Nb_5Si_3 phase. Figure 2.15 shows the correlated data of several experimental data provided by other work. The fracture toughness of Nb_5Si_3 ($D8_1$) can be increased by the addition of Ti up to a maximum of ~ 30 at.%.

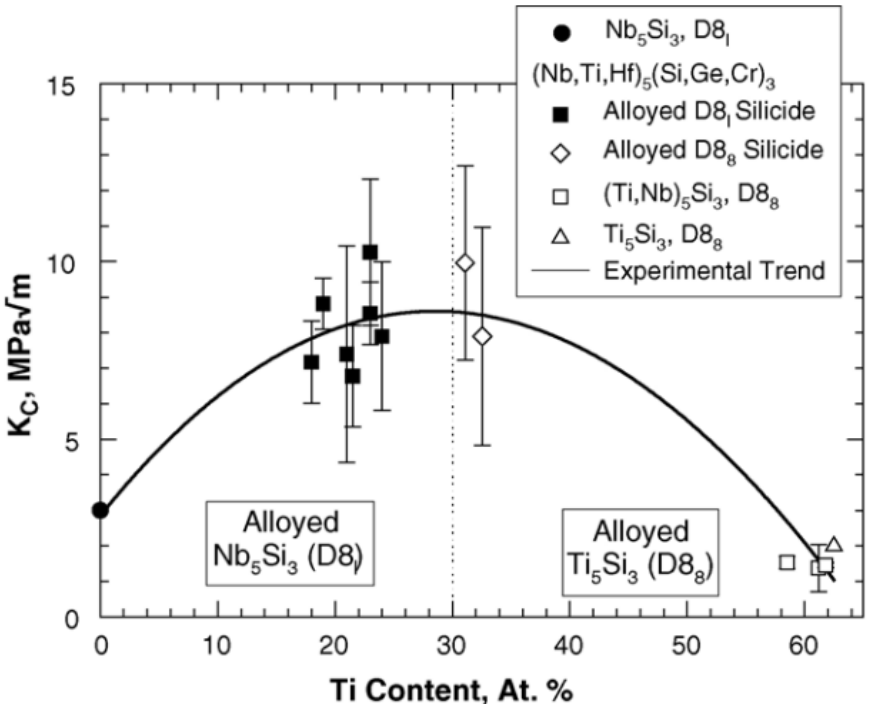

Figure 2.15 Correlation of fracture toughness of Nb_5Si_3 as a function of at.% Ti (Chan, 2005).[21]

In the same paper, the fracture toughness of $(Nb,Ti)Cr_2$ was looked at as a function of Cr content and the result shown in Figure 2.16. As can be seen, the C14 Laves phase has higher fracture toughness than the C15 Laves phase, making the former, the more desirable Laves phase to be present in the final microstructure of Nb-based *in-situ* composites.

[21] Reprinted from Materials Science and Engineering A, 409, Chan, K. S., Alloying effects on the fracture toughness of Nb-based silicides and Laves phases, 257-269, Copyright (2014), with permission from Elsevier.

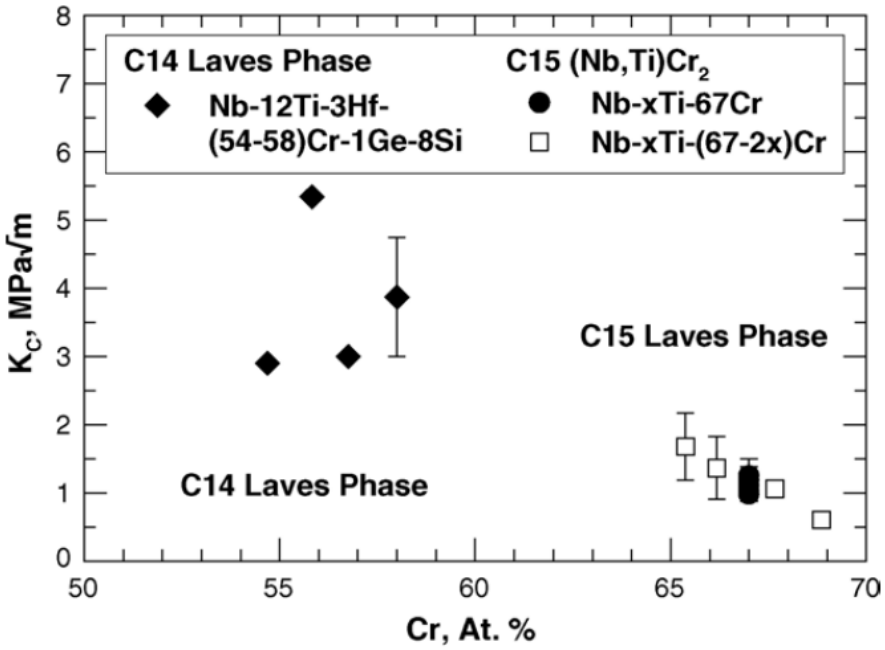

Figure 2.16 Correlation of fracture toughness of (Nb,Ti)Cr_2 phase as a function of at.% Cr (Chan, 2005).[22]

2.3.4 High temperature strength

It has been seen throughout the literature that the incorporation of a ductile phase into a intermetallic material can substantially improve the room temperature fracture toughness of Nb-based *in-situ* composites. However this improvement in fracture toughness is often seen at the loss of high temperature strength, as the volume fraction of Nb_{ss} is increased in order to improve fracture toughness. Therefore, approaches to the design of Nb-based *in-situ* composites will have to accommodate the desired fracture toughness, 20 MPa √m, whilst maintaining high temperature strength.

Subramanian et al., (1997) produced an overview of results of experimental data dealing with the mechanical properties and phase equilibria of many Nb-based alloys and Figure 2.17 shows the yield strength of a range of composites as a function of temperature.

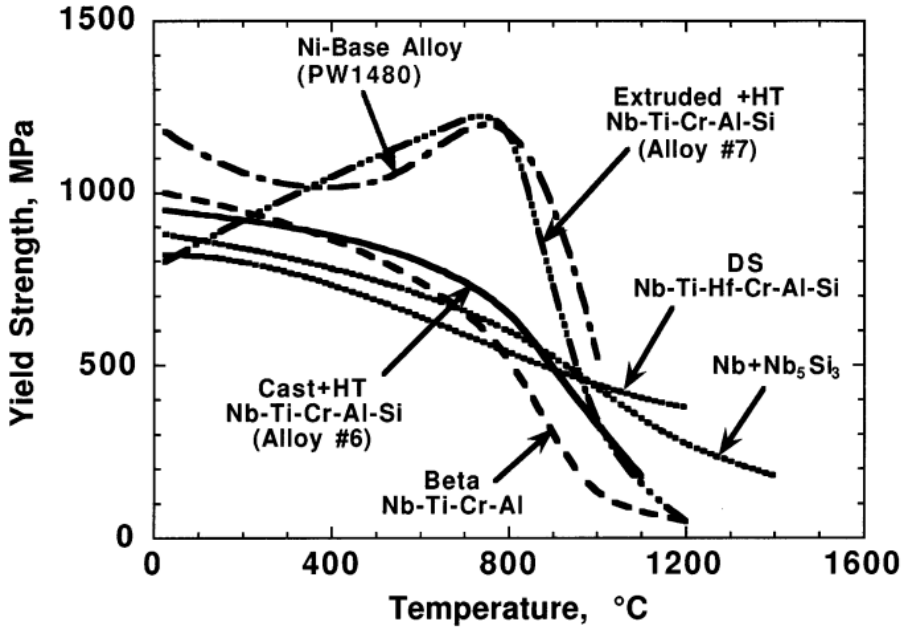

Figure 2.17 Yield strength versus temperature data for several Nb-based *in-situ* composites compared with a Ni-based superalloy (Subramanian et al., 1997).[22]

A wide variety of yield strengths can be seen depending on alloy composition and processing method. It should be noted that at temperatures below 1000 ^{o}C, the difference in strength of cast and heat treated, and extruded and heat treated Nb-Ti-Cr-Al-Si is substantial. Also, above 1000 ^{o}C, the directionally solidified Nb-Ti-Hf-Cr-Al-Si alloy shows the best yield strength, ~400 MPa at 1200 ^{o}C.

Kim et al., (2002) looked at the microstructure and high temperature strength at 1500 ^{o}C of binary and ternary Nb_{ss}/Nb_5Si_3 composites alloyed with Mo. They found that the high temperature strength of binary alloys depended more on microstructure morphology than on the volume fraction of individual phases. Figure 2.18 shows the 0.2% offset yield strength of differently processed alloys as a function of Si content.

[22] Reprinted from Materials Science and Engineering A, 239-240, Subramanian, P. R., Mendiratta, M. G., Dimiduk, D. M. and Stucke, M. A., Advanced intermetallic alloys--beyond gamma titanium aluminides, 1-13, Copyright (2014), with permission from Elsevier.

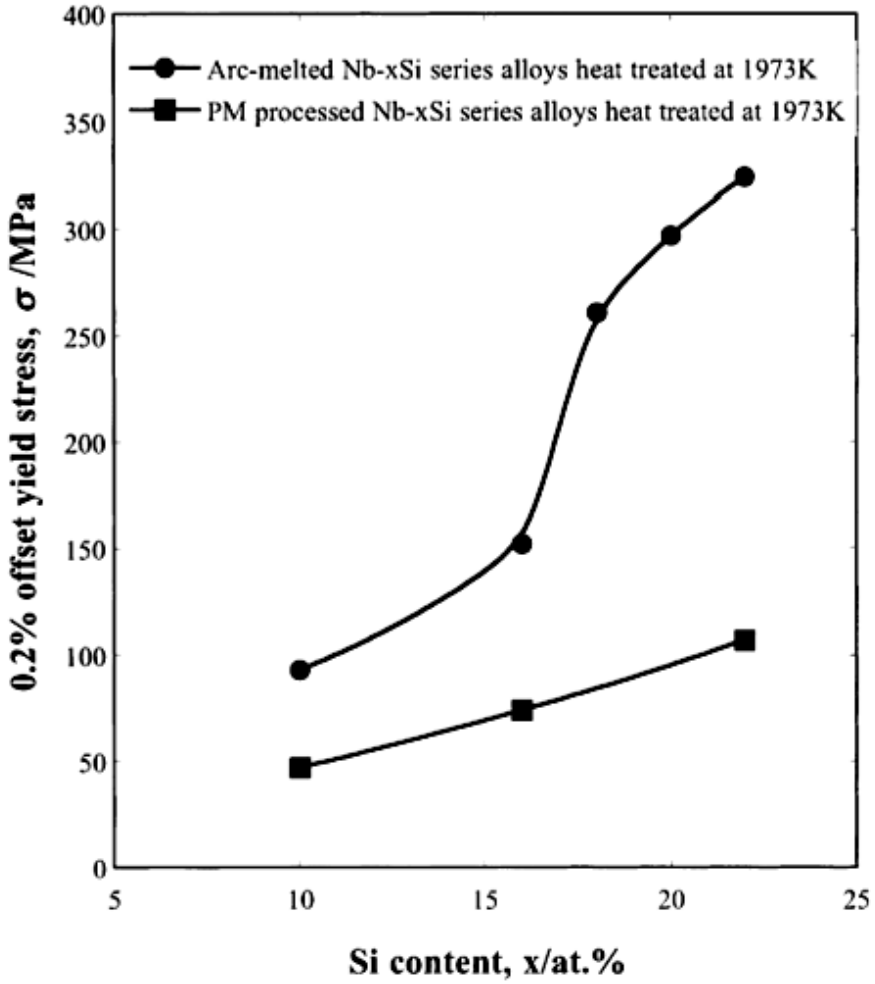

Figure 2.18 0.2 % offset yield strength as a function of Si content of binary alloys produced by arc-melting and powder processing (PM) (Kim et al., 2002).[23]

They attributed the higher yield strength of the arc-melted (AM) alloys due to the transition from a hypoeutectic microstructure to a eutectic-like structure, which was not seen in the PM alloys. This change in microstructure caused a rapid rise in yield strength of the AM alloys at ~16 at.% Si.

Figure 2.19 shows the results of the yield strength of ternary alloys, alloyed with Mo, as a function of Mo content. The yield strength of Nb-22Si-*x*Mo is always higher than that of Nb-16Si-*x*Mo. For the latter, the 0.2% offset yield strength

[23] Reprinted from Intermetallics, 10, Subramanian, P. R., Kim, W.-Y., Tanaka, H. and Hanada, S., Microstructure and high temperature strength at 1773 K of Nb_{ss}/Nb_5Si_3 composites alloyed with molybdenum, 625-634, Copyright (2014), with permission from Elsevier.

increases with the addition of Mo up to 15 at.% Mo and then decreases with further additions of Mo. This decrease in yield strength is attributed to the transformation of αNb_5Si_3 to βNb_5Si_3. The Nb-22Si-*x*Mo follows a different trend. Upon addition of 5 at.% Mo the yield strength decreases and then increases with the addition of up to 25 at.% Mo. This initial decrease in yield strength can be explained by the microstructure of the alloy changing from Nb_{ss} particle dispersion to a maze-like structure.

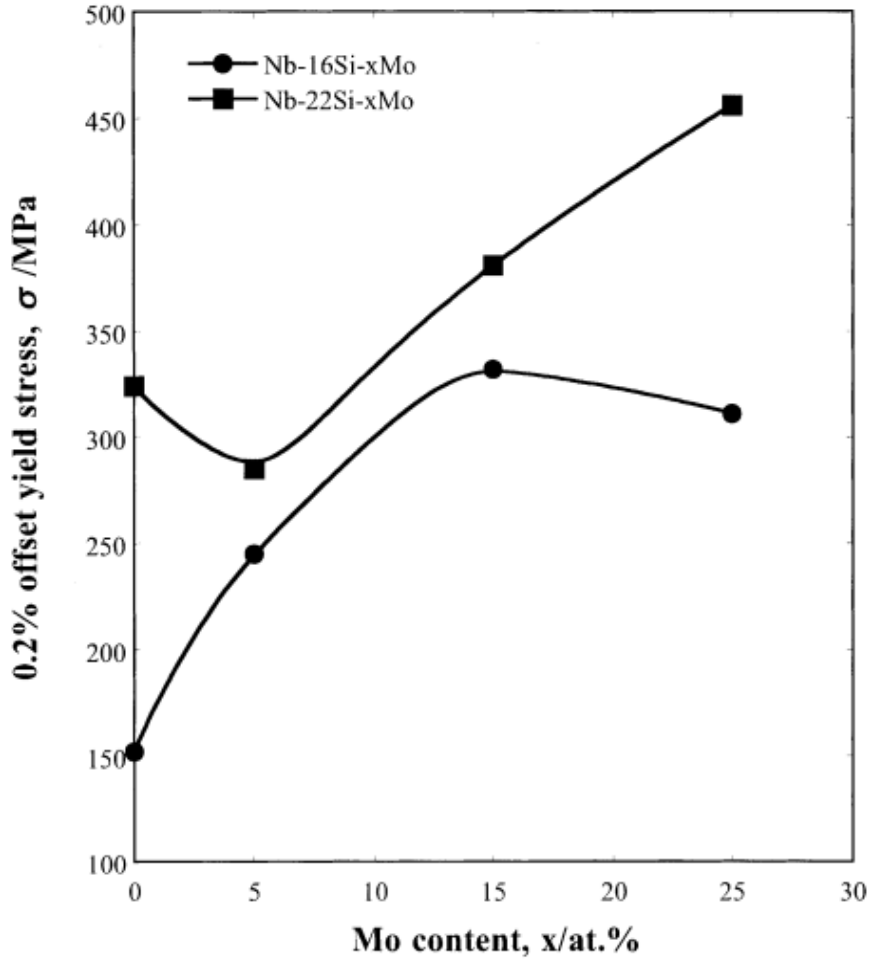

Figure 2.19 0.2% offset yield stress (at 1500 ^{o}C) of ternary alloys Nb-16Si-*x*Mo and Nb-22Si-*x*Mo series produced by arc-melting (Kim et al., 2002).[23]

The general increase in yield strength with increasing Mo content is due to the preferential partitioning of Mo to the Nb_{ss} during solidification, thereby acting as

a solid solution strengthening element and increasing the strength of the Nb_{ss} phase.

As mentioned earlier, in order for Nb-based *in-situ* composites to be successful in replacing Ni-based superalloys in high temperature structural applications, they need to be able to achieve the performance and properties that Ni-based alloys possess, and be able to operate at higher temperatures (>1300 ^{o}C). High temperature strength seen in the literature possessed by these composites makes them a very attractive material for use in the high pressure, high temperature section of a gas turbine.

2.3.5 Creep properties

` Creep is a very important deformation mechanism for materials being used for high temperature applications, and for Nb-based *in-situ* composites, creep behaviour is controlled by a combination of creep in the metallic, Nb_{ss} phase and creep in the silicide phase. A goal for creep performance of Nb-bases alloys that is widely accepted, is that there must be less than 1% creep in 125 hours at temperatures of 1200 ^{o}C and stresses of >170 MPa (Balsone et al., 2001). If there is minimal primary creep, this corresponds to a secondary, steady-state creep rate of $2.2 \times 10^{-8}\ s^{-1}$.

Figure 2.20 shows the secondary creep rates of several alloys including monolithic Nb_5Si_3 and binary Nb alloys. As can be seen, Nb_5Si_3 possesses excellent creep properties, easily possessing the desired goal of creep rate. Also, a combination of Nb and Nb_5Si_3 crosses the desired level of $2.2 \times 10^{-8}\ s^{-1}$ showing that it will take careful design of possible composites to possess the desired creep properties.

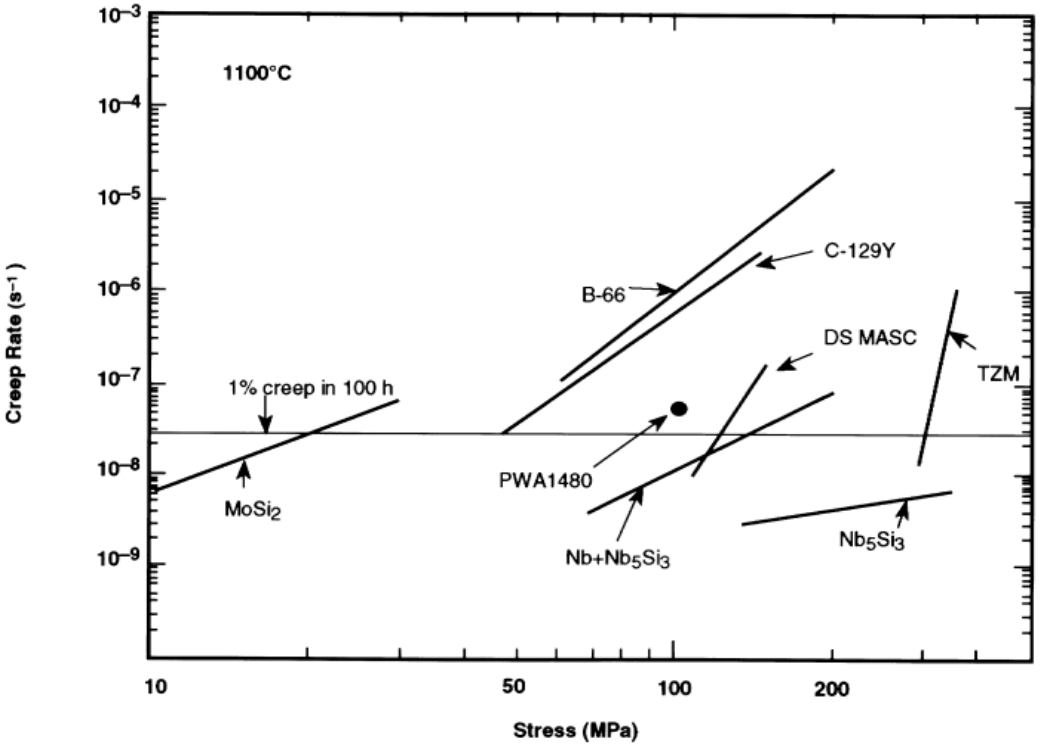

Figure 2.20 Comparison of secondary creep rates for several alloys including monolithic Nb_5Si_3 and DS MASC alloy (for MASC see Figure 2.12) (Bewlay and Jackson, 2000).[14]

Subramanian et al., (1995) looked at the compressive creep behaviour of Nb_5Si_3 in the temperature range of 1100 – 1400 ^oC and between stress levels of 30 – 418 MPa. They determined the stress exponent, n from the equation $\dot{\varepsilon} = B\sigma^n$, to be close to unity at all temperatures apart from at 1400 ^oC which shows n~2.2 at stresses higher than 174 MPa. Due to the exponent being close to unity, the deformation mechanism must be a diffusional, Nabarro-Herring mechanism, and that the creep process is rate limited by the diffusion of Nb. Bewlay et al., (2001b) also investigated the creep behaviour in monolithic phases in Nb-based *in-situ* composites and agreed that the deformation mechanism in Nb_5Si_3 is the bulk diffusion of Nb via a Nabarro-Herring mechanism, but that the mechanism in Nb_3Si is controlled by dislocation glide, despite the complex dislocation structures of the phase.

Bewlay et al., (2001a) looked at the effect of silicide volume fraction on the creep behaviour of Nb-silicide based *in-situ* composites and Figure 2.21 shows the results of creep strain rate versus Si content at different stress levels. Creep rate increases with stress level for a constant Si concentration, and a minimum value of creep was determined at a Si content of 18 at.% Si which corresponds to a volume fraction of ~0.6 silicide in binary Nb-18Si alloys. At lower stress levels, the curve moves down the graph and can eventually cross the goal of 2.2 x 10^{-8} s^{-1} creep rate. Bewlay also published in a patent application the effect of a Nb: (Hf + Ti) ratio on creep properties of Nb-based *in-situ* composites. It is shown that if the concentrations of (Hf + Ti) are kept low then the creep rate decreases.

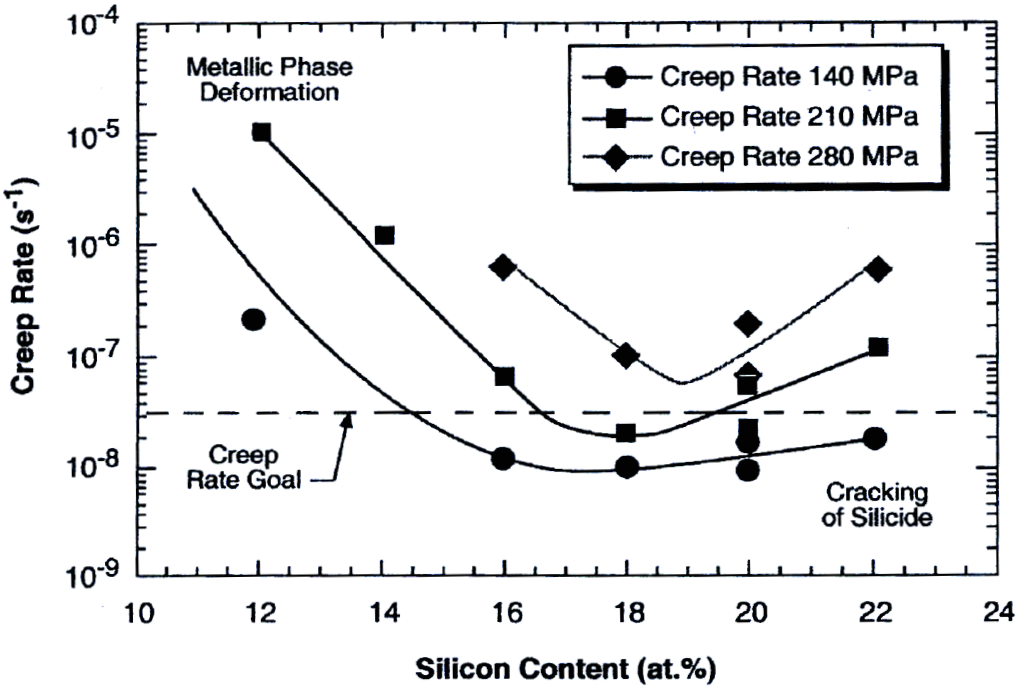

Figure 2.21 Secondary creep rate (at 1200 ^{o}C) versus Si content at different stress levels of Nb-Ti-Hf-Si alloys (Bewlay et al., 2001a).[24]

[24] Permission obtained from John Wiley and Sons, Intermetallic Compounds: Principles and Practice, Vol. 3, Bewlay, B. P., Jackson, M. R. and Gigliotti, M. F. X. Niobium Silicide High Temperature In Situ Composites, 2002, Copyright 2014

Chapter 3

Literature review: Oxidation and Environmental degradation

3.1 Introduction

Thus far, Nb-silicide based *in-situ* composites have shown excellent properties, such as high temperature fracture toughness and creep strength, and their potential use at high temperatures (>1800 ^{o}C) is very high. However, there is still one major barrier that has restricted their development and use at the required temperatures to replace Ni – based superalloys. The oxidation resistance of these alloys is poor, and has been described as catastrophic by some researchers. The incorporation of a ductile Nb_{ss} phase has substantially improved the fracture toughness of these alloys; however, its presence is the main cause of the poor oxidation resistance. These alloys, whilst will undoubtedly have a coating system applied to them for use in next generation gas turbines, require some inherent oxidation resistance themselves in case of a coating failure during service.

Based on the current, state of the art Ni – based superalloys, a reasonable goal for Nb-silicide based *in-situ* composites has been outlined in the literature. A long term goal for metal loss/recession rate of 0.25 μm/h at 1315 ^{o}C has been suggested and the most advanced Nb-silicide alloy is far from reaching this goal, managing to achieve this recession rate at 1200 ^{o}C (Bewlay et al., 2003).There is also a short term goal outlined in the literature; that of the uncoated alloy being able to survive a demanding engine test. The uncoated alloy will be required to lose < 200 μm in 10 h of test demonstration at 1370 ^{o}C, if it is to survive (Balsone et al., 2001, Bewlay et al., 2003). Figure 3.1 shows a comparison of oxidation behaviour of silicide based composites compared with Ni-based superalloys as a function of temperature. As can be seen, whilst each new development of Nb-silicide based *in-situ* composites brings the materials closer to the desired goal, by the year 2000 they were still a long way from achieving it.

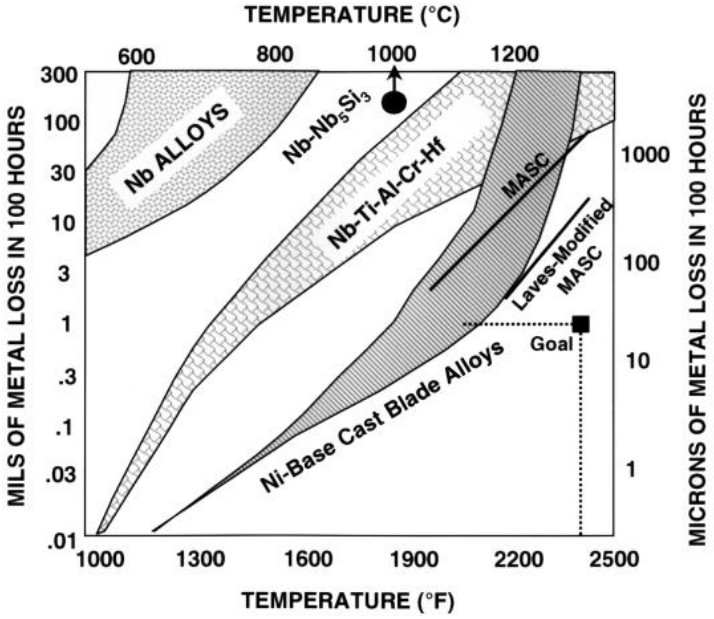

Figure 3.1 Oxidation behaviour of silicide-based composites shown as a function of temperature, and compared with both Ni-based superalloys and monolithic Nb alloys (Bewlay and Jackson, 2000).[24]

3.2 Oxidation of Nb

Figure 3.2 shows the Nb-O binary phase diagram and shows the formation of three stable oxides NbO, NbO_2 and Nb_2O_5. The latter exists in polymorphic forms, an orthorhombic and monoclinic, Nb_2O_5. The solubility of O in Nb is high (about 9 at.% at 1915 ^oC) and it has been shown that this can be increased by the Ti additions. The oxidation mechanism of Nb was studied quite early (Kubaschewski and Hopkins, 1960). They showed that the kinetic laws for the oxidation of Nb change with temperature. Below 500 ^oC, the oxide scale formed is composed of Nb_2O_5 and was adherent and “apparently porefree”. At 500 ^oC a parabolic-linear transition was observed due to cracking of the scale and above 500 ^oC the cracking was more pronounced, leading to a linear oxidation behaviour. They also observed that at high temperatures (>1000 ^oC) a coherent oxide layer was formed, however was not adherent and flaked off easily. This lack of adherence is due to stress at the

metal/oxide interface caused by fivefold volume expansion between Nb and Nb_2O_5 (Nb: 10.9 cm^3 mol^{-1}, Nb_2O_5: 58.3 cm^3 mol^{-1}).

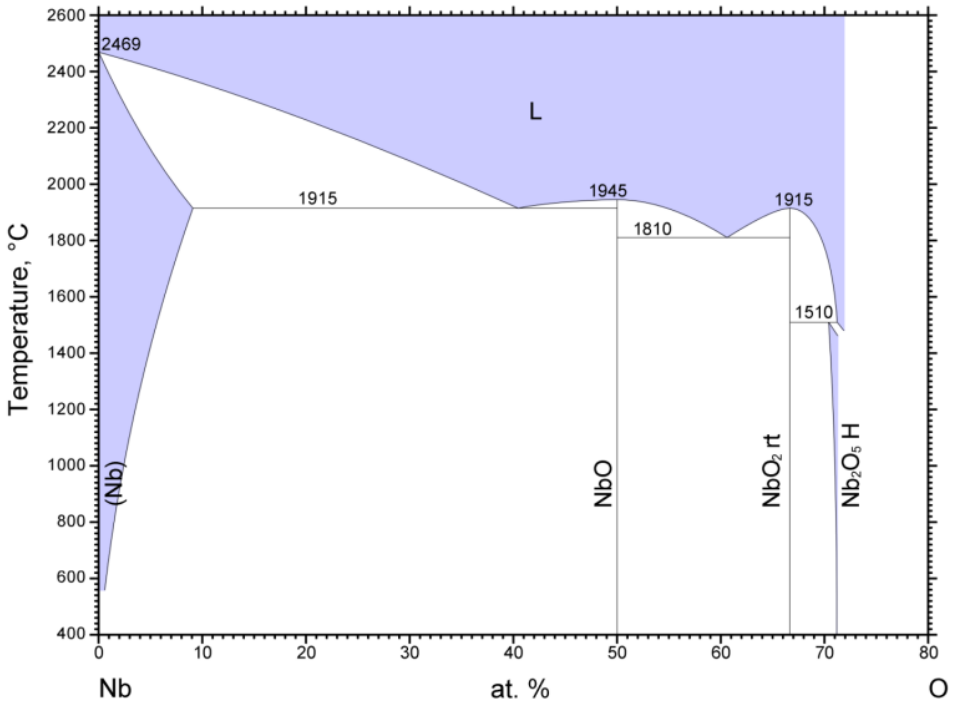

Figure 3.2 Nb-O binary phase diagram (Okamoto, 1990b).

The problem, therefore, is twofold. The oxidation of Nb leads to an Nb_2O_5 oxide scale to be formed on the surface. This scale, unlike Al_2O_3 on Al, does not protect the metal from further oxidation (Perepezko, 2009) and so further metal loss occurs, and also, the Pilling-Bedworth Ratio (PBR) for Nb_2O_5 is 2.7 (Zelenitsas and Tsakiropoulos, 2006a). This means that the oxide scale is not very adherent to the metal and therefore, spallation of the oxide layer occurs.

Several early papers dealt with the oxidation behaviour of niobium including the oxides that were formed during oxidation at several temperatures (Hurlen, 1961, Kofstad and Kjollesdal, 1961). Below 650 ^oC there exists a “pre-transition period” followed by an accelerated, breakaway oxidation and increased weight gain. The pre transition period involves dissolution of oxygen into the metal and the formation of oxide phases NbO_x and NbO_z. The accelerated breakaway oxidation occurs at

the onset of Nb_2O_5 nucleation at the surface leading to a porous, non-protective scale. Above 650 ^oC, NbO decomposes into NbO_2, which is oxidised further to Nb_2O_5. The NbO_2 forms a compact layer and so its formation is assumed to be the reason for the initial parabolic kinetics of the oxidation process. The linear behaviour that follows is once again attributed to the formation of Nb_2O_5. Between $800-850\,^oC$, Nb_2O_5 experiences a modification from $\gamma \rightarrow \alpha Nb_2O_5$ (with γNb_2O_5 being described as a metastable, monoclinic phase). The formation of αNb_2O_5 is characterised by pronounced whisker formation and growth, which are single crystals of αNb_2O_5 with the monoclinic axis parallel to the whisker axis. Whisker formation is believed to occur via a plastic flow mechanism that results from growth stresses within the oxide scale. Rarely are topographical images of the oxides formed during oxidation studies reported in the literature.

3.2.1 Stresses involved during oxidation

A number of stress sources may arise during oxidation of materials and metals depending upon the reaction mechanisms. These may include effects of oxygen dissolution in metals, volume ratios of oxide to metal (Pilling-Bedworth ratio) and many others

When oxygen dissolves into a metal, large stresses may result from lattice expansions caused by interstitial oxygen being present. Pawel and Campbell (1966) looked at this during the oxidation of Ta (and Nb) by oxidising one side of a rectangular specimen. Oxidation caused bending of the sample and even cylindrical bending. Oxygen dissolution into the metal and along grain boundaries can lead to the formation of oxides, leading to an internal volume expansion that is constrained by the sample. Relieving this stress can lead to deformation of the material and even cracking of the oxidised material.

As mentioned, the PBR of Nb_2O_5 is 2.7, which means that large biaxial compressive stress will exist in the oxide scale as the oxide is not able to expand

freely, and tensile stresses will exist in the substrate material. With such large stresses, therefore felt at the substrate/scale interface, it is common for oxide films to spall and crack after a certain level of oxide thickness.

3.3 Oxidation behaviour in the pest range (750 – 900 ^{o}C)

These alloys suffer from catastrophic 'pest' oxidation in the temperature range 750 – 900 ^{o}C. Pesting occurs due to preferential oxidation of some microstructural features, such as grain boundaries, and coupled with oxygen embrittlement can lead to self-pulverisation of the oxide and the metal. Westbrook and Wood (1964) put forward a model for pest oxidation describing in more detail how the temperature range for pesting is specific to each material. Several studies have looked at how to combat the pesting effect through the addition of alloying elements with the majority of the work conducted at 800 ^{o}C (Geng and Tsakiropoulos, 2007, Geng et al., 2006c, Geng et al., 2007b, Mathieu et al., 2012, Menon et al., 2004, Zelenitsas and Tsakiropoulos, 2006a, Bewlay et al., 2003). Zelenitsas and Tsakiropoulos (2006a) reported that pest oxidation occurred in alloys of Nb-24Ti-18Si (at.%) and Nb-24Ti-18Si-5Cr (at.%) but was avoided by the synergy of Ti, Cr and Al.

The addition of as little as 1.5 at.% Sn has been seen to eliminate pest oxidation in Nb-silicide based *in-situ* composites (Balsone et al., 2001, Bewlay et al., 2003). Whether or not additions of Sn can aid oxidation resistance at higher temperatures (>1100^{o}C) is still unknown. Balsone et al., (2001) suggested that Sn has a minimal effect on oxidation at higher temperatures, but Geng et al., (2007) showed that through the formation of Nb_3Sn, oxidation resistance at higher temperatures can indeed be improved. There are some common features observed when oxidising Nb silicide alloys at 800 ^{o}C for 100 h, as shown in Figure 3.3. The cracking of the silicide has been reported throughout the literature (Bewlay et al.,

2003, Geng and Tsakiropoulos, 2007, Geng et al., 2006c, Geng et al., 2007b, Mathieu et al., 2012, Menon et al., 2004, Zelenitsas and Tsakiropoulos, 2006a) but not many have reported the presence of fine needle like precipitates within the Nb_{ss} phase. Also, within the literature, there is very little work showing the topography of the oxide scale itself. It would surely be beneficial to provide some evidence of the topography of the oxide scale that forms and could aid the identification of the oxides that have formed on the surface.

Identification of the oxides that form at 800 ^{o}C has been primarily conducted through the use of x-ray diffraction (XRD), both conventional and glancing angle, and limited use of scanning electron microscopy and energy dispersive x-ray spectroscopy (SEM-EDS) and a variety of oxides are seen. The more common oxides are Nb_2O_5, TiO_2, SiO_2, $TiNb_2O_7$, $Ti_2Nb_{10}O_{29}$, $AlNbO_4$, $CrNbO_4$, $xNb_2O_5.yTiO_2$ (Geng and Tsakiropoulos, 2007, Geng et al., 2006c, Geng et al., 2007b, Mathieu et al., 2012, Menon et al., 2004, Zelenitsas and Tsakiropoulos, 2006a).

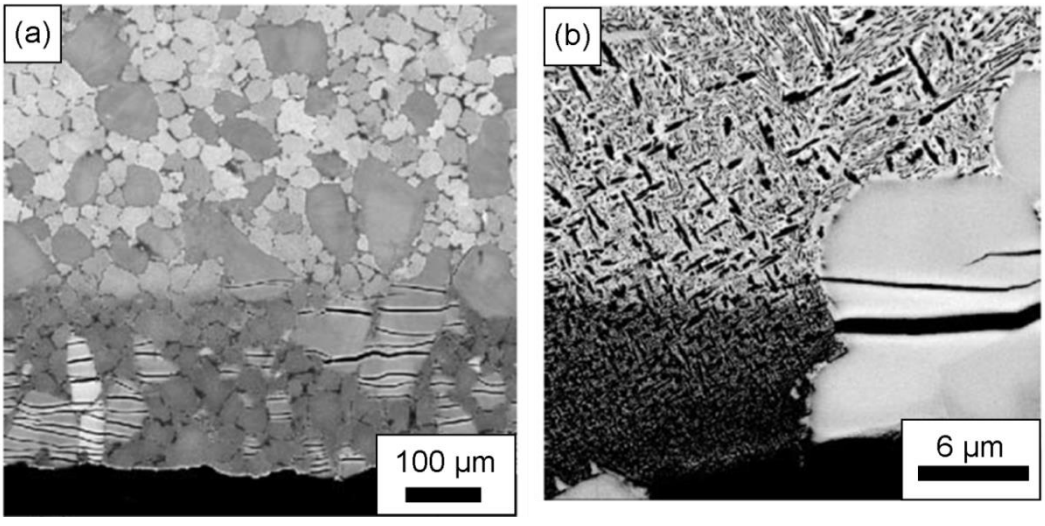

Figure 3.3 Images of a Nb-Si alloy oxidised at 800 and 900 ^{o}C (Menon et al., 2004). Images show (a) cracking of the intermetallic phase parallel to surface of the sample and (b) oxide precipitates in the Nb_{ss} phase leading to cracking of the intermetallic.[25]

[25] Springer and the Metallic Materials with High Structural Efficiency, 2004, Microstructural Effects and Kinetics of High Temperature Oxidation in Nb-Si Base Alloys, Menon, E., Parthasarathy, T. and Mendiratta, M., figure 6(a),

3.4 Oxidation at high temperatures (>1100 ^{O}C)

For use at high temperatures, a suitable coating is likely to be applied to aid oxidation resistance and act as a thermal barrier. However, the assumption that the coating will provide the oxidation resistance is foolish and even more so if the coating is to be fully relied upon. Materials used at high temperatures need to have some inherent oxidation resistance themselves in order to survive during service if the coating fails. The oxidation of these Nb-silicide based *in-situ* composites is the major barrier holding back the use of the alloys in high temperature applications and although the desired goal is continuously being approached with each new development phase, alloys are still some way off.

The high temperature oxidation behaviour of Nb-based silicide *in-situ* composites is typically characterised by high metal recession rates, spallation of the oxide, and general structural disintegration. Also, due to the fast diffusion of oxygen through the oxide layers and dissolution of oxygen within the Nb_{ss} phase, substantial hardening and embrittlement on the Nb_{ss} phase can occur (Subramanian et al., 1997). The oxidation resistance of Nb-silicide based composites, at 1200 and 1300 ^{o}C, toughened with Nb_{ss} is substantially improved over that of binary Nb-Si and binary Nb-Nb_5Si_3 alloys by the addition of elements such as Ti, Cr, Al and Hf (Bewlay and Jackson, 2000). As would be expected, the different alloying elements, and their different compositions, will have a different effect on the oxidation behaviour of these alloys. However, it has been seen that good oxidation resistance can be achieved for chemistries with Nb:(Ti + Hf) ratios of 1.8-2.1 at.% and Si levels at 17-19 at.% (Balsone et al 2001). As mentioned earlier, this chemistry will also help creep resistance of the alloys.

The incorporation of Cr-rich Laves phase has also seen a marked improvement in the oxidation resistance of Nb-silicide based *in-situ*

composites. Figure 3.4 shows the oxidation response of a Nb + silicide + Laves phase alloy compared with a Nb + silicide alloy (MASC) at 1204 and 1316 ^{o}C. It can be seen that there is a substantial improvement in the oxidation resistance by the addition of Cr-rich Laves phase. The phase chemistry of this alloy is reported to be ~25 vol% Nb_{ss}, 33 vol% Laves phase and 42 vol% of M_5Si_3 silicide phase (Bewlay and Jackson, 2000). Although the oxidation resistance has been improved, it has surely occurred at the compromise of fracture toughness as the addition of such a large volume fraction of a brittle intermetallic phase will have undoubtedly lowered the fracture toughness. It has also been suggested that the presence of Cr-rich Laves phase is detrimental to the oxidation resistance of Nb silicide alloys at 800 ^{o}C when the alloy contains Al (Zelenitsas and Tsakiropoulos, 2006a).

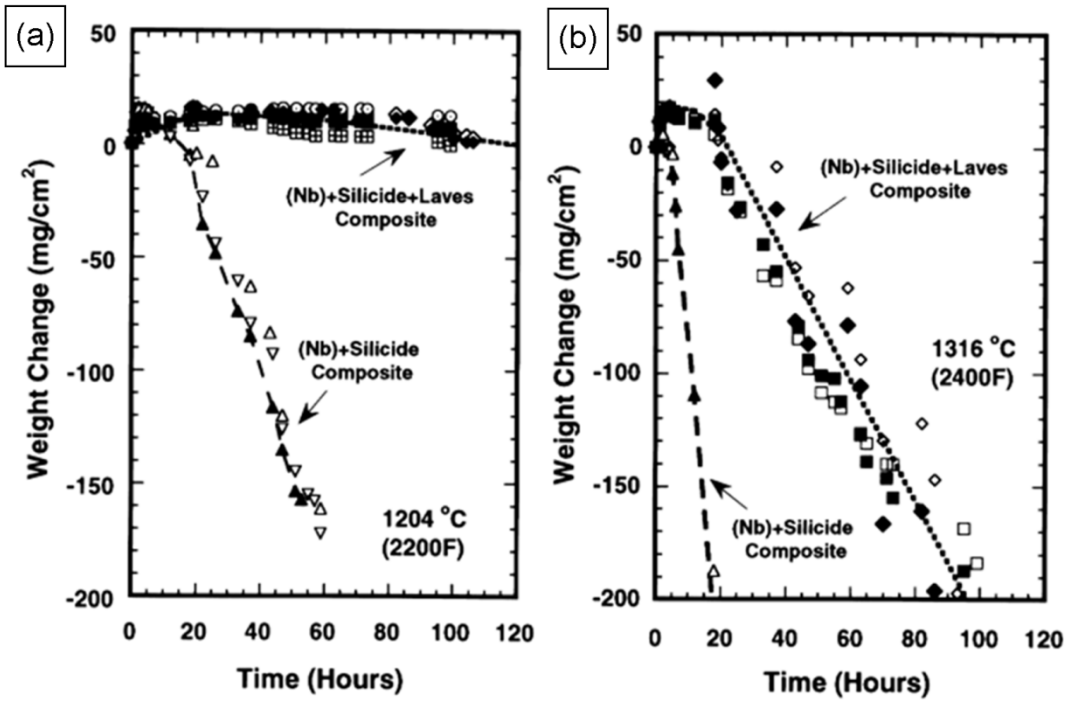

Figure 3.4 Comparison of the oxidation resistance of Nb-18Ti-7Hf-20Cr-2Al-18Si with the MASC alloy behaviour. Data (a) for four samples of MASC and nine of the modified alloy at 1200 ^{o}C, (b) two samples of baseline composition and four of the Laves phase modified alloy at 1315 ^{o}C (Bewlay and Jackson, 2000).[24]

A range of different alloying elements have been added to these alloys in order to improve their oxidation resistance. Addition of Ti, Cr, Al, Sn, Ge and Hf have all been investigated and seen to improve oxidation resistance. The levels of these elements need to be carefully controlled as if too much is added, then other desirable properties, such as creep-rupture strength, fracture toughness and the melting point can be compromised. The effects of minor additions of elements such as Mo, V, W, Ta, Zr, B and Ge on the oxidation resistance have also been investigated. From the results of these experiments it was determined that Mo, W and V are detrimental for oxidation resistance, B (>3 at.%) was beneficial to oxidation resistance and the replacement of Si with Ge also improved oxidation resistance (Zelenitsas and Tsakiropoulos, 2006a).

It is commonly seen that during oxidation at higher temperatures, it is the Nb_{ss} phase that is aggressively attacked, as shown in Figure 3.5(a), with the formation of multiple oxides within the Nb_{ss} phase. What has only recently been discussed is that the M_5Si_3 intermetallic phase is also attacked during oxidation at 1200 ^{o}C, shown in Figure 3.5(b), which had been previously reported to be immune to oxidation (Menon et al., 2001)

The attack of the intermetallic phase shown in Figure 3.5(b) shows an inward attack from the grain boundary to the centre of the grain with the formation of oxides in a similar morphology to that of a eutectic during solidification. This would suggest that the attack of the intermetallic phase occurs from all areas of the grain boundary surrounding the phase and that there is no directionality when attack of the phase occurs. It was also shown, but not commented on or discussed, that there is some internal modification of the intermetallic during oxidation at 1200 ^{o}C reaching from the grain boundary to the bulk of the grain. Whilst Geng et al.,(2006c) comment on the formation of TiO_2 particles inside the Nb_{ss}, there is no mention of any oxide particles within the Nb_5Si_3 phase or the lighter areas of contrast within the

Nb_5Si_3 phase. In fact, Geng et., al. (2006c) are the only group to show this internal attack of the intermetallic phase. If this feature appears during this research, it will be investigated to understand why this is happening.

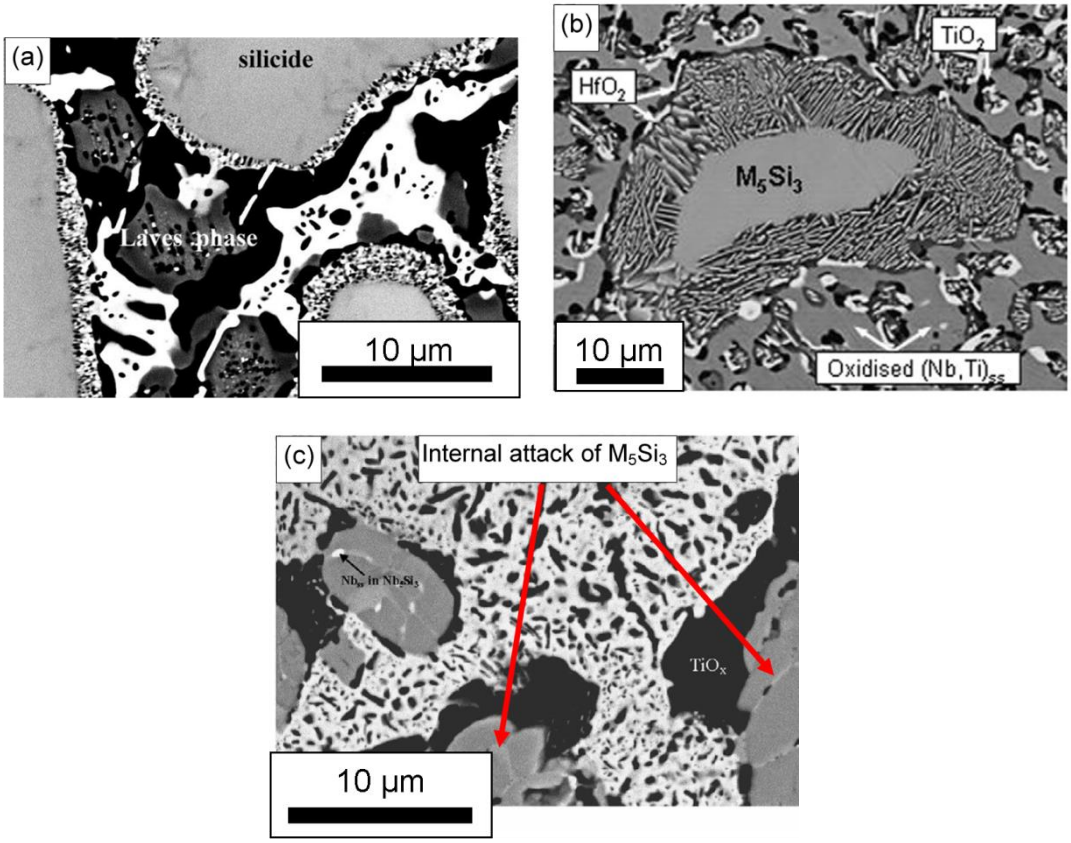

Figure 3.5 BSE images showing attack of (a) Nb_{ss} phase (Menon et al., 2001)[26], (b) Inward attack of M_5Si_3 phase (Mathieu et al., 2012)[27] and (c) internal attack of Nb_5Si_3 (Geng et al., 2006c)[28] after oxidation at 1200 ^oC.

Wagner's theory deals with the mechanism of oxidation of metals and it has been applied throughout the literature with other materials. There are a few issues with applying this model to Nb silicides. Firstly, it only deals with single phase

[26] Reprinted from Niobium; Science & Technology, Niobium 2001 Limited. Menon, E. S. K., Mendiratta, M. G. and Dimiduk, D. M. 2001. Oxidation behaviour of complex Niobium based alloys. Figure 6(a), 2001 with permission from CBMM North America

[27] Reprinted from Corrosion Science, 60, Mathieu, S., Knittel, S., Berthod, P. and Vilasi, M, On the oxidation mechanism of niobium-base in situ composites, 181-192, Copyright (2014), with permission from Elsevier.

[28] Reprinted from Materials Science and Engineering A, 441, Geng, J., Tsakiropoulos, P. and Shao, G., Oxidation of Nb-Si-Cr-Al in situ composites with Mo, Ti and Hf additions, 26-38, Copyright (2014), with permission from Elsevier.

materials; it assumes the oxide scale is a single phase, protective and adherent and that there is no solid solubility of oxygen in the material. However it is clear that with Nb silicides, these assumptions are unjustified. Recently there has been research into modelling the oxidation behaviour of multiphase alloys and Nb silicide alloys (Wang et al., 1991a, Wang et al., 1991b, Nijdam et al., 2003, Nijdam and Sloof, 2008, Yao et al., 2009a, Yao et al., 2009b, Gesmundo et al., 1993). Gesmundo et al., (1993) out forward a model for the isothermal oxidation of two phase alloys and determined a relationship between the parabolic rate constant of the two phase alloy in terms of the volume fractions and the parabolic rate constants of the constituent elements. This relationship has been used and extended by others showing good promise (Yao et al., 2009a, Chan, 2004). Yao et., al., (2009a) extended the steady state diffusional analysis of Wang et., al.,(1991a) to a three phase alloy. Work is still needed to produce a full and complete model of oxidation of multiphase alloys that can incorporate solid solubility of oxygen and the formation of mixed, ternary oxides.

3.5 Phase equilibria of oxides

During oxidation of complex Nb silicides, a wide variety of oxides can form, including simple binary oxides, such as TiO_2, and complex mixed oxides, such as $TiNb_2O_7$ and $CrNbO_4$. It is worth considering any oxide phase diagrams of elements present within the alloys to predict which oxides form and, perhaps, why.

3.5.1 Nb_2O_5 – TiO_2 binary

Figure 3.6 shows that Nb_2O_5 and TiO_2 can combine to form several intermediate oxides $Nb_{24}TiO_{62}$, $Nb_{14}TiO_{37}$, $Nb_{10}Ti_2O_{29}$ and Nb_2TiO_7, with the latter two oxides being commonly identified in the oxide scales produced on Nb silicides. There is also $Nb_2Ti_2O_{19}$, however this oxide is not stable below ~1420

^{o}C. Figure 3.6 also shows that the mixture of Nb_2O_5 and TiO_2 produce oxides with melting points between 1400 – 1500 ^{o}C, therefore there is a possibility that there could be melting of the oxide scale if the materials are to be used at very high temperatures.

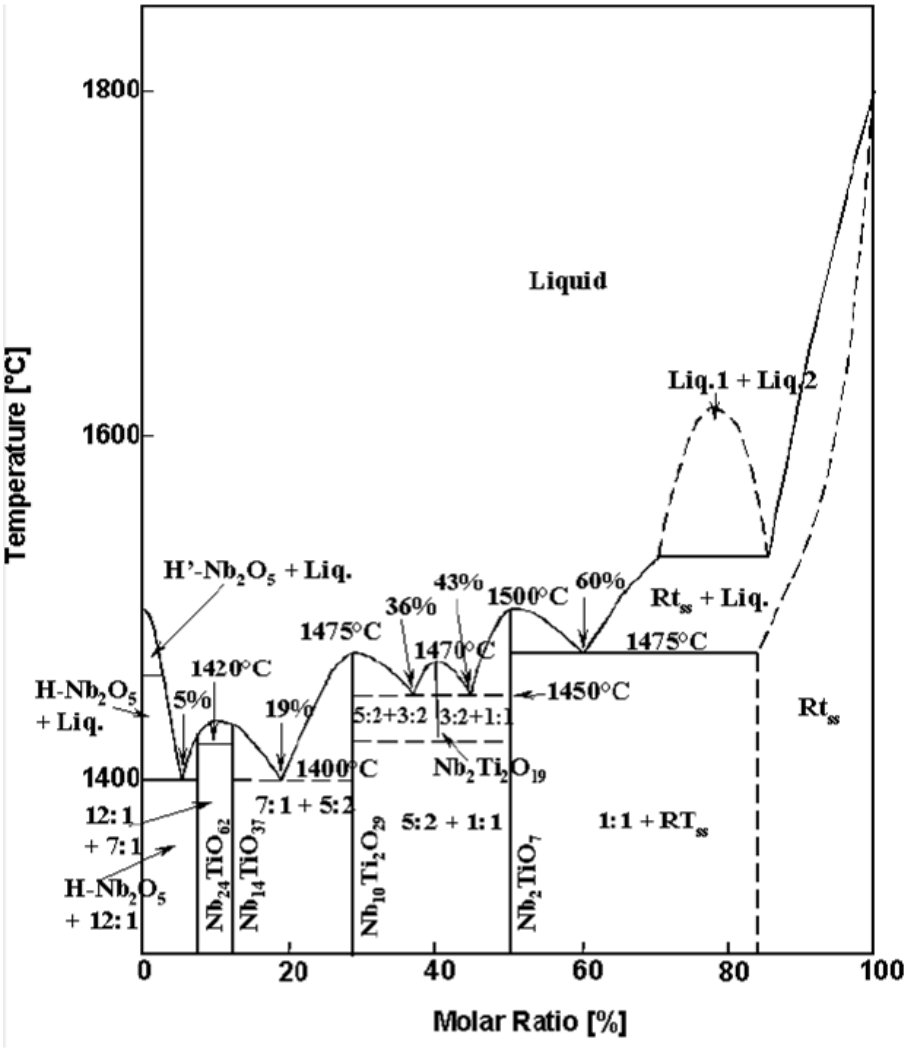

Figure 3.6 Schematic of the Nb_2O_5 – TiO_2 phase diagram (Reich et al., 2001).[29]

3.5.2 Nb_2O_5 – SiO_2 binary

Figure 3.7 shows the Nb_2O_5 – SiO_2 phase diagram and the important fact to take is that these oxides do not mix at any temperature and again can produce

[29] Permission obtained from John Wiley and Sons, Fuel Cells, 1, Reich, C. M., Kaiser, A. and Irvine, J. T. S., Niobia Based Rutile Materials as SOFC Anodes, 2001, Copyright 2014

melting points of 1448 ^{o}C. According to this phase diagram, the structure of SiO_2 below 1448 ^{o}C is tridymite, which is a hexagonal crystal structure with lattice parameters of *a* = 5.0300 Å, *c* = 8.2200 Å, and so it could be expected that it will be a crystalline form of SiO_2 rather than an amorphous that will form during oxidation at 1200 ^{o}C.

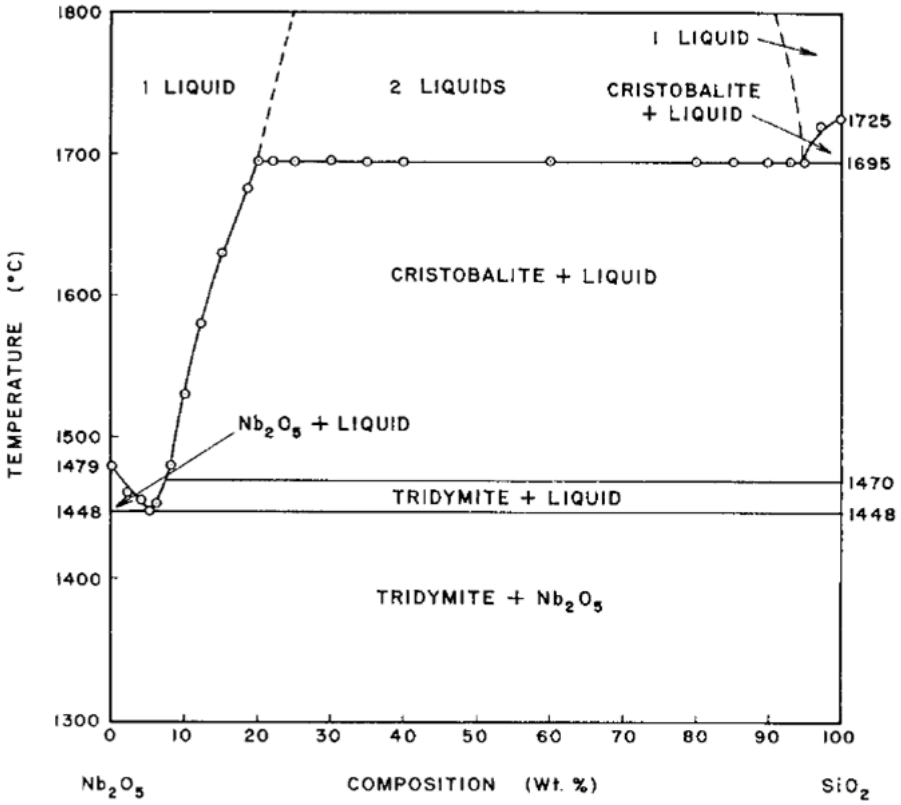

Figure 3.7 Schematic of the Nb_2O_5 – SiO_2 phase diagram (Ibrahim and Bright, 1962).[30]

3.5.3 Nb_2O_5 – GeO_2 binary

Figure 3.8 shows the binary phase diagram of the Nb_2O_5 – GeO_2 system. The system is characterised by one eutectic point at ~97 % GeO_2 at 1090 ^{o}C and one peritectic point at 1420 ^{o}C where the binary compound $9Nb_2O_5.GeO_2$ is formed from Nb_2O_5 and liquid. The phase diagram also shows that as the level of GeO_2

[30] Permission obtained from John Wiley and Sons, Journal of the American Ceramic Society, 45, Ibrahim, M. and Bright, N. F. H. , The Binary System Nb2O5— SiO2, 1962., Copyright 2014

increases, the melting point decreases, and can decrease below 1200 ^{o}C which is the temperature of some oxidation tests performed on Nb silicide.

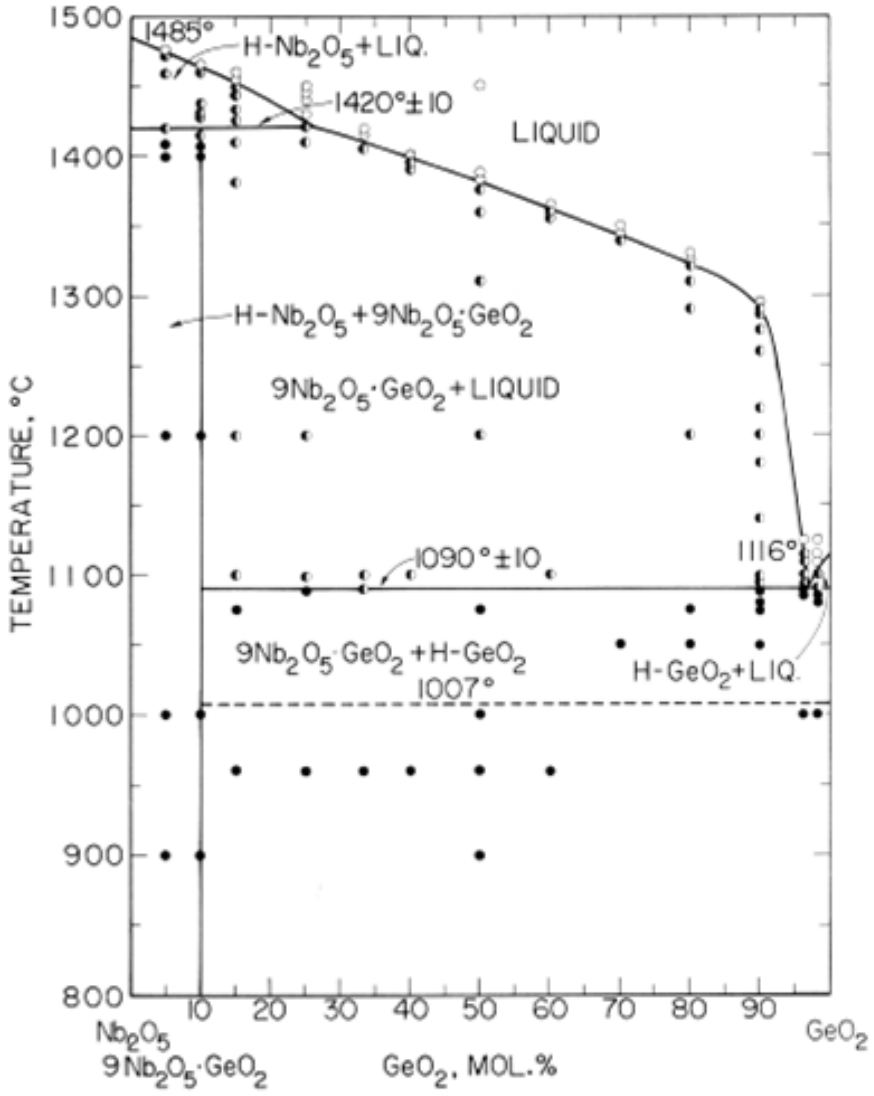

Figure 3.8 Phase diagram of the Nb_2O_5 – GeO_2 binary system (Levin, 1966). H-Nb_2O_5 (high temperature form of Nb_2O_5) and H-GeO_2 (Quartz form of GeO_2).

3.5.3 SiO_2 – TiO_2 binary

Figure 3.9 shows the binary phase diagram of the SiO_2 and TiO_2 system (Ehrman et al., 1999). Again, like the SiO_2 – Nb_2O_5 system, SiO_2 and TiO_2 do not mix at any temperature and the system contains a eutectic point at ~14 % TiO_2. Unlike the Nb_2O_5 – SiO_2 system, it is the Cristobalite form of SiO_2 that is stable below ~1800 ^{o}C rather than the Tridymite form. Cristobalite is a tetragonal crystal

structure with lattice parameters of a = 4.9709 Å, c = 6.9278 Å. Both SiO_2 and TiO_2 are likely to form within the oxide scale or substrate material during oxidation testing.

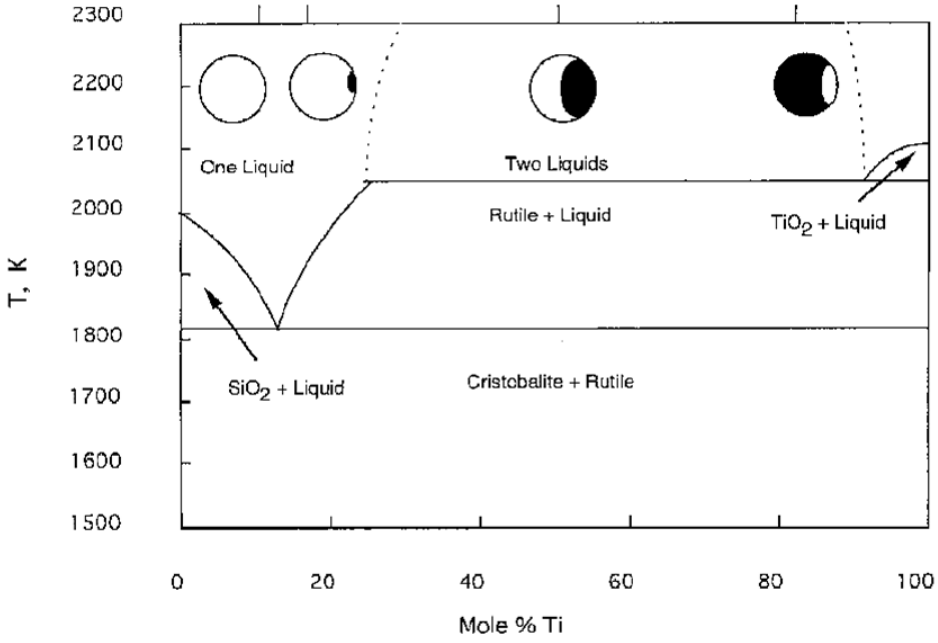

Figure 3.9 Phase diagram of SiO_2 – TiO_2 binary system (Ehrman et al., 1999).[31]

3.5.4 Y_2O_3 – Al_2O_3 binary

Figure 3.10 shows the phase diagram of the Y_2O_3 – Al_2O_3 oxide system (Medraj et al., 2006). Several intermediate oxides are present $Y_4Al_2O_9$ (Y_2A), $YAlO_3$ (YA) and $Y_3Al_5O_{12}$ (Y_3A_5) with all of these oxides stable below 1820 ^oC, the eutectic temperature of Y_3A_5 and Al_2O_3. As most oxidation experiments for Nb silicides are conducted ≤1500 ^oC, if there is any interaction of these two oxides, it will not be through a melting/solidification process. All of the oxides present in this system are line compounds and possess negligible solubility ranges for other elements. This means that the oxides should remain fairly stoichiometric. It has been shown from the Nb_2O_5 – TiO_2 binary oxide system that a common oxide formed during the oxidation of Nb silicide alloys is $TiNb_2O_7$, which corresponds to a 50:50 mixture of

[31] Permission obtained from Cambridge University Press, Journal of Materials Research, 14, Pope, D. P., Ehrman, S. H., Friedlander, S. K. and Zachariah, M. R., Phase segregation in binary SiO2/TiO2 and SiO2/Fe2O3 nanoparticle aerosols formed in a premixed flame, 1999, Copyright 2014

Nb_2O_5 and TiO_2. If we apply the same conditions to the Y_2O_3 – Al_2O_3 system, then the likely oxide to form is $YAlO_3$ (YA).

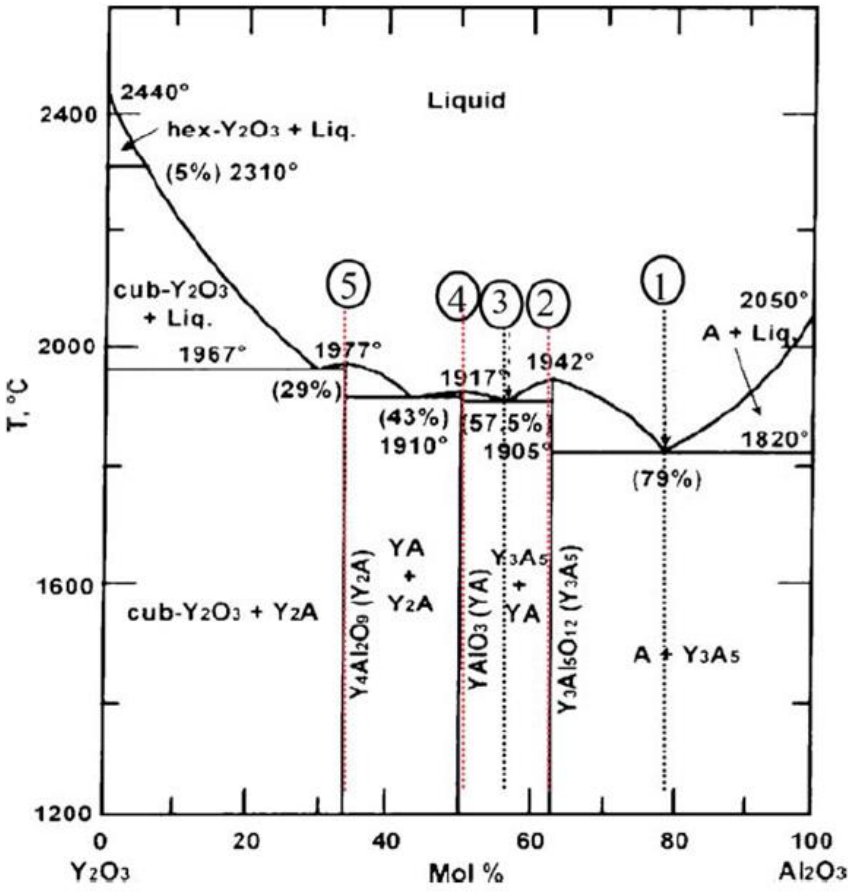

Figure 3.10 Phase diagram of the Y_2O_3 – Al_2O_3 oxide system (Medraj et al., 2006).[32]

3.6 Effects of Y addition on oxidation behaviour

Additions of Y and other 'reactive elements' have been seen throughout the literature to be beneficial for oxidation resistance when growing Al_2O_3 or Cr_2O_3 protective scale. For both it has been documented that Y reduces both the growth rate of the oxide scale and also improves the adhesion of the oxide scale through several mechanisms including mechanical keying, reduced growth stresses, increased scale plasticity, creating vacancy sinks to eliminate voids or enhanced chemical bonding at the substrate scale interface (Park, 1989, Ramanarayanan et

[32] Thompson, W. T., High temperature neutron diffraction study of the Al2O3–Y2O3 system, 3515-3524, Copyright (2014), with permission from Elsevier.

al., 1988, Tian and Guo, 2009, Smialek, 2000a, Hou and Stringer, 1995, Pint, 1996, Saito and Önay, 1990). Figure 3.11 shows a schematic of reactive element additions on growth rate and degree of spallation of M-Cr-Al-X alloys oxidised at 1100 ^{o}C for 100 h. The graph shows that only small levels of additions of the reactive elements are required to achieve the optimal beneficial effects when dealing with the formation of Al_2O_3 scales. The level of Y added to the alloys studied in this work was based on these observations.

Whilst much work has been conducted on the reactive element effect when dealing with Al_2O_3 and Cr_2O_3 formers, work looking into SiO_2 formers is non-existent. If these Nb-Si alloys are to be used in service, work needs to be looked into the effect of the reactive element effect on SiO_2 forming alloys.

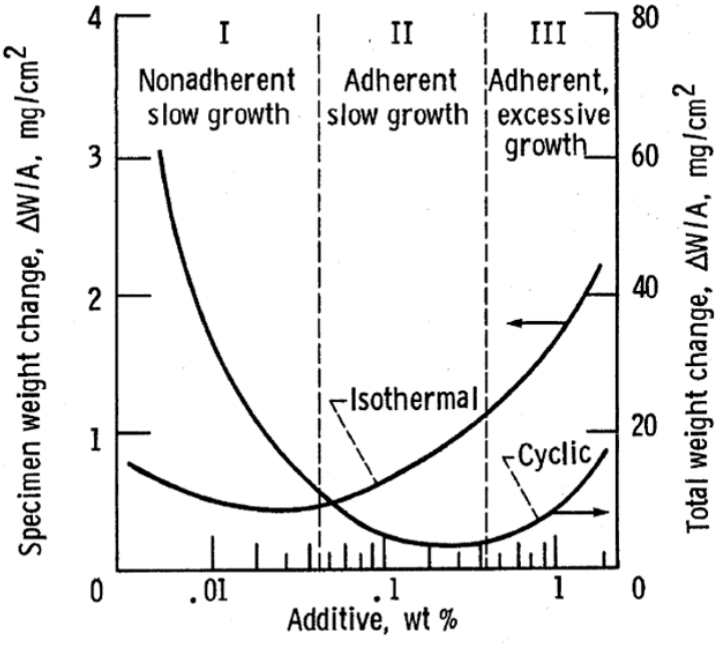

Figure 3.11 Schematic of effects of dopant level on the oxidation behaviour of M-Cr-Al-X alloys oxidised at 1100 ^{o}C for 100 h (Smialek, 2000a).[33]

[33] Springer and the Journal of Materials, 2000, Maintaining adhesion of protective Al_2O_3 scales, Smialek, J., figure 3, copyright 2014) is given to the publication in which the material was originally published, with kind permission from Springer Science and Business Media

Chapter 4

Experimental method

4.1 Selection of alloy compositions

The nominal compositions of the alloys that were designed and produced are listed in Table 4.1.

Table 4.1 Nominal alloy composition (at. %).

Alloy	Nb	Ti	Si	Cr	Al	Ge	Y
AT1	42	24	18	5	5	5	1
AT2	47	24	18	2	5	3	1
AT3	50	24	18	2	2	3	1
AT4	47.95	24	18	2	5	3	0.05

The alloy compositions were designed to build upon previous work conducted within the research group. Alloy AT1 can be compared with ZF6 (Nb-24Ti-18Si-5Cr-5Al-5Ge) and ZF9 (Nb-24Ti-18Si-5Cr-5Al-5Ge-5Hf) (Li, 2012) without the addition of Y. The Ti level was kept at 24 at.% throughout as up to this level has been reported in the literature to be beneficial for fracture toughness of both the Nb_{ss} and the silicide phases without the formation of hexagonal Ti_5Si_3 (Chan, 2005). Silicon was kept at 18 at.% as this has been reported to be the best level for creep performance of these alloys (Bewlay et al., 2001a). The level of Y was kept at 1 at.% for AT1, AT2 and AT3 for two reasons. Firstly, enough Y was required in order to analyse via EDX and investigate its partitioning behaviour. Secondly, initial thoughts in the research field were that Y_2O_3 moulds could be used for DS of Nb silicide materials, Y was included in the alloys with the assumption that there would be contamination of the melt by Y_2O_3 during casting. It has been reported in the literature the possible use of Y_2O_3 as a mould material for industrial manufacture (Ma et al., 2012a, Ma et al., 2012b, Ma et al., 2012c) and it has been reported that there is some interaction between the melt and the mould wall creating a porous interaction layer. The level of Y is higher than would be seen for Ni superalloys to account for this contamination. Alloy AT4 was designed with much lower Y to be more comparable with Ni superalloys and also it had been reported

that in low levels it is beneficial for oxide scale adherence (Park, 1989, Smialek, 2000a).

4.2 Preparation of the ingots

High purity elements, Nb (99.99 wt.%), Ti (99.99 wt.%), Si (99.999 wt.%), Cr (99.99 wt.%), Al (99.99 wt.%), Ge (99.99 wt.%), and Y (99.99 wt.%), were used as the starting materials for the preparation of the ingots. The alloys were prepared via arc-melting and casting high purity elements in a water cooled, Mo crucible under a high purity Ar atmosphere using a non-consumable W electrode, the equipment is shown in Figure 4.1. The chamber was evacuated to $<10^{-3}$ Pa by a rotary pump and a diffusion pump. The chamber was backfilled with Ar to a pressure of ~50 kPa prior to melting. A small Ti piece was melted as an O_2 getter prior to melting each ingot. Each alloy was melted and turned at least 4 times to ensure homogenisation of the composition. The 10 g buttons were cut in half and a 2 mm slice cut from each half. One was prepared for microscopy; one was wrapped in Ta foil for heat treatment. Heat treatments were conducted at either 1300 ^{o}C or 1500 ^{o}C for 100 or 200 h in a tube furnace under an Ar atmosphere. An Al_2O_3 boat was filled with pure Ti sponge and placed inside the furnace at the entrance to act as an O_2 getter, however, oxide was present on the surface of the sample after heat treatment; this oxide layer was removed prior to examination. A typical 10 g ingot is shown in Figure 4.2.

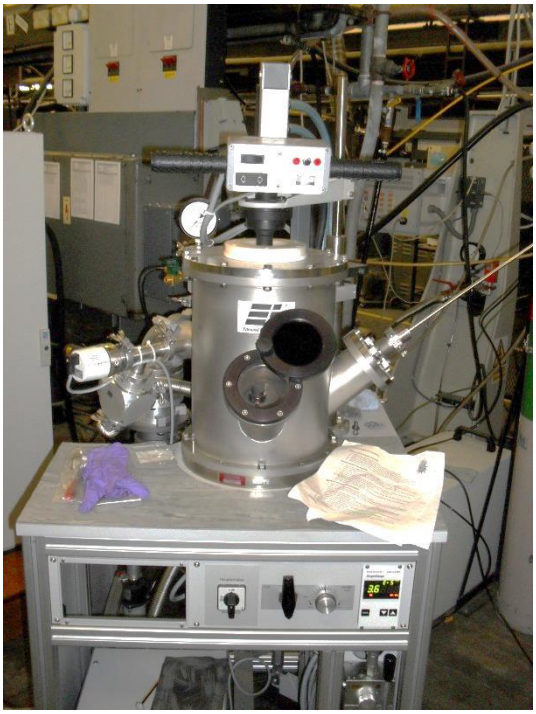

Figure 4.1 Photograph of the arc-melter used in the present study.

Figure 4.2 Photograph of typical 10 g ingot.

4.3 Specimen preparation

Samples were mounted in either conductive Bakelite (KonductoMount – for as cast and heat treated samples) or resin (for the oxidised samples) with the intention for use in electron microscopy. All samples were ground using a progression of SiC papers from p240, p400, p800, p1200, p4000 with the oxide samples spending much more time on the higher grit papers. Samples were polished using 1 µm diamond suspension, and finally using colloidal silica (Silco) to remove as many scratches as possible. As the sample is part intermetallic, conductive Silver dag (from Agar Scientific) was used on the sample to guarantee that the conductive charge would be removed from the sample. Oxidised samples were carbon coated prior to microscopy as well.

4.4 Scanning electron microscopy and energy dispersive x-ray spectroscopy (SEM/EDS)/Electron probe micro analysis and wavelength dispersive x-ray spectroscopy (EPMA/WDS)

The microstructures of the as cast, heat treated and oxidised alloys were studied using scanning electron microscopy (SEM) with energy-dispersive x–ray spectroscopy (EDX) and/or electron probe micro analysis (EPMA) with wavelength dispersive x-ray spectroscopy (WDX). Secondary electron images (SEI) and back scattered images (BSE) were taken using an FEI Inspect F high resolution SEM using 15 kV (for the cross sections of the oxides) and 20 kV (for as cast, heat treated and topographical oxide images) as the accelerating voltage. The alloy compositions were determined using a Phillips PSEM 500 SEM fitted with EDX capability using 25 kV and a Jeol JSM 6400 using an accelerating voltage of 20 kV. Elemental x-ray maps were collected using a Phillips XL30 high resolution microscope fitted with Quantax EDS detector from Bruker. High purity standards

(99.999 wt.%) of Nb, Ti, Si, Cr, Al, Ge and Y were used for quantitative determination of the alloy and phases present using ZAF corrections. High purity cobalt was used for calibration of the system prior to EDX analyses. Due to the spatial resolution of the microscope and under the accelerating voltage, EDX analyses were conducted on phases greater than 5 μm. Within each area, large area EDX analysis (conducted at 320 x magnification) and spot analyses were conducted (at 1250x magnification). At least 10 large area analyses were conducted in each area of the button to determine macrosegregation within the as cast alloy, and at least 10 spot analysis were conducted in each phase. The analysis data provided shows the maximum, minimum and average values together with the standard deviation.

Areas of the button that were investigated were the top (in contact with the Ar atmosphere), the centre (last liquid to solidify and therefore the closest to equilibrium) and at the bottom (area in contact with the water cooled copper crucible) to investigate the effect of cooling rate on the microstructure. The chemical analysis data that is provided in subsequent chapters is presented in tables showing the maximum and minimum levels of elements determined along with the average values accompanied with the standard deviations.

Electron probe microanalysis (EPMA) was conducted to investigate the contamination of the microstructure by O_2 and during heat treatments and after the thermogravimetric (TGA) experiments. Analysis was conducted using a Cameca SX 100 microprobe fitted with wavelength dispersive x-ray spectroscopy (WDX). An acceleration voltage of 15 kV was used and no feature smaller than 4 μm was analysed; the WDX allowed for better resolution. The Phi-Rho-Z matrix correction approach was used to quantitatively determine compositions. Standards used for calibration were Nb, TiO_2, Y_2O_3 (for Y and O), Ge, Cr, $CaSiO_3$ (for Si) and Al_2O_3 (for Al). Quantitative line scans were conducted on the samples that were oxidised on at 800 ^oC for 100 h with each line scan beginning as close to the oxide/substrate

interface and terminating in the bulk of the sample. The purpose for these lines scans was to determine the average depth of oxygen penetration into the material; a schematic of the lines scans taken are shown in Figure 4.3. Ten line scans were taken for each AT1, AT2 and AT3 and each line scan measured 100 µm in length.

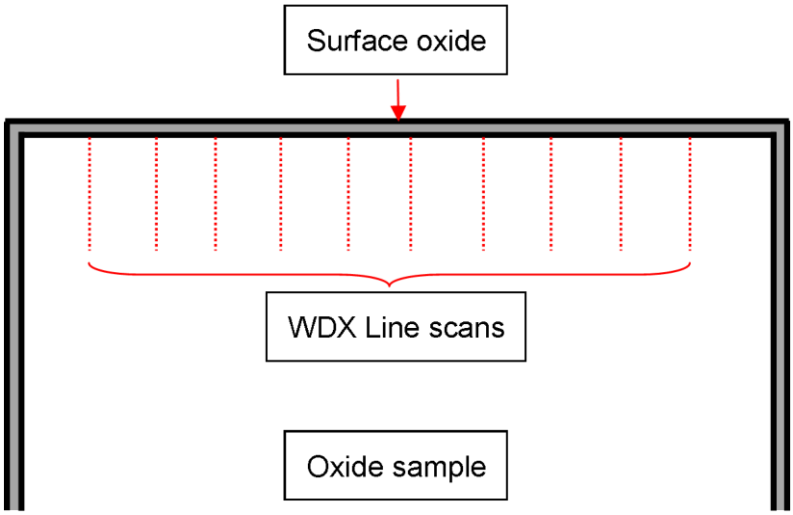

Figure 4.3 Schematic of quantitative WDX line scans collected on samples oxidised at 800 ^{o}C for 100 h. Ten line scans were taken for each sample and started as close to the oxide/substrate interface. Each line scan measures 100 µm in length.

4.5 X-ray diffraction

X-ray diffraction (XRD) was conducted to investigate the phases present within each alloy in as cast, heat treated and oxidised conditions. For the as cast and heat treated specimens, samples were crushed and powdered for XRD. This eliminated texture from the patterns that would be present in diffraction patterns collected from bulk specimens and allowed for a more confident identification of the phases from the signals present. For the oxidised ingots either glancing angle x-ray diffraction (GA-XRD) was used to probe the different layers of the adherent oxide scales, or the scale was removed (if practically possible) and powdered for XRD phase identification.

4.5.1 Powder X-ray diffraction

Powder XRD was conducted using a STOE STADI P diffractometer, Cu $K\alpha_1$ radiation (λ = 1.54056 Å), with a linear position sensitive detector for lattice parameter collection and structural refinement, and an image plate detector for phase identification. The radiation source was excited by an acceleration voltage of 40 kV and 35 mA and a step size of 0.1 ^{o}/sec was used. Powder was prepared in an agate pestle and mortar and glued onto an acetate disc which was transparent to the incident x-ray beam.

4.5.2 Structural refinement

Structural refinement was conducted using the XRD patterns using the Rietveld method (Rietveld, 1967, Rietveld, 1969). Refinement was conducted using the EXPGUI (Toby, 2001) interface for GSAS, General Structure and Analysis Systems (Larson and Dreele, 2000) . The errors quoted are as given by GSAS. Thermal parameters (U_{iso}) were set as 0.025 Å^2 for all positions. Several constraints were applied at the start of refinement. The thermal parameters were constrained to be the same for all atoms sharing a particular site. The total occupancy of sites was set to unity. The background was refined using a shifted Chebyschev function with 6 terms. Following this, the lattice parameters and profile parameters of all phases were refined. Where the refinement indicated that a specific crystal site was shared by multiple atoms, atomic coordinates, thermal parameters or fractions were refined simultaneously as appropriate. Site occupancies were initially refined manually by inclusion of the relevant elements to levels that were comparable to the EDX data collected for the phases present. Site occupancies were further refined by the software, however are only reported to two decimal places. The whole process was repeated to convergence with negligible shifts in atomic variables.

When conducting the refinement, there are several statistical measures that need to be monitored. They are R_{wp} (Weighted profile R-factor), R_p (unweighted

profile R-factor), R_{exp} (expected profile R-factor) and reduced χ^2 (overall measure of the 'goodness of fit') and equations below ((4.1)-(4.4)) show how these values are calculated. The lower the values the overall better fit of the data.

$$R_{wp}^2 = \frac{\sum_i w_i (y_{oi} - y_{ci})^2}{\sum_i y_{oi}} \quad (4.1)$$

$$R_p = \frac{\sum_i |y_{oi} - y_{ci}|}{\sum_i y_{oi}} \quad (4.2)$$

$$R_{exp}^2 = \frac{N - P}{\sum_i w_i y_{y_{oi}}^2} \quad (4.3)$$

$$\chi^2 = \frac{R_{wp}}{R_{exp}} \quad (4.4)$$

y_{oi} = observed intensity at data point i, y_{ci} = calculated intensity at data point i, w_i = weighting factor, N = number of data points, P = number of least-squares variables.

It is worth noting that none of the previous equations include any parameter dealing with the structural model that is used/determined from/during the refinement. Fortunately, the structures of the phases that could be present (Nb_{ss}, Nb_5Si_3 etc.) have been determined with information regarding lattice parameters, atomic coordinates and bond lengths available from crystallographic information files (CIF) available from the ICSD database. Therefore, the structural information that was used was regarding the phases present is correct.

Refinements were conducted to provide information about the lattice parameters of the more complex silicide phases and also to provide information

about site substitution within the crystal structures. Such data is scarce and rarely reported. The software works by calculating structure factors (equation (4.5)) for each reflection, based on structural information provided about the crystal structures of the phases present, and generates a calculated diffraction pattern. This calculated pattern can then be fitted to the observed pattern collected by altering certain features including lattice parameters of phases, peak shapes and site substitutions.

$$F_{(h,k,l)} = \sum_{j=1}^{N} f_{(j)} exp^{2\pi i\left(hx_{(j)}+ky_{(j)}+lz_{(j)}\right)} \quad (4.5)$$

F = the structure factor, f = atomic scattering factor, i = imaginary number $(\sqrt{-1})$, hkl = miller indicies, xyz = atomic coordinates. The structure factor tells us what reflections to expect (hkl) for a crystal structure with atoms located at coordinates (xyz) (Cullity, 1978).

4.5.3 Glancing angle x-ray diffraction

A Seimens D5000 X-ray diffractometer with $CuK\alpha_{1+2(average)}$ (λ=1.540562 Å) was used for Glancing angle XRD. This technique allows monochromatic, parallel x-rays to fall on a sample at a specific incident angle and the diffraction pattern is collected by a moving detector. The penetration depth and interaction volume of the x-rays depend upon the incident angle of the beam and with smaller incident angles, the depth of penetration is lower. This allows for different incident angles to investigate different depths of oxide layers. This also allows for phases present within a thin oxide layer to be studied. The angles chosen to study the alloys in this study were 1^o, 2.5^o, 5^o and 10^o. It is likely that there will be contribution to the diffraction pattern from the substrate material beneath the oxide layer; however this is expected and can be accounted for.

4.6 Thermogravimetric analysis (TGA)

Thermogravimetric analysis (TGA) was conducted on the as cast samples at two different temperatures to investigate oxidation behaviour. Isothermal oxidation tests were conducted at 800 ^{o}C (within the pest region) and at 1200 ^{o}C for 100 h. Thermogravimetric experiments were conducted using a Netzch STA 449 Jupiter F3 Simultaneous TGA–DSC. Cubic specimens were prepared (as close to 3 x 3 mm^2) for TGA and placed in Al_2O_3 crucibles and placed on to the TGA balance. The initial weight was then calibrated with the furnace covering the sample. The furnace was then lowered over the sample and was not preheated prior to lowering over the sample. The furnace was heated and cooled at a rate of 3 ^{o}C/min to ensure the entire sample was at the test temperature and to minimise the risk of any spallation of oxide layer during the cool down period. The furnace was kept at the desired temperature for 100 h, therefore the entire test ran for 112 h. The base of the crucible was in contact with the thermocouple, thus, temperature and weight gain could be measured simultaneously. The oxide scales were investigated using SEM/EPMA(WDX)/XRD.

Due to the complexity and multitude of the oxides formed both on the alloy surface to form the oxide layer and within the substrate when the alloys are oxidised at 1200 ^{o}C for 100 h, shorter TGA experiments were conducted to investigate how the oxides interact to form the complex, ternary oxides reported in the literature. The shorter isothermal tests at 1200 ^{o}C were conducted at 1, 10, 20, 50 h on alloys AT2 and AT4.

4.7 Transmission Electron Microscopy (TEM)

Due to the size of some features within the oxidised samples being much smaller than 5 µm, SEM/EDX analysis was not a viable option to thoroughly investigate the oxides and identify those that have been formed. Therefore

Transmission Electron Microscopy (TEM) was used to aid the identification of the oxides and determine their crystal structure (as many of the oxides possess different crystal structures). Investigation of the oxides was conducted using an FEI Tecnai 20 TEM with an accelerating voltage of 200 kV, capable of 0.24 nm resolution and probe size down to 1 nm in diameter. Computerised goniometer "CompuStage" allowed easy and accurate specimen position control and a fully embedded EDAX EDS system was used for qualitative microanalysis. Microscopy was conducted on samples created by Focussed Ion Beam (FIB).

4.7.1 Focused Ion Beam Milling (FIB)

Due to the delicate nature and minimum number of the oxide samples, standard ion milling of thin samples was impractical and therefore the use of Focused Ion Beam (FIB) milling was used to generate sample for TEM. Samples were generated using a Quanta 300 D SEM with an accelerating voltage of 20 kV, fitted with a high current FIB using Ga^+ ions, which used an accelerating voltage of 30 kV. The desired area was located and the sample was tilted to 52^o and carbon was deposited on the top of the sample to further protect the sample and provide a marker for milling the trenches on either side of the desired area. Trenches were sputtered using 30 kV Ga^+ ions and beam currents between 1 – 5 nA. The samples were lifted out using an Oxford Instruments Omniprobe and were attached to half a copper ring and thinned to below 100 nm using the ion beam. Samples were then ready for investigation using TEM.

Chapter 5

Study of the effect of Y additions on the microstructure, phase stability and oxidation behaviour of an Nb-Si alloy.

5.1 Introduction

The present work follows on from a systematic study of Nb-silicide alloys containing Ti, Cr, Al and Ge. The motivation for this work was to include Y additions to see (1) the effect of Y additions on the microstructures of these alloys including its segregation behaviour during solidification and its effects on the stability of common phases (2) if the scale adhesion of any oxide layer formed could be improved and (3) if oxygen diffusion down the grain boundaries can be inhibited, which can result in embrittlement of the Nb_{ss} phase and have a detrimental effect on room temperature fracture toughness. This chapter deals with the effect of Y additions on the microstructure morphology, phase stability and oxidation behaviour of a single, complex Nb silicide alloy.

5.2 Results

5.2.1 Microstructure

5.2.1.1 As cast

The alloy was designed with a nominal composition of Nb-24Ti-18Si-5Cr-5Al-5Ge-1Y. The large area EDX analysis (Table 5.1) puts the actual composition at 41.6Nb-24.4Ti-18.4Si-4.5Cr-5.2Al-4.4Ge-1.6Y. Unlike other work there was no evident loss of Si (Mendiratta and Dimiduk, 1993). Figure 5.1 shows typical BSE images of the as cast microstructure present at the top of the ingot (where the melt was in contact with the chamber atmosphere) and at the centre of the ingot (where the last liquid to solidify is present) with Figure 5.2 showing the microstructure present at the bottom of the ingot (where the melt was in contact with the Cu hearth). The microstructure at the centre of the ingot is slightly coarser than that of the rest of the microstructure due to the slower cooling rate experienced. At the top of the ingot, an interdendritic eutectic morphology is seen and there is a higher fraction of this structure seen at the top than in the centre of the ingot. The large

area EDX data shows large scale chemical inhomogeneity of Si ($C_{max} – C_{min} = 5.1$). The phases present in the as cast microstructure are the Nb_{ss} phase (white phase in Figure 5.1 and Figure 5.2) and the high temperature βNb_5Si_3 (grey phase in Figures 5.1 and 5.2), as suggested by Table 5.1, and the XRD data presented in Figure 5.4(a). Unlike alloys of similar Cr level (ZF6 (Li, 2012) KZ5 in (Zelenitsas and Tsakiropoulos, 2005) and JG4 in (Geng et al., 2007a)), there is no evidence of the high temperature C14 Cr_2Nb Laves phases. Both phases exhibit light and dark contrast, which is attributed to microsegregation of Ti. Titanium preferentially partitions (but not completely) to the Nb_{ss} phase and as the βNb_5Si_3 is the primary phase, as solidification continues, Ti is rejected into the melt, which is why most of the Ti rich areas are at the edges and boundaries between the Nb_{ss} and the βNb_5Si_3. Whilst some of these areas were large enough to be analysed within the Nb_{ss} phase (>5 μm in diameter), similar areas within the βNb_5Si_3 phase were too small and therefore, no data is provided in Table 5.1. Within the Nb_{ss} phase, there are areas of high Y and Ge content (shown in Figure 5.5), however these areas are difficult to distinguish in the BSE image and difficult to analyse owing to their small size (~5 μm) and similar contrast to the Nb_{ss} phase.

Figure 5.2(a-c) shows images of the microstructure found at the very bottom of the ingot. Figure 5.2(b-c) show images of the microstructures highlighted in Figure 5.2(a) at higher magnifications. The microstructure at the very bottom of the ingot exhibits two transitions. Firstly, from a fine grain eutectic structure, to a coarser, more ‘irregular’ eutectic type structure where the dendrites are growing perpendicular to the chilled surface. Secondly, from the ‘irregular’ eutectic type structure to the morphology that is seen throughout the rest of the ingot.

5.2.1.2 Heat treated (1500 ^{o}C for 100 h)

The microstructure at the centre of the heat treated specimen is shown in Figure 5.3 with the microstructure at the same areas shown to that of the as cast ingot. The microstructure has coarsened; the areas of darker contrast within the dendrites have disappeared, as have the 'eutectic like' areas between the dendrites. The XRD data (Figure 5.4(b)) shows the presence of Nb_{ss} phase (white) and the high temperature βNb_5Si_3 (grey). It appears that there has been no transformation of βNb_5Si_3 to the low temperature αNb_5Si_3. The most dramatic change in the microstructure has been through the appearance of dark grey and black phases, which from the elemental x-ray maps (Figure 5.6) have been determined to be Ti_xN_y (black) and Y_2O_3 (dark grey) particles. These phases seem to be located mostly within the Nb_{ss} phase through contamination by N_2 and O_2 during the heat treatment process.

The EDX data in Table 5.1 shows that the chemical inhomogeneity of Si has been reduced from 5.1 to 2.4. What is noticeable from Table 5.1 is the reduction in Al content, which is likely due to the formation of a thin Al containing oxide layer on the surface of the alloy during heat treatment; this layer was removed before analysis. The data (in Table 5.1) for the two phases has been separated into the different areas where the data was collected. This was done due to a marked difference in Ti content of the Nb_{ss} phase. At the top and bottom of the ingot (as located in the as cast specimen), the Ti content of the Nb_{ss} phase is lower than that of the centre. This is due to a higher volume fraction of the Nb_{ss} phase being present at the top and bottom of the ingot allowing more contaminants (such as N_2 and O_2) to diffuse into the microstructure and react with the Ti to form Ti_xN_y particles. There is a similar trend for the βNb_5Si_3, however the difference is much less significant. Table 5.2 shows EPMA data collected for the Y_2O_3 particles. The data suggests that the phase is almost stoichiometric Y_2O_3, with small amounts of Nb, Ti and Si.

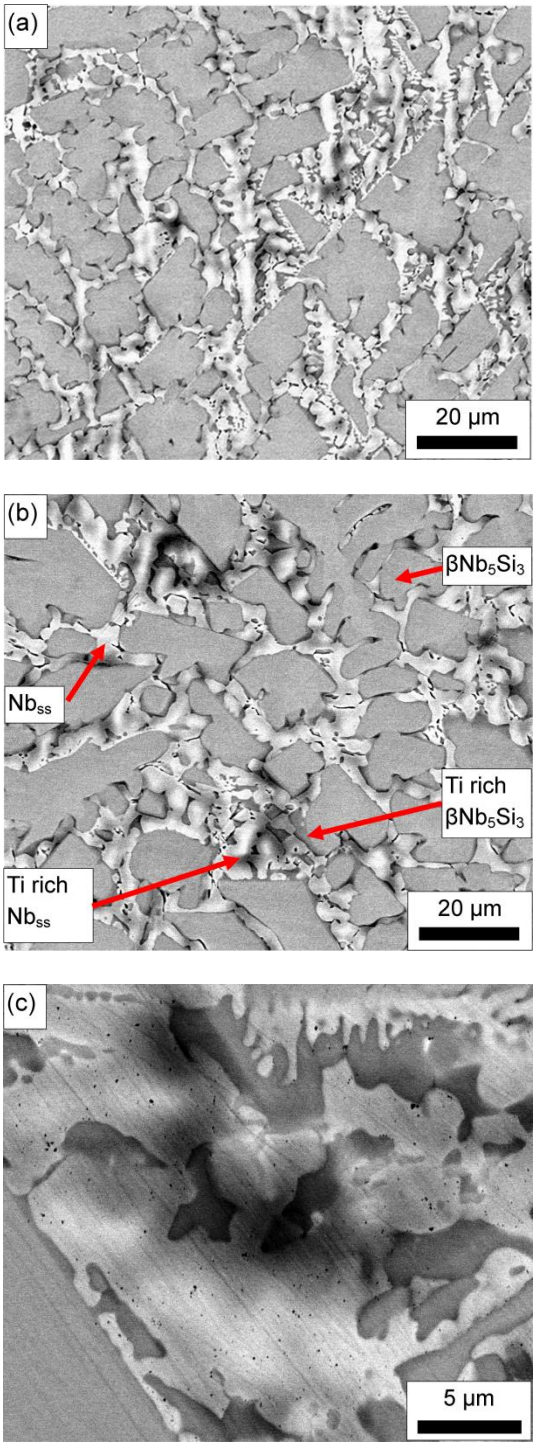

Figure 5.1 Typical BSE images (taken in the FEI Inspect F microscope) of the as cast microstructure taken at 2400x magnification at areas (a) top, (b-c) centre with (c) being a higher magnification image of the interdendritic structure. Each image shows the Nb_{ss} phase (white phase) and the βNb_5Si_3 (grey phase) along with chemical inhomogeneity of Ti (darker areas of contrast in both phases).

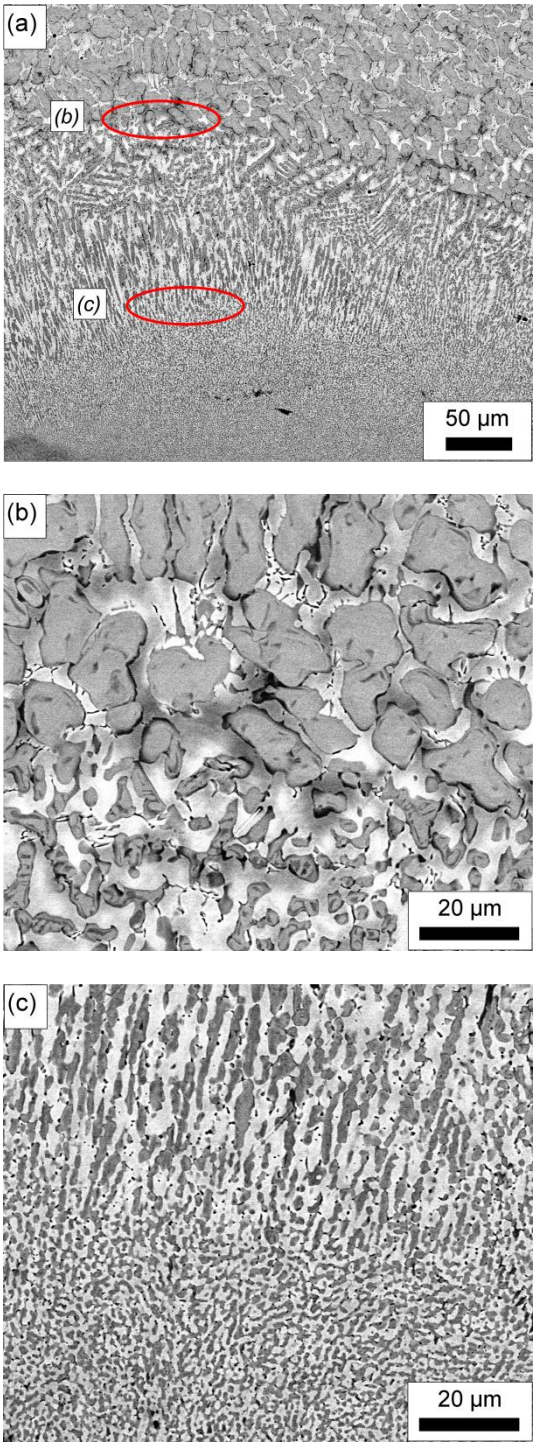

Figure 5.2 BSE images (taken in the FEI Inspect F microscope) of the as cast microstructure taken at 640x and 2400x magnification of several areas at the bottom of the ingot (in contact with the Cu hearth). Each image shows the Nb_{ss} phase (white phase) and the βNb_5Si_3 (grey phase) along with chemical inhomogeneity of Ti (darker areas of contrast in both phases). The highlighted areas in (a) are shown in images (b) and (c) at higher magnifications.

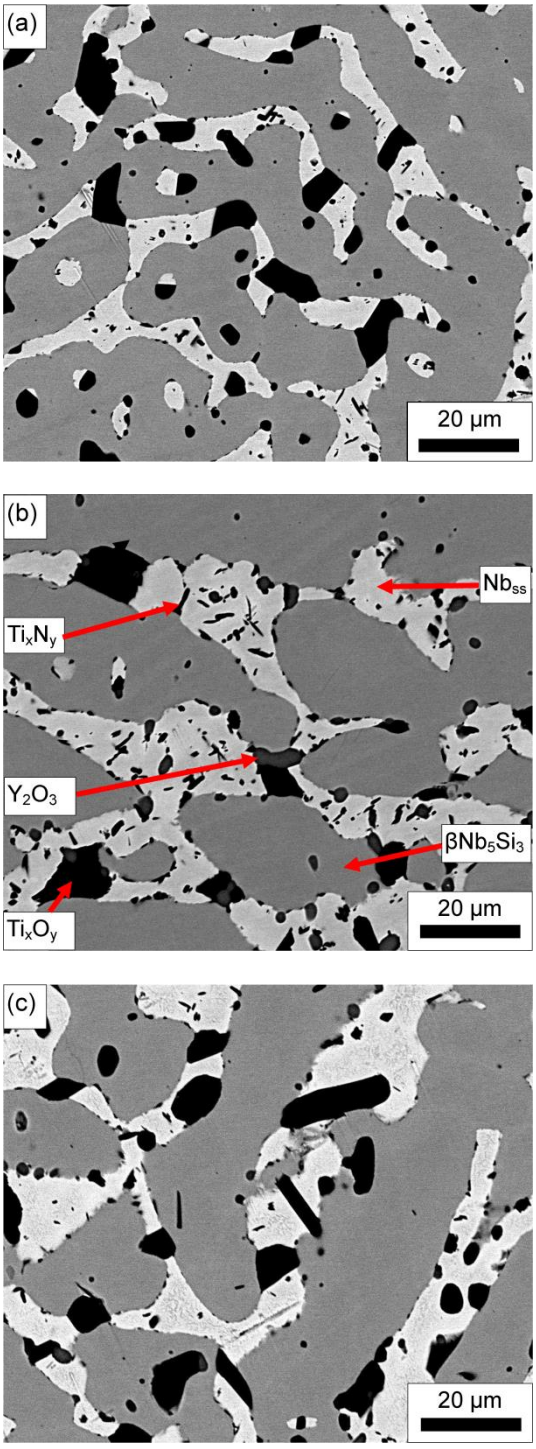

Figure 5.3 Typical BSE images (taken in the FEI Inspect F microscope) of the heat treated (1500 ^{o}C for 100 h) microstructure taken at 2400x magnification at areas (a) top, (b) centre and (c) bottom of the heat treated ingot. Microstructure reveals the presence of Nb_{ss}, βNb_5Si_3 along with Ti_xN_y, Ti_xO_y and Y_2O_3 particles.

Table 5.1 Chemical analysis (at.%) for the as cast and heat treated (1500 ^{o}C for 100 h) AT1. Data presented are the maximum, minimum, average and the standard deviation of the element content.

As cast	Nb	Ti	Si	Cr	Al	Ge	Y
Top	42.0-41.4	24.9-24.1	18.4-17.6	4.6-4.3	5.6-5.1	4.5-4.1	1.9-1.4
	41.7±0.1	24.6±0.1	18.1±0.1	4.5±0.1	5.3±0.1	4.2±0.1	1.6±0.1
Bulk	41.8-41.4	24.8-23.4	20.4-18.2	4.5-3.7	5.2-4.7	4.8-4.3	1.9-1.3
	41.5±0.1	24.1±0.3	19.0±0.5	4.2±0.1	5.1±0.1	4.5±0.1	1.6±0.1
Bottom	41.9-40.8	25.5-23.8	18.9-15.3	5.7-4.2	5.8-4.9	4.6-3.9	2.2-1.3
	41.5±0.1	24.5±0.4	18.0±1.9	4.7±0.3	5.4±0.1	4.3±0.1	1.7±0.1
Bottom $_{(Below\ Transition)}$	42.7-42.3	26.5-25.9	13.2-12.1	7.1-6.6	5.6-5.2	4.5-4.3	2.2-2.0
	42.5±0.1	26.2±0.1	12.6±0.2	6.8±0.1	5.4±0.1	4.4±0.1	2.1±0.1
Bottom Eutectic[a]	41.8	29.3	10	7.7	6.4	2.8	2.1
Nb_{ss}	55.9-48.1	30.4-25.1	3.8-1.9	9.8-7.3	8.0-7.1	2.1-1.0	1.3-0.2
	51.7±4.7	27.9±1.6	2.4±0.4	8.5±0.4	7.6±0.1	1.4±0.1	0.6±0.1
Ti-rich Nb_{ss}	45.4-37.7	36.4-32.5	3.8-1.9	14.8-10.6	7.5-7.0	1.5-0.9	0.8-0.6
	41.4±9.8	34.3±2.7	2.6±0.6	12.6±3.1	7.3±0.1	1.1±0.1	0.7±0.1
βNb_5Si_3	43.2-41.7	20.2-18.6	29.9-27.3	1.1-0.9	4.1-2.2	5.4-4.8	0.9-0.0
	42.5±0.2	19.1±0.2	28.9±0.5	1.0±0.1	3.0±0.2	5.1±0.1	0.5±0.1
Heat treated *(1500 ^{o}C for 100 h*							
Top	43.5-42.7	26.8-25.3	19.0-18.0	4.1-3.6	3.0-2.7	4.4-4.1	2.0-1.4
	43.1±0.1	25.9±0.2	18.5±0.1	3.9±0.1	2.8±0.1	4.2±0.1	1.7±0.1
Bulk	43.5-42.6	25.98-24.7	19.8-17.9	4.3-4.0	3.1-2.5	4.4-4.0	1.7-1.4
	43.1±0.1	25.4±0.2	18.9±0.3	4.1±0.1	2.9±0.1	4.2±0.1	1.6±0.1
Bottom	44.3-42.4	26.3-24.9	19.3-17.4	4.4-3.5	2.8-2.0	4.4-3.7	2.2-1.5
	43.6±0.7	25.5±0.4	18.6±0.4	3.9±0.1	2.5±0.1	4.1±0.1	1.8±0.1
$Nb_{ss\ (Top)}$	67.7-64.1	20.0-17.4	1.2-09	9.7-8.6	3.6-2.3	1.1-0.6	1.8-0.9
	66.1±1.0	18.5±0.7	1.1±0.1	9.1±0.1	3.1±0.2	0.9±0.1	1.3±0.1
$Nb_{ss\ (Centre)}$	61.5-59.6	23.7-21.6	1.3-0.7	10.6-9.2	4.0-2.3	1.2-0.8	1.7-0.5
	60.6±0.6	22.7±0.6	1.0±0.1	10.0±0.2	3.5±0.4	1.0±0.1	1.1±0.2
$Nb_{ss\ (Bottom)}$	69.8-64.5	20.5-17.8	1.4-0.8	10.1-7.9	2.6-0.9	1.3-0.8	2.0-0.9
	66.4±3.4	18.9±0.8	1.1±0.1	9.2±0.5	2.1±0.4	1.0±0.1	1.2±0.1
$\beta Nb_5Si_{3\ (Top)}$	45.6-41.5	20.9-16.3	27.9-26.0	2.6-2.2	3.1-1.3	6.1-5.2	1.0-0.5
	43.1±1.8	18.9±2.1	27.0±0.4	2.4±0.1	2.3±0.4	5.6±0.1	0.8±0.1
$\beta Nb_5Si_{3\ (Centre)}$	41.5-39.8	22.0-20.5	27.8-26.1	2.5-2.1	3.1-2.3	5.4-4.9	1.0-0.4
	40.5±0.3	21.5±0.3	26.9±0.2	2.4±0.1	2.7±0.1	5.2±0.1	0.8±0.1
$\beta Nb_5Si_{3\ (Bottom)}$	42.6-40.9	21.1-19.9	27.5-26.3	2.6-2.3	2.4-1.2	6.1-5.3	1.1-0.5
	41.8±0.3	20.6±0.2	26.8±0.2	2.4±0.1	2.0±0.3	5.7±0.1	0.8±0.1

[a] Refers to the fine eutectic at the very bottom of the ingot shown in Figure 2(a).

Only one data set taken.

Table 5.2 Chemical analysis (at.%) (EPMA/WDS) of Y_2O_3 particles of heat treated (1500 ^oC for 100 h) AT1.

Nb	Ti	Si	Cr	Al	Ge	Y	O
0.2-0.0	0.9-0.1	1.3-0.1	0	0	0	41.7-39.3	60.2-58.4
0.1±0.1	0.3±0.1	0.2±0.1				40.2±0.4	59.4±0.3

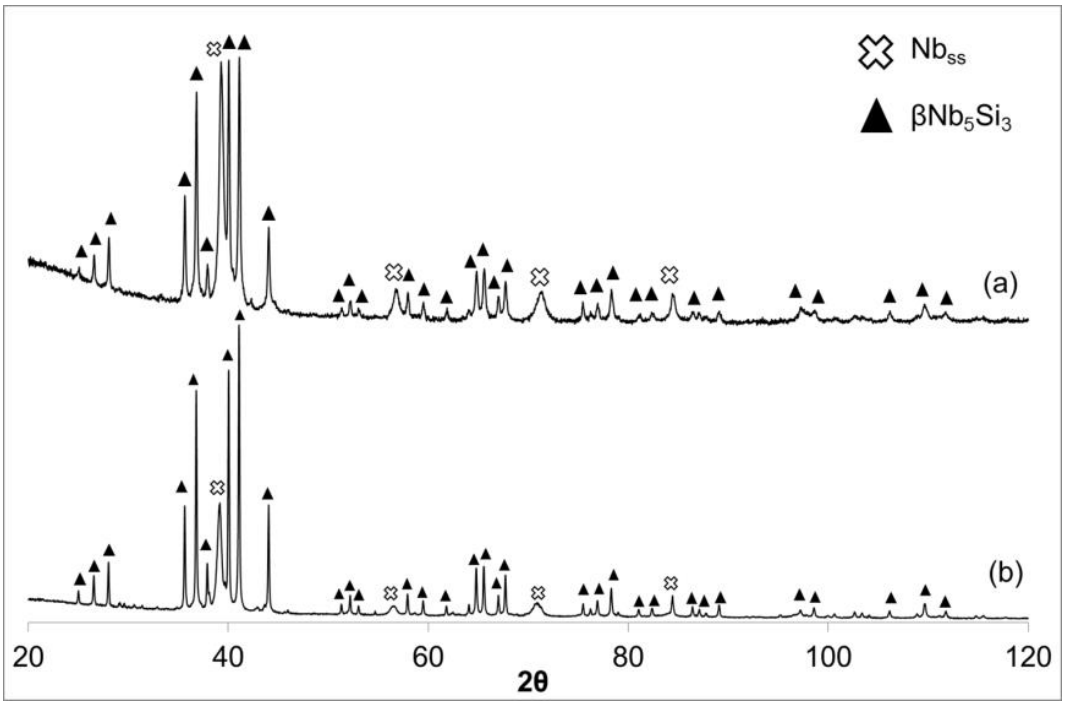

Figure 5.4 Powder x-ray diffraction pattern of AT1 (a) as cast and (b) heat treated condition (1500 ^oC for 100 h). Analysis of XRD data using the Rietveld method using GSAS and EXPGUI will be discussed in the discussion section

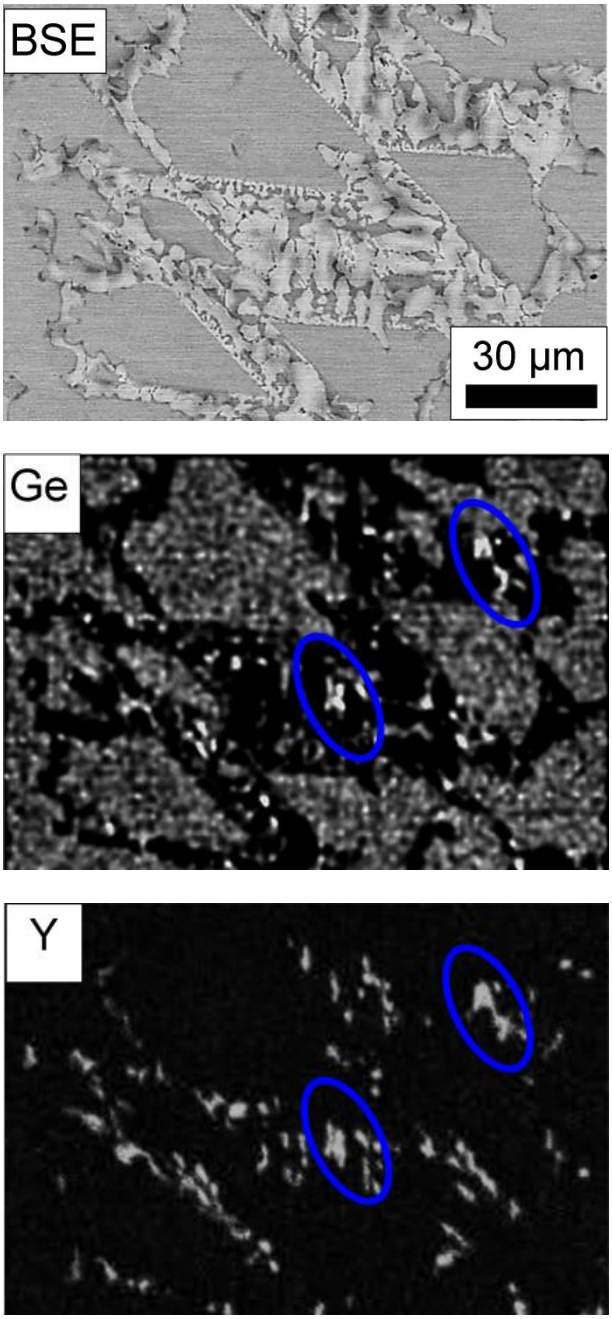

Figure 5.5 Elemental x-ray maps (collected on Phillips XL30 microscope) showing the correlation between Ge and Y in the microstructure of as cast AT1.

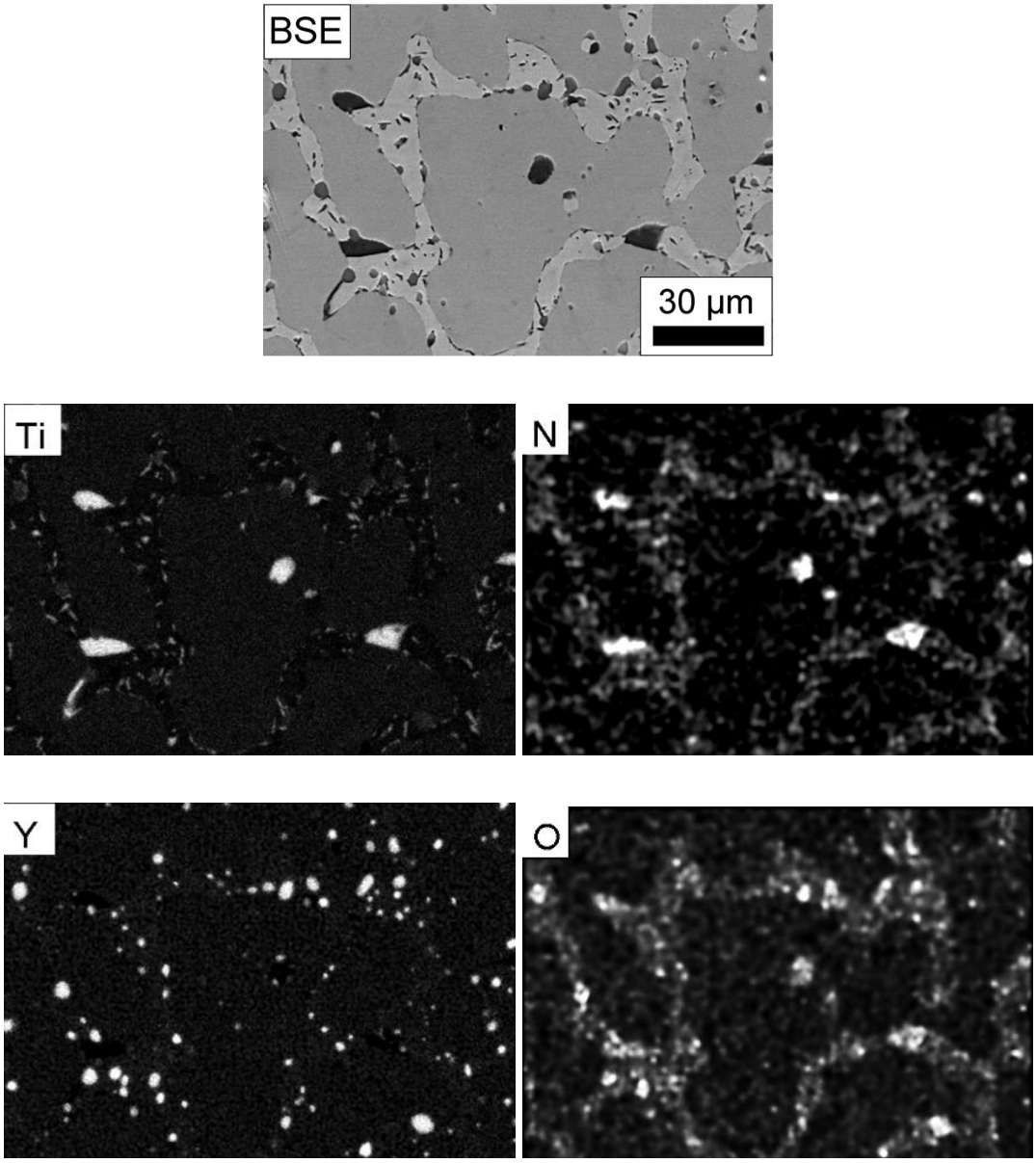

Figure 5.6 Elemental x-ray maps (collected on Phillips XL30 microscope) and BSE image of a selected area of the heat treated microstructure of AT1. Maps are shown for Ti, Y, O and N. Images collected on Phillips XL30 microscope.

5.2.2 Oxidation behaviour

5.2.2.1 Summary of Results

Figure 5.7 shows the specimens after each isothermal TGA experiment at 800 ^{o}C and 1200 ^{o}C for 100 h

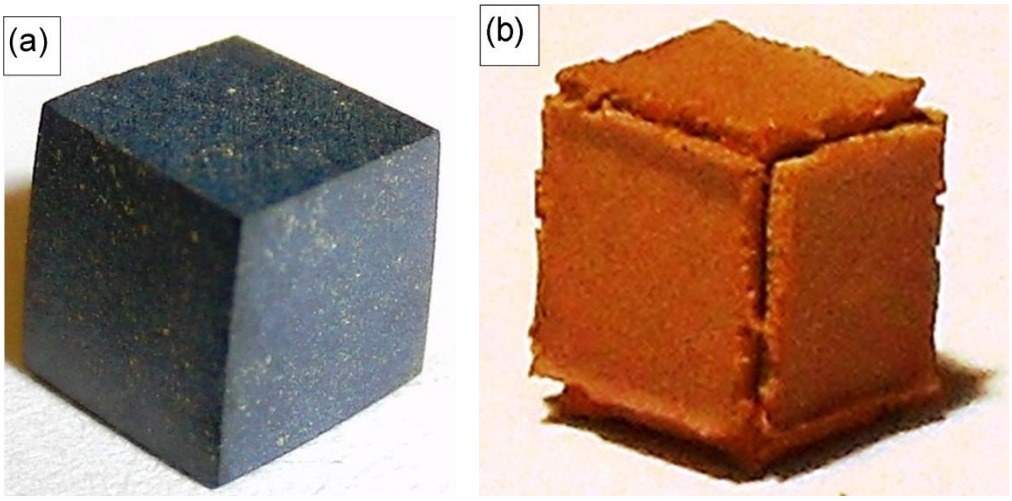

Figure 5.7 Cubic specimens after isothermal oxidation at (a) 800 ^{o}C and (b) 1200 ^{o}C for 100 h under flowing air.

Table 5.3 Comparison of rate constants, weight change per unit area and volume fraction of Nb_{ss} phase for alloys KZ5, ZF6, ZF9 and AT1 at both 800 and 1200 ^{o}C

	800 ^{o}C		1200 ^{o}C			
	K_p (g^2 cm^{-4} s^{-1})	ΔW/A (mg cm^{-2})	K_p (g^2 cm^{-4} s^{-1})	K_l (g cm^{-2} s^{-1})	ΔW/A (mg cm^{-2})	V_f Nb_{ss} (%)
KZ5 (Nb-24Ti-18Si-5Cr-5Al)	-	~35	-	-	-	48-55
ZF6 (KZ5 + 5Ge)	2.3 x 10^{-12}	0.91	2.0 x 10^{-9} (<20 h)	9.7 x 10^{-8}	39.9	17
ZF9 (ZF6 + 5Hf)	8.4 x 10^{-13}	0.55	1.8 x 10^{-9} (<20 h)	1.0 x 10^{-7}	41.4	-
AT1 (ZF6 + 1Y)	1 x 10^{-12}	0.6	-	1.0 x 10^{-7}	41.1	39

ΔW/A = weight change per unit area.

Table 5.3 shows a summary of the rate constants and overall weight gain of alloy AT1 after oxidation at both 800 ^{o}C and 1200 ^{o}C for 100 h. Alloys KZ5 (Nb-24Ti-18Si-5Cr-5Al), ZF6 (Nb-24Ti-18Si-5Cr-5Al-5Ge) and ZF9 (Nb-24Ti-18Si-5Cr-5Al-5Ge-5Hf) are included for comparison purposes.

The rate constants were determined by the equations:

$$\left(\frac{\Delta W}{A}\right)^2 = k_p t \tag{5.1}$$

$$\left(\frac{\Delta W}{A}\right) = k_l t \tag{5.2}$$

where ΔW is the overall weight change (g/cm^2), A is the surface area (cm^2) and t is time (s), k_p and k_l are the parabolic and linear rate constants. This table will be referred to in the following sections.

Table 5.3 shows that the addition of Y had a small effect on the oxidation performance at 800 ^{o}C, lowering the overall weight change from 0.91 to 0.61 mg/cm^2 and the parabolic rate constant from 2.3 x10^{-12} to 1 x 10^{-12} g^2 cm^{-4} s^{-1}. The addition of Y had no effect on the oxidation performance at 1200 ^{o}C.

5.2.2.2 Oxidation at 800 ^{o}C for 100 h

The oxidation behaviour of the alloy was studied at 800 ^{o}C for 100 h to be able to make suitable comparisons with other alloys presented in the literature. Results of the TGA experiment are shown in Figure 5.8 where the weight change is plotted as a function of time. At 800 ^{o}C, the isothermal oxidation kinetics of AT1 were parabolic and the rate constant and weight change per unit area are shown

in Table 5.3 and are compared with alloys KZ5 (Zelenitsas and Tsakiropoulos, 2006a), ZF6 and ZF9 (Li, 2012). Chemical analysis of the Nb_{ss} close to the substrate/oxide interface (Table 5.4) shows 31.8 at.% oxygen now present, which is comparable with values provided in the literature (Geng et al., 2006c, Geng et al., 2007b, Li, 2012, Mathieu et al., 2012). The data shows that all elements in the Nb_{ss} phases are being used to form the oxides and that Nb and Ti are used more than any other element. Chemical analysis shows that no oxygen is present in the βNb_5Si_3.

Figure 5.9 shows several images of the specimen oxidised at 800 ^{o}C. Figure 5.9(a) shows a SEI topographical image of the oxide scale, (b) shows a BSE cross section of the oxide sample and (c) shows the presence of oxide precipitates within the Nb_{ss} phase. The topographical image shows fine, 'whisker-like' oxides that have grown up and away from the surface the of Nb_{ss} phase. It is difficult to know which oxide these are as very little literature contains topographical oxide images, however, (Kofstad and Kjollesdal, 1961) produced an image of Nb_2O_5 grown on pure Nb after oxidation and so it is reasonable to assume that these whisker-like oxides are Nb_2O_5. Glancing angle XRD data (Figure 5.10) identifies Nb_2O_5 and several other oxides such as TiO_2, $Ti_2Nb_{10}O_{29}$, GeO_2, SiO_2. The topographical image shows cracking of the oxide scale, which accounts for the intermittent accelerated weight gain in the TG curve. The cross sectional image shows that there is cracking of the βNb_5Si_3 parallel to the surface, which is a common feature in these alloys (Zelenitsas and Tsakiropoulos, 2006a, Geng et al., 2007b, Menon et al., 2004, Mathieu et al., 2012). It also shows that the majority of the oxidation damage is confined to the Nb_{ss} phase (confirmed by the elemental x-ray maps in Figure 5.13). The elemental X-ray maps show no evidence of a single oxide being formed, or any movement of elements within the microstructure to protect the sample from degradation. Also the average depth of oxygen penetration into the sample is ~25 μm, which is confirmed by the EPMA/WDX line scan data

in Figure 5.11. Figure 5.9(c) shows similar oxide precipitation within the Nb_{ss} phase similar to that reported by (Menon et al., 2004) in a similar pattern of that the oxides are needles or rods and precipitate at ~90 ^{o} to each other. An EDX line scan (Figure 5.12) suggests that these oxides are mainly Ti rich precipitates.

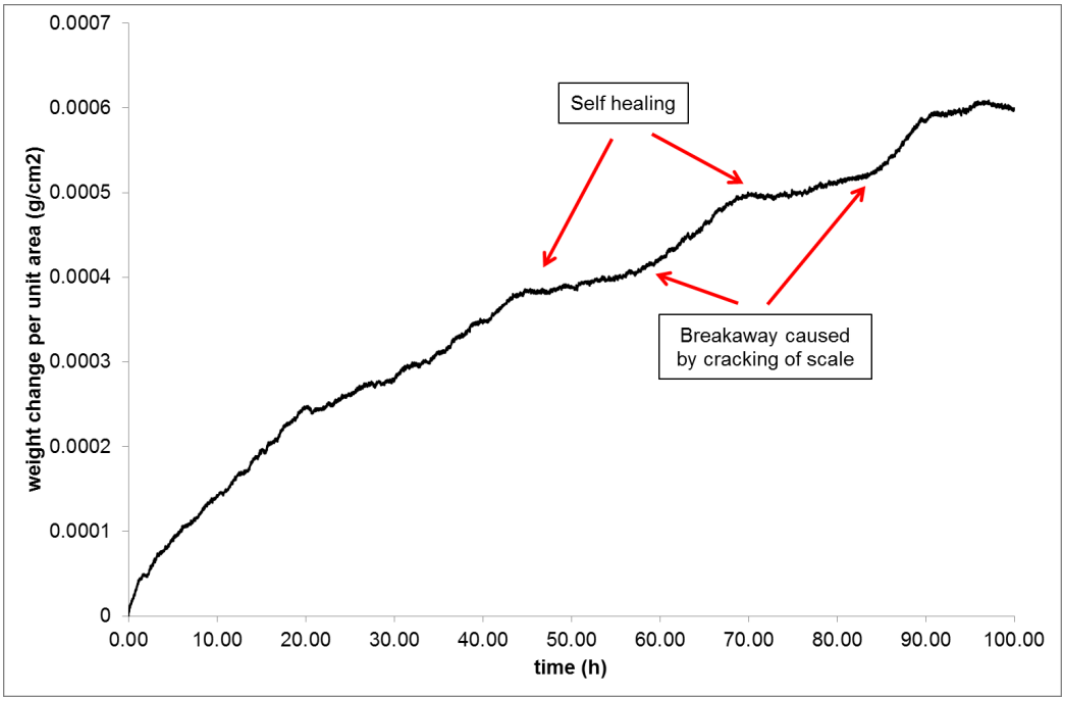

Figure 5.8 Weight change per unit area curves for AT1 oxidised at 800 ^{o}C for 100 h.

Table 5.4 Chemical analysis (EPMA/WDS) of the Nb_{ss} and Nb_5Si_3 phases before and after oxidation at 800 ^{o}C for 100 h

		Nb	Ti	Si	Cr	Al	Ge	Y	O
Nb_{ss}	As cast	55.9-48.1	30.4-25.1	3.8-1.9	9.8-7.3	8.0-7.1	2.1-1.0	1.3-0.2	-
		51.7±4.7	27.9±1.6	2.4±0.4	8.5±0.4	7.6±0.1	1.4±0.1	0.6±0.1	-
	800 ^{o}C/100 h	36.8-32.8	20.8-18.2	3.5-1.0	7.7-5.3	5.4-4.6	1.1-0.4	1.3-0.1	33.1-30.2
		34.8±0.2	19.2±0.1	1.7±0.1	6.6±0.1	5.0±0.1	0.6±0.1	0.3±0.1	31.8±0.2
βNb_5Si_3	As cast	43.2-41.7	20.2-18.6	29.9-27.3	1.1-0.9	4.1-2.2	5.4-4.8	0.9-0.0	-
		42.5±0.2	19.1±0.2	28.9±0.5	1.0±0.1	3.0±0.2	5.1±0.1	0.5±0.1	-
	800 ^{o}C/100 h	43.4-40.7	21.0-17.4	31.8-25.5	1.8-0.9	4.0-2.0	6.4-5.3	0.3-0.1	-
		41.7±0.1	19.0±0.1	29.0±0.3	1.2±0.1	3.0±0.1	5.9±0.3	0.2±0.1	-

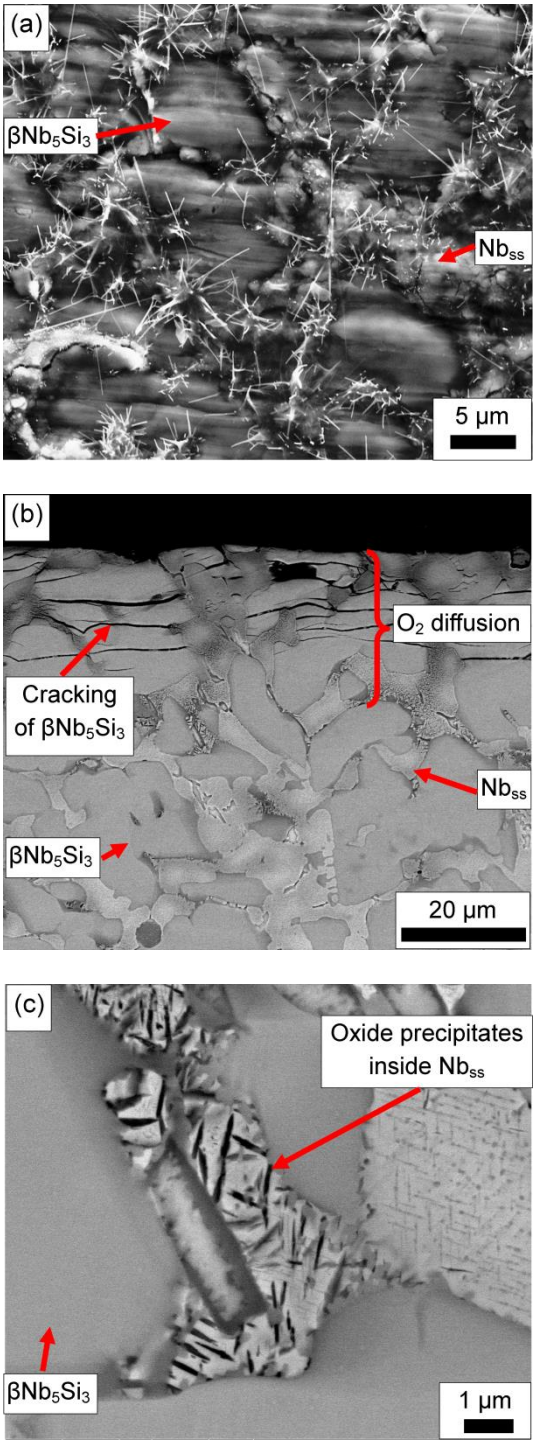

Figure 5.9 Electron microscope images (taken in the FEI Inspect F microscope) of oxidised AT1 at 800 ^{o}C for 100 h showing (a) Topographical features of the oxide scale, (b) BSE image of the cross section of the oxidised AT1 and (c) oxide precipitation within the Nb_{ss} phase.

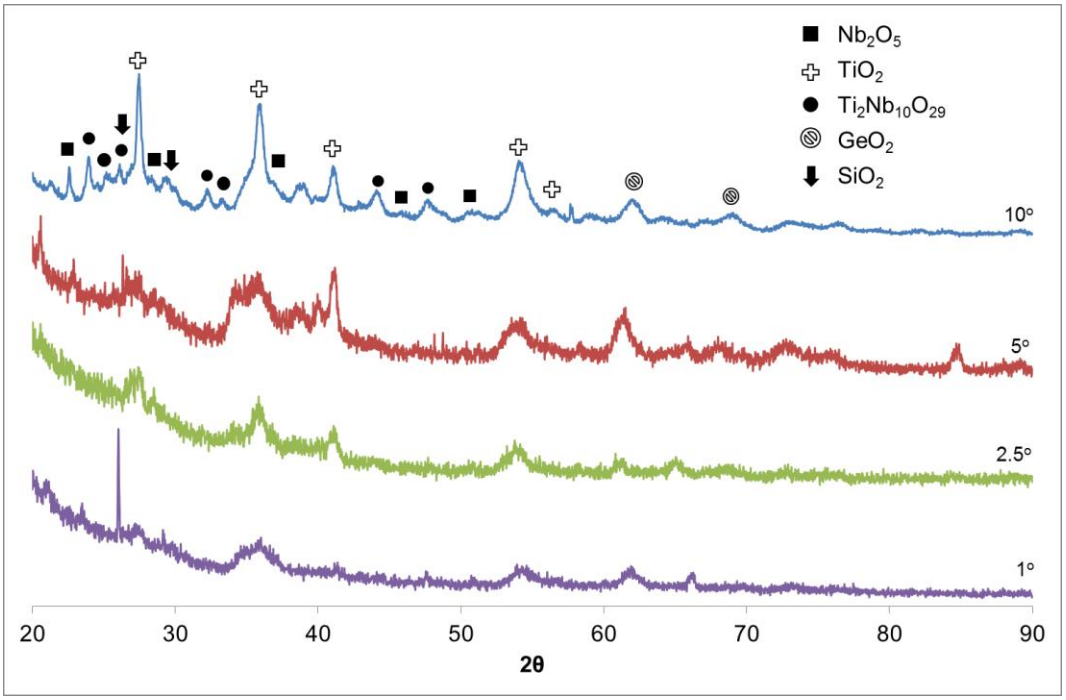

Figure 5.10 Glancing angle XRD patterns of the oxide scale produced after oxidation at 800 ^{o}C for 100 h.

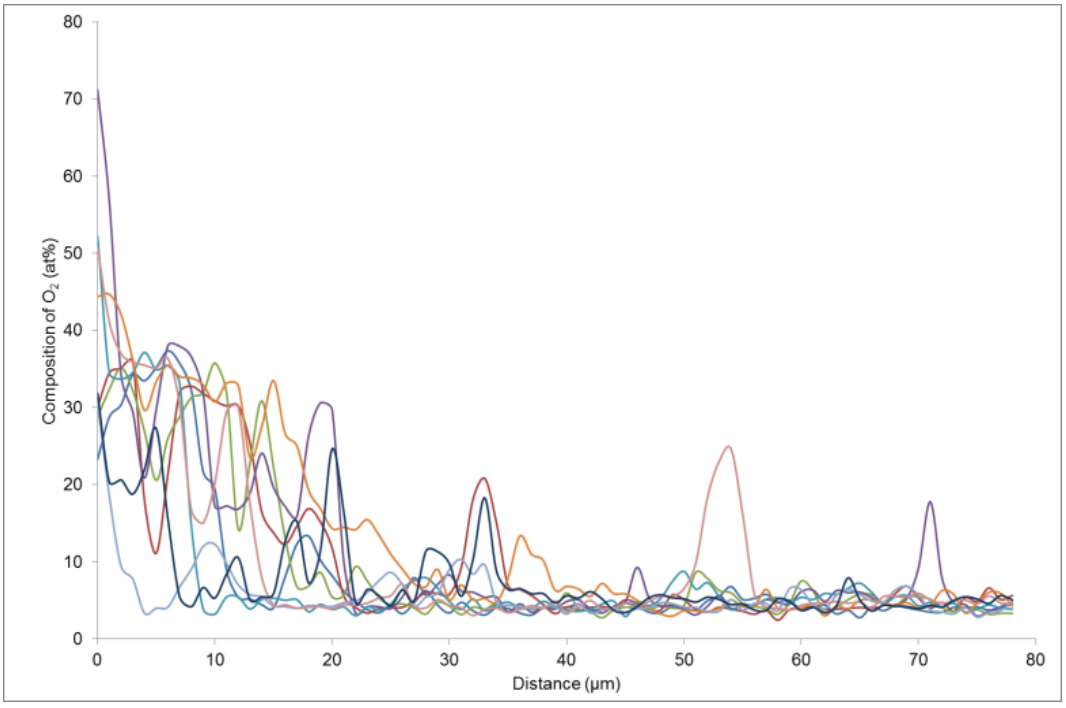

Figure 5.11 WDX line scans of oxygen content only (10 in total). Line scan begins from the oxide/substrate interface into the bulk of AT1 oxidised at 800 ^{o}C for 100 h.

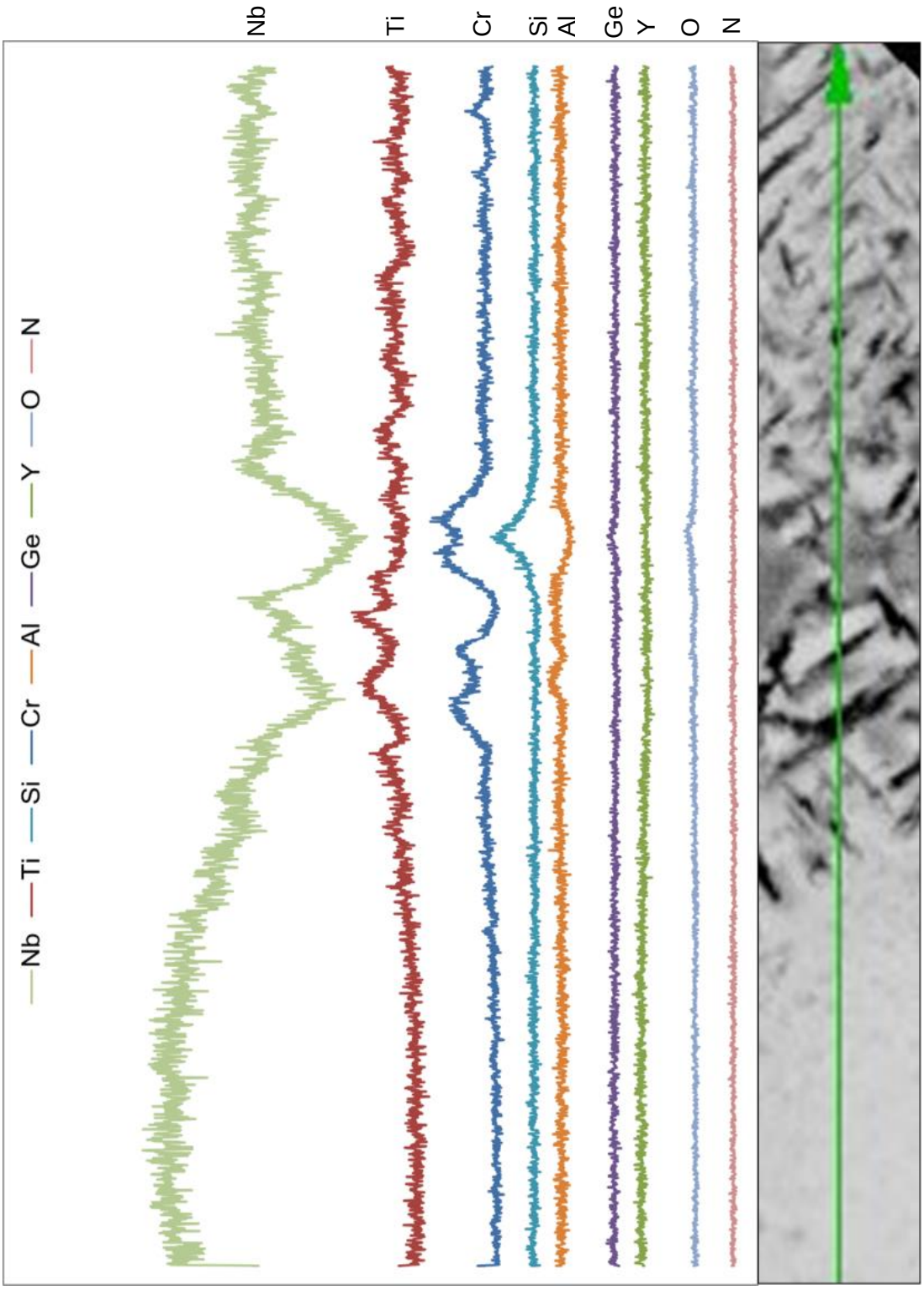

Figure 5.12 EDX line scan over the oxide precipitates within the Nb_{ss} phase after oxidation at 800 ^{o}C for 100 h. Data collected using Cameca SX100 Microprobe.

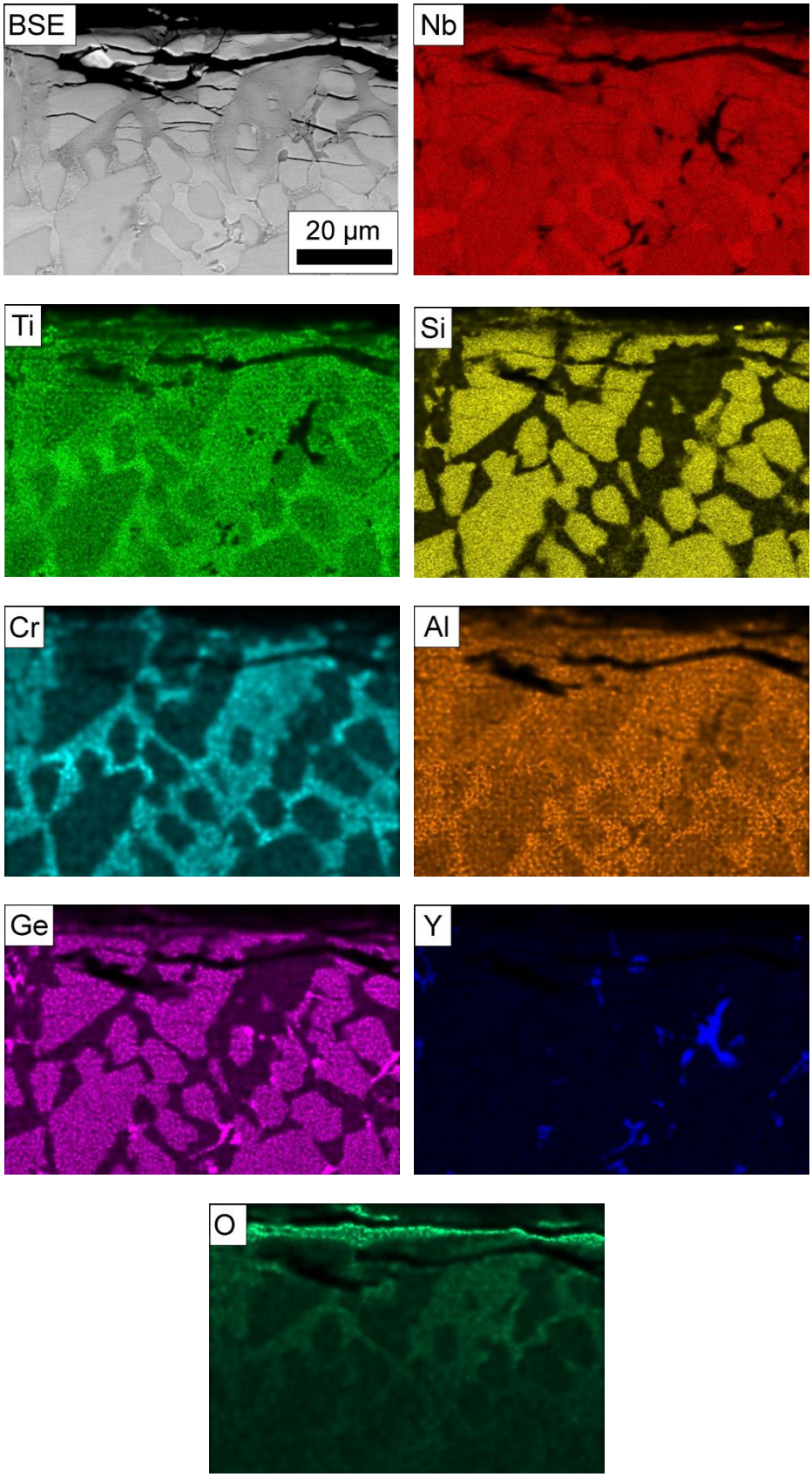

Figure 5.13 Elemental x-ray maps (collected on Phillips XL30 microscope) of the oxide specimen after oxidation at 800 ^{o}C for 100 h.

5.2.2.3 Oxidation at 1200 ^{o}C for 100 h

At 1200 ^{o}C, whilst the oxide scales did not spall off during the oxidation, very little force was required to remove them for XRD. Oxide scale was only present on the surface of the specimen, not at the edges or corners (Figure 5.7(b)). The oxidation kinetics of AT1 followed a linear behaviour (Figure 5.14) and the rate constant and weight gain were identical to that of ZF6 and ZF9 (Li, 2012) (Table 5.3) suggesting that the addition of Y has had no effect on the oxidation resistance of this alloy. Figure 5.15 shows (a) the topographical features of the oxide scale and (b-c) BSE cross section of the oxide scale at different magnifications. The morphology of the oxide scale is similar to that reported by others (Geng et al., 2006c, Geng et al., 2007a). Chemical analysis reveals Nb_2O_5 and a $TiNbO_4$ present in the oxide scale (Table 5.5). Although there are multiple oxides formed in the scale, they are too small to be quantitatively analysed with confidence. Powder XRD (Figure 5.18) revealed the presence of Nb_2O_5, $TiNb_2O_7$, $Ti_{0.6}Nb_{0.2}Cr_{0.2}O_2$, GeO_2, SiO_2 and Y_2O_3, which are also suggested by qualitative x-ray mapping (Figure 5.20). Within the oxide scale, there is no layering of specific oxides or elements within the x-ray maps (Figure 5.19) suggesting that there is no preferential formation of oxides during the oxidation process, all oxides are formed simultaneously.

Internal oxidation of the substrate material was observed, as shown in Figure 5.16(a-b). Oxidation damage is mainly confined to the Nb_{ss} phase with some lesser effect felt by the βNb_5Si_3 phase. Figure 5.17(a) shows the inward attack of the βNb_5Si_3 by the oxidation process and also, the presence of oxides within the βNb_5Si_3 phase, which no one has reported previously. Chemical analysis using TEM conducted on samples created from FIB (Figures 23(a) and 24) suggests that the attack of the βNb_5Si_3 leads to the formation of Nb_5Ge_3, SiO_2 and $Ti_xNb_yO_z$ mixture. Also, there is internal attack of the βNb_5Si_3 with the formation of TiO_2 precipitates within the intermetallic (Figure 5.25). There is an overall main internal diffusion of oxygen into the substrate and the formation of several oxides within the Nb_{ss} phase

(Figure 5.16 and Figure 5.17(b)) which are too small to be analysed by EDX or WDX. Qualitative x-ray mapping suggests multiple oxide formation within the substrate material (Figures Figure 5.21 and Figure 5.22). They suggest the formation of oxides of Ti (likely TiO_2), Y and Al (likely Y_2O_3 and Al_2O_3) and also a $Y_xAl_yO_z$ (likely $YAlO_3$ assuming a 50:50 mixture of Y and Al). There are also still present areas of Nb_{ss} with Cr and the βNb_5Si_3, all of which has been corroborated by EDX analysis in the TEM (Figure 5.24, 5.25 and 5.26). The x-ray maps also show a Ge rich layer below the surface of the oxide scale and this has been previously reported to be due to the formation of Nb_5Ge_3 during oxidation (Menon et al., 2001).

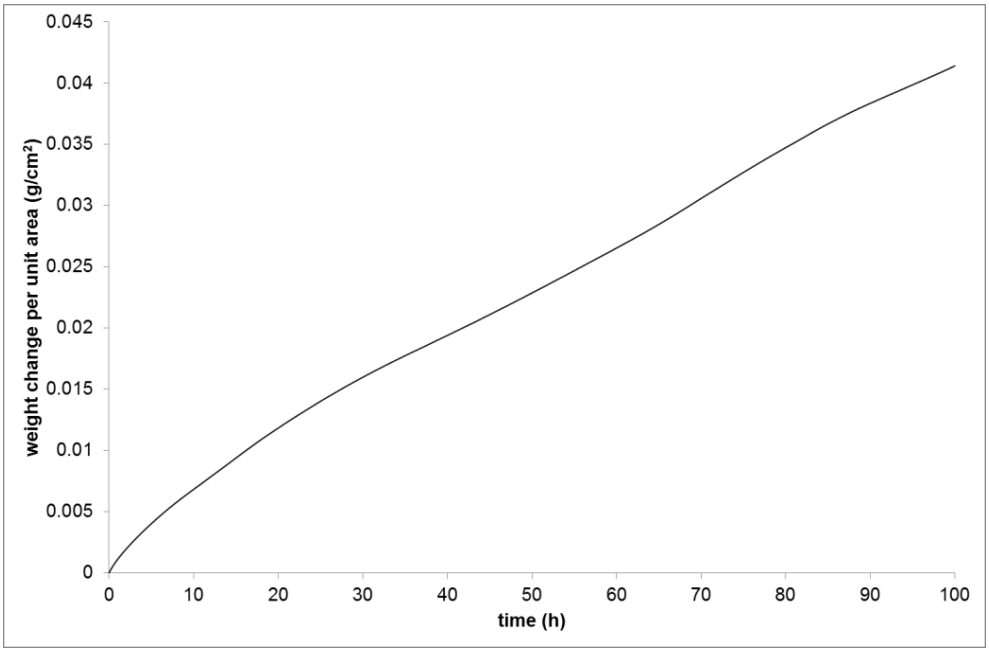

Figure 5.14 Weight change per unit area curves for AT1 oxidised at 1200 °C for 100 h.

Table 5.5 Chemical analysis (at.%) (EPMA/WDX) of phases present in the oxide scale after oxidation at 1200 °C for 100 h

	Nb	Ti	Si	Cr	Al	Ge	Y	O
Nb rich oxide	23.2-21.5	8.2-6.9	0.2-0.1	0.3-0.1	1.4-0.2	0.1-0.0	0.3-0.1	69.5-68.0
	22.2±0.1	7.5±0.1	0.1±0.1	0.2±0.1	0.9±0.1	0.1±0.1	0.2±0.1	68.9±0.1
Ti rich oxide	9.0-7.3	17.2-14.3	0.4-0.1	5.3-2.4	3.9-2.1	1.0-0.1	0.1-0.0	68.8-66.7
	8.3±0.1	16.2±0.1	0.2±0.1	3.8±0.2	3.0±0.1	0.6±0.1	0.1±0.1	67.8±0.1

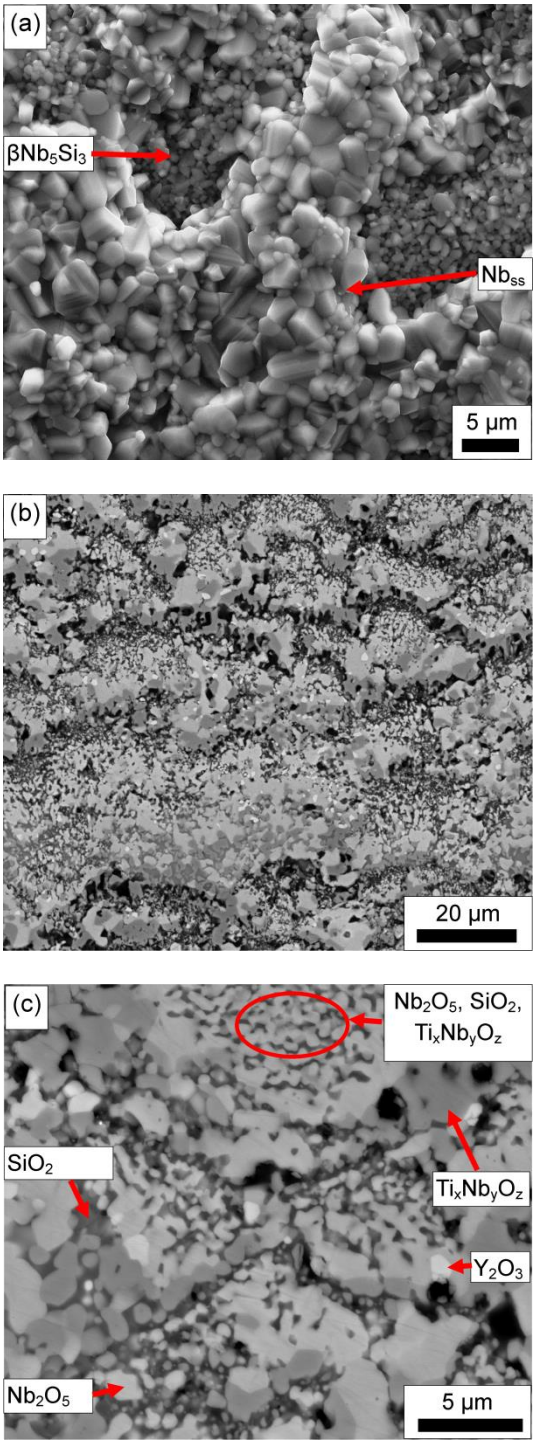

Figure 5.15 SEI and BSE images (taken in the FEI Inspect F microscope) of alloy AT1 oxidised at 1200 ^{o}C for 100 h. Images show (a) SEI topographical features of the oxide scale, (b) low magnification BSE image of the oxide scale and (c) higher magnification BSE image of the oxide scale.

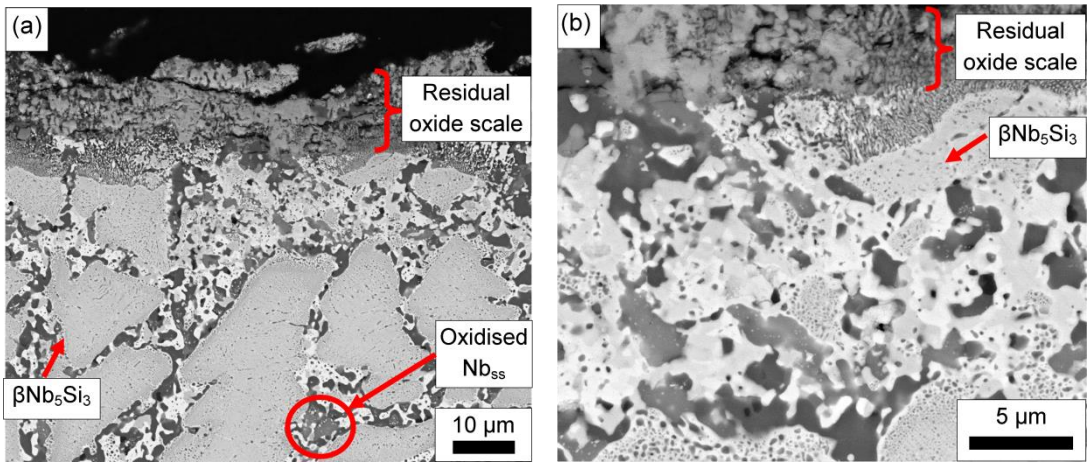

Figure 5.16 Cross sectional BSE images (taken in the FEI Inspect F microscope) of the susbtrate material from alloy AT1 oxidised at 1200 ^{o}C for 100 h. Images show (a) the substrate material showing oxidation of the Nb_{ss} phase and (b) higher magnification of the oxide/substrate interface.

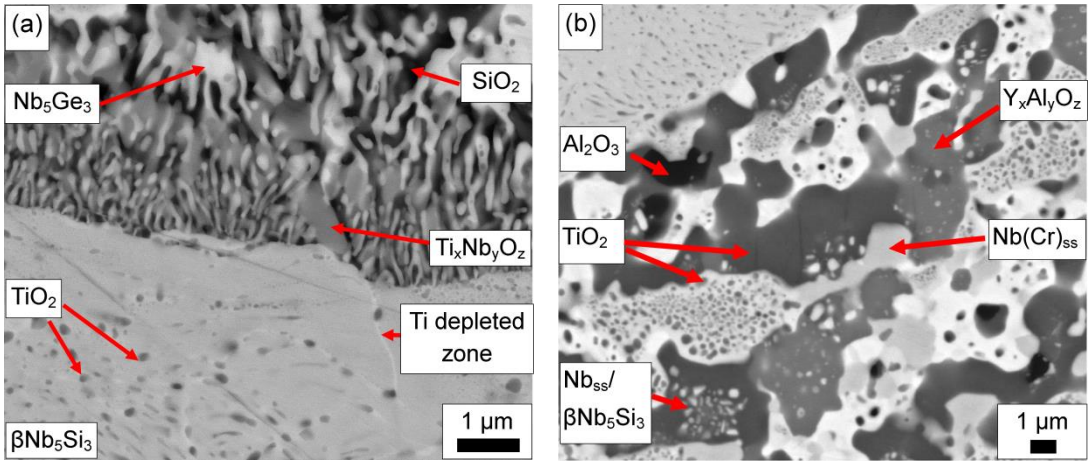

Figure 5.17 Cross sectional BSE (taken in the FEI Inspect F microscope) images of the susbtrate material from alloy AT1 oxidised at 1200 ^{o}C for 100 h. Images show (a) oxidation attack of the βNb_5Si_3 and (b) the substrate material showing oxidation of the Nb_{ss} phase.

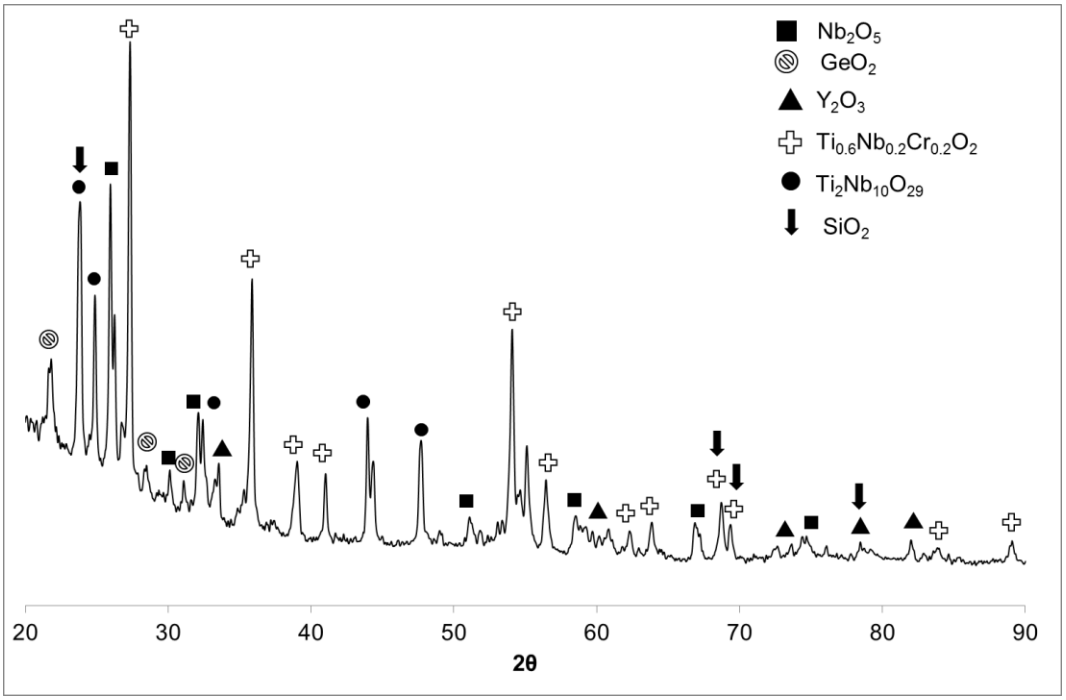

Figure 5.18 Powder XRD pattern of the oxide scale produced on AT1 after oxidation at 1200 ^{o}C for 100 h

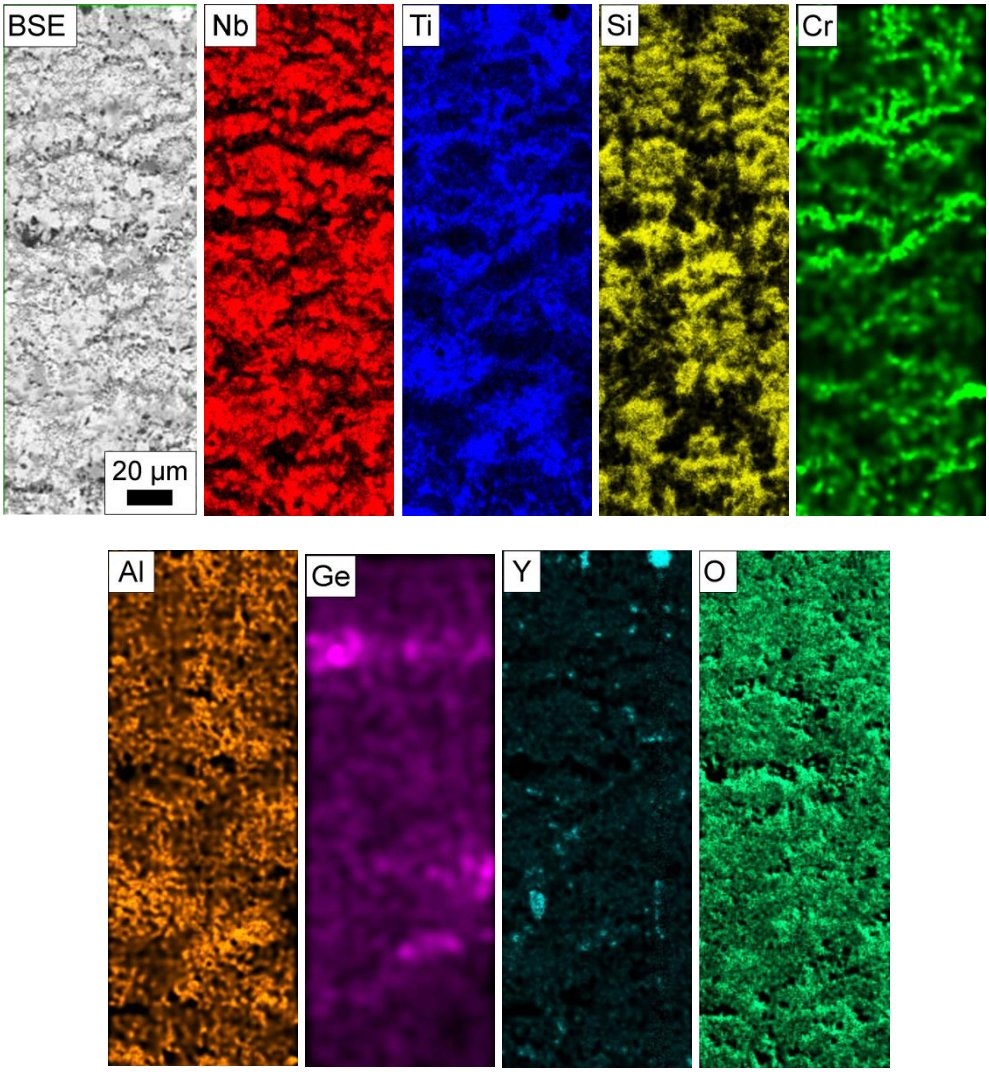

Figure 5.19 Elemental x-ray maps (collected on Phillips XL30 microscope) of the oxide scale produced during oxidation of AT1 at 1200 ^{o}C for 100 h. Map includes the full thickness of the oxide scale.

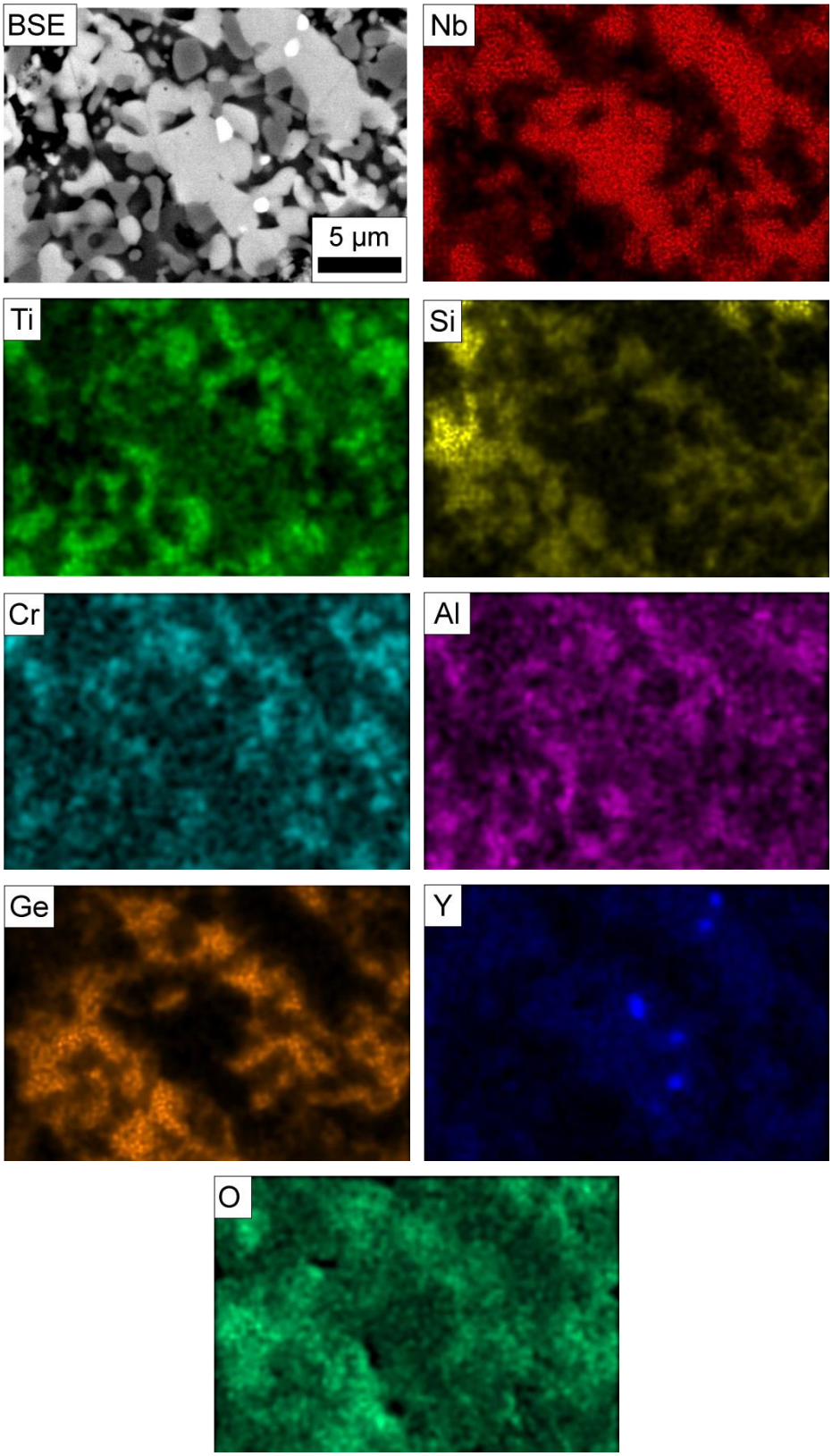

Figure 5.20 Elemental x-ray maps (collected on Phillips XL30 microscope) of the oxide scale produced during oxidation of AT1 at 1200 ^{o}C for 100 h.

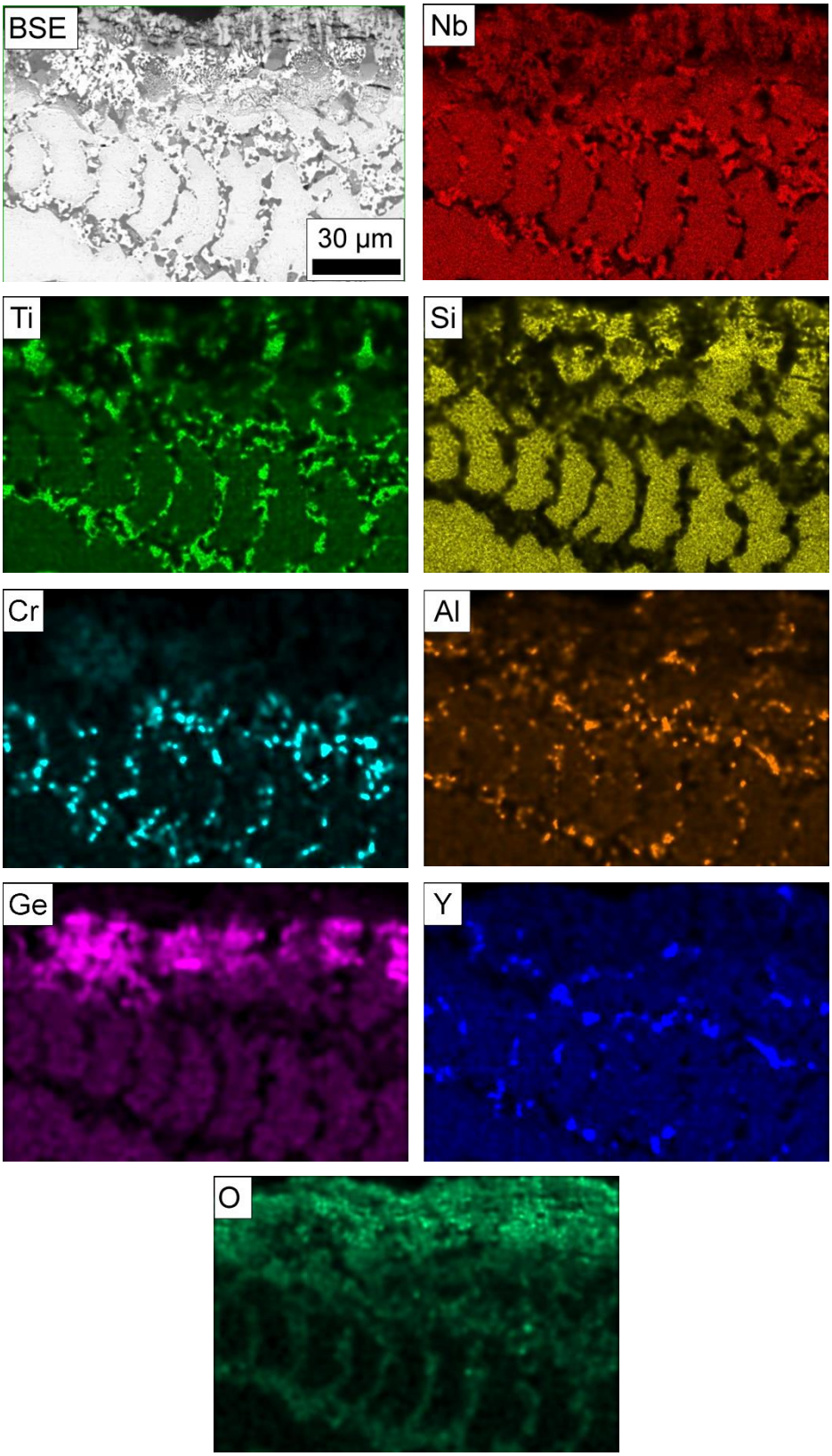

Figure 5.21 Elemental x-ray maps (collected on Phillips XL30 microscope) of the substrate material of AT1 after oxidation at 1200 ^{o}C for 100 h.

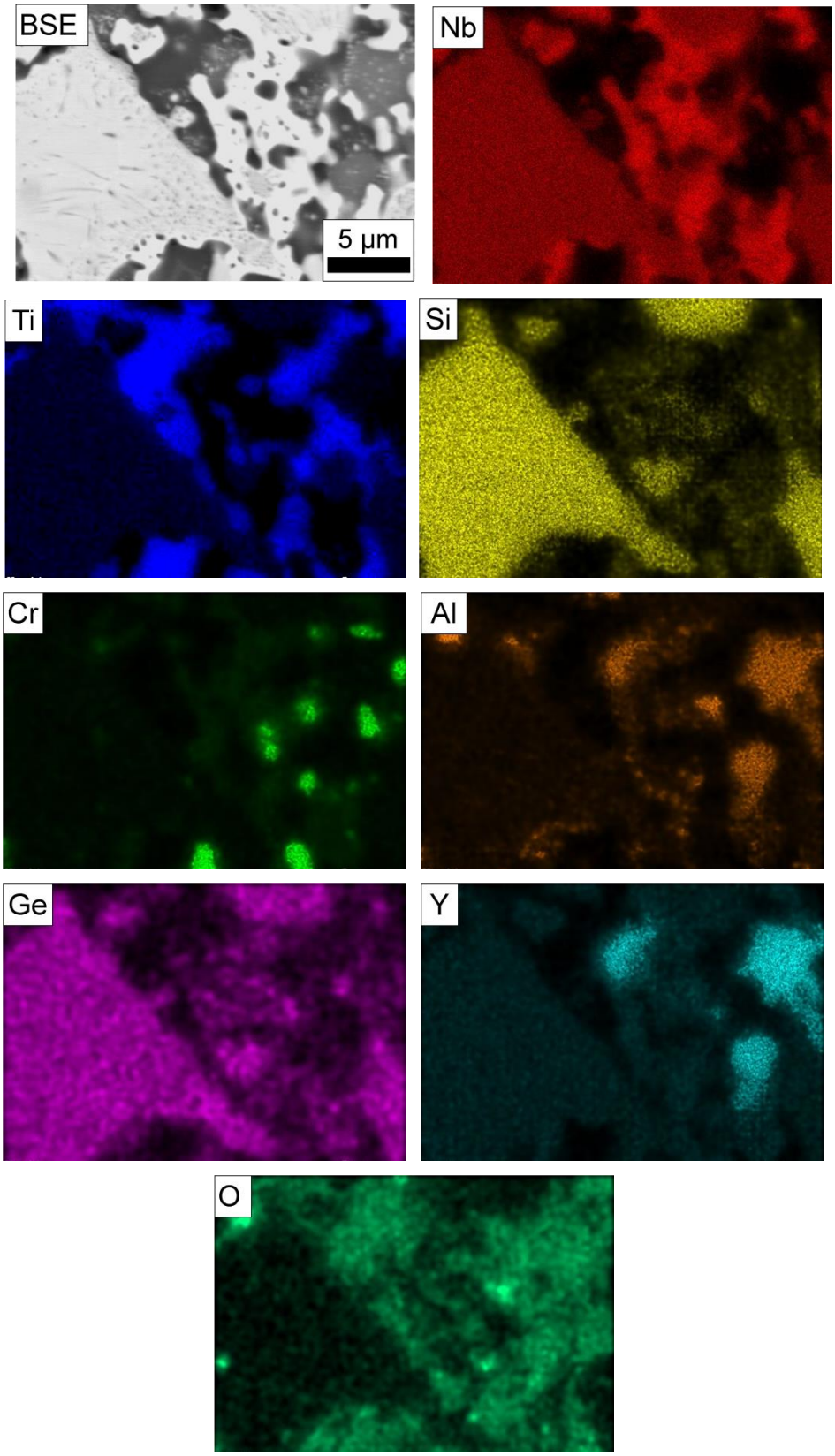

Figure 5.22 Elemental x-ray maps (collected on Phillips XL30 microscope) of the substrate material of AT1 after oxidation at 1200 ^{o}C for 100 h. Area is a high magnification of the Nb_{ss} area containing multiple oxides.

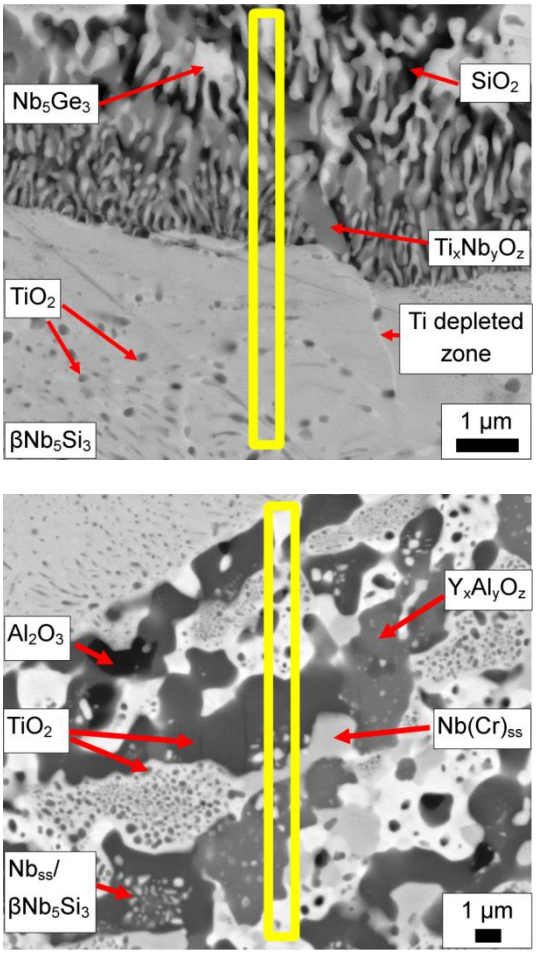

Figure 5.23 BSE images (taken in the FEI Inspect F microscope) of (a) the inward and internal attack of the Nb_5Si_3 and (b) internal attack of the Nb_{ss} region after oxidation at 1200 ^{o}C for 100 h. Yellow rectangles show the typical regions the FIB/TEM samples were taken from.

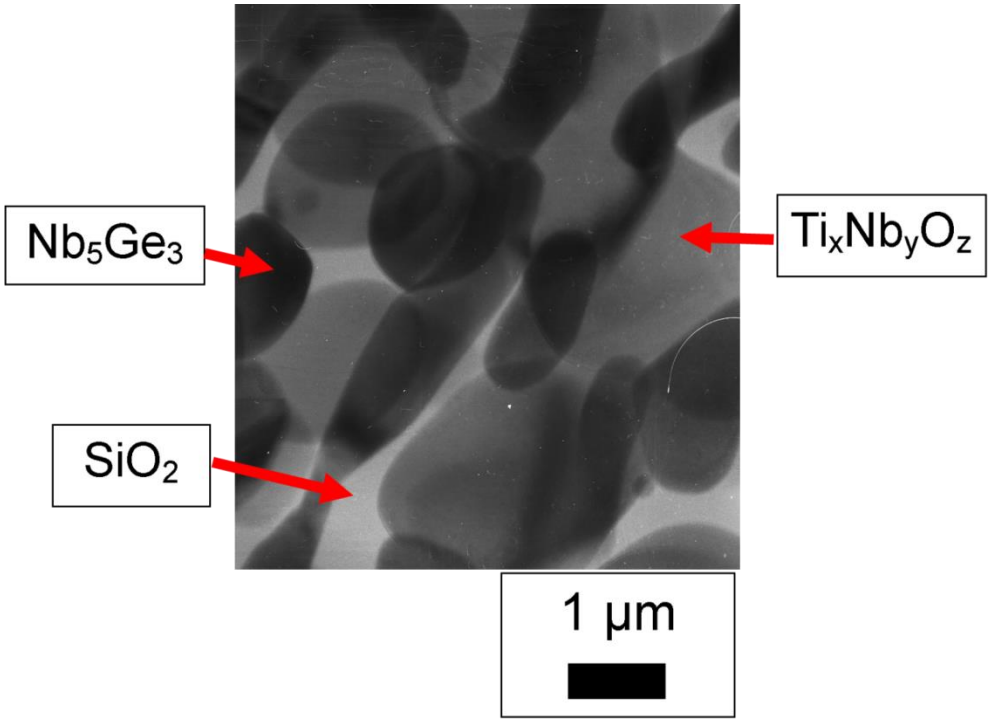

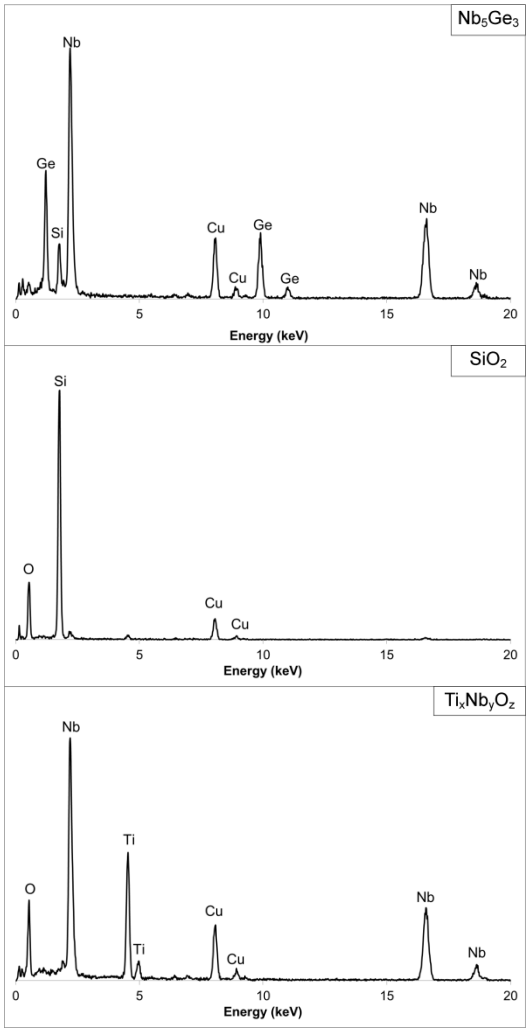

Figure 5.24 Bright field TEM image (collected on the FEI Tecnai 20) of the inward attack zone of the Nb_5Si_3 and the qualitative EDX patterns collected for the individual phases.

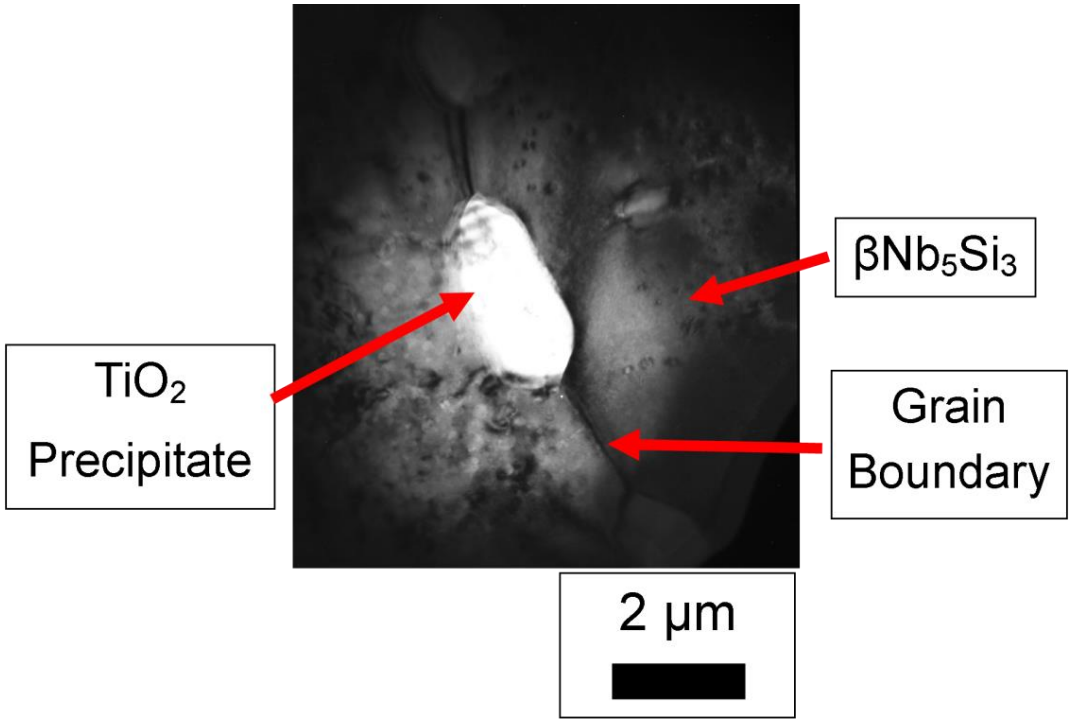

Figure 6.1

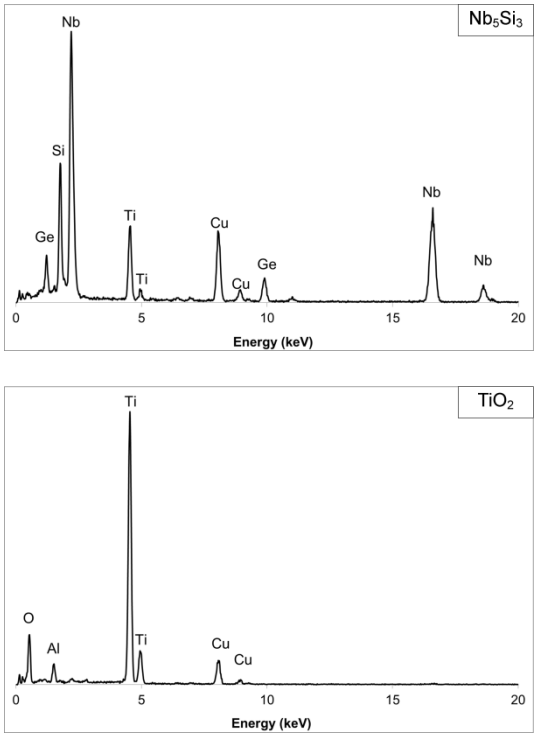

Figure 5.25 Bright field TEM image (collected on the FEI Tecnai 20) of the internal oxide precipitates in the Nb_5Si_3 and the qualitative EDX patterns collected for the individual phases.

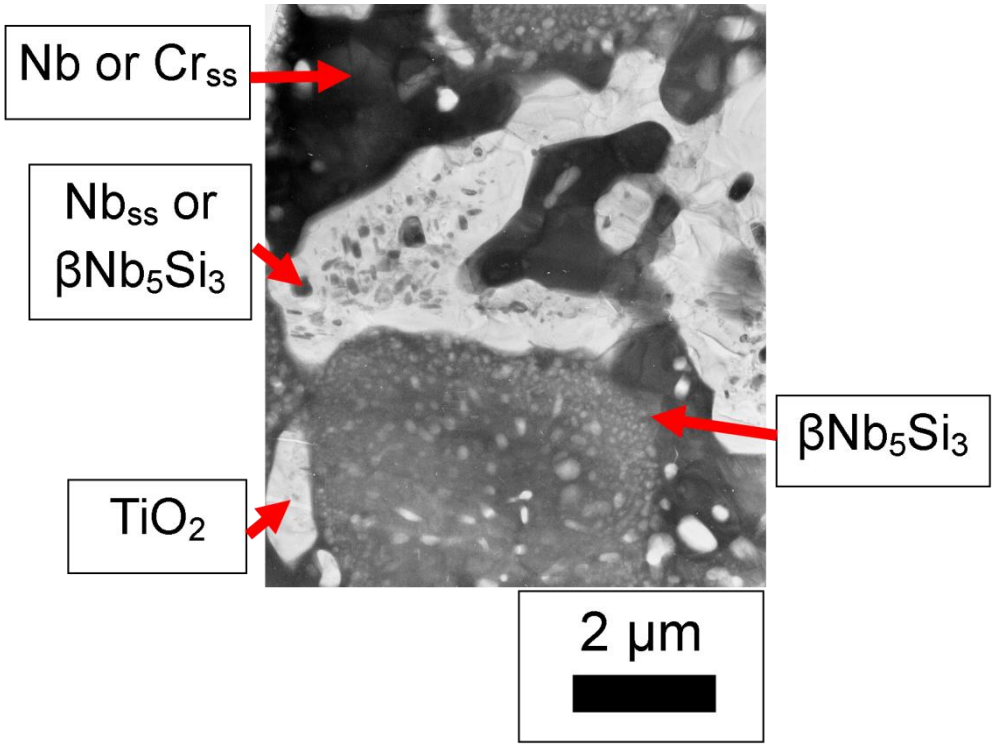

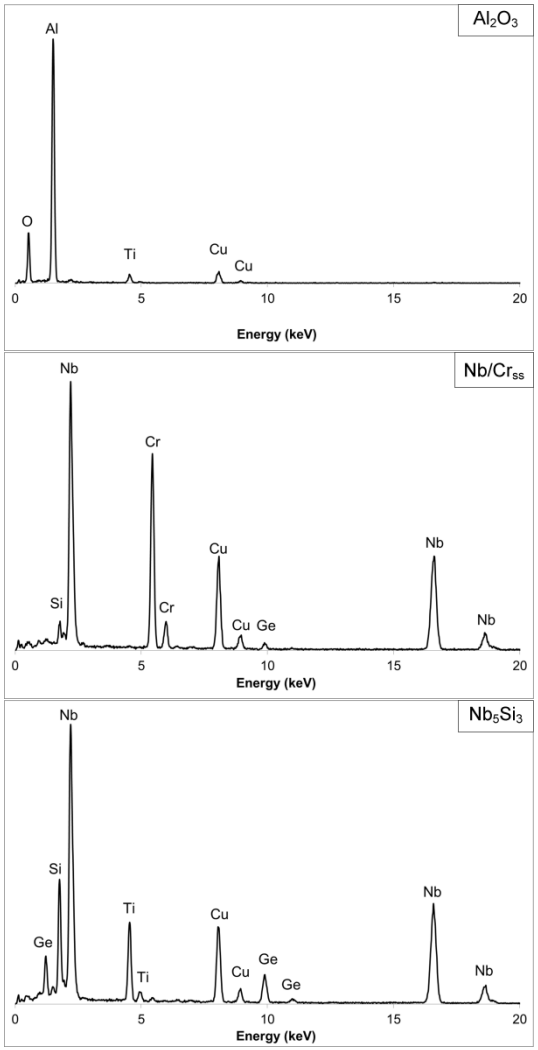

Figure 5.26 Bright field TEM image (collected on the FEI Tecnai 20) of the Nb_{ss} area of the substrate material after oxidation at 1200 ^{o}C for 100 h and the qualitative EDX patterns collected for the individual phases.

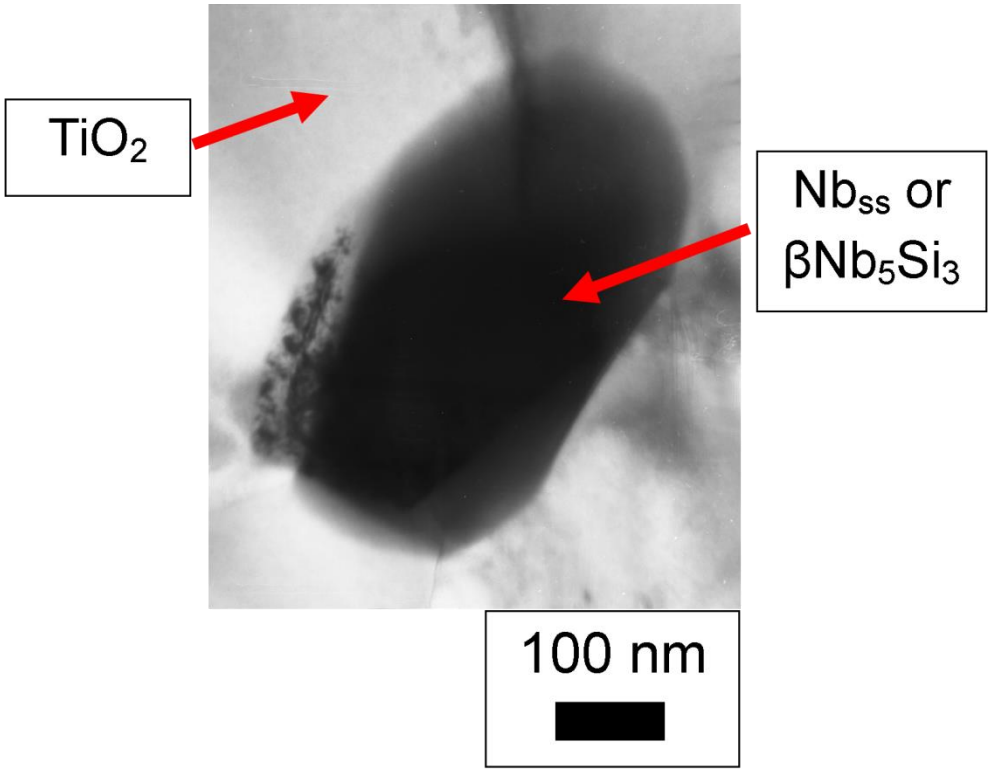

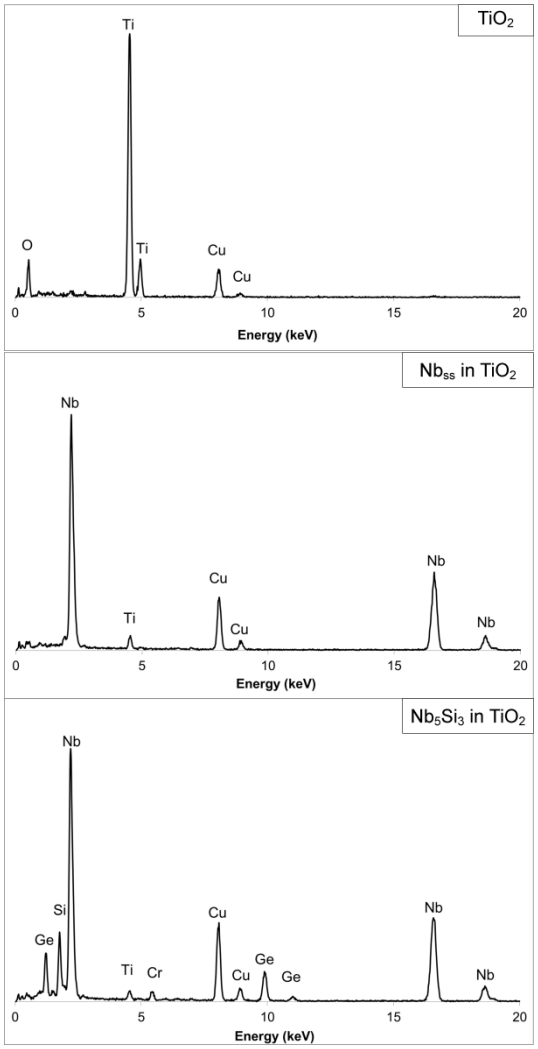

Figure 5.27 Bright field TEM image (collected on the FEI Tecnai 20) of the Nb_{ss} or βNb_5Si_3 within the TiO_2 and the qualitative EDX patterns collected for the individual phases.

5.3 Discussion

5.3.1 Microstructure

The proposed solidification path for this alloy is $L \rightarrow L + \beta Nb_5Si_3 \rightarrow L + \beta Nb_5Si_3 + (Nb_{ss} + \beta Nb_5Si_3)_{eutectic} \rightarrow \beta Nb_5Si_3 + (Nb_{ss} + \beta Nb_5Si_3)_{eutectic} + Nb_{ss}$. During solidification, the bottom of the alloy (where the ingot was in contact with the water cooled copper crucible) experienced a greater cooling rate, as is shown by a finer microstructure shown in Figure 5.2(a-c). There is a clear transition where the microstructure changes from a more 'eutectic-like' structure to that which is seen in the bulk. Figure 5.2(a-c) however, shows a double transition of a specific area of the bottom of the ingot. Non equilibrium, rapid solidification of Nb-Si based alloys can often be governed by non-equilibrium conditions and therefore a metastable phase diagram, such as those provided by Bendersky et. al., (1987) and Abbaschian and Lipschutz, (1997) must be consulted. According to these diagrams, the eutectic of $Nb_{ss} + Nb_3Si$ is suppressed and a new eutectic of $Nb_{ss} + \beta Nb_5Si_3$ is formed at a slightly higher Si content than that of the equilibrium phase diagram, 20 at.% in (Bendersky et al., 1987) and 18.6 at.% in (Abbaschian and Lipschutz, 1997). From Table 5.1, for the bottom eutectic data, Si+Ge+Al = 19.2 at.% which correlates with the previous values. Due to the shape of the coupled zone within these metastable systems, the eutectic of $Nb_{ss} + \beta Nb_5Si_3$ can form even with an off eutectic composition. A transition from a more regular eutectic structure to an anomalous eutectic structure within a non faceting-faceting system has been explained elsewhere (Li and Kuribayashi, 2003). Upon the formation of the eutectic, both phases share the solidification planar interface. The faceting βNb_5Si_3 will experience slow growth due to attachment difficulties of atoms to the interface ahead of that phase and the Nb_{ss} phase is allowed to grow faster. Eventually the Nb_{ss} phase is allowed to grow freely forming an anomalous eutectic.

The phases that have been seen in both as cast and heat treated alloys are Nb_{ss} and βNb_5Si_3. From the Nb-Ge binary system (Geng et al., 2011), Nb_5Ge_3 is isomorphous with the high temperature βNb_5Si_3 (W_5Si_3 prototype, *tI*32, I4/mcm space group), therefore the addition of Ge is expected to stabilise the βNb_5Si_3 phase to lower temperatures. From the Y-Si and Y-Ge binary systems (Massalski, 1986), Y_5Si_3 and Y_5Ge_3 possess hexagonal crystals structures (Mn_5Si_3 prototype, *hP*16, $P6_3$/mcm space group) and therefore are not isomorphous with either α or βNb_5Si_3 and therefore the addition of Y should destabilise the tetragonal Nb_5Si_3 and potentially promote the formation of the metastable γNb_5Si_3 or Ti_5Si_3 phase. Li and Tsakirpoulos (2012) reported that in alloy ZF6 (nominal composition Nb-24Ti-18Si-5Cr-5Al-5Ge) the phases present in the as cast ingot were Nb_{ss}, βNb_5Si_3 and Cr_2Nb Laves phase and, during heat treatment, there was a partial phase transformation of βNb_5Si_3 to αNb_5Si_3 (Li, 2012). The presence of the latter was determined by two signals in the XRD pattern. Li (2012) also comment in other research that Ge additions should stabilise the αNb_5Si_3 phase, not the βNb_5Si_3, whereas a recent thermodynamic assessment of the Nb-Ge binary phase diagram by (Geng et al., 2011) comments that Nb_5Ge_3 has the same crystal structure as the high temperature βNb_5Si_3 (W_5Si_3 structure), and other research has shown that the Nb_5Ge_3 phase has the W_5Si_3 structure (Jorda et al., 1978), which suggests that Ge should stabilise the βNb_5Si_3 not αNb_5Si_3. Hence, it is proposed that the presence of αNb_5Si_3 in ZF6 (Li, 2012) is incorrect and the addition of Y does not hinder the phase transformation of β to α as the level of Y in the βNb_5Si_3 is very low (< 1 at.%).

It is worth comparing alloy AT1 with alloy KZ5 (nominal composition Nb-24Ti-18Si-5Cr-5Al) in (Zelenitsas and Tsakiropoulos, 2005) and ZF6 (nominal composition Nb-24Ti-18Si-5Cr-5Al-5Ge) from (Li, 2012). The microstructure of the as cast AT1 is similar to the as cast microstructures of the alloys previously mentioned, the difference being that no data has been collected to suggest the presence of Cr_2Nb Laves phase. If the Laves phase is present in the as cast

microstructure, the volume fraction is too small for any characteristic peaks to appear in the XRD pattern, and the phase itself is too small to be analysed confidently using EDS.

Li (2012) reported macrosegregation of Si, Cr, Ti and Al, with $C_{max} - C_{min}$ = 4.3, 2.1, 2.4 and 2.6 respectively. With alloy AT1, there is macrosegregation of Si and Ti only, with $C_{max} - C_{min}$ = 5.1 and 2.1 respectively (Table 5.1). Therefore, the addition of a small amount of Y has reduced the macrosegregation of Cr, Al and Ti. The addition of Y has, however, enhanced the macrosegregation of Si. The microstructure of AT1 also possessed areas of high Y and Ge content. According to the Nb-Y phase diagram (Massalski, 1986), Nb and Y are immiscible at all temperatures (even as liquids) therefore Y is rejected into the melt ahead of the solid liquid interface. Therefore, the last areas of liquid to solidify will be rich in Y. The reason why Ge follows the Y is unexpected, but can be explained due to the fact that Nb_5Ge_3 is isomorphous with βNb_5Si_3 and as the primary βNb_5Si_3 forms, Ge is withdrawn from the melt and the melt becomes lean in Ge. As the Nb_{ss} forms, whatever Ge is left is rejected into the melt along with the Y. The last liquid to solidify is therefore richer in Y and Ge than any other element. This last liquid being rich in Y and Ge could also account for why there is no evidence for the formation of Cr_2Nb Laves phase between the dendrites as seen in both alloys KZ5 and ZF6.

The most obvious consequence of heat treatment is that there has been contamination of the microstructure by N and O which has resulted in formation of Ti_xN_y and Y_2O_3 particles. Most of the contamination (Figure 5.3) of the microstructure seems to be restricted to the Nb_{ss} phase. According to the Nb-O phase diagram (Massalski, 1986), Nb has a very high solubility for O (~9 at.%) therefore, O and N have likely penetrated the microstructure through the Nb_{ss} phase, or down the grain boundaries, reacting with the Ti and Y to form Ti_xN_y and Y_2O_3.

5.3.1.1 Structural Refinement

Structural refinement was conducted using the XRD patterns of both as cast and heat treated samples and the results are presented in Figure 5.29 and Table 5.6 and Table 5.7. When conducting the refinement several assumptions were made. Firstly, that both phases are perfect crystals with site occupancies totalling unity, even though this is unlikely in non-equilibrium solidified crystal structures as there is bound to be some form of distortion to the lattice, or vacancies present within the crystal lattice. Secondly, the elements included whilst modelling the Nb_{ss} phase were the Nb, Ti and Al. Changes in scattering due to substitution of Ti for Cr, and Si for Al will be negligible, therefore their compositions within the phases will be combined. The levels of Ge and Y present in the Nb_{ss} phase are small and can be ignored. When modelling the βNb_5Si_3, Ge was also included.

The assumptions made were that Ti would occupy Nb sites (and vice versa) and that Ge would occupy Si sites in the βNb_5Si_3. The same assumptions were made when modelling all phases in both the as cast and heat treated conditions. Thirdly, due to the difference in composition of both Nb_{ss} and βNb_5Si_3 in the heat treated samples (due to contamination of the microstructure by O_2 and N_2), the compositions used for the site occupancies are those found at the centre of the ingot (from Table 5.1), and the data from the top and bottom were not included. Substitution of Nb for Ti (and other smaller elements such as Cr) will create a shorter bond and that is why we see a contraction in the lattice parameter of the Nb_{ss} phase in the as cast ingots from 3.30 to 3.2398 Å. After heat treatment the lattice parameters of the Nb_{ss} phase increased to 3.2531 Å. We see an expansion in the lattice parameter (albeit a very small one) as the level of some of the smaller elements (such as Al, Ti to form Ti_xN_y and Y to form Y_2O_3) has decreased allowing more Nb-Nb bonds to be present and the lattice parameter to move back towards the pure Nb_{ss} phase value.

Figure 5.28 shows the crystal structure of tetragonal βNb_5Si_3 and the large atoms are the Nb atoms, and the smaller atoms are Si atoms. The 'M' and 'L' stand for the more close packed and less close packed layers respectively, and the (I) and (II) denote which atom is being referred to in Table 5.7. As the crystal structure of βNb_5Si_3 phase is body-centred tetragonal, it is likely there will be some anisotropic effects. The lattice parameter (*a*) experiences an expansion from 10.02 to 10.06 Å, (*c*) sees a contraction from 5.07 to 5.03 Å. This is a similar effect seen by Chen et al., (2007a) and Kang et al., (2009) who modelled the substitution of Nb for Ti in βNb_5Si_3. Table 5.6 shows a comparison of the results from this work and the work previously mentioned. The change in the lattice parameters are similar to those found by Kang et al., and the c/a ratio is almost identical. Table 5.7 shows that Ti preferentially occupies the Nb(I) site on the 'close packed plane' but not exclusively. After heat treatment at 1500 ^{o}C, an increase in the proportion of Ti(+Cr) is seen on the Nb(I) site showing that Ti(+Cr) has moved from the Nb(II) site onto this site.

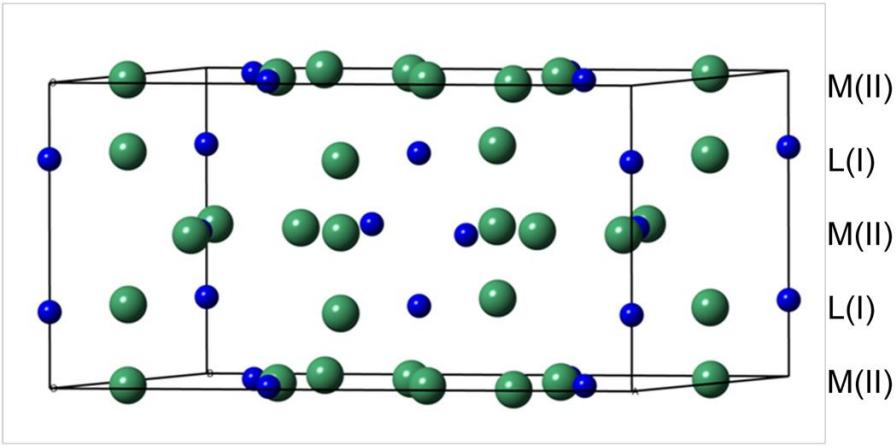

Figure 5.28 Crystal structure and stacking order of βNb_5Si_3. The large, green atoms are Nb (or Ti) and the small, blue atoms are the Si. (M = more closed packed, L = less closed packed, I and II refer to the site notation presented in Table 5.7).

Table 5.6 Lattice parameter and volume fraction results of Rietveld refinement on XRD data for AT1 as cast and heat treated (1500 ^{o}C for 100 h). The reference values were generated from the crystallographic information file used for the refinement. Also included are the lattice parameter results from other work.

			AT1		Other work	
		Reference	As cast	Heat treated	(Chen et. al. 2007a)	(Kang et. al. 2009)
Nb_{ss}	a(Å)	3.3	3.23983(9)	3.25313(14)	-	-
	c(Å)	-	-	-	-	-
	V(Å^3)	35.95	34.007	34.427	-	-
	Volume fraction		0.39	0.25	-	-
βNb_5Si_3	a(Å)	10.02	10.0566(17)	10.0572(18)	10.062	10.048
	c(Å)	5.07	5.03481(15)	5.03263(6)	5.050	5.031
	c/a	0.506	0.5006	0.5004	0.5020	0.5007
	V(Å^3)	509.03	509.199	509.038	-	-
	Volume fraction		0.61	0.75	-	-

Errors in brackets are those reported by GSAS. Errors are to the same number of decimal places as the value before it (e.g. 10.0566(17) = 10.0566 ± 0.0017).

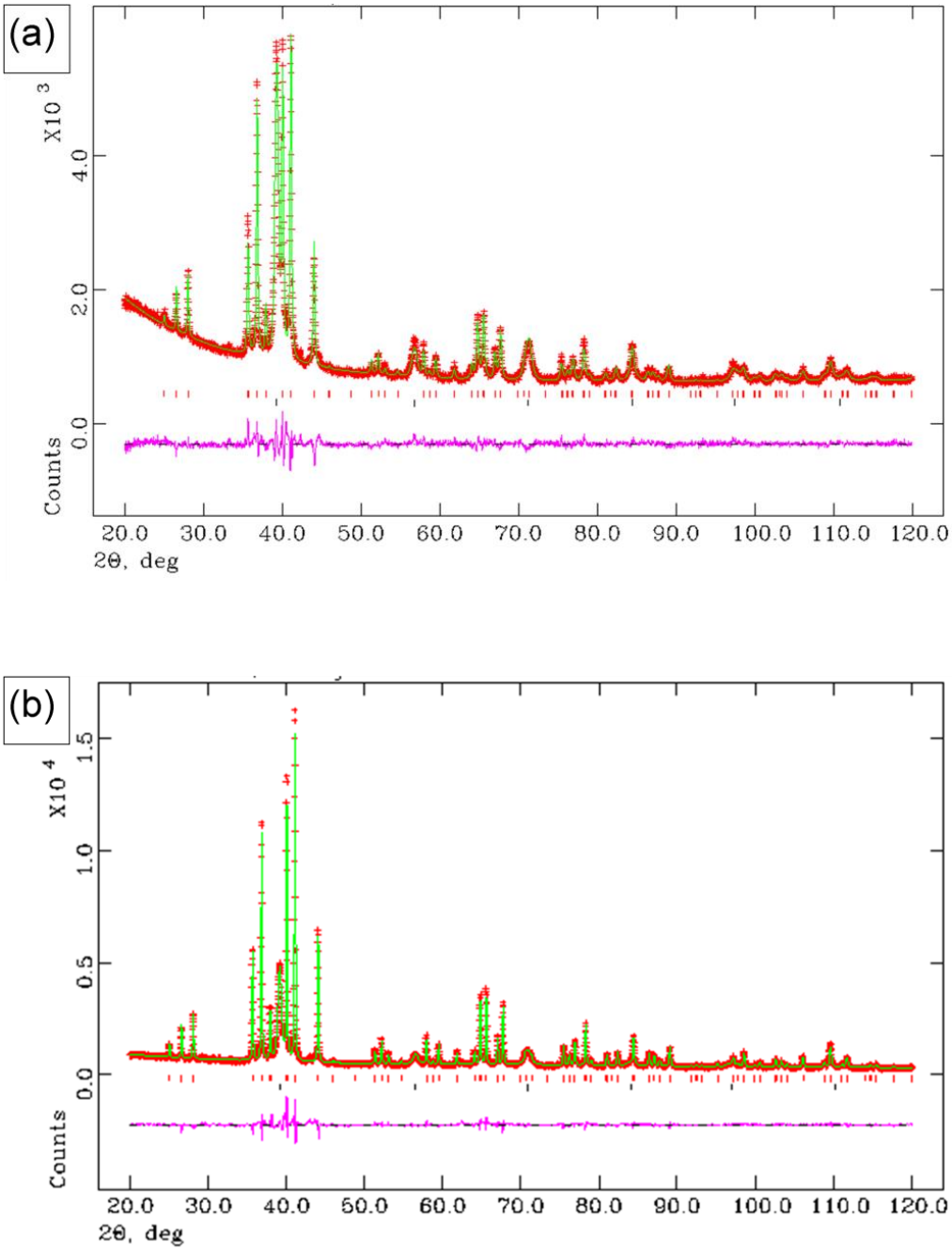

Figure 5.29 Calculated (solid green line), experimentally observed (red crosses) and difference (pink line underneath) diffraction profiles after the Rietveld refinement of AT1 (a) as cast and (b) heat treated (1500 ^{o}C for 100 h)

Table 5.7 Results of structural refinement of crystal structure using XRD data for AT1 in the as cast and heat treated (1500 ^{o}C for 100 h) conditions. The reference values were generated from the crystallographic information file used for the refinement.

	Reference	As cast	Heat treated
χ^2	-	1.564	3.876
R_p (%)	-	3.1	5.6
R_{wp} (%)	-	4.1	7.3
Nb_{ss}			
x=y=z	0	0	0
site occupancy	1.0Nb	0.56Nb/0.33Ti/0.11Al	0.60Nb/0.35Ti/0.05Al
Uiso (Å^2)	0.025	0.03113(6)	0.03078(8)
βNb_5Si_3			
atom site Nb(I)			
x	0	0	0
y	0.5	0.5	0.5
z	0.25	0.25	0.25
site occupancy	1.0Nb	0.55Nb/0.45Ti	0.35Nb/0.65Ti
Uiso (Å^2)	0.025	0.01693(10)	0.01026(7)
atom site Nb(II)			
x	0.074	0.08041(16)	0.07838(12)
y	0.223	0.21783(17)	0.21748(12)
z	0	0	0
site occupancy	1.0Nbi	0.7Nb/0.3Ti	0.75Nb/0.25Ti
Uiso (Å^2)	0.025	0.01194(5)	0.02368(3)
atom site Si(I)			
x=y	0	0	0
z	0.25	0.25	0.25
site occupancy	1.0Si	1.0Si	1.0Si
Uiso (Å^2)	0.025	0.01364(22)	0.01223(13)
atom site Si(II)			
x	0.17	0.16119(31)	0.16264(23)
y	0.67	0.66119(30)	0.66264(23)
z	0	0	0
site occupancy	1.0Si	0.8Si/0.2Ge	0.8Si/0.2Ge
Uiso (Å^2)	0.025	0.01877(15)	0.01368(9)

Errors in brackets are those reported by GSAS

5.3.2 Oxidation behaviour at 800 ^{o}C

At 800 ^{o}C, alloy AT1 did not exhibit any pesting behaviour, confirming the beneficial effects of Ge on the oxidation resistance of these alloys (Li, 2012). The addition of Y lowered the overall weight gain and improved the oxidation rate constant compared with alloy ZF6 even without the presence of C14 Cr_2Nb Laves phase. This data would suggest that the addition of Y has the same effect on the oxidation resistance as the presence of Laves phase in the alloy. The BSE images reveal that it is the Nb_{ss} phase that is preferentially attacked, by the darker contrast in the image. The average depth of O_2 penetration in the bulk material is ~25 µm, which is similar to 20 – 50 µm in similar alloys reported by Menon et al.,(2001) after oxidation at 800 ^{o}C for 48 – 150 h, but less than the internal diffusion thickness of MASC reported by Mathieu et al., (2012) after oxidation at 815 ^{o}C, which is reported to be ~115 µm. Cracking of the βNb_5Si_3 phase parallel to the surface of the sample is a common feature observed after oxidation as inward diffusion of O_2 through the Nb_{ss} phase causes the formation of internal oxides (Figure 5.9(c)). The formation of these oxides causes internal stresses that build up and are released by cracking of the intermetallic phase (Menon et al., 2004, Mathieu et al., 2012, Zelenitsas and Tsakiropoulos, 2006a, Geng and Tsakiropoulos, 2007, Geng et al., 2006c, Geng et al., 2007b). It seems as though the addition of Y has not reduced grain boundary diffusion of oxygen during oxidation at 800 ^{o}C due to the lack of Y_2O_3 particles located at grain boundaries close to the sample/oxide interface. The formation of Y_2O_3 in the sample is sporadic and likely due to the presence of Y and Ge rich areas of the as cast microstructure. It seems as though Y has been unable to move from these locations to create Y_2O_3 at grain boundaries. What is possible is that the addition of Y has reduced oxygen diffusion through the Nb_{ss} phase.

The volume fraction of the Nb_{ss} phase in alloy KZ5 is reported to be 48 – 55 % and the addition of Ge in alloy ZF6 reduced the volume fraction of the Nb_{ss} phase to 17.1 ± 3.7 %. Alloy AT1 has Nb_{ss} phase at volume fraction of 39 % as determined

by structural refinement using the Rietveld method. It is highly unlikely that the addition of 1 at.% Y has led to such a dramatic increase in the volume fraction of Nb_{ss} and therefore the author believes that the volume fraction of Nb_{ss} reported by Li in alloy ZF6 is incorrect (Li, 2012). This value is important as previous research suggests that the oxidation behaviour is susceptible to the volume fraction of the Nb_{ss} phase.

5.3.3 Oxidation behaviour at 1200 ^{o}C

At 1200 ^{o}C the oxidation kinetics changed from more parabolic to a linear behaviour. Others have reported that at the early stages of oxidation, the behaviour follows a parabolic law and transitions to a linear behaviour after a certain period of time (Geng et al., 2007b, Li, 2012), however this was not the case with alloy AT1. Therefore, the addition of Y has removed the early parabolic behaviour. The linear rate constants for alloys ZF6 and AT1 are the same; hence, Y addition has had no effect on the linear oxidation kinetics.

The thickness of the oxide scale produced on alloy AT1 is ~200 µm, which is ~50 % decrease in oxide scale thickness compared with alloy ZF6 (Li, 2012). The addition of Y has reduced the oxide scale thickness, however, it has not reduced the overall weight gain after oxidation at 1200 ^{o}C (41 mg/cm^2 for AT1 and 39.9 mg/cm^2 for ZF6). The addition of Hf to ZF6 (alloy ZF9 in (Li, 2012)) increased the oxide scale thickness from 395 ± 12 to 465 ± 27 µm. Therefore the addition of Y is far more beneficial for reducing the oxide scale thickness than addition of Hf. The main diffusion zone of oxygen in AT1 is ~180 µm, which is almost double that seen in alloy JG4 of ~100 µm (Geng et al., 2006c). Therefore, Hf is far more beneficial for reducing the oxygen diffusion into the substrate material than Y.

Internal attack of the βNb_5Si_3 phase lead to the formation of Nb_5Ge_3, Nb_2O_5 and SiO_2 being present at the intermetallic/oxide interface. It is proposed that as the Si is being consumed to form SiO_2, this leads to the βNb_5Si_3 now being rich in Ge

instead of Si and therefore the formation of Nb_5Ge_3 is possible. Also, internal formation of TiO_2 precipitates has led to Ti depleted areas of the intermetallic and therefore led to the light contrast seen within the BSE image of the intermetallic. The TEM image shown in Figure 5.25 shows what appears to be a grain boundary on either side of the TiO_2 internal precipitate. However, a grain boundary would appear black on a BSE SEM image, whereas the regions either side of many of the internal precipitates appear lighter in contrast than the βNb_5Si_3 phase. It is proposed, therefore, that this internal attack of the βNb_5Si_3 is due to the formation of sub-grains formed from a recovery process during oxidation with the areas around the sub-grain boundary being lean in Ti content to form TiO_2 particles. It is commonly seen that the Nb_{ss} phase oxidises much more rapidly than the βNb_5Si_3 and it has been seen that during oxidation at 800 ^oC, oxide precipitation leads to fracture of the βNb_5Si_3 to relieve the stress that builds up in the system. It is likely therefore that at 1200 ^oC the same process occurs only now, the intermetallic is ductile enough that cracking of it no longer occurs, therefore the only method left to reduce the stress within the system would be through dislocation movement and the formation of sub-grain boundaries within the βNb_5Si_3. Similar observations were made by Geng et al., (2006c) however not commented on, after the oxidation of a heat treated alloy, so any argument about the stress being present from the solidification procedure can be dismissed.

The data and discussion provided in this chapter and in the following chapters will allow for a mechanism of oxidation of Nb silicide alloys to be proposed. This mechanism will be discussed at the end of the thesis once all data has been provided.

5.4 Conclusions

In this work the microstructure, solidification and phase stability of a complex Nb silicide alloy has been investigated. The alloy was prepared via arc melting high purity elements in a water cooled, copper crucible and studied in the as cast and heat treated (1500 ^{o}C for 100 h) conditions.

- The phases present in the as cast alloy were the Nb_{ss} and βNb_5Si_3, with the latter being the primary phase. The two phases also formed a small volume fraction of an Nb_{ss} + βNb_5Si_3 eutectic, mainly at the interface of the two phases.
- There is no suggestion of the presence of C14 Cr_2Nb Laves phase in the as cast microstructure. Hence the addition of Y has suppressed its formation.
- After heat treatment, the phases present were the Nb_{ss} and βNb_5Si_3, therefore the addition of Y has had no effect on destabilising the βNb_5Si_3.
- During heat treatment, contamination of the microstructure by O_2 and N_2 lead to the formation of Ti_xN_y and Y_2O_3. Yttrium performed the role of oxygen scavenger creating a stable oxide.
- Structural refinement showed that Ti additions prefer to occupy the Nb(I) less closed packed site within the βNb_5Si_3. There is movement of Ti(+Cr) from the Nb(II) to the Nb(I) site of the βNb_5Si_3 during heat treatment at 1500 ^{o}C for 100 h.
- Structural refinement also showed the changes in lattice parameter of the βNb_5Si_3 crystal structure due to alloying additions. The crystal experiences an expansion in (*a*) and contraction in (*c*).
- Addition of Y has a minor beneficial effect on improving the oxidation resistance on Nb silicide alloys at 800 ^{o}C but no real effect on the oxidation behaviour at 1200 ^{o}C.

- Addition of Y is beneficial for reducing oxide scale thickness, but Hf is more beneficial for reducing oxygen diffusion into the bulk substrate material.
- Rod shaped oxides formed within the Nb_{ss} phase are likely to be TiO_2.
- The βNb_5Si_3 is not immune to attack via oxidation mechanisms with the formation of SiO_2, Nb_5Ge_3 and $Ti_xNb_yO_z$ forming at the grain/oxide interface and the internal formation of TiO_2 precipitates.
- Internal formation of TiO_2 is attributed to diffusion of O along new sub-grain boundaries within the βNb_5Si_3 grain. Titanium reacts with the O to form TiO_2 creating areas of lighter contrast within the βNb_5Si_3 on the BSE image following the sub-grain boundary.

Chapter 6

The effect of Cr:Al ratio on microstructure and phase stability of complex Nb silicide alloys

6.1 Introduction

Much of the work on Nb silicide alloys has kept the Cr level at ~5 at.% which is thought to be the minimum level in order to form a small volume fraction of Cr_2Nb Laves phase. This chapter looks at the effect of Ge and Y additions, which are thought to improve oxidation resistance, on the microstructure of Nb silicide alloys whilst keeping the Cr content at 2 at.% and varying the Al content from 5 at.% to 2 at.%. The effects of Ge and Y additions on the microstructure of a reference alloy (Li, 2012) (and Chapter 5) have been previously reported.

6.2 Results

6.2.1 Nb-24Ti-18Si-2Cr-5Al-3Ge-1Y (AT2)

6.2.1.1 As cast

The alloy was designed with a nominal composition of Nb-24Ti-18Si-2Cr-5Al-3Ge-1Y, but the large area EDS analysis (Table 6.1) puts the actual composition at 44.7Nb-25.0Ti-19.4Si-1.5Cr-5.4Al-2.6Ge-1.4Y making AT2 a hypereutectic alloy. The large area chemical analysis shows inhomogeneity of Si ($C_{max} - C_{min} = 2.1$), but no macrosegregation of any of the other alloying elements.

Figure 6.1 shows typical BSE images of areas of the ingot in contact with the water cooled copper crucible, the centre of the ingot and at the top of the ingot in contact with the chamber atmosphere. The microstructure of this alloy is different to the alloy AT1 (Nb-24Ti-18Si-5Cr-5Al-5G3-1Y – Chapter 5). The bottom of AT2 shows a more dual phase (non-eutectic) microstructure and the centre contains a higher volume fraction of an interdendritic eutectic like structure, whereas the microstructure of AT1 (Chapter 5) showed a more eutectic microstructure at the bottom, with only a minor level of interdendritic eutectic present in the centre. The microstructure present at the centre is also finer in AT2 than in AT1.

The phases present in the as cast microstructure of AT2 are Nb_{ss} (white phase in Figure 6.1) and the high temperature βNb_5Si_3 (grey phase in Figure 6.1) as

suggested by the EDX data (Table 6.1) and the XRD data in Figure 6.3(a). There is no evidence of the low temperature αNb_5Si_3 hence, lowering the Cr and Ge content does not alter the stability of the βNb_5Si_3 phase in the as cast alloy and does not aid the formation of any other phases. Elemental x-ray maps (Figure 6.4) show that, similar to alloy AT1 (Chapter 5), there are areas of the Nb_{ss} rich in Y and Ge which are too small to analyse with confidence (<5 µm). Darker regions of contrast within the individual phases are attributed to enrichment of the outer regions by Ti during solidification. This has been seen previously in several research papers (Geng and Tsakiropoulos, 2007, Geng et al., 2007a, Zelenitsas and Tsakiropoulos, 2006b, Zelenitsas and Tsakiropoulos, 2005, Vellios and Tsakiropoulos, 2010) and in the previous chapter of this thesis. Within the microstructure of cast AT2, these Ti rich areas are too small (< 5 µm) in both phases to analyse confidently and therefore no data is provided in Table 6.1.

6.2.1.2 Heat treated (1500 ^{o}C for 100 h)

Upon heat treatment the microstructure changes dramatically and typical BSE images are shown in Figure 6.2(a-b). Firstly, the microstructure has coarsened and areas of microsegregation have been eliminated. The microstructure still contains the two major phases of Nb_{ss} and βNb_5Si_3, however, the heat treatment process has allowed for the formation of γNb_5Si_3 (*hP16, $D8_8$* confirmed by XRD in Figure 6.3(b)) at the top of the ingot and introduced contaminants and the formation of Y_2O_3 and Ti_xN_y particles (Figure 6.5). The contamination is mainly located within the Nb_{ss} grains, which has been seen in many other's research (Zelenitsas and Tsakiropoulos, 2005, Geng and Tsakiropoulos, 2007, Geng et al., 2007a, Thandorn and Tsakiropoulos, 2010). There appears to be no formation of Nb_3Si and no phase transformation of βNb_5Si_3 to αNb_5Si_3, therefore lowering the Cr and Ge content does not seem to have had any effect on the phase transformation of βNb_5Si_3 to αNb_5Si_3, but has allowed the γNb_5Si_3 to form during heat treatment.

The chemical analysis suggests partitioning of Ti from the βNb_5Si_3 to the γNb_5Si_3 with the Ti levels being 21.4 and 28.0 at.% respectively. EDS data in Table 6.1 shows that the macrosegregation of Si has remained the same ($C_{max} - C_{min} = 2.1$), however there does now appear to be macrosegregation of both Nb and Ti with $C_{max} - C_{min} = 2.8$ and 2.9, respectively.

Table 6.1 shows that the Nb_{ss} has lower Ti content at the top than that of the Nb_{ss} at the centre. This is likely due to the formation of more Ti_xN_y particles within the Nb_{ss} phase at the top than at the centre. The βNb_5Si_3 phase sees no such effect with the phase chemistry being constant throughout the alloy microstructure and the lack of particles formed within the phase. There is also the presence of Y_2O_3 particles within the heat treated microstructure, likely formed from the Y rich areas of the cast microstructure. The presence of these phases is confirmed by elemental x-ray maps in Figure 6.5.

Table 6.1 Chemical analysis (at.%) for the as cast and heat treated (1500 ^{o}C for 100 h) AT2. Data presented includes the maximum, minimum, average values with standard deviations of the element contents.

As cast	Nb (at.%)	Ti (at.%)	Si (at.%)	Cr (at.%)	Al (at.%)	Ge (at.%)	Y (at.%)
Top	45.1-44.4	25.3-24.5	19.7-18.6	1.7-1.4	5.8-5.3	2.8-2.4	1.9-1.0
	44.8±0.1	25.0±0.1	19.3±0.1	1.6±0.1	5.5±0.1	2.6±0.1	1.4±0.1
Bulk	44.8-44.3	25.5-24.2	20.5-19.0	1.6-1.3	5.6-4.9	2.8-2.5	1.8-1.2
	44.6±0.1	24.9±0.2	19.7±0.3	1.4±0.1	5.3±0.1	2.7±0.1	1.5±0.1
Bottom	45.2-44.5	25.4-24.4	20.1-18.4	1.6-1.4	5.9-4.9	2.8-2.4	1.7-1.1
	44.8±0.1	25.1±0.1	19.2±0.2	1.5±0.1	5.3±0.1	2.6±0.1	1.5±0.1
Nb_{ss}	58.0-52.4	32.6-27.5	5.2-2.5	3.3-2.0	8.0-6.9	1.3-0.7	1.2-0.0
	55.1±3.4	29.9±2.6	3.2±0.7	2.7±0.2	7.4±0.1	1.0±0.1	0.7±0.1
βNb_5Si_3	44.0-42.9	19.6-17.9	31.1-28.7	0.5-0.2	3.8-3.0	3.4-3.1	1.0-0.2
	43.4±0.1	18.7±0.2	30.4±0.5	0.3±0.1	3.4±0.1	3.2±0.1	0.6±0.1
Heat treated *(1500 ^{o}C for 100 h*							
Top	47.6-45.1	24.2-21.6	20.5-19.3	1.5-1.1	5.3-4.2	3.1-2.5	2.1-1.2
	46.4±0.6	23.0±0.9	20.0±0.1	1.3±0.1	4.9±0.1	2.8±0.1	1.6±0.1
Bulk	46.1-45.0	24.5-22.9	20.9-18.4	1.5-1.1	5.5-4.9	3.0-2.3	2.5-1.6
	45.4±0.1	23.7±0.2	20.0±0.6	1.2±0.1	5.2±0.1	2.7±0.1	1.9±0.1
Bottom	46.2-44.8	24.1-23.2	20.4-18.8	1.4-1.2	5.8-5.3	2.8-2.4	2.0-1.5
	45.5±0.1	23.6±0.1	19.8±0.2	1.2±0.1	5.5±0.1	2.7±0.1	1.7±0.1
$Nb_{ss\ (top)}$	67.4-65.9	24.0-22.3	2.8-1.0	2.8-2.4	5.4-3.9	1.0-0.6	1.4-0.7
	66.5±0.4	23.3±0.4	1.3±0.3	2.6±0.1	4.4±0.2	0.7±0.1	1.1±0.1
Nb_{ss}	60.3-59.1	28.2-27.2	1.2-0.7	3.1-2.8	8.3-6.6	0.8-0.5	1.2-0.0
	59.8±0.2	27.7±0.1	0.9±0.1	3.0±0.1	7.4±0.3	0.6±0.1	0.6±0.3
βNb_5Si_3	41.6-38.4	23.3-19.9	29.9-28.1	0.9-0.6	5.3-4.0	3.8-3.2	0.9-0.2
	40.2±1.0	21.4±1.1	29.0±0.3	0.8±0.1	4.5±0.2	3.6±0.1	0.5±0.1
Ti rich $\beta Nb_5Si_{3\ (top)}$	35.4-33.7	29.1-27.0	29.5-28.9	0.6-0.3	3.9-3.0	4.2-3.8	1.0-0.6
	34.5±0.2	28.0±0.4	29.2±0.1	0.4±0.1	3.3±0.1	3.9±0.1	0.7±0.1

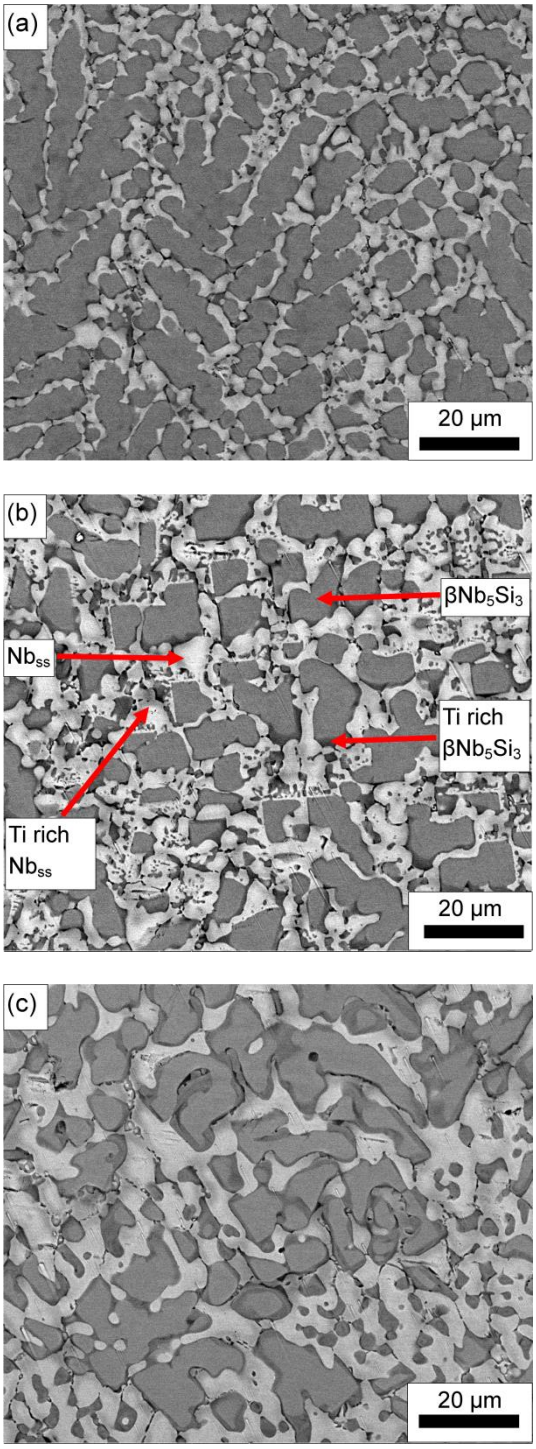

Figure 6.1 Typical BSE images (taken in the FEI Inspect F microscope) taken at 2400x mag of the as cast AT2 at areas at (a) the top, (b) the centre and (c) the bottom of the ingot. Each image shows the $(Nb,Ti)_{ss}$ phase (white phase) and the $\beta(Nb,Ti)_5Si_3$ (grey phase), along with chemical inhomogeneity of Ti (darker areas of contrast in both phases).

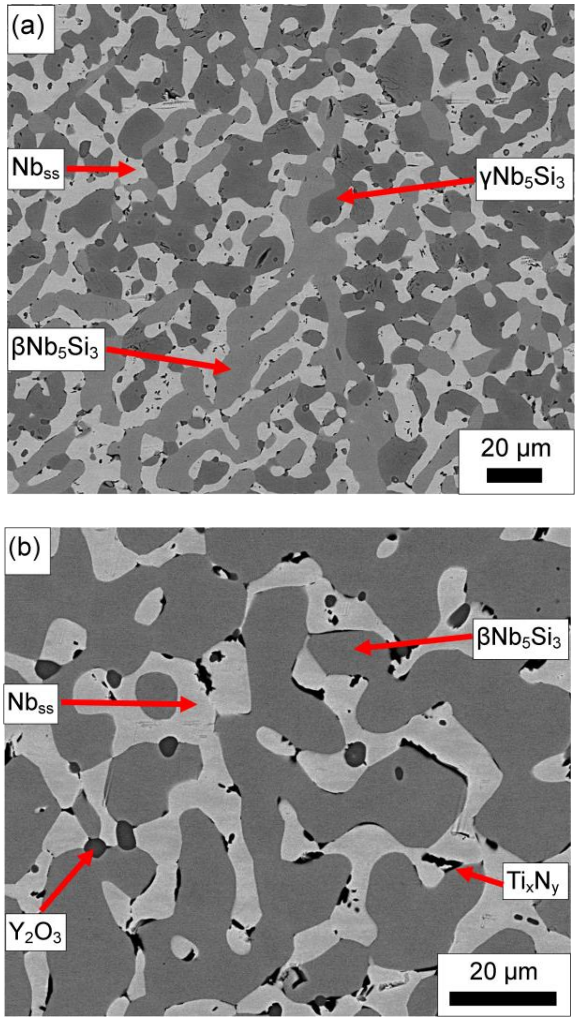

Figure 6.2 BSE image of the heat treated AT2 at areas at (a) the top and (b) the centre. Each image shows the $(Nb,Ti)_{ss}$ phase (white phase) and the $\beta(Nb,Ti)_5Si_3$ (grey phase), and Ti rich Nb_5Si_3 (dark grey phase - likely γNb_5Si_3). The presence of Y_2O_3 and Ti_xN_y particles is shown in (b).

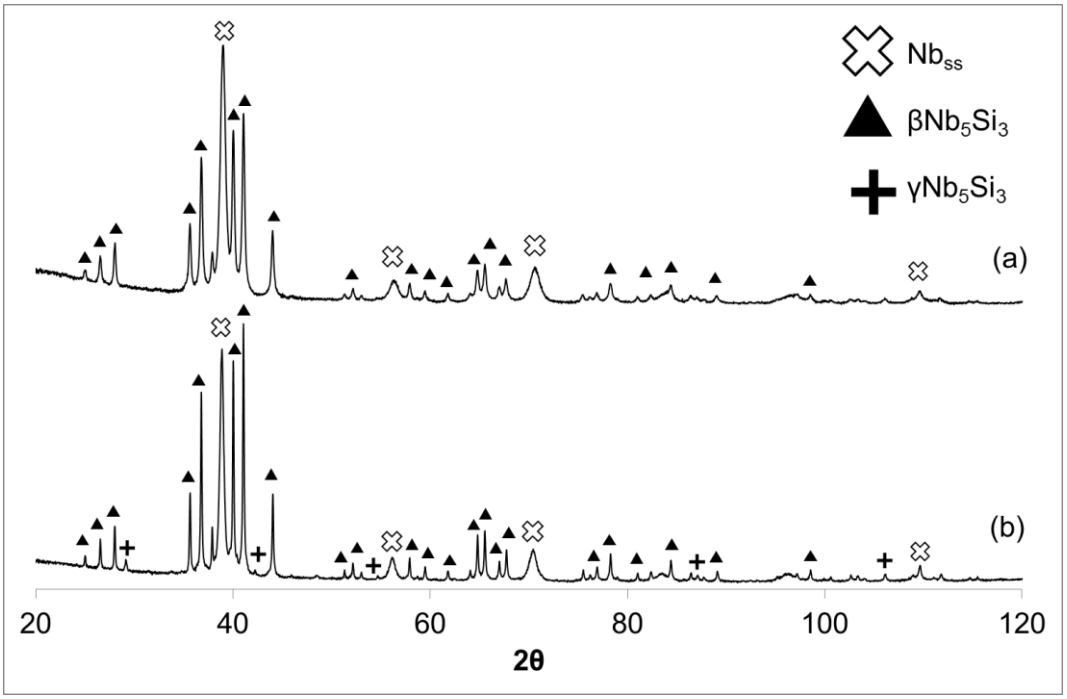

Figure 6.3 Powder x-ray diffraction pattern of AT2 (a) as cast and (b) heat treated condition (1500 ^{o}C for 100 h).

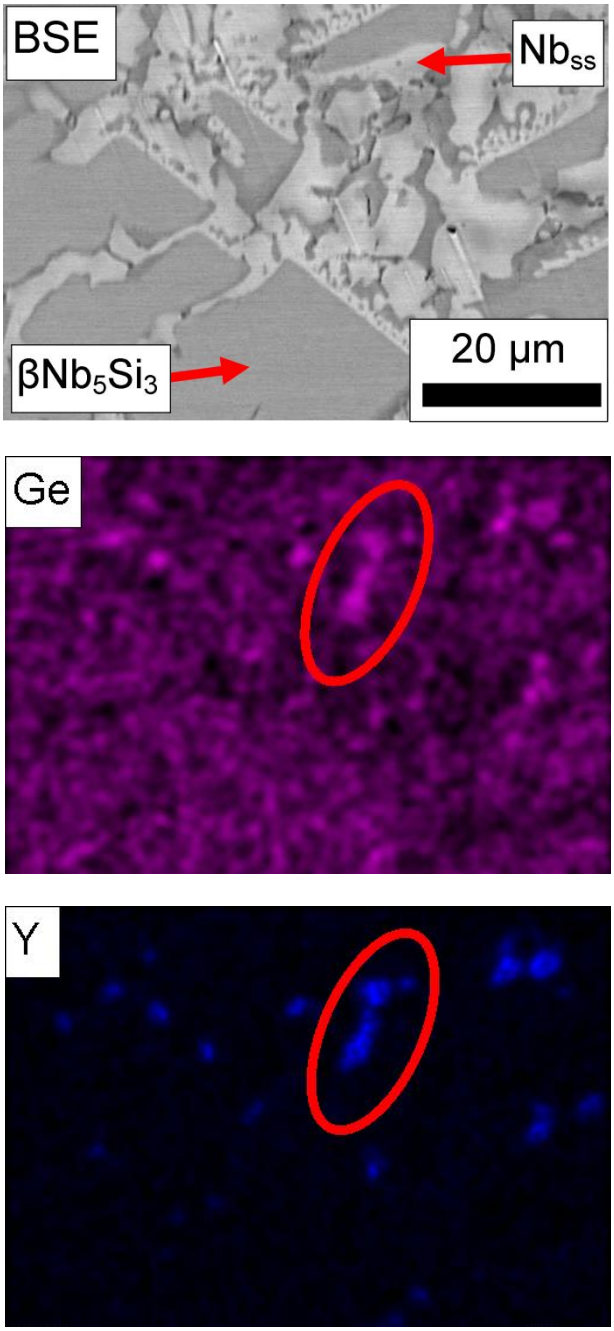

Figure 6.4 Elemental x-ray maps (collected on Phillips XL30 microscope) showing the correlation between Ge and Y in as cast AT2.

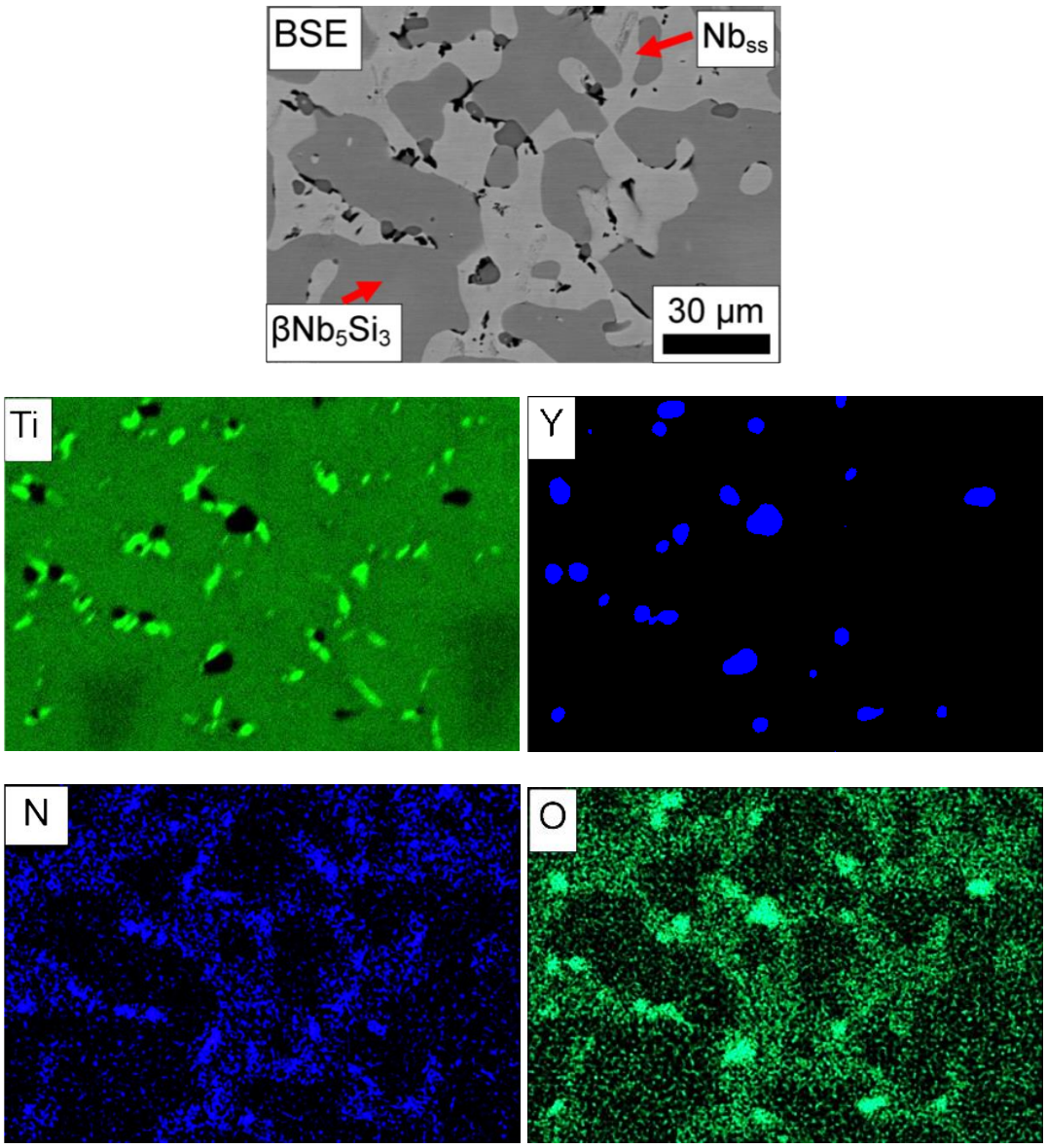

Figure 6.5 Elemental x-ray maps (collected on Phillips XL30 microscope) and BSE image of a selected area of the heat treated microstructure of AT2. Maps are shown for Ti, Y, N and O.

6.2.2 Nb-24Ti-18Si-2Cr-2Al-3Ge-1Y (AT3)

6.2.2.1 As cast

The alloy was designed with a nominal composition of Nb-24Ti-18Si-2Cr-2Al-3Ge-1Y, but the large area EDS analysis (Table 6.2) puts the actual composition at 48.8Nb-24.1Ti-18.4Si-1.8Cr-2.67Al-2.64Ge-1.8Y. Large area chemical analysis shows no macrosegregation of any elements with $C_{max} - C_{min}$ of Si = 1.4 (at.%) therefore lowering the Al content improves homogeneity of Si within the as cast alloy. Figure 6.6 shows typical BSE images of the microstructure present at the top, centre and bottom of the ingot. Chemical analysis and XRD (Table 6.2 and Figure 6.9(a)) confirm the presence of βNb_5Si_3 and the Nb_{ss} phase. Although there is no chemical data or peaks in the XRD pattern to confirm its presence, it is proposed that Nb_3Si is present in the form of a eutectic (Nb_{ss} + Nb_3Si) in the interdendritic regions. The presence of Nb_3Si is suggested from areas of lighter contrast seen within the eutectic surround the primary βNb_5Si_3 grains (Figure 6.6(c)). Microsegregation of Ti is seen within each phase as areas of darker contrast. These areas, whilst clearly visible, are too small (<5 μm) to be confident of any analysis and therefore no data is provided. Figure 6.6 shows the microstructure at the centre is coarser than that at the top or bottom of the ingot, due to its slower cooling rate, and some highly faceted βNb_5Si_3 grains. Figure 6.6(d) shows a transition from a finer, dual phase morphology of a continuous matrix of Nb_{ss} together with Nb_5Si_3 grains, to a more coarser dual phase structure. This then leads into the microstructure seen in the centre, which consists of primary βNb_5Si_3 dendrites surrounded by a eutectic of βNb_5Si_3 and Nb_{ss}. Chemical analysis shows that below the transition at the bottom of the ingot, the Si+Ge+Al = 18.5 at.% (Table 6.2) whereas the eutectic at the centre has Si+Ge+Al = 16.3 at.% (Table 6.2). Elemental x-ray maps (Figure 6.10) show the presence of Y and Ge rich areas of the Nb_{ss} phase.

6.2.2.2 Heat treated (1500 ^{o}C for 100 h)

The microstructure of the heat treated specimen is shown in Figure 6.7(a) and the image is of the microstructure present at the centre of the ingot. The difference in the microstructure after the heat treatment process is dramatic. Firstly, all areas of microsegregation of Ti have been eliminated, secondly, all areas of eutectic have disappeared and thirdly, there is contamination of the microstructure, shown by new phases (as before Y_2O_3 and Ti_xN_y) appearing within the Nb_{ss} phase. Finally, the microstructure is now dominated by Nb_3Si rather than by either of the others. The heat treatment has allowed this phase to grow at the expense of the βNb_5Si_3 phase. The XRD now confirms the presence of all three phases (Figure 6.3b). The chemical analysis data shows macrosegregation of Nb, Ti and Si with $C_{max} - C_{min}$ = 3.3, 4.0 and 2.9 at.% respectively. Data in Table 6.2 confirms the presence of Nb_3Si phase with contents of Si+Al+Ge = 25.1 at.%.

6.2.2.3 Heat treated (1300 ^{o}C for 100 h)

It was of interest to know how and where the Nb_3Si was forming during the heat treatment process. A separate heat treatment of the as cast sample was conducted at 1300 ^{o}C for 100 h. At this temperature, the kinetics of the phase transformation should be slow enough for a minor level of Nb_3Si to form to reveal information about is formation. The results of this heat treatment are shown in Table 6.3 and Figure 6.7(b-c). They show that the Nb_3Si forms where the eutectic is located in the as cast microstructure at the/next to the grain boundary of βNb_5Si_3. The presence of the Nb_3Si phase is confirmed with Si+Al+Ge = 27 at.%.

6.2.2.4 Heat treated (1500 ^{o}C for 200 h)

A section of the previously heat treated sample of AT3 (1500 ^{o}C for 100 h) was placed back into the furnace under the same conditions and heat treated for a further 100 h. Figure 6.8 shows BSE images taken from the top and centre of the

ingot. Chemical analysis reveals the presence of Nb_{ss} and Nb_5Si_3 separated into Ti rich and non Ti rich Nb_5Si_3. The Ti rich Nb_5Si_3 was located at the top of the ingot only (Figure 6.8(a)). X-ray diffraction analysis confirms the presence of Nb_{ss} and different structure of Nb_5Si_3. Analysis reveals tetragonal α and βNb_5Si_3 and hexagonal γNb_5Si_3 (the latter two structures being suggested by only one or two characteristic signals in the XRD pattern). The dominant phases are the Nb_{ss} and αNb_5Si_3.

Chemical analysis (Table 6.3) shows that after a 200 h heat treatment at 1500 ^oC, contamination of the Nb_{ss} by O_2 is drastic, with levels of oxygen reaching 9.0 at.%. According to the Nb-O binary phase diagram (Figure 3.2) the solubility of O in Nb increases with temperature until 1915 ^oC, where the solubility limit of O is 9 at.%. It can be suggested that the addition of different alloying elements can affect the solubility of O in Nb, in this case, increasing the solubility limit at 1500 ^oC from ~5 at.% to 9 at.%.

Table 6.2 Chemical analysis of AT3 in all as cast and heat treated (1500 ^{o}C for 100 h) conditions. Data presented includes the maximum, minimum, average values with standard deviations of the element contents.

As cast	Nb (at.%)	Ti (at.%)	Si (at.%)	Cr (at.%)	Al (at.%)	Ge (at.%)	Y (at.%)
Top	49.1-48.4	24.7-23.6	18.8-17.8	1.9-1.6	2.9-2.3	2.8-2.5	2.1-1.7
	48.8±0.1	24.0±0.1	18.3±0.1	1.8±0.1	2.6±0.1	2.6±0.1	1.9±0.1
Bulk	49.1-48.4	24.7-23.9	18.6-18.0	2.-1.7	2.8-2.4	2.9-2.4	1.9-1.2
	48.7±0.1	24.3±0.1	18.3±0.2	1.9±0.1	2.6±0.1	2.6±0.1	1.7±0.1
Bottom	49.7-48.1	25.0-23.2	19.2-17.8	2.0-1.7	2.8-2.2	2.8-2.3	1.7-1.3
	48.9±0.3	23.9±0.3	18.7±0.3	1.8±0.1	2.6±0.1	2.6±0.1	1.7±0.1
Bottom $_{(below\ transisiton)}$	52.7-48.8	26.7-25.8	14.6-12.7	2.5-2.1	1.9-1.7	3.1-2.5	2.5-1.4
	51.1±1.5	26.3±0.1	13.9±0.6	2.3±0.1	1.8±0.1	2.8±0.1	1.8±0.1
Nb_{ss}	68.0-61.6	26.9-22.1	3.4-2.4	3.1-1.5	3.4-2.3	1.0-0.7	1.3-0.5
	65.5±5.6	24.4±3.4	3.0±0.1	2.4±0.3	3.0±0.1	0.9±0.1	1.0±0.1
βNb_5Si_3	45.0-43.9	18.5-17.2	32.0-31.2	0.5-0.3	2.2-1.7	3.7-3.1	0.9-0.1
	44.4±0.1	17.7±0.2	31.7±0.1	0.5±0.1	1.9±0.1	3.4±0.1	0.6±0.1
Eutectic	60.1-55.1	23.2-21.7	13.4-10.1	2.1-1.6	2.0-1.8	2.5-1.7	2.1-1.8
	57.6±0.2	22.3±0.1	12.2±0.1	1.8±0.1	1.9±0.1	2.2±0.1	1.9±0.1
Heat treated *(1500 ^{o}C for 100 h)*							
Top	53.0-50.6	22.2-18.4	21.5-19.9	0.9-0.5	1.6-1.0	2.8-2.1	2.7-1.8
	51.8±0.3	21.0±0.8	20.6±0.2	0.6±0.1	1.2±0.2	2.4±0.1	2.2±0.1
Bulk	52.8-51.6	21.2-20.0	20.6-19.2	1.2-0.7	1.9-1.1	2.8-2.1	3.0-2.3
	52.1±0.2	20.6±0.1	19.9±0.1	0.9±0.2	1.5±0.1	2.4±0.1	2.6±0.1
Bottom	51.2-49.7	22.4-20.6	19.9-18.7	1.8-1.3	3.0-1.8	3.0-2.4	2.5-2.0
	50.4±0.1	21.6±0.2	19.4±0.2	1.7±0.1	2.1±0.1	2.8±0.1	2.2±0.1
Nb_{ss}	76.8-67.7	23.4-16.4	1.2-0.7	4.0-2.6	2.5-0.5	0.9-0.4	1.5-0.4
	71.0±8.9	21.0±5.2	1.1±0.1	3.6±0.2	1.7±0.5	0.7±0.4	1.0±0.1
βNb_5Si_3	44.2-43.0	19.2-17.6	33.0-21.6	0.4-0.1	1.7-1.0	3.4-2.9	1.2-0.6
	43.7±0.3	18.6±0.4	32.3±0.3	0.2±0.1	1.3±0.1	3.2±0.1	0.8±0.1
Nb_3Si	53.4-49.8	23.8-19.5	22.3-21.8	0.5-0.3	0.8-0.4	2.9-2.3	1.7-0.6
	51.3±1.4	22.4±2.1	21.9±0.1	0.3±0.1	0.6±0.1	2.6±0.1	1.0±0.1

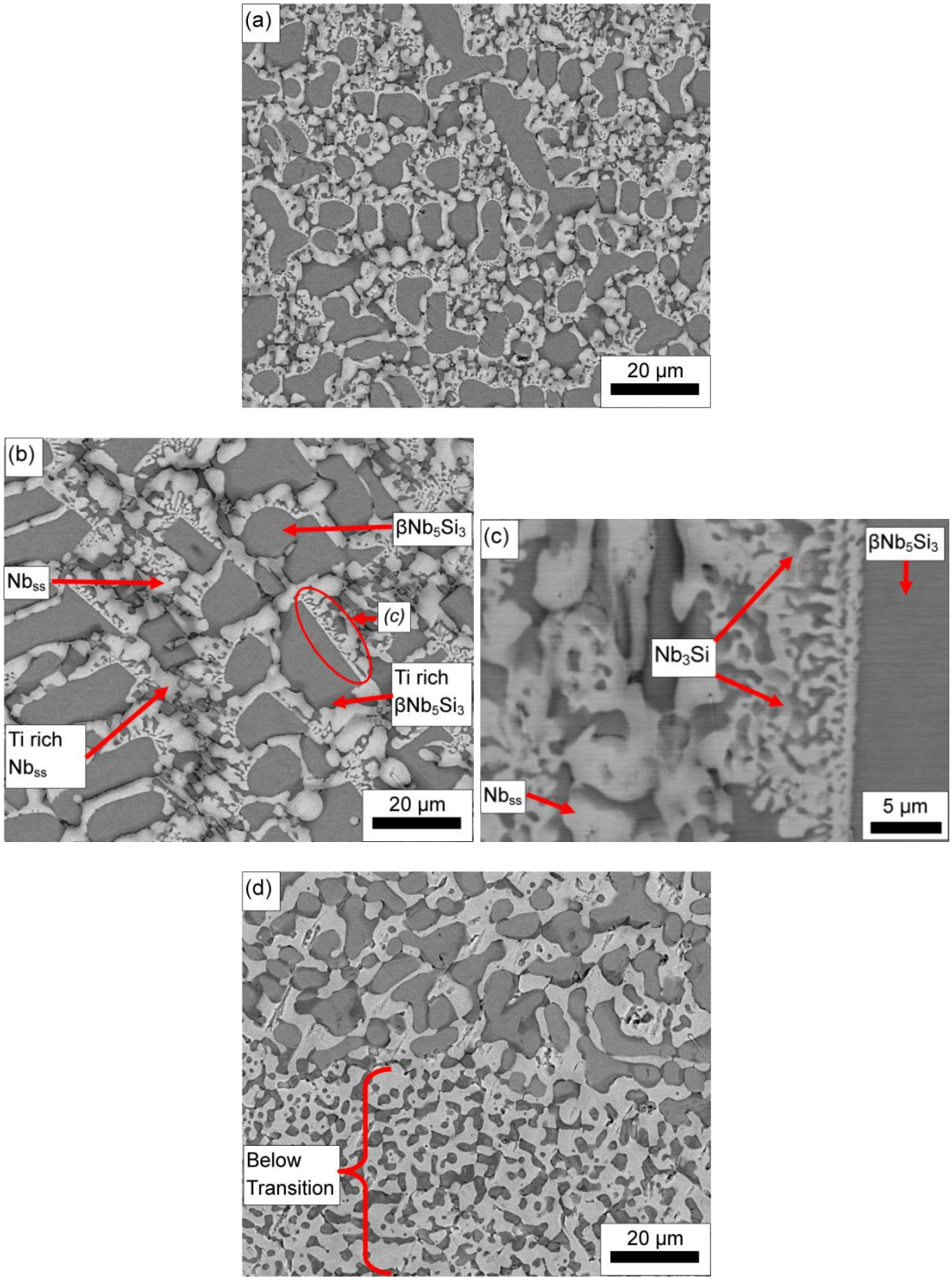

Figure 6.6 Typical BSE images (taken in the FEI Inspect F microscope) of as cast AT3 (a) top of ingot, (b-c) centre of ingot and eutectic and (d) bottom of ingot in contact with crucible. Each image shows Nb_{ss} (white phase) and βNb_5Si_3 (grey phase). Nb_3Si is located in (c) (light grey phase).

Table 6.3 Chemical analysis of AT3 heat treated (1300 ^{o}C for 100 h and 1500 ^{o}C for 200 h). Data presented includes the maximum, minimum, average values with standard deviations of the element contents.

Heat treated *(1300 ^{o}C for 100 h)*	Nb	Ti	Si	Cr	Al	Ge	Y	O
Nb_{ss}	63.1-57.5	26.3-22.7	1.0-0.6	4.4-3.9	2.7-1.1	0.4-0.2	0.4-0.2	7.6-5.7
	61.0±0.2	24.9±0.1	0.7±0.1	4.1±0.1	1.9±0.1	0.3±0.1	0.2±0.1	6.8±0.1
Nb_3Si	43.7-43.2	29.2-28.8	24.2-23.4	0.4-0.3	0	3.3-3.2	0.5-0.2	-
	43.4±0.1	29.0±0.1	23.8±0.1	0.3±0.1	0	3.2±0.1	0.2±0.1	-
βNb_5Si_3	44.0-39.4	20.2-15.8	35.9-34.2	0.4-0.2	1.6-0.9	4.4-3.8	0.3-0.1	-
	42.5±0.1	17.0±0.1	35.0±0.1	0.3±0.1	1.1±0.1	3.9±0.1	0.2±0.1	-
Heat treated *(1500 ^{o}C for 200 h)*								
Nb_{ss} [a]	66.4-62.6	21.7-18.9	0.9-0.5	4.4-3.6	2.4-1.7	0.6-0.4	0.3-0.2	8.6-6.6
	64.5±0.1	20.3±0.1	0.6±0.1	4.0±0.1	2.2±0.1	0.5±0.1	0.2±0.1	7.7±0.1
Nb_{ss} [b]	68.2-65.9	16.8-14.2	0.7-0.6	4.8-4.2	3.0-2.3	0.7-0.6	0.3-0.2	9.3-8.6
	67.1±0.3	15.3±0.4	0.6±0.1	4.6±0.1	2.6±0.1	0.6±0.1	0.2±0.1	9.0±0.1
Nb_5Si_3	43.7-38.6	21.9-16.2	36.0-30.6	1.2-0.1	1.8-0.1	5.6-3.5	0.4-0.1	-
	42.0±0.2	18.5±0.2	33.8±0.2	0.5±0.1	0.9±0.1	4.1±0.1	4.1±0.1	-
γNb_5Si_3	35.3-33.6	27.1-25.3	33.1-32.5	0.6-0.5	1.5-0.8	5.5-4.4	0.3-0.1	-
	34.4±0.1	26.1±0.1	32.7±0.1	0.5±0.1	1.2±0.1	4.8±0.1	0.3±0.1	-

[a] located at the top and centre

[b] located at the bottom

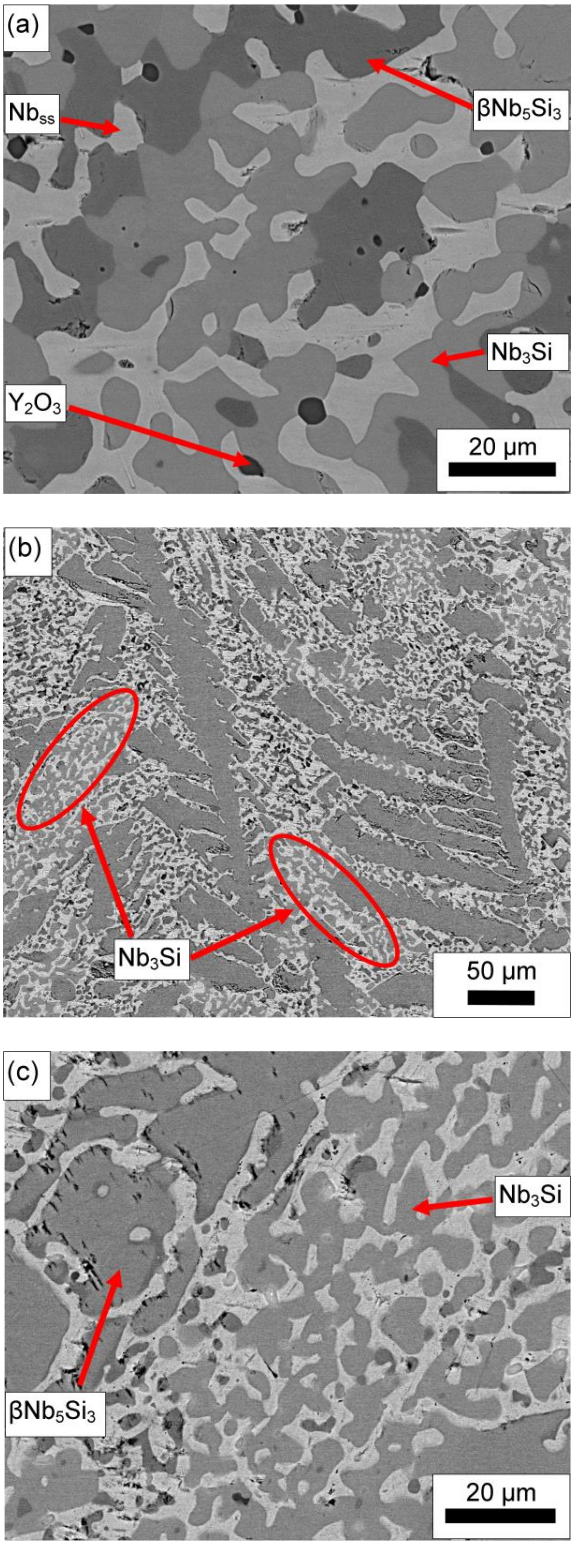

Figure 6.7 BSE images (taken in the FEI Inspect F microscope) of heat treated AT3. Images show (a) AT3 heat treated at 1500 ^{o}C for 100 h, (b) AT3 heat treated at 1300 ^{o}C for 100 h, (c) AT3 heat treated at 1300 ^{o}C for 100 h close up of region with Nb_3Si formation.

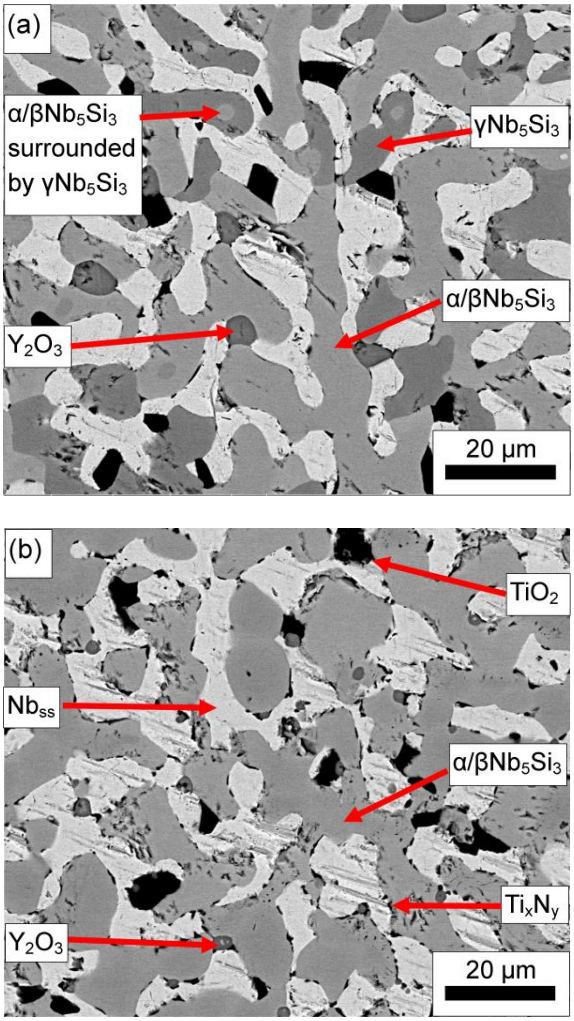

Figure 6.8 BSE images (taken in the FEI Inspect F microscope) of AT3 heat treated at 1500 ^{o}C for 200 h. Images show microstructure present at (a) top of ingot and (b) the centre of the ingot.

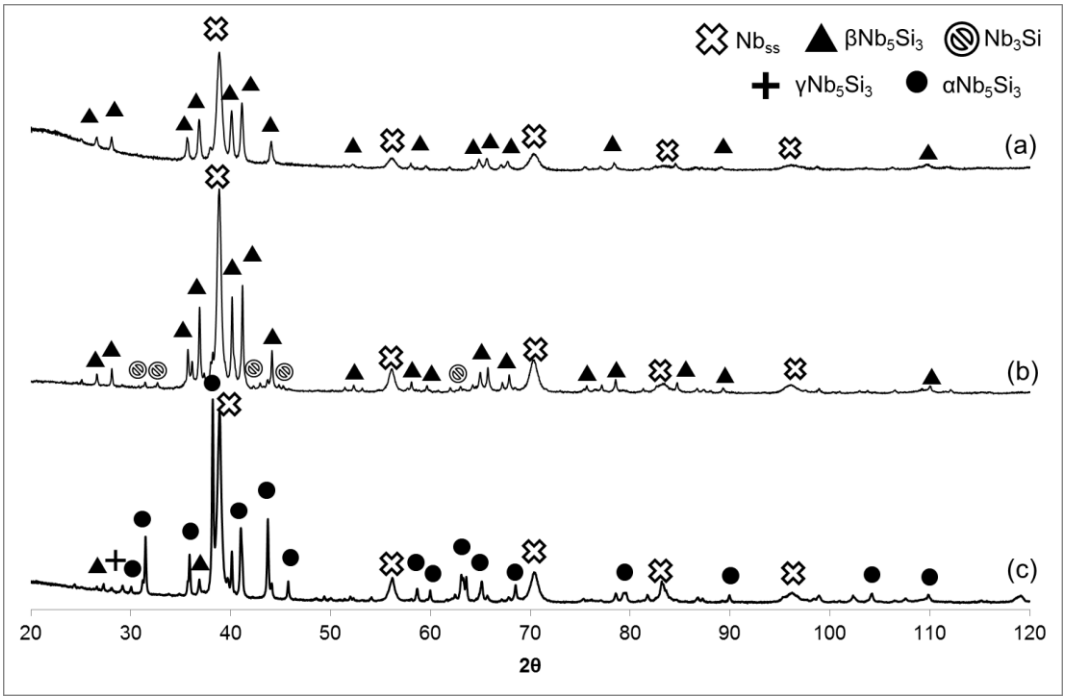

Figure 6.9 Powder x-ray diffraction pattern of AT3 (a) as cast, (b) heat treated condition (1500 ^{o}C for 100 h) and (c) second heat treated condition (1500 ^{o}C for 200 h).

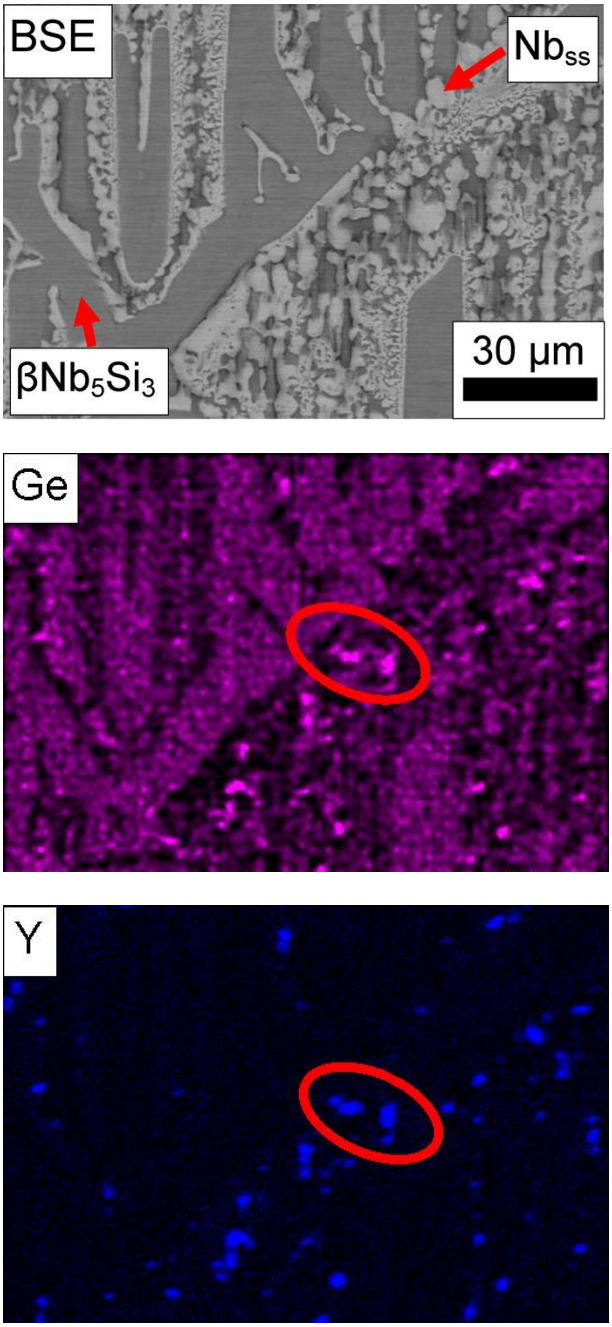

Figure 6.10 Elemental x-ray maps (collected on Phillips XL30 microscope) showing the correlation between Ge and Y in as cast AT3.

6.3 Discussion

6.3.1 Nb-24Ti-18Si-2Cr-5Al-3Ge-1Y (AT2)

6.3.1.1 As cast

The solidification path proposed for AT2 is L → L + βNb_5Si_3 → L + βNb_5Si_3 + (βNb_5Si_3 + Nb_{ss}) → βNb_5Si_3 + (βNb_5Si_3 + Nb_{ss}) + Nb_{ss}. This is the same solidification path for alloy AT1 previously reported (Chapter 5). Lowering the levels of Cr and Ge has had no effect on the solidification path and the only change in microstructure at the centre of the ingot is a higher level of the interdendritic eutectic of Nb_{ss} + βNb_5Si_3. The higher level of eutectic is expected as alloy AT1 had Si+Ge+Al = 28 at.% but AT2 had Si+Ge+Al = 26 at.%. The overall alloy composition is closer to the eutectic point in the Nb-Si binary phase diagram. Both Cr and Ge are reported to be beneficial for stabilising the Nb_5Si_3 phase and therefore lowering levels of these elements should promote the formation of the Nb_3Si phase, along with the overall alloy composition being closer to the eutectic point in the Nb-Si phase diagram; however this is not the case in as cast alloy AT2. The effect of lowering Cr and Ge on stabilising the Nb_3Si phase is either not a great effect, or requires a greater reduction in the levels for the effect to be noticeable in the as cast material. The main difference of as cast AT2 to as cast AT1 is that the bottom of the ingot (in contact with the Cu crucible) is a more dual phase, globular type structure than a fine eutectic (as seen in as cast AT1, Chapter 5). A similar effect was seen in the literature with alloy ZF1 (Zifu and Tsakiropoulos, 2010). The effect was attributed to the melt experiencing undercooling above some critical value ($\Delta T_{critical}$) and according to Li and Kuribayashi (2003) $\Delta T_{critical} \sim 0.25\Delta T_{max}$ where $\Delta T_{critical}$ and ΔT_{max} are the critical value for anomalous eutectic formation and the maximum undercooling that can be experienced by the eutectic system. As the anomolous eutectic grew, the latent heat of solidification was released into the melt ahead of the solid/liquid interface allowing slower growth rates and eventually leading to a more regular eutectic to form in the bulk (Zifu and Tsakiropoulos, 2010). Similar

effects are seen in the centre of the ingot surrounding the βNb_5Si_3 grains. The βNb_5Si_3 solidifies as the primary phase and with the high entropy of fusion, this leads to faceted morphology of the grain. Around this, the eutectic of Nb_{ss} and βNb_5Si_3 forms and a similar decoupled eutectic growth occurs. The centre experiences a slower cooling rate so the growth rate of the βNb_5Si_3 is reduced compared with the Nb_{ss} phase. This phase is therefore allowed to grow more freely between the primary βNb_5Si_3 phase.

6.3.1.2 Heat treated (1500 ^oC 100 h)

After this heat treatment, the bulk microstructure exhibited an almost co-continuous structure of Nb_{ss} and βNb_5Si_3. Like alloy AT1 (Chapter 5), there has been contamination of the microstructure by O_2 and N_2 leading to the formation of Y_2O_3 and Ti_xN_y particles. These are likely to have formed in the Y and Ti rich areas of the Nb_{ss}. There is no evidence for the phase transformation of βNb_5Si_3 to the αNb_5Si_3 or the formation of Nb_3Si, reinforcing the suggestion that the effect of lowering Ge and Cr levels has little effect on destabilising the βNb_5Si_3 phase. What has occurred is the formation of hexagonal γNb_5Si_3 near the top of the ingot. It has been reported that interstitials such as oxygen and carbon stabilise the hexagonal γNb_5Si_3, however, neither of these were found in any phase or any area of the microstructure after heat treatment. The table presented in Chapter 1 (Table 1.15) shows that both Cr and Ge, in conjunction with Nb, Si, Ti and Y, form both tetragonal and hexagonal crystal structures. While no hexagonal crystal structures were observed in alloy AT1 (Chapter 5), they are present in AT2. It is proposed that above a certain alloying level, additions of Cr and Ge have a more potent effect on stabilising the tetragonal crystal structure, and below this critical level they stabilise the hexagonal crystal structures. It is proposed that this level is ~ 3 at.%.

6.3.2 Nb-24Ti-18Si-2Cr-2Al-3Ge-1Y (AT3)

6.3.2.1 As cast

The microstructure of the as cast AT3 is different to that of AT1 (Chapter 5) and AT2. The microstructure consists of primary βNb_5Si_3 with a much higher volume fraction of interdendritic eutectic of Nb_{ss} + βNb_5Si_3 than seen in either AT1 or AT2 and XRD confirms the presence of those two phases. The higher volume fraction of eutectic is due to the overall alloy composition being even closer to the eutectic point with Si+Ge+Al = 23 at.% (28 and 26 at.% for AT1 and AT2 respectively). There is also the presence of Nb_3Si at the edge of the βNb_5Si_3, the volume fraction of this phase is too small to be observed in the XRD pattern. The microstructure at the base of the ingot exhibits a similar transition to that of AT2, from an anomalous eutectic structure to a more regular eutectic morphology in the bulk of the ingot and an explanation of how undercooling and kinetic attachment difficulties lead to such a microstructure has been provided in the previous section.

6.3.2.2 Heat treated (1500 ^oC for 100 h and 1300 ^oC for 100 h)

After the first heat treatment (1500 ^oC for 100 h), the most observable change is that the microstructure is dominated by the Nb_3Si phase, rather than either the βNb_5Si_3 or the Nb_{ss} phase. The presence of Nb_3Si in the as cast microstructure is suggested by a heat treatment at 1300 ^oC for 100 h. This heat treatment revealed that Nb_3Si grows from the areas of eutectic surrounding the edge of the βNb_5Si_3 in the as cast microstructure.

With the Si+Al+Ge = 23.7 at.% for the alloy AT3 means that composition of the alloy lies between the eutectic of Nb_{ss} + Nb_3Si and the peritectic transformation of L + $\beta Nb_5Si_3 \rightarrow Nb_3Si$, suggesting that both are possible for the alloy AT3. The arguments that follow deal with several hypothesis for formation of Nb_3Si and how the observations from the heat treatment experiments suggest that Nb_3Si is formed

in the as cast microstructure and how its growth and stability within the microstructure has been affected by the reduction of Al.

1) *Nb_3Si is formed from solidification in the as cast microstructure through the peritectic phase transformation L + βNb_5Si_3 → Nb_3Si and this transformation continues during heat treatment.*

Peritectic solidification characteristically occurs with the secondary phase (in the case of Nb-Si alloys is Nb_3Si) surrounding the primary phase (in this case – βNb_5Si_3). If hypothesis 1 is to be accepted, there should be evidence within the microstructure of Nb_3Si surrounding βNb_5Si_3 grains within the microstructure, and Figure 6.6(c) clearly shows no evidence of a lighter phase surrounding the primary βNb_5Si_3 dendrites.

Also Bendersky et al.,(1987) state:

"For alloys near a peritectic reaction, solidification of the high temperature phase (in this case, Nb_5Si_3) can continue below the peritectic temperature……."

and Bertero et al.,(1991) state:

"…..βNb_5Si_3 is not a potent nucleation site for Nb_3Si."

It has also been discussed in the literature that under non equilibrium conditions, the formation of Nb_3Si is bypassed altogether in favour of a metastable eutectic of Nb_{ss} + βNb_5Si_3. There is partial evidence for the peritectic phase transformation L + βNb_5Si_3 → Nb_3Si in the heat treated (1500 ^oC for 100 h) microstructure. Figure 6.7(a) shows two instances of the primary βNb_5Si_3 grains surrounded by the Nb_3Si, which suggests that the phase transformation does occur.

It is concluded that whilst the phase transformation is suggested by the heat treatment process, there is no evidence to suggest Nb_3Si forms from the peritectic transformation in the as cast ingot.

2) *Nb_3Si is formed in the as cast microstructure as a eutectic of $L \rightarrow Nb_{ss}$ + Nb_3Si and during heat treatment.*

With the lack of evidence for a peritectic phase transformation within the as cast microstructure, the other hypothesis is that Nb_3Si is formed in a eutectic of Nb_{ss} + Nb_3Si. The lighter areas of contrast seen in Figure 6.6(c) would suggest that Nb_3Si is formed in the interdendritic regions. Also, the heat treatment (1300 ^{o}C for 100 h) shows that the appearance of Nb_3Si arises within the interdendritic areas where the eutectic morphology is located (Figure 6.7(b and c)). Heat treatment is therefore providing the necessary energy for a coarsening of the eutectic and therefore the increase in volume fraction of the Nb_3Si at the expense of the βNb_5Si_3 phase. This also accounts for the lack of the βNb_5Si_3 surrounded by the Nb_3Si as the peritectic transformation is bypassed (along with the knowledge from Bendersky et. al and Bertero et. al in the previous explanation).

The question remains why there is no evidence of Nb_3Si in the XRD pattern, as its presence in a eutectic with Nb_{ss} would have formed Nb_3Si in sufficient volume fraction for a signal to be seen in powder XRD. It has been shown in the literature that the addition of elements (such as Ti) can lower the temperatures of the eutectic and peritectic transformation within the Nb-Si system. It is possible that the peritectic transformation temperature has been lowered to a similar temperature of the eutectic transformation.

Bendersky et al.,(1987) also comment:

"Under rapid quenching conditions, growth competition between Nb_3Si and Nb_5Si_3 will be won by Nb_5Si_3."

If Nb_3Si forms from the eutectic, it is possible that the initial βNb_5Si_3 will continue to form and effectively inhibit the growth of the Nb_3Si during solidification. This would account for the lack of any evidence of Nb_3Si in the as cast XRD pattern.

3) *Nb_3Si is not formed in the as cast ingot and forms in during the heat treatment.*

This hypothesis is supported by the lack of any Nb_3Si signals in the powder XRD pattern and lack of chemical analysis data (EDX/WDX) to confirm its presence. As already discussed there is no evidence to support a peritectic transformation in the as cast microstructure with no Nb_3Si surrounding the βNb_5Si_3. There is evidence to suggest the peritectic transformation in the heat treated microstructure (Figure 6.7(a)). However, if the hypothesis is to be true, it is expected that the heat treatment at both 1300 and 1500 ^oC for 100 h would show (in the microstructure) the majority of Nb_3Si surrounding and consuming βNb_5Si_3. What is seen is that Nb_3Si appears first in the interdendritic regions suggesting a coarsening of the eutectic of Nb_{ss} + Nb_3Si.

For all of the arguments presented it is proposed that the hypothesis (2) is accepted to be the more likely based on the results and the arguments provided.

6.3.2.3 Heat treated (1500 ^oC for 200 h*)*

After a further heat treatment of 100 h at 1500 ^oC, the microstructure now consisted of Nb_{ss} and the low temperature αNb_5Si_3, with minor additions of high

temperature βNb_5Si_3 and hexagonal γNb_5Si_3. Some of the Ti rich γNb_5Si_3 have α or βNb_5Si_3 present inside suggesting that the formation of γNb_5Si_3 begins at the grain boundary and progresses into the bulk of the grain. Therefore, it is likely that the grain boundary has provided the nucleation site for this phase transformation. The question remains whether αNb_5Si_3 has formed from a eutectoid decomposition of $Nb_3Si \rightarrow Nb_{ss} + \alpha Nb_5Si_3$, or from a volumetric change of $\beta Nb_5Si_3 \rightarrow \alpha Nb_5Si_3$.

6.3.3 Structural Refinement

Structural refinement was conducted using the XRD patterns of both as cast and heat treated (1500 ^oC for 100 h) ingots of both alloys, and the results are presented in Table 6.4 and Table 6.5 and Figure 6.11 and Figure 6.12. Refinement was not conducted on alloy AT3 heat treated for 200 h. The procedure for conducting the refinement was outlined in the previous chapter for alloy AT1 and the experimental section (Chapters 4 and 5). The results in Table 6.4 show a contraction of the lattice parameter of the Nb_{ss} phase in the as cast alloy for both AT2 and AT3 from 3.3 to 3.26 and 2.27 Å respectively, and a slight expansion after heat treatment to 3.27 and 3.28 Å respectively. Similar to what has been reported in the literature, the βNb_5Si_3 experienced an expansion in (*a)* and a contraction in (*c)*. The expansion and contraction in AT2 are similar to those reported in Chapter 5 for alloy AT1, but those felt by AT3 are much less severe. Both of the refinements show that Ti(+Cr) occupy both Nb sites within the crystal structure but preferentially occupy the less closed packed Nb sites (Nb(I)) and that movement of Ti(+Cr) from the Nb(II) to Nb(I) sites occur during heat treatment process. Both refinements also show that Ge prefers to occupy the Si(II) sites. Both of these finding agree with previously reported results for alloy AT1 in Chapter 5 (Kang et al., 2009, Chen et al., 2007a).

Table 6.4 also gives the results of the volume fractions of the individual phases within the alloy microstructure of the as cast and heat treated (1500 ^oC for

100 h). The volume fraction of Nb_{ss} in the as cast alloy has increased through the reduction of Cr and Ge from 0.39 (alloy AT1, Chapter 5) to 0.44 (alloy AT2). The volume fraction is increased by further reductions in the Al content from 0.44 (AT2) to 0.49 (AT3). In AT1 and AT2 there was an increase in the volume fraction of the βNb_5Si_3 after heat treatment, however in alloy AT3, there was a reduction in the volume fraction of βNb_5Si_3 with the Nb_3Si now being present. This is further evidence that the Nb_3Si is forming at the expense of the βNb_5Si_3 phase.

Table 6.4 Lattice parameter results of Structural Refinements of both AT2 and AT3 in both conditions.

			AT2		AT3	
		Reference	As cast	Heat treated	As cast	Heat treated
Nb_{ss}	a(Å)	3.3	3.26488(7)	3.27380(7)	3.2452(9)	3.27666(7)
	c(Å)	-	-	-	-	-
	V(Å^3)	35.95	34.802	35.09	35.111	35.18
	V_f	-	0.44(2)	39(2)	0.49(2)	40(2)
βNb_5Si_3	a(Å)	10.02	10.06205(17)	10.06414(11)	10.04481(29)	10.03419(21)
	c(Å)	5.07	5.03615(15)	5.03241(9)	5.03394(27)	5.02429(19)
	c/a	0.506	0.5001	0.5	0.5011	5.007
	V(Å^3)	509.03	509.885	509.72	507.92	505.87
	V_f		0.56(2)	61(2)	51(2)	40(2)
Nb_3Si	a(Å)	10.22	-	-	-	10.19865(85)
	c(Å)	5.19	-	-	-	5.18842(87)
	c/a	-	-	-	-	0.509
	V(Å^3)	542.41	-	-	-	539.66
	V_f	-	-	-	-	17(2)

Errors in brackets at those given by GSAS. Errors are to the same number of decimal places.

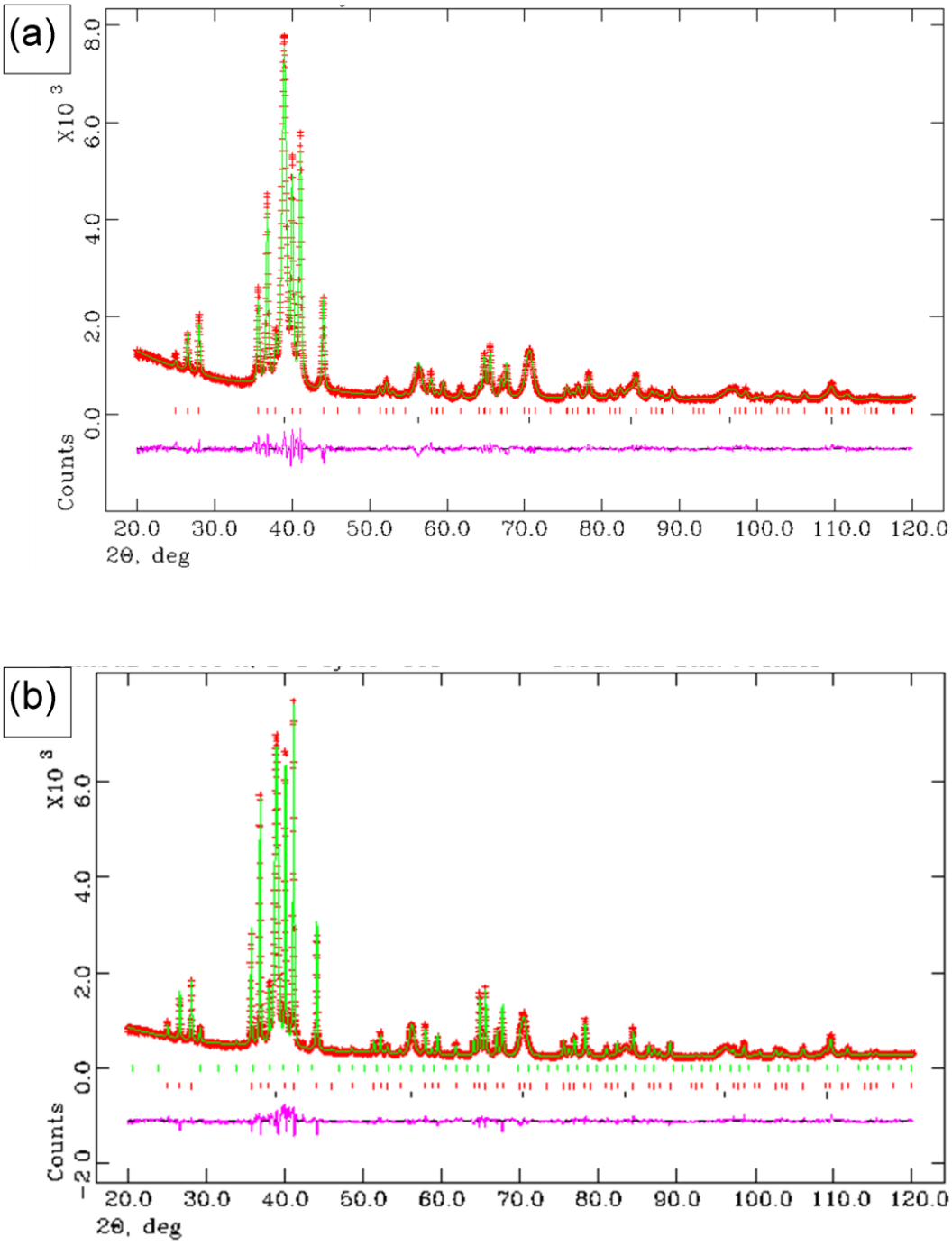

Figure 6.11 Results of structural refinements of AT2 (a) as cast and (b) heat treated 1500 ^{o}C for 100 h.

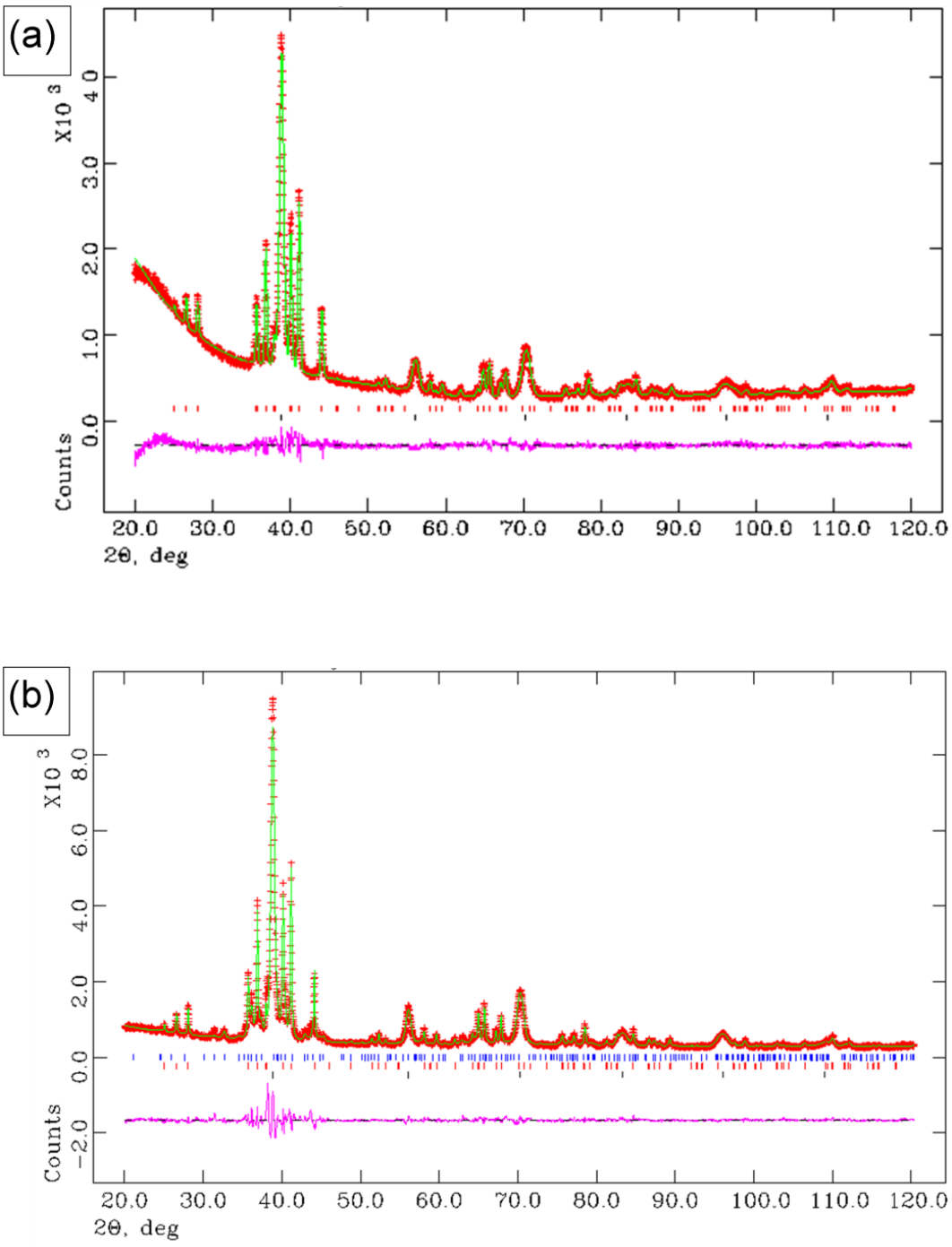

Figure 6.12 Results of structural refinements of AT3 (a) as cast and (b) heat treated 1500 ^{o}C for 100 h.

Table 6.5 Site occupancy results from Structural Refinements.

		AT2		AT3	
	Reference	As cast	Heat treated	As cast	Heat treated
χ^2	-	1.715	2.249	1.463	3.589
Rp (%)	-	3.84	5.1	4.01	5.6
Rwp (%)	-	5.11	6.8	5.08	8
Nb $_{ss}$					
x=y=z	0	0	0	0	0
site occupancy	1.0Nb	0.57Nb/0.31Ti/0.12Al	0.6Nb/0.3Ti/0.1Al	0.67Nb/0.26Ti/0.07Al	0.75Nb/0.25Ti
Uiso (Å ^{2}*)*	0.025	0.03342(4)	0.03196(5)	0.02517(5)	0.02388(4)
βNb $_5$***Si*** $_3$					
atom site Nb(I)					
x	0	0	0	0	0
y	0.5	0.5	0.5	0.5	0.5
z	0.25	0.25	0.25	0.25	0.25
site occupancy	1.0Nb	0.55Nb/0.45Ti	0.45Nb/0.55Ti	0.55Nb/0.45Ti	0.50Nb/0.50Ti
Uiso (Å ^{2}*)*	0.025	0.02526(8)	0.01952(8)	0.01550(13)	0.02110(13)
atom site Nb(II)					
x	0.074	0.07910(13)	0.07936(15)	0.07809(23)	0.07645(24)
y	0.223	0.21812(13)	0.21766(15)	0.21940(26)	0.21799(26)
z	0	0	0	0	0
site occupancy	1.0Nbi	0.70Nb/0.30Ti	0.7Nb/0.3Ti	0.75Nb/0.25Ti	0.7Nb/0.3Ti
Uiso (Å ^{2}*)*	0.025	0.02752(4)	0.02994(5)	0.04224(8)	0.02470(7)
atom site Si(I)					
x=y	0	0	0	0	0
z	0.25	0.25	0.25	0.25	0.25
site occupancy	1.0Si	1.0Si	1.0Si	1.0Si	1.0Si
Uiso (Å ^{2}*)*	0.025	0.03593(18)	0.02901(20)	0.03226(38)	0.03534(32)
atom site Si(II)					
x	0.17	0.16385(27)	0.163556(30)	0.16672(51)	0.16481(49)
y	0.67	0.66385(27)	0.66356(30)	0.66672(51)	0.66482(49)
z	0	0	0	0	0
site occupancy	1.0Si	0.87Si/0.13Ge	0.85Si/0.15Ge	0.85Si/0.15Ge	0.85Si/0.15Ge
Uiso (Å ^{2}*)*	0.025	0.02950(12)	0.02337(13)	0.02628(24)	0.01702(19)

Errors in brackets at those given by GSAS. Errors are to the same number of decimal places as the values.

Table 6.6 Site occupancy results from Structural Refinements.

		AT3
Nb_3Si	Reference	Heat treated
atom site Nb(I)		
x	0.1653	0.16858(11)
y	0.6525	0.64360(13)
z	0.7185	0.71618(23)
site occupancy	1.0Nb	0.7Nb/0.3Ti
Uiso ($Å^2$)	0.025	0.02330(30)
atom site Nb(II)		
x	0.1043	0.10467(12)
y	0.2665	0.25928(17)
z	0.523	0.55988(23)
site occupancy	1.0Nb	0.6Nb/0.4Ti
Uiso ($Å^2$)	0.025	0.02622(29)
atom site Nb(III)		
x	0.0603	0.06307(15)
y	0.5364	0.53765(14)
z	0.237	0.23347(27)
site occupancy	1.0Nb	0.3Nb/0.3Ti
Uiso ($Å^2$)	0.025	0.03676(38)
atom site Si(I)		
x	0.0442	0.061881
y	0.2782	0.282356
z	0.0293	0.068396
site occupancy	1.0Si	0.9Si/0.1Ge
*Uiso ($Å^2$)**	0.025	0.01094(70)

Errors in brackets at those given by GSAS. Errors are to the same number of decimal places as the values.

The refinement for alloy AT3 (heat treated 1500 ^oC for 100 h) included Nb_3Si (Table 6.6) and showed that there is no obvious preference of Ti to substitute for Nb in the crystal structure (Figure 6.13) on any of the three Nb sites, which agrees with previous results reported in the literature (Chen et al., 2011).

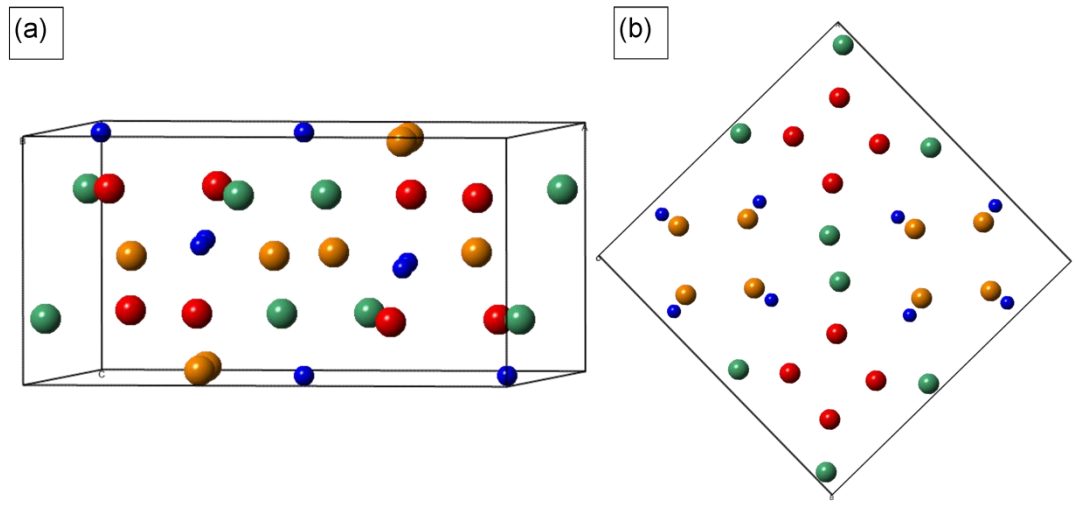

Figure 6.13 Crystal structure of Nb_3Si, (a) side view, (b) top view. In this image and in the refinement (Table 6.6) Nb(I) = large red spheres, Nb(II) = large orange spheres, Nb(III) = large green spheres and Si = small blue spheres. Top view included to make comparison with (Chen et al., 2011)

6.4 Conclusions

In this study, the microstructure and phase stability of complex Nb-Si alloys has been investigated and the main conclusions are as follows:

- Both alloys can be classified as hypereutectic alloys with the βNb_5Si_3 phase being the primary/major phase present within the microstructure.
- Additions of Al destabilise the formation of the Nb_3Si phase, and the effect of Al is far more potent than that of Cr as Nb_3Si is seen in AT3 (Nb-24Ti-18Si-2Cr-2Al-3Ge-1Y) but not in AT2 (Nb-24Ti-18Si-2Cr-5Al-3Ge-1Y), which is in agreement with work reported in the literature.
- Lowering the Al content promoted the formation of Nb_3Si and αNb_5Si_3.
- It is proposed that in alloy AT3, the Nb_3Si is formed is the as cast microstructure from the eutectic reaction $L \rightarrow Nb_{ss} + Nb_3Si$.

- Lowering the Al content did not stabilize the Nb_3Si phase as it was no longer present in the microstructure heated at 1500 ^{o}C for 200 h, but promoted the phase transformation and formation of the low temperature αNb_5Si_3 phase.
- Minor additions of Ge in synergy with Ti, Cr and Y allow the formation of the hexagonal γNb_5Si_3.
- Structural refinement shows changes to the lattice parameters of crystal structures present within the microstructure. The lattice parameter of Nb_{ss} experiences a contraction, whereas βNb_5Si_3 experiences an expansion in *(a)* and a contraction in *(c)*. The lattice parameters of Nb_3Si experience little change from the reference values.

Chapter 7

Effect of Ge and Y addition on the oxidation behaviour of complex Nb silicide based alloys at 800 ^{o}C.

7.1 Introduction

Oxidation studies conducted at temperatures in the 'pest' range generally see common features during the oxidation process, including O_2 ingress through the Nb_{ss} phase and cracking of the intermetallic phase parallel to the surface (Geng et al., 2006c, Geng et al., 2007b, Zelenitsas and Tsakiropoulos, 2006a, Mathieu et al., 2012, Menon et al., 2004). In this chapter, the effects of additions of Ge and Y on the isothermal oxidation performance of complex Nb silicide alloys based on Nb-Ti-Si-Cr-Al composition at 800 ^{o}C for 100 h are reported; the effect of Cr:Al ratio will also be discussed.

7.2 Results

7.2.1 Pre-oxidation microstructures

Although the microstructures prior to oxidation will not be discussed in great detail here (for a thorough analysis refer to Chapter 6), some important information will be repeated in this section. Figure 7.1 shows the pre oxidation microstructures and Table 7.1 summarises the phases present and volume fraction of the Nb_{ss} phase.

Table 7.1 Alloy designation, nominal composition and volume fraction of phases of each alloy in the as cast condition (as determined by Rietveld Refinement in Chapter 6)

Alloy	Nominal Composition (at.%)	Phases	Nb_{ss}	βNb_5Si_3
AT2	Nb-24Ti-18Si-2Cr-5Al-3Ge-1Y	Nb_{ss} and βNb_5Si_3	44	56
AT3	Nb-24Ti-18Si-2Cr-2Al-3Ge-1Y	Nb_{ss}, βNb_5Si_3 and Nb_3Si^*	49	51

*Volume fraction was too small to confidently determine.

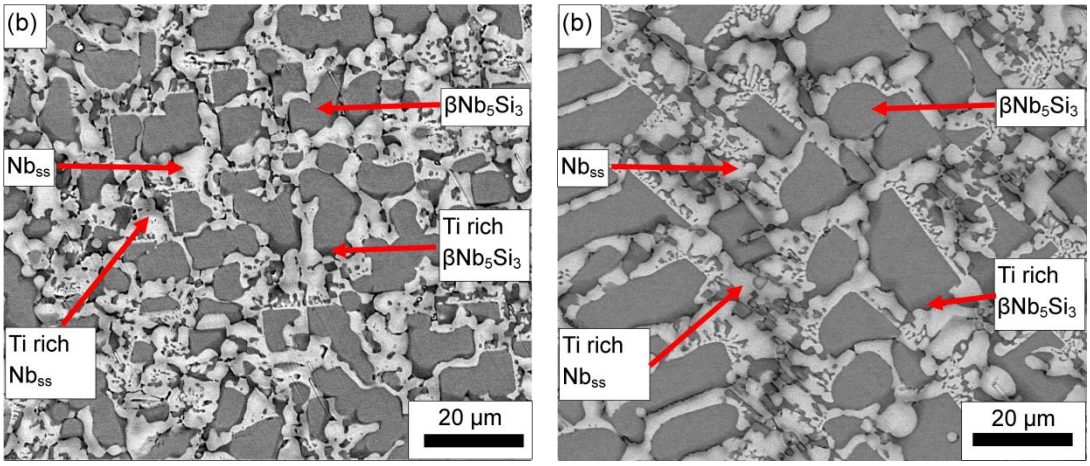

Figure 7.1 Typical BSE images (taken in the FEI Inspect F microscope) of the centre of the (a) AT2 and (b) AT3 in the as cast condition. Phases present are the Nb_{ss} (white) and the βNb_5Si_3 (grey). Alloy AT3 also contains Nb_3Si, which is difficult to distinguish.

7.2.2 Isothermal oxidation kinetics

The oxidised samples after each experiment (prior to XRD investigation) and the isothermal TG curves are shown in Figure 7.2 and Figure 7.3, with Figure 7.3(a) showing the TG curves for both AT2 and AT3 and (b) showing only the TG curve for AT2. The total weight gain and rate constants are summarised in Table 7.2. The rates were calculated using equation 7.1.

$$\left(\frac{\Delta W}{A}\right)^2 = k_p t \tag{7.1}$$

Both Figure 7.2 and Figure 7.3 show that the worse oxidation behavior was exhibited by alloy AT3 with the lower Al content. Figure 7.2 shows that after the TG experiment AT2 exhibited an adherent oxide scale, whist AT3 exhibited catastrophic pesting in half of the ingot sample, whereas the other half remained in the same cuboidal shape as that prior to oxidation. Both alloys exhibited parabolic type

behavior with AT3 exhibiting a much higher overall weight gain per unit area, 25.6 mg/cm^2 compared with AT2 with 1.2 mg/cm^2. Alloy AT2 exhibited breakaway oxidation and self-healing of the oxide scale, similar to that seen in AT1, just not to the same degree.

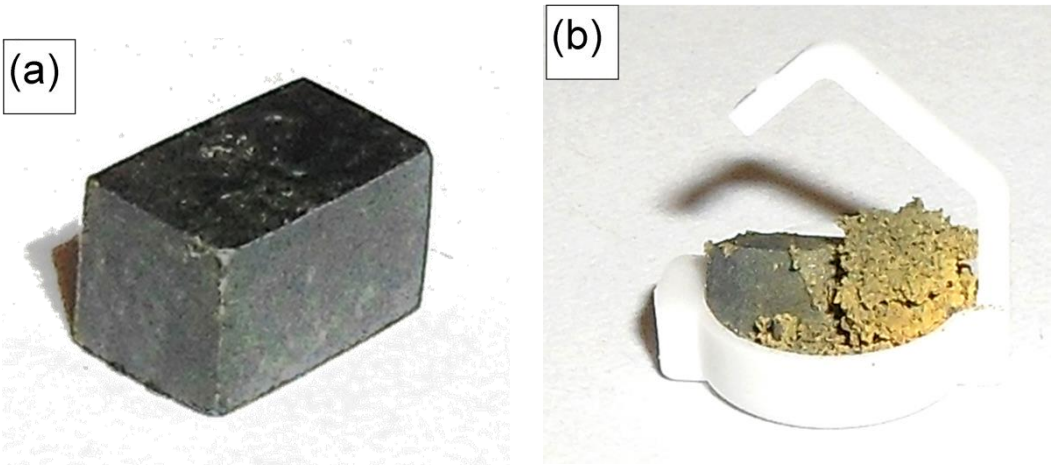

Figure 7.2 Samples after each TGA experiment (a) AT2 and (b) AT3 oxidised at 800 ^{o}C for 100 h. Alloy AT3 exhibited pesting and parts of the sample became a powder.

Table 7.2 Summary of rate constants, overall weight gain and volume fraction of Nb_{ss} for alloys AT2 and AT3 oxidised at 800 ^{o}C for 100 h.

Alloy	K_p (g^2 cm^{-4} s^{-1})	$\Delta W/A$(mg cm^{-2})	V_f Nb_{ss}
AT2	5 x 10^{-12}	1.2	44
AT3	2 x 10^{-9}	25.6	49

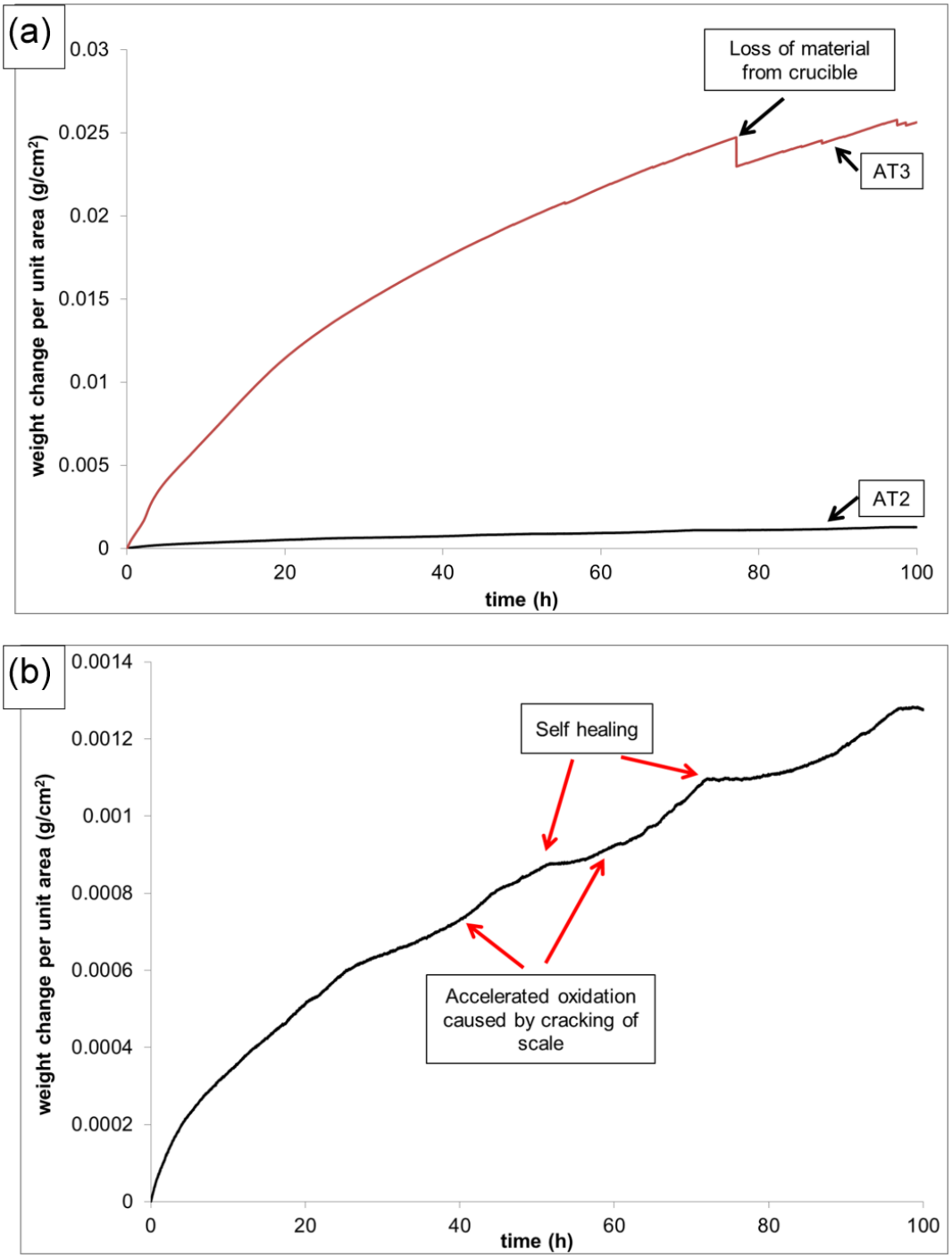

Figure 7.3 Weight change per unit area curves showing (a) AT2 and AT3 oxidised at 800 ^{o}C for 100 h, (b) AT2 oxidised at 800 ^{o}C.

7.2.3 Nb-24Ti-18Si-2Cr-5Al-3Ge-1Y (AT2)

As Figure 7.2(a) shows, the oxide scale formed on AT2 after the oxidation study was adherent to the substrate material and removing the scale to perform powder XRD was impractical. Figure 7.5 shows the glancing angle XRD data ($\gamma = 1^o$, 2.5^o, 5^o and 10^o). The XRD data shows the presence of Nb_2O_5, TiO_2, $Ti_2Nb_{10}O_{29}$, SiO_2 and GeO_2.

Figure 7.4 shows several images of the specimen after oxidation at 800 ^oC for 100 h. Figure 7.4(a) shows an SEI topographical image of the oxide scale, (b) shows a BSE image of the cross section of the oxidised specimen and (c) shows presence of oxide precipitates within the Nb_{ss} phase. The topographical features are different to those reported for alloy AT1 (Chapter 5). The oxide surface of AT2 does not possess the 'whisker like' features reported for AT1. There is cracking of the oxide scale, more so than that reported for alloy AT1, which accounts for the intermittent accelerated weight gain shown in Figure 7.3. The cracking is mainly located where the Nb_{ss}/βNb_5Si_3 interface is caused by the different oxidation rates and growth rates of oxide scale produced on each phase. The TG curve also shows a self-healing effect of the oxide scale.

Figure 7.4(b) shows a cross sectional image of alloy AT2 after oxidation. The oxide scale is thin and is difficult to see on the image. There is a diffusion zone which can be separated due to the differing contrast of the Nb_{ss} phase. This diffusion zone is ~35 µm thick, as shown in the electron image and confirmed by the EPMA line scans in Figure 7.6. The βNb_5Si_3 exhibited cracking parallel to the surface of the specimen within the diffusion zone. Figure 7.4(c) shows oxide precipitation within the Nb_{ss} phase at the extent of the diffusion zone, which was seen in alloy AT1 (Chapter 5) and within the literature (Menon et al., 2004).

Table 7.3 shows chemical analysis of the Nb_{ss} phase within the diffusion zone of the oxidised sample. The data reveals a high level of oxygen present within the Nb_{ss} phase (36.2 at.%). According the Nb-O binary phase diagram, the

maximum solid solubility of oxygen in Nb at 800 °C is ~2 at.%, the value of 36 at.% would indicate a mixture of Nb_{ss} and NbO within the diffusion zone. The data also shows that the level of all elements present in the Nb_{ss} have decreased, suggesting that all elements are being used to form the oxide scale, or the oxide precipitates show in Figure 7.4. Elemental x-ray maps shown in Figure 7.7 show no large scale movement of elements from the substrate to the substrate/scale interface at this temperature.

Table 7.3 Chemical analysis (EPMA/WDS, at.%) of the Nb_{ss} phase in the as cast condition (prior to oxidation) and after oxidation at 800 °C for 100 h.

AT2	Nb	Ti	Si	Cr	Al	Ge	Y	O
As cast	58.0-52.4	32.6-27.5	5.2-2.5	3.3-2.0	8.0-6.9	1.3-0.7	1.2-0.0	-
	55.1±3.4	29.9±2.6	3.2±0.7	2.7±0.2	7.4±0.1	1.0±0.1	0.7±0.1	-
800 °C	40.4-33.0	21.1-17.2	3.1-1.3	3.1-1.7	5.0-4.2	0.5-0.2	0.2-0.1	39.3-34.3
for 100 h	35.5±2.4	19.4±0.3	1.6±0.1	2.3±0.1	4.6±0.1	0.3±0.1	0.2±0.1	36.2±0.8

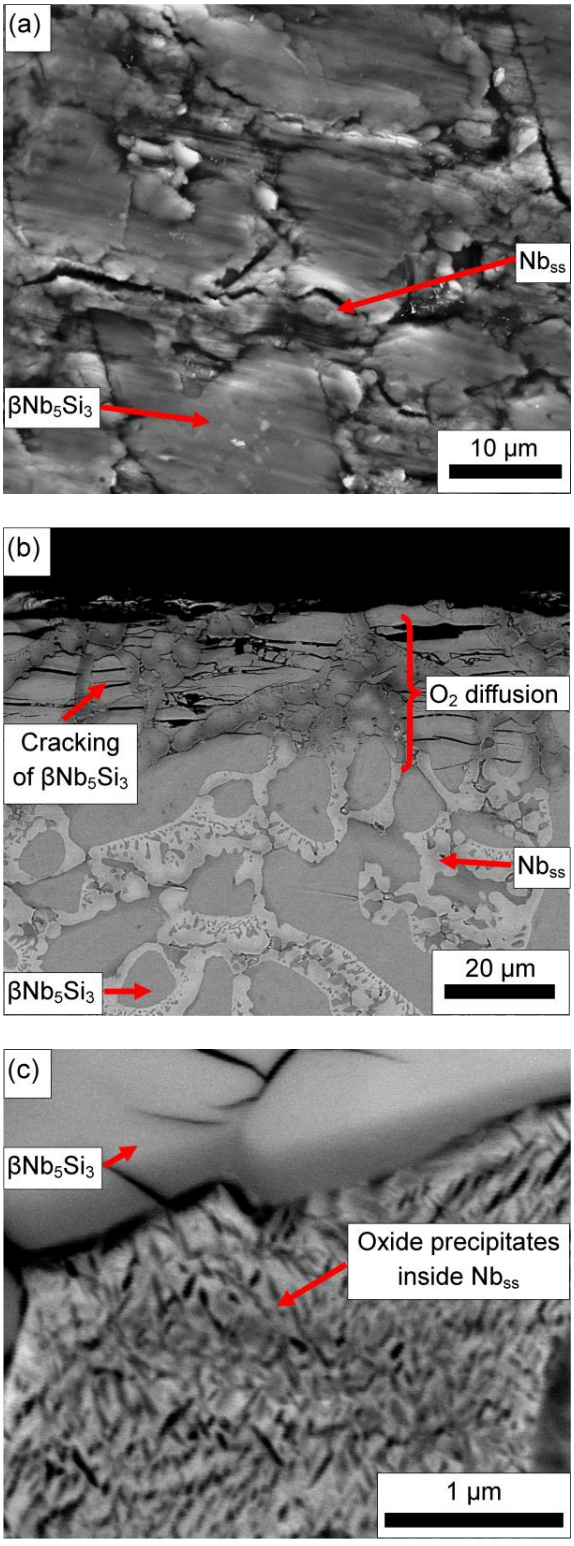

Figure 7.4 Electron images (taken in the FEI Inspect F microscope) of oxidised AT2 at 800 ^{o}C for 100 h showing (a) topographical features of the oxide scale, (b) BSE image of the cross section of the oxidised AT2 and (c) oxide precipitation within the Nb_{ss} phase.

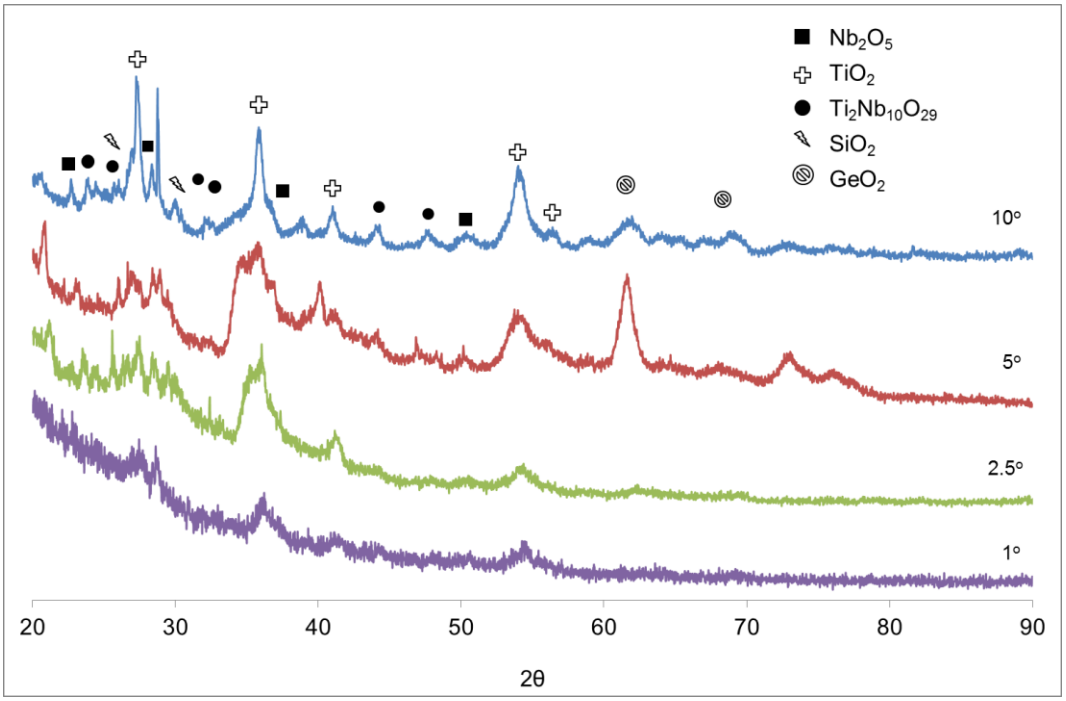

Figure 7.5 Glancing angle XRD patterns of the oxide scale produced on AT2 after oxidation at 800 °C for 100 h.

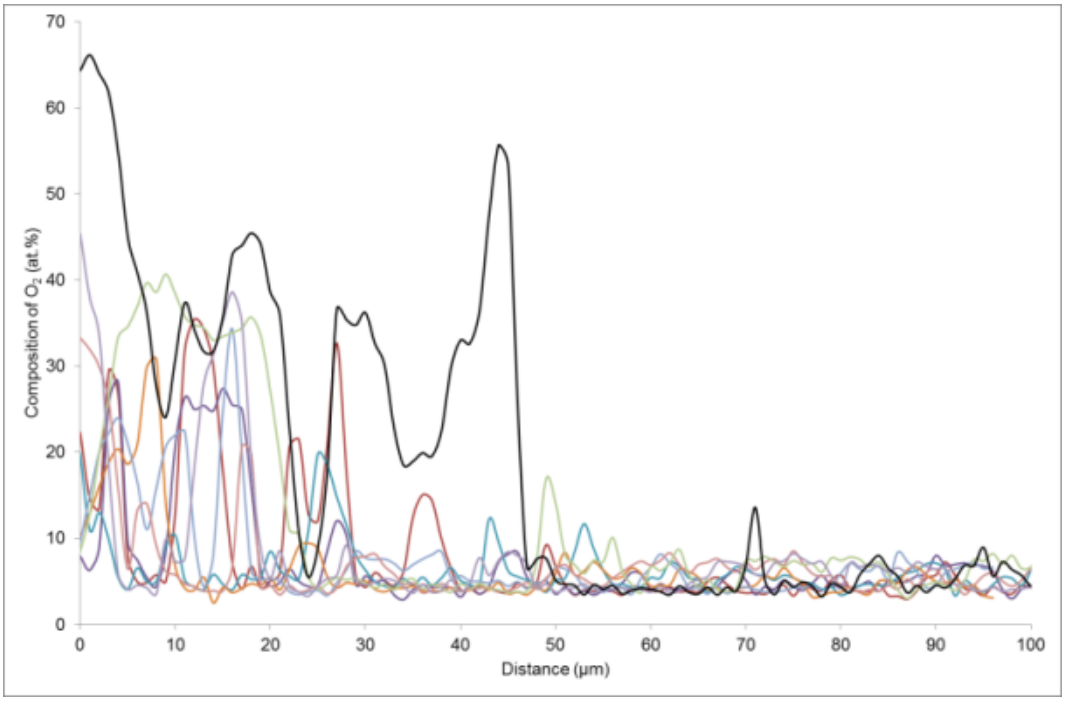

Figure 7.6 WDX line scans (10 in total) from the oxide/substrate interface into the bulk of AT2 oxidiesed at 800 °C for 100 h.

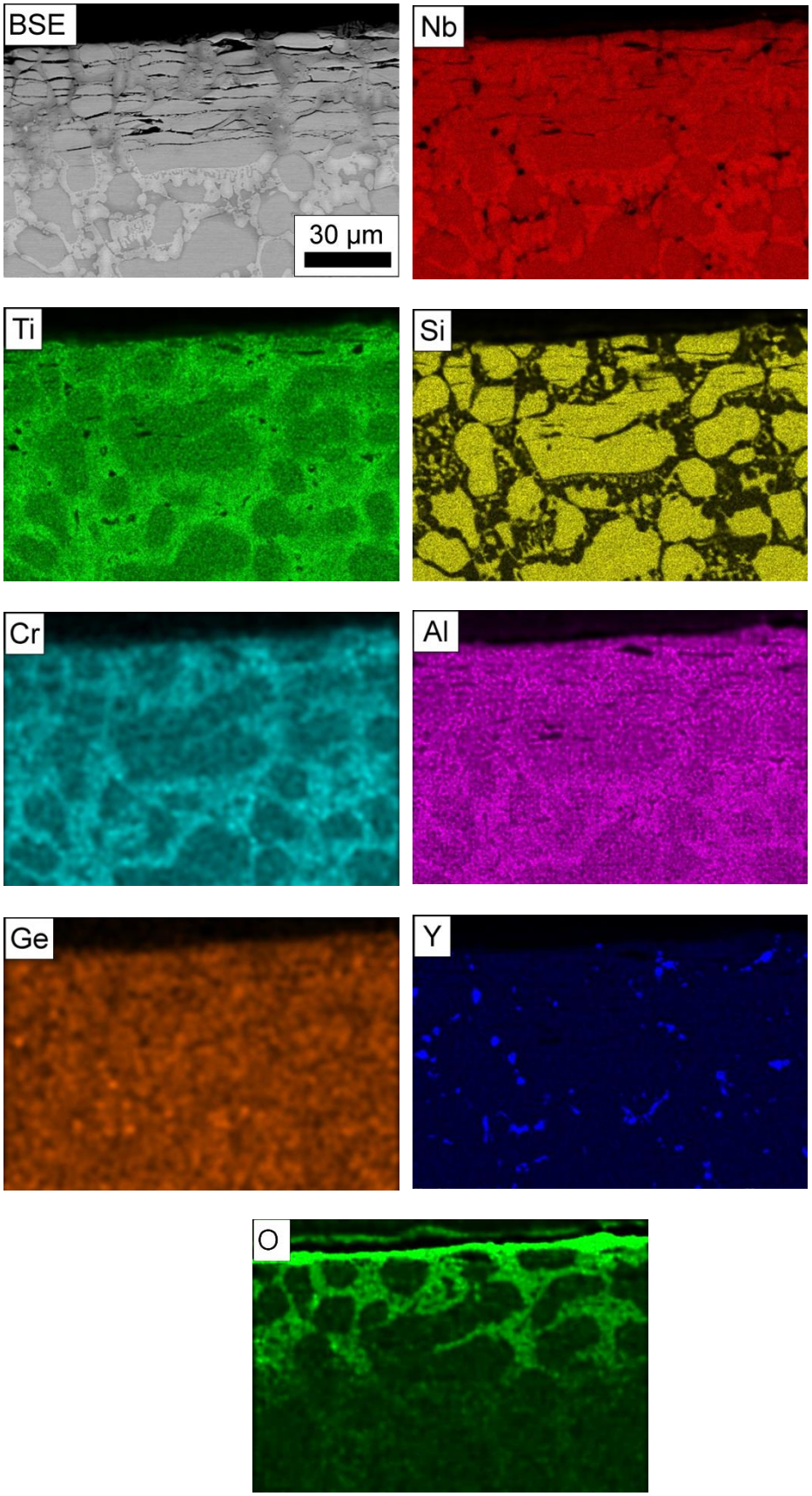

Figure 7.7 Elemental x-ray maps (collected on Phillips XL30 microscope) of AT2 oxidised at 800 ^{o}C for 100 h.

7.2.4 Nb-24Ti-18Si-2Cr-2Al-3Ge-1Y (AT3)

Figure 7.2(b) shows that about half of the specimen survived the oxidation process, whereas the other half did not and suffered catastrophic pesting behavior. This allowed for powder XRD to be conducted on the oxide scale, the results of which are shown in Figure 7.9. The diffractogram reveals that there are two forms of Nb_2O_5 present in the oxide scale. Both the orthorhombic and monoclinic forms are present along with TiO_2. Whilst it was expected, there were no characteristic peaks for the βNb_5Si_3 phase.

Figure 7.8(a) shows a topographical image of the oxide scale (taken from the half that did not suffer catastrophic pesting behavior) and shows severe cracking of the oxide scale which accounts for the higher weight gain compared with AT2 during oxidation. The cracking is not primarily located at the $Nb_{ss}/\beta Nb_5Si_3$ interface but is now observed all over the oxide surface. The oxide scale features are similar to the oxide scale produced on AT2 with the absence of 'whiskers' on the surface seen in AT1 (Chapter 7.5). Figure 7.8(b) shows a cross sectional image of the specimen after oxidation. The image shows a damaged oxide scale (~20 µm thick) and a diffusion zone (~50 µm thick), both distances contribute to the EPMA line scans in Figure 7.10 and an overall diffusion zone of ~70 µm. Similar to AT1 and AT2, there is cracking of the βNb_5Si_3 parallel to the surface and oxide precipitation within the Nb_{ss} at the extent of the diffusion zone (Figure 7.8(c)). Chemical analysis of the Nb_{ss} phase close to the oxide scale (Table 7.4) reveals similar results to alloy AT1 and AT2 after oxidation at 800 ^{o}C, although the levels of oxygen in the Nb_{ss} are lower than that observed in AT2. Figure 7.11 shows qualitative EDX x-ray maps which suggest that there is no large scale movement of any elements towards the substrate/oxide interface.

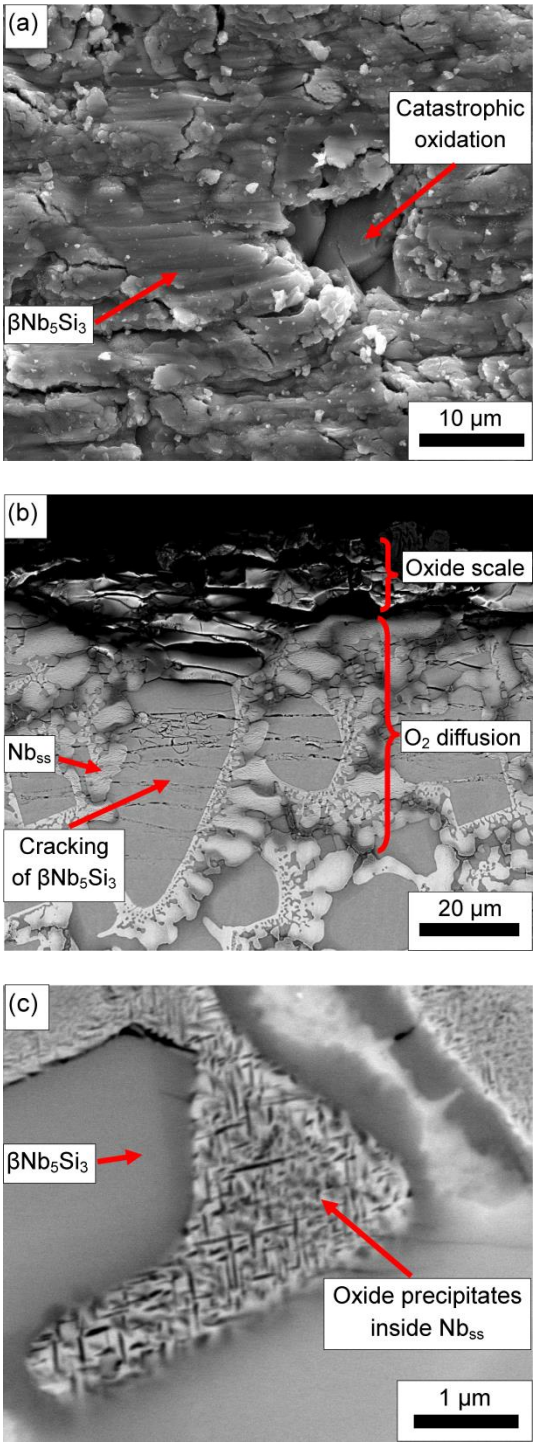

Figure 7.8 Electron images (taken in the FEI Inspect F microscope) of oxidised AT3 at 800 ^{o}C for 100 h showing (a) topographical features of the oxide scale, (b) BSE image of the cross section of the oxidised AT3 and (c) oxide precipitation within the Nb_{ss} phase.

Table 7.4 Chemical analysis (EPMA/WDS, at.%) of the Nb_{ss} phase both in the as cast condition (prior to oxidation) and after oxidation at 800 ^{o}C for 100 h.

AT3	Nb	Ti	Si	Cr	Al	Ge	Y	O
As cast	68.0-61.6	26.9-22.1	3.4-2.4	3.1-1.5	3.4-2.3	1.0-0.7	1.3-0.5	-
	65.5±5.6	24.4±3.4	3.0±0.1	2.4±0.3	3.0±0.1	0.9±0.1	1.0±0.1	-
800 ^{o}C for 100 h	49.0-45.7	17.0-15.7	1.6-1.4	2.1-1.5	1.8-1.4	0.5-0.4	0.3-0.2	32.1-29.0
	47.7±0.5	16.2±0.1	1.5±0.1	1.8±0.1	1.6±0.1	0.4±0.1	0.2±0.1	30.6±0.3

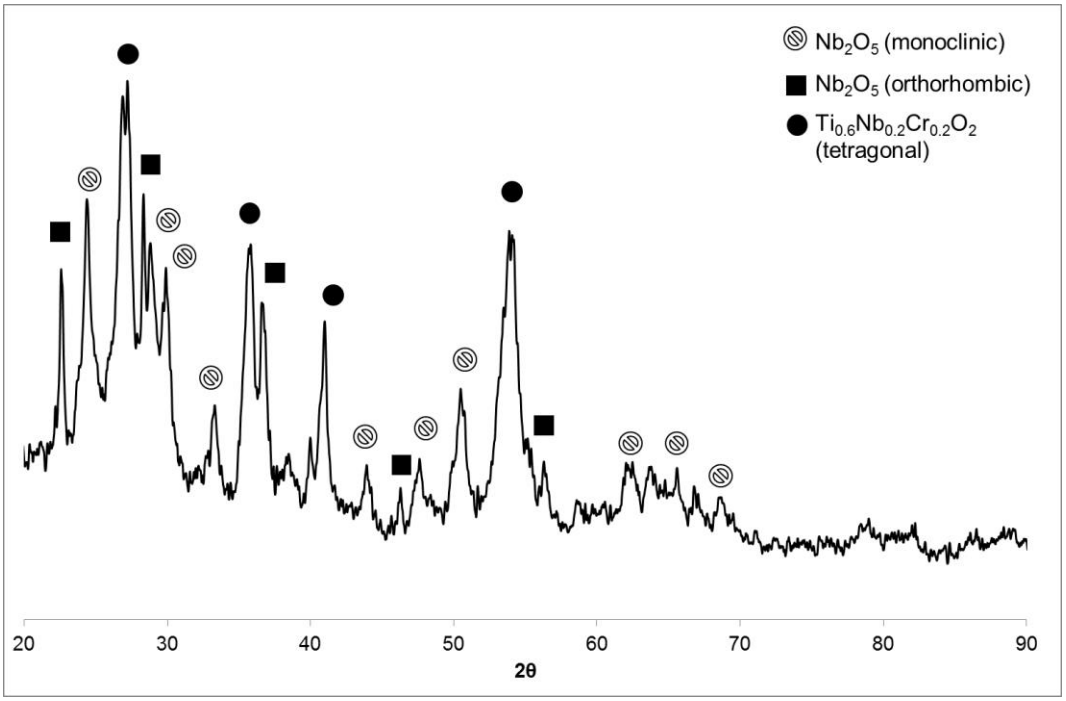

Figure 7.9 Powder XRD pattern for the oxide scale produced on AT3 after oxidation at 800 ^{o}C.

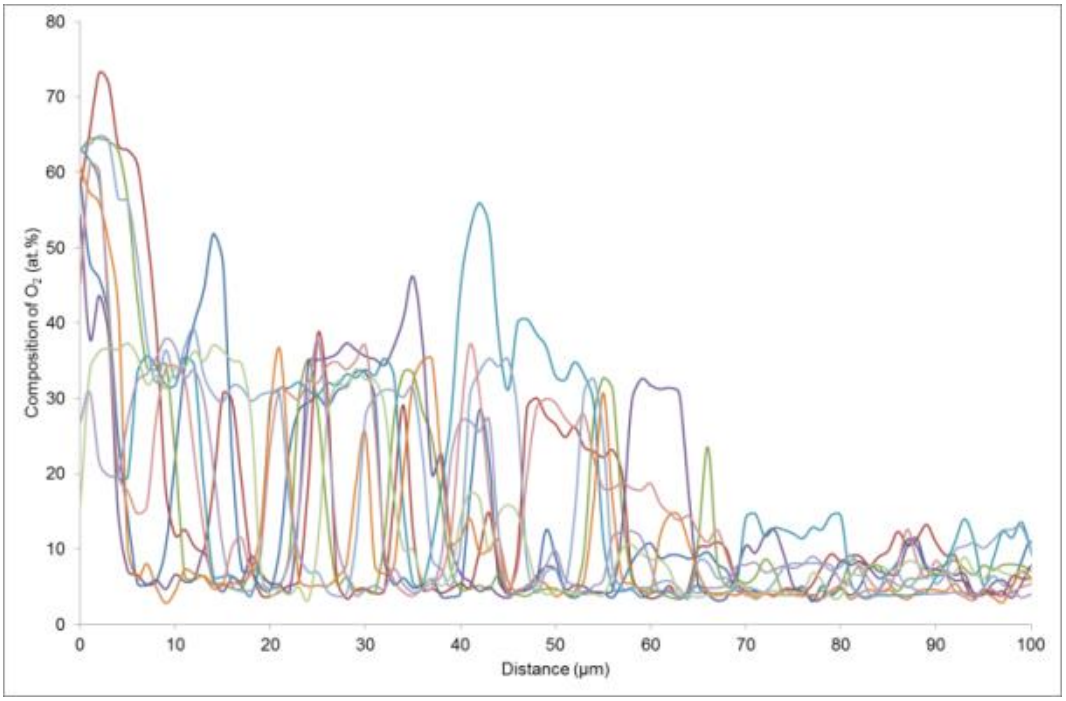

Figure 7.10 EPMA line scans from the oxide surface to the bulk of AT3 oxidised at 800 ^{o}C for 100 h.

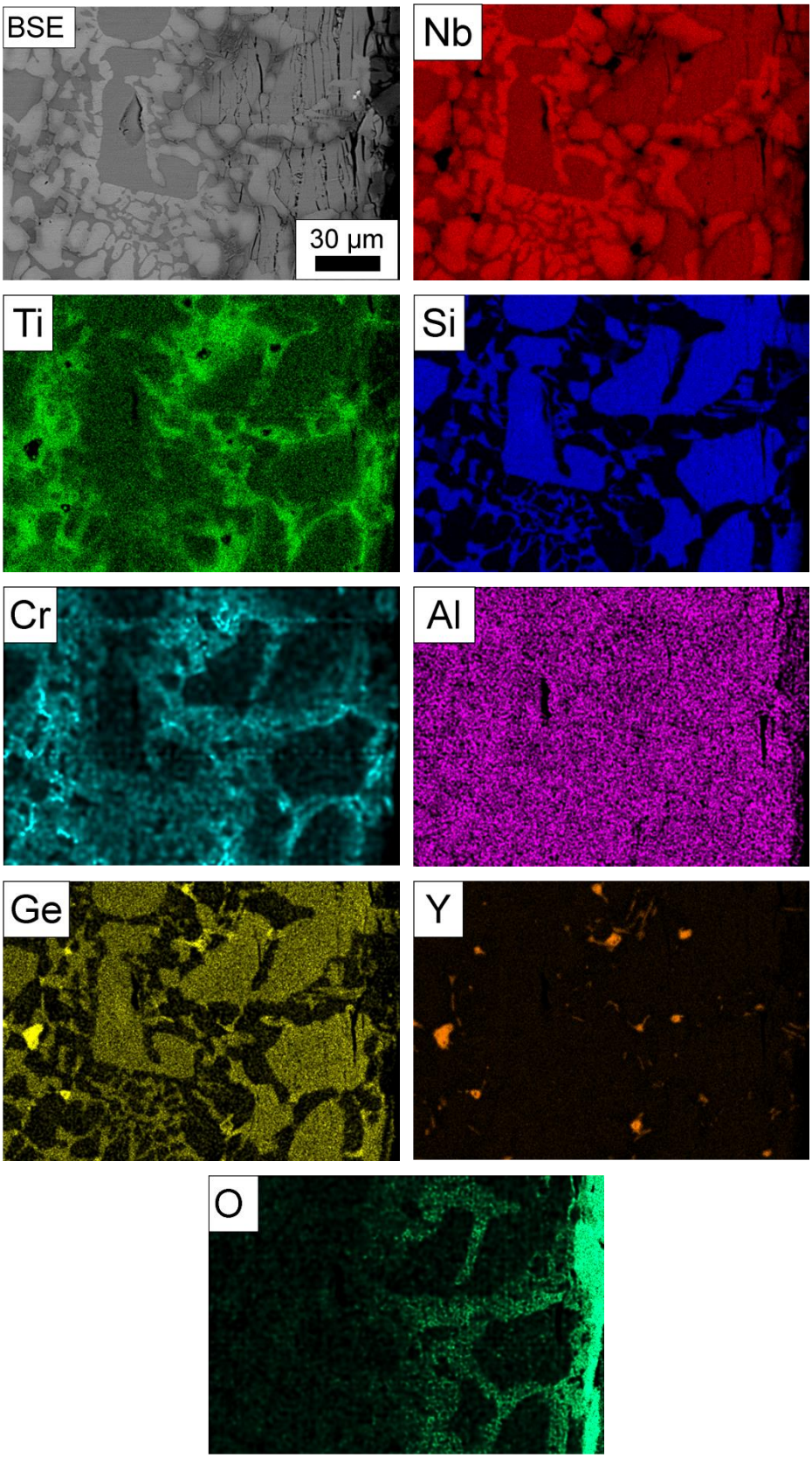

Figure 7.11 Elemental x-ray maps (collected on Phillips XL30 microscope) of AT3 oxidised at 800 ^{o}C for 100 h.

7.3 Discussion

7.3.1 Nb-24Ti-18Si-2Cr-5Al-3Ge-1Y (AT2)

Alloy AT2 did not exhibit any pesting behavior but instead possessed an adherent oxide layer formed from common oxides reported in the literature and also those reported for alloy AT1 in Chapter 5 of this thesis. The data shows that lowering both the Cr and Ge content of the alloy composition leads to a reduction in oxidation performance with a fivefold increase in the oxidation rate constant compared with alloy AT1 (5×10^{-12} and 1×10^{-12} g^2 cm^{-4} s^{-1} respectively), and a two fold increase in the overall weight gain from 0.6 mg cm^{-2} to 1.27 mg cm^{-2} for AT1 and AT2 respectively. This data suggests that whilst Cr and Ge additions are important for oxidation resistance at these temperatures, it may be possible to keep the levels of these alloying elements low enough, so the fracture toughness or melting temperature is not compromised, but still maintain a good level of oxidation resistance. The reduction in oxidation performance is also attributed to the increased volume fraction of the Nb_{ss} phase present in the microstructure, and the volume of eutectic. An increased fraction of grain boundary area will allow more pathways for the oxygen to diffuse down and into the substrate material. This is confirmed by the increase in the average diffusion depth of oxygen shown by the EPMA line scan data. Chromium and Ge additions, therefore, inhibit the diffusion of oxygen into the bulk material providing beneficial effects at 800 ^{o}C.

This work highlights something that is potentially beneficial to the oxidation resistance of these alloys. It was reported in Chapter 5 that the addition of Y inhibited the formation of Cr-rich Laves phase in the as cast microstructures and that the oxidation performance of alloy AT1 (Nb-24Ti-18Si-5Cr-5Al-5Ge-1Y) was improved over alloy KZ5 (Nb-24Ti-18Si-5Cr-5Al) and ZF6 (Nb-24Ti-18Si-5Cr-5Al-5Ge). Zelenitsas and Tsakiropoulos (2006a) showed that at 800 ^{o}C the alloys that contained Cr-rich Laves phase in simpler Nb alloys performed worse during

oxidation. This work showed that reducing the Cr and Ge levels, reduced the oxidation performance and the literature informs that Cr partitions to the Nb_{ss} phase. All of this evidence and data suggest that Cr is beneficial for oxidation resistance at 800 ^{o}C of Nb-Si alloys as long as it does not lead to the formation of minor levels of Cr-rich Laves phase.

7.3.2 Nb-24Ti-18Si-2Cr-5Al-3Ge-1Y (AT3)

Alloy AT3 exhibited catastrophic pesting behavior for half of the sample and the other half remained intact during oxidation. The half of the sample that survived was the part of the sample that was originally in contact with the water cooled copper hearth during casting and solidification (see Chapter 6, Figure 6.6(d)) rather than the microstructure seen at the top or centre of the ingot (Chapter 6, Figure 6.6(a-c)). The microstructure present at the bottom of the ingot had a lower grain boundary area compared with the centre due to the reduction in eutectic morphology. It is proposed that the lower grain boundary area reduced the level of oxygen penetration into the substrate material and reduced the formation of internal oxide precipitates. Hence, there was less internal stress build up within the substrate leading to less cracking of the βNb_5Si_3 phase and less damage to the material. The higher grain boundary area and eutectic morphology at the centre and top of the ingot, coupled with an increase in the perimeter of the test piece at the corners, led to a higher level of cracking and damage to the substrate material, leading to catastrophic damage to the sample.

One thing that is certain is that Al is very beneficial for the oxidation resistance of Nb-Si alloys. Lowering the Al content lead to a twenty fold increase in weight gain from 1.27 to 25.63 mg/cm^2 and that was even with a loss of material from the crucible. The lower Al content also led to an increase in the parabolic rate constant of three orders of magnitude from 5 x 10^{-12} to 2 x 10^{-9} g^2 cm^{-4} s^{-1}, and according to the TG curve, there is no evidence of any self-healing effect during the

oxidation study. Therefore it is proposed that Al is very beneficial to allow a self-healing effect from the substrate material. Also, the Al content is vital to reduce the overall oxygen diffusion distance into the substrate material. Lowering the Al content led to a two fold increase in the oxygen diffusion distance from ~35 to ~70 µm. The beneficial nature of Al additions was also seen by Zelenitsas and Tsakiropoulos (2006a) with alloys KZ4 (Nb-24Ti-18Si-5Cr) and KZ7 (Nb-24Ti-18Si-5Al with a reduction in the overall weight gain from 83.7 mg/cm^2 to 20.1 mg/cm^2 after 85 h of oxidation.

7.4 Conclusions

- The oxidation behavior of alloys AT2 and AT3 at 800 ^{o}C has been studied and both alloys exhibited parabolic oxidation kinetics.
- The oxidation resistance of these alloys is controlled by the diffusion of oxygen into the Nb_{ss} phase rather than the βNb_5Si_3.
- The oxidation resistance was dramatically worsened by the reduction in Al content from 5 at.% to 2 at.%, confirming the beneficial effects of Al on the oxidation resistance of Nb silicides alloys at 800 ^{o}C.
- During oxidation, an internal diffusion zone was formed in both alloys and the lowering of the Al content led to an increase in the diffusion zone from 35 to 70 µm. Aluminium is therefore vital for reducing the diffusion rate of oxygen into the microstructure.
- The pesting of alloy AT3 is attributed to the increase in volume fraction of Nb_{ss} phase and an increase in the eutectic morphology at the centre and top of the ingot. The microstructure that is present at the bottom of the ingot survived the oxidation process due to a reduction in the eutectic morphology and a reduction in the grain boundary area.
- Cr is beneficial for oxidation resistance at 800 ^{o}C as long as there is no formation of minor levels of Cr-rich Laves phase.

Chapter 8

The effect of larger ingot manufacture on microstructure and oxidation resistance; the effect of Y reduction on the oxidation resistance; and the effect of Cr and Ge reduction on the oxidation resistance of Nb silicide alloys at 1200 ^{o}C

8.1 Introduction

So far, in this work, and in the majority of the work in the literature, these complex Nb silicide alloys have been made as small, prototype sized ingots (10 – 20 g). This chapter aims to make comparisons between the alloy AT2 (Nb-24Ti-18Si-2Cr-5Al-3Ge-1Y) produced as both a 10 g and 600 g ingot. This alloy was chosen as it was seen to have the best oxidation resistance of all alloys made for this research. Comparisons will be made on microstructure morphology, stability of phases and the oxidation behaviour at both 800 and 1200 ^{o}C for 100 h. Along with alloy AT2, a new alloy AT4 (Nb-24Ti-18Si-2Cr-5Al-3Ge-0.05Y) was made to 600 g to investigate the effect of Y reduction to the aforementioned properties. Literature work has shown that ppm levels of Y perform best for increasing scale adherence of Al_2O_3 scales grown on Ni alloys (Smialek, 2000a) and so the level was reduced to see if these benefits could be gained.

Within the literature, most of the oxidation work is conducted for 100 h, with very few pieces of work investigating shorter timescales. As has been reported in this work, the oxidation products for these alloys are complex and more detailed investigation is required to fully understand the oxidation behaviour. Shorter tests would allow for observations (if any) on preferential oxide formation early on in the oxidation process and any interaction of oxides during the process within the oxide scale or the substrate material. Therefore, this chapter will also discuss the results of intermediate oxidation tests of alloy AT2 (600 g) conducted for 1, 10, 20 and 50 h at 1200 ^{o}C as this is where the most catastrophic damage occurs.

8.2 Results

8.2.1 Microstructures

8.2.1.1 Nb-24Ti-18Si-2Cr-5Al-3Ge-1Y (AT2 - 10 g and 600 g)

The microstructure of alloy AT2 (10 g) has been previously discussed in Chapter 6 and so will not be discussed in detail in this chapter; however, some important information will be repeated. Figure 8.1 shows typical BSE images of the microstructure present at the centre of alloy AT2 (10 g and 600 g). Both microstructures contain the Nb_{ss} and βNb_5Si_3 phases with the former being a more continuous phase and the latter being highly faceted due a high entropy of fusion. In both ingots there is microsegregation of Ti however in the 600 g ingot, this is only present within the βNb_5Si_3 whereas in the 10 g ingot, microsegregation of Ti is visible in both the βNb_5Si_3 and the Nb_{ss} phase as seen by the darker areas of contrast within the phase. Table 8.1 shows the chemical analysis of the centre of the ingot and the individual phases present within AT2 (600 g). The analysis is comparable with the data collected for AT2 (10 g) apart from the Nb levels being slightly higher and the Ti being slightly lower in both large area and phase analysis. Chemical analysis data is only presented for the centre of the ingot as the samples for the oxidation studies were taken from the centre of the ingot and therefore, the top and bottom were not investigated.

Table 8.1 Chemical analysis of AT2 (600 g). The data was collected from the centre of the ingot as this is where the samples were taken for oxidation studies. The data presented contains the maximum and minimum values with the average and the standard deviations.

As cast	Nb (at.%)	Ti (at.%)	Si (at.%)	Cr (at.%)	Al (at.%)	Ge (at.%)	Y (at.%)
Bulk	49.3-47.6	24.3-21.7	20.7-15.3	2.2-1.4	4.8-3.8	3.2-2.4	2.2-1.7
	48.4±0.1	22.8±0.1	18.1±0.3	1.7±0.1	4.3±0.1	2.9±0.1	1.9±0.1
Nb_{ss}	62.1-56.5	29.4-25.2	3.5-2.3	4.0-3.1	6.4-5.3	1.4-1.1	1.4-1.1
	58.7±0.5	27.4±0.2	2.6±0.1	3.5±0.1	5.9±0.1	0.8±0.1	1.2±0.1
βNb_5Si_3	46.0-44.6	18.0-16.5	29.8-28.5	0.7-0.3	3.5-2.7	4.2-3.6	1.2-0.9
	45.5±0.2	17.0±0.2	29.1±0.1	0.4±0.1	3.1±0.1	3.9±0.1	1.0±0.1

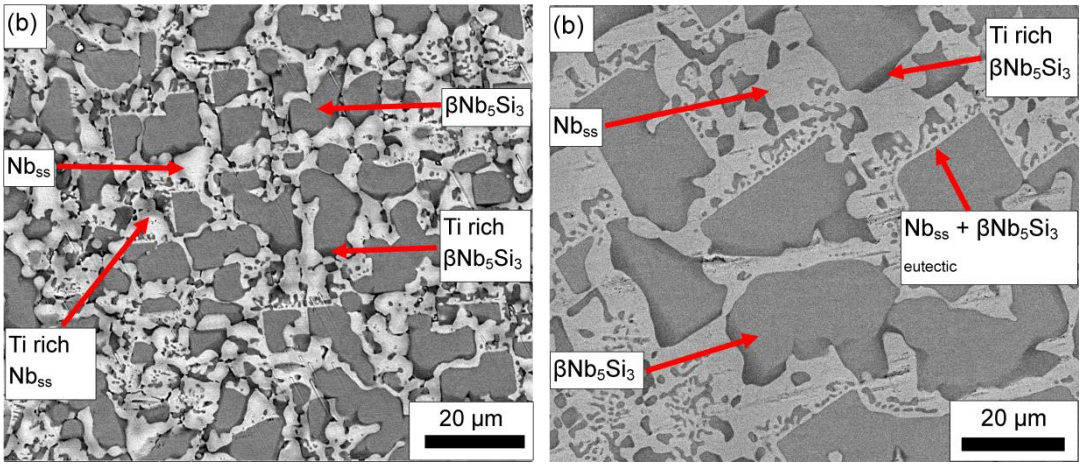

Figure 8.1 BSE images (taken in the FEI Inspect F microscope) of alloy AT2 in as cast condition. Image shows (a) AT2 made as 10 g ingot and (b) AT2 made as 600 g ingot.

8.2.2 Nb-24Ti-18Si-2Cr-5Al-3Ge-0.05Y (AT4 – 600 g)

8.2.2.1 As cast

This alloy was designed with a nominal composition of Nb-24Ti-18Si-2Cr-5Al-3Ge-0.05Y, however Table 8.2 puts the actual composition at 49.1Nb-23.8Ti-17.3Si-2.1Cr-4.7Al-3.0Ge-xY. The levels of Y are too low to be confidently

determined from EDX analysis. Figure 8.2(a-d) shows typical BSE images of the as cast microstructure present at the top, centre and bottom of the as cast ingot. The microstructure at the centre is considerably coarser than that present at the top or bottom and coarser compared with the microstructure present at the centre of the smaller 10 g cast ingots. This is due to the centre of a larger casting having a much slower cooling rate. The microstructure consists of large faceted βNb_5Si_3 grains surrounded by the Nb_{ss} phase. There is also an interdendritic eutectic morphology which is more apparent in the microstructure present at the top of the ingot. The large area EDX data shows large scale chemical inhomogeneity of Nb, Ti and Si with $C_{max} – C_{min}$ = 3.6, 3.9 and 7.7 at.% respectively. Generating alloys using arc melting has a disadvantage of creating large scale macrosegregation and production of a larger ingot will enhance this.

The phases present in the as cast microstructure are the Nb_{ss} (white phase in Figure 8.2) and the high temperature βNb_5Si_3 phase (grey phase in Figure 8.2) as suggested by Table 8.2 and the powder XRD pattern shown in Figure 8.4(a). Similar to the large 600 g casting of alloy AT2, there is only microsegregation of Ti present in the βNb_5Si_3 phase at the centre of the ingot causing the darker areas of contrast within the phase. There are darker regions of contrast within the Nb_{ss} phase present at the top and bottom of the ingot, which suggests microsegregation of Ti in these regions which are too small to analyse with confidence (<5 μm). Chemical analysis confirmed the microsegregation of Ti with an increase in the average Ti content of the βNb_5Si_3 from 16.7 to 23.3 at.%. This is coupled with an increase in the Cr content from 0.4 to 0.8 at.%, which has been reported by others in the literature (Zelenitsas and Tsakiropoulos, 2005). There is no evidence of the presence of Cr rich Laves phase in the microstructure.

8.2.2.2 Heat treated (1500 ^{o}C for 100 h)

The microstructure at the centre of the heat treated specimen is shown in Figure 8.3(a-c), the microstructure has coarsened, the areas of darker contrast within the βNb_5Si_3 phase have disappeared and any areas of eutectic have been eliminated. The XRD data (Figure 8.4(b)) shows the presence of the Nb_{ss} and the high temperature βNb_5Si_3 phase. It appears there has been no transformation from βNb_5Si_3 to αNb_5Si_3. Like other heat treated alloys, there has been some contamination of the microstructure by N and led to the formation of Ti_xN_y particles (black particles in Figure 8.3). There are also minor instances of the presence of Y_2O_3 particles within the heat treated microstructure.

The EDX data in Table 8.2 shows that chemical inhomogeneity of Nb, Ti and Si still exist with $C_{max} – C_{min}$ = 6.3, 3.6 and 8.2 at.%. Now, however, there is slight macrosegregation of Al with $C_{max} – C_{min}$ = 2.2 at.%. The EDX data collected for the heat treated specimen was taken from the phases present at the centre of the ingot.

Table 8.2 Chemical analysis of both as cast and heat treated (1500 ^{o}C for 100 h) AT4. The data presented contains the maximum and minimum values with the average and the standard deviations.

As cast	Nb (at.%)	Ti (at.%)	Si (at.%)	Cr (at.%)	Al (at.%)	Ge (at.%)
Top	51.2-48.6	26.1-23.0	18.7-12.7	2.6-1.9	5.3-4.6	3.3-2.2
	49.8±0.1	25.1±0.1	15.0±0.3	2.3±0.1	5.1±0.1	2.7±0.1
Bulk	50.5-47.6	24.4-22.3	19.9-15.9	2.3-1.7	4.9-4.5	3.5-2.5
	49.1±0.1	23.3±0.1	18.0±0.3	2.0±0.1	4.6±0.1	3.1±0.1
Bottom	49.3-47.9	24.0-22.2	20.4-17.9	2.4-1.7	4.9-4.1	3.8-2.6
	48.4±0.1	23.0±0.1	19.0±0.1	1.9±0.1	4.5±0.1	3.3±0.1
Nb_{ss}	57.0-54.7	31.6-29.9	2.2-1.9	4.3-3.9	6.8-6.4	1.0-0.6
	56.0±0.1	30.5±0.1	2.0±0.1	4.1±0.1	6.6±0.1	0.8±0.1
βNb_5Si_3	46.5-45.6	17.0-16.4	30.4-29,8	0.6-0.3	3.2-2.5	4.5-3.8
	45.9±0.1	16.7±0.1	30.0±0.1	0.4±0.1	2.8±0.1	4.1±0.1
Ti rich βNb_5Si_3	43.0-36.1	26.5-20.0	28.4-27.2	1.0-0.5	4.1-3.3	5.4-4.5
	39.4±0.6	23.3±0.6	27.7±0.1	0.8±0.1	3.8±0.1	5.0±0.1
Heat treated *(1500 ^{o}C for 100 h*						
Top	49.9-46.2	24.9-21.3	22.7-18.3	2.1-1.5	5.1-3.8	3.8-3.1
	47.6±0.4	22.4±0.5	20.6±0.9	1.7±0.1	4.3±0.1	3.4±0.1
Bulk	52.5-47.5	24.1-22.0	21.5-14.5	2.1-1.4	4.9-4.2	3.5-2.3
	49.6±0.5	23.1±0.1	18.1±1.0	1.8±0.1	4.5±0.1	2.9±0.1
Bottom	52.1-48.4	24.6-22.7	20.7-16.5	2.0-1.5	3.6-2.9	3.9-3.0
	49.9±0.4	23.1±0.1	18.6±0.7	1.9±0.1	3.1±0.1	3.4±0.1
Nb_{ss}	63.9-61.1	27.3-24.3	2.0-1.1	3.6-3.0	6.3-5.7	0.8-0.3
	62.3±0.1	26.2±0.1	1.5±0.1	3.4±0.1	6.0±0.1	0.6±0.1
βNb_5Si_3	46.4-41.8	21.0-17.5	29.6-27.0	1.1-0.8	4.0-3.2	4.5-3.5
	43.7±0.2	19.2±0.1	28.5±0.1	0.9±0.1	3.5±0.1	4.2±0.1

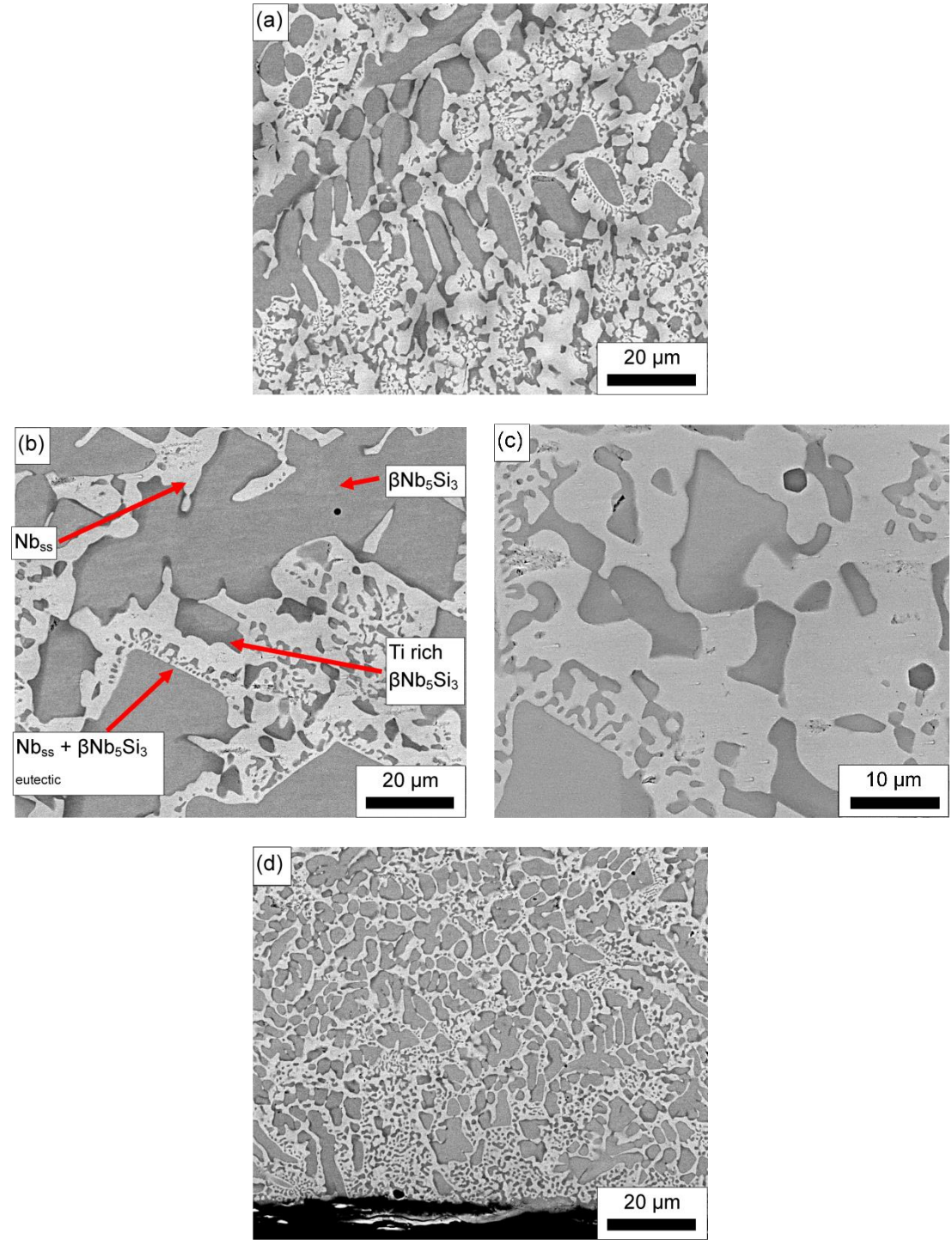

Figure 8.2 BSE images (taken in the FEI Inspect F microscope) of alloy AT4 in as cast condition. Images show microstructure present at (a) top, (b-c) centre and (d) bottom of ingot.

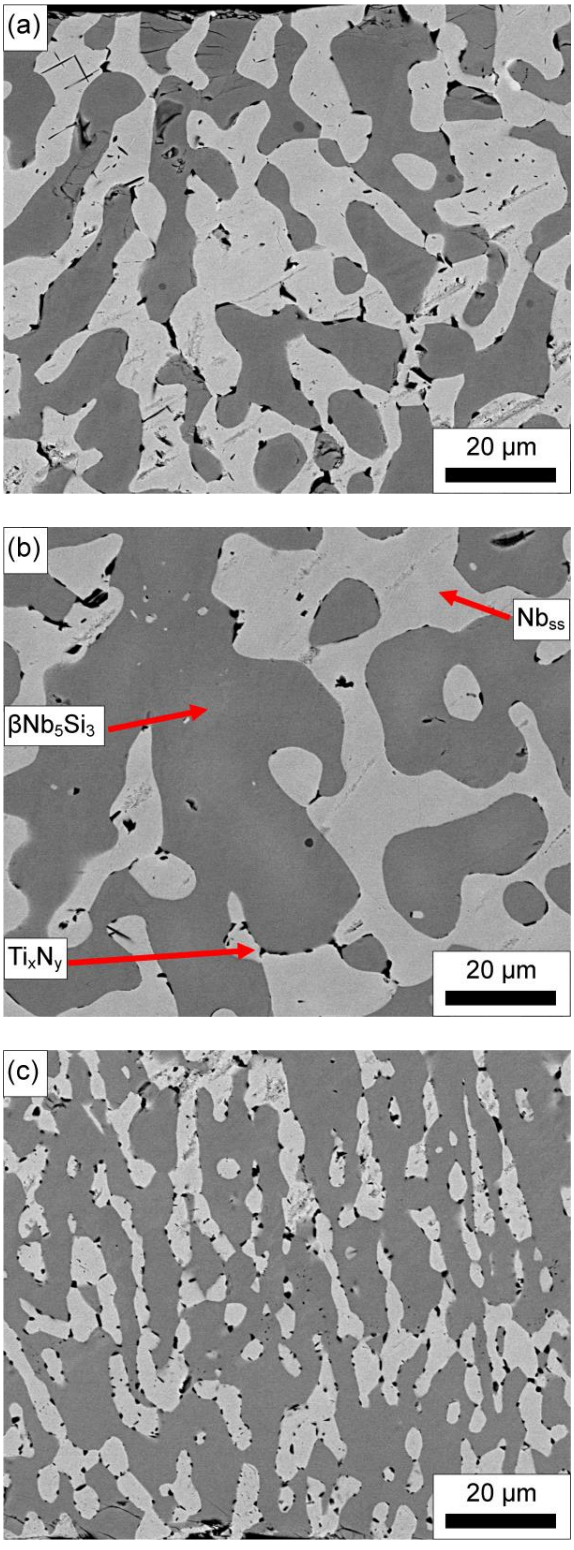

Figure 8.3 BSE images (taken in the FEI Inspect F microscope) of alloy AT4 in heat treated (1500 ^{o}C for 100 h) condition showing microstructure present at the (a) top, (b) centre and (c) bottom of the ingot.

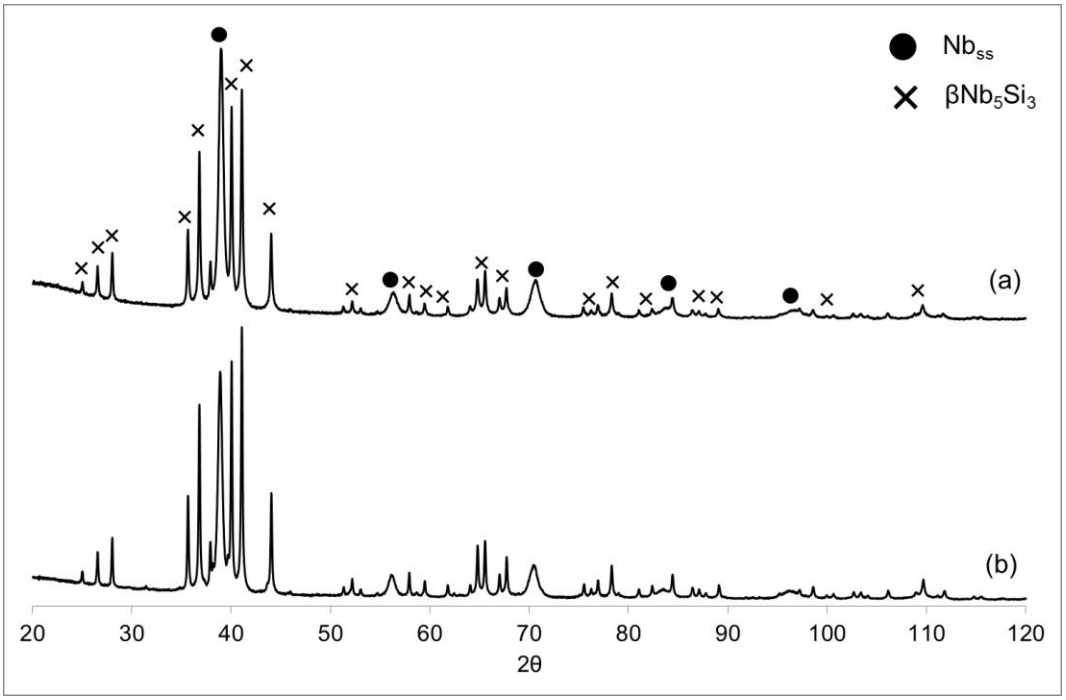

Figure 8.4 Powder XRD patterns of AT4 in (a) as cast condition and (b) heat treated (1500 ^{o}C for 100 h) condition.

8.2.3 Oxidation behaviour

8.2.3.1 Isothermal Oxidation Kinetics

The rate constants and overall weight gain during oxidation of each alloy at both 800 and 1200 ^{o}C are summarised in Table 8.3 including the values reported in the previous chapter for alloy AT2 oxidised at 800 ^{o}C for 100 h. The rates were calculated using the same equations that were reported in Chapters 5 and 6.

Table 8.3 Summary of rate constants and weight gain during oxidation of each alloy at 800 and 1200 ^{o}C for 100 h. Also included is the volume fraction of Nb_{ss} phase present within the microstructure of each alloy.

	800 ^{o}C		1200 ^{o}C			V_f Nb_{ss}
	K_p (g^2 cm^{-4} s^{-1})	ΔW (mg cm^{-2})	K_p (g^2 cm^{-4} s^{-1})	K_l (g cm^{-2} s^{-1})	ΔW (mg cm^{-2})	
AT2 (10 g)	5×10^{-12}	1.27	1×10^{-11} (< 17 h)	8×10^{-9}	3.3	
AT2 (600 g)	5×10^{-11} (< 42 h)	10.05	4×10^{-9} (< 14 h)	1×10^{-7}	58	44
AT4 (600 g)	6×10^{-11} (< 14 h)	20.07	3×10^{-9} (< 14 h)	1×10^{-7}	56	

8.2.3.2 Oxidation at 800 ^{o}C for 100 h

Figure 8.5 shows the specimens AT2 (10 g), AT2 (600 g) and AT4 (600 g) after isothermal oxidation at 800 ^{o}C for 100 h. The images show that AT2 (10 g) did not exhibit pesting behaviour but possessed an adherent oxide scale whereas AT2 (600 g) and AT4 (600 g) exhibited slight pesting behaviour. Not only that but the oxide scales produced on both AT2 (10 g) and AT2/AT4 (600 g) were a different colour, suggesting a change in the oxidation behaviour to some degree.

Figure 8.6 shows the isothermal TG curves for all three samples and shows that whilst the curve for the AT2 (10 g) alloy shows a parabolic behaviour for the full 100 h test with a rate constant of 5 x 10^{-12} g^2 cm^{-4} s^{-1}, the alloys made as 600 g ingots show a transition from an initial parabolic behaviour to an accelerated linear oxidation behaviour after a period of time, indicating a complete breakdown of the protective oxide scale. Table 8.3 shows that this initial parabolic behaviour was present for much longer for the AT2 than for AT4 lasting 42 and 14 h respectively. Also, the overall weight gain during the oxidation test was much higher for the 600 g ingots than the 10 g ingot and a reduction in the Y content from AT2 (600 g) to AT4 (600 g) leads to a 100 % increase in the overall weight gain as well from 10.05 to 20.07 mg/cm^2 respectively.

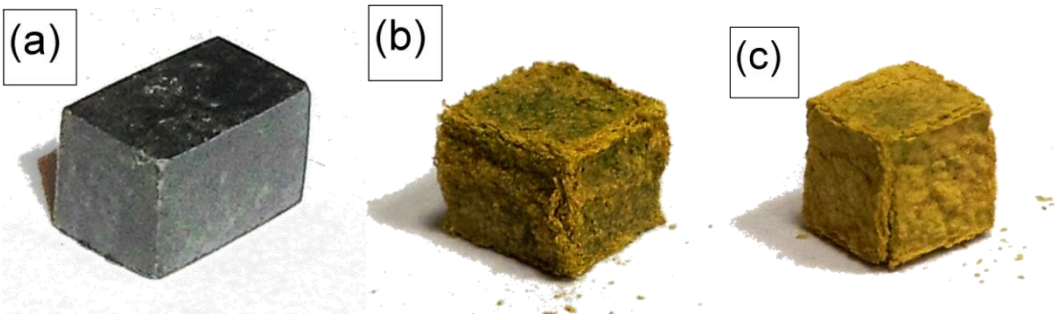

Figure 8.5 Images of samples after oxidation at 800 ^{o}C for 100 h. Images show (a) AT2 (10 g), (b) AT2 (600 g) and (c) AT4.

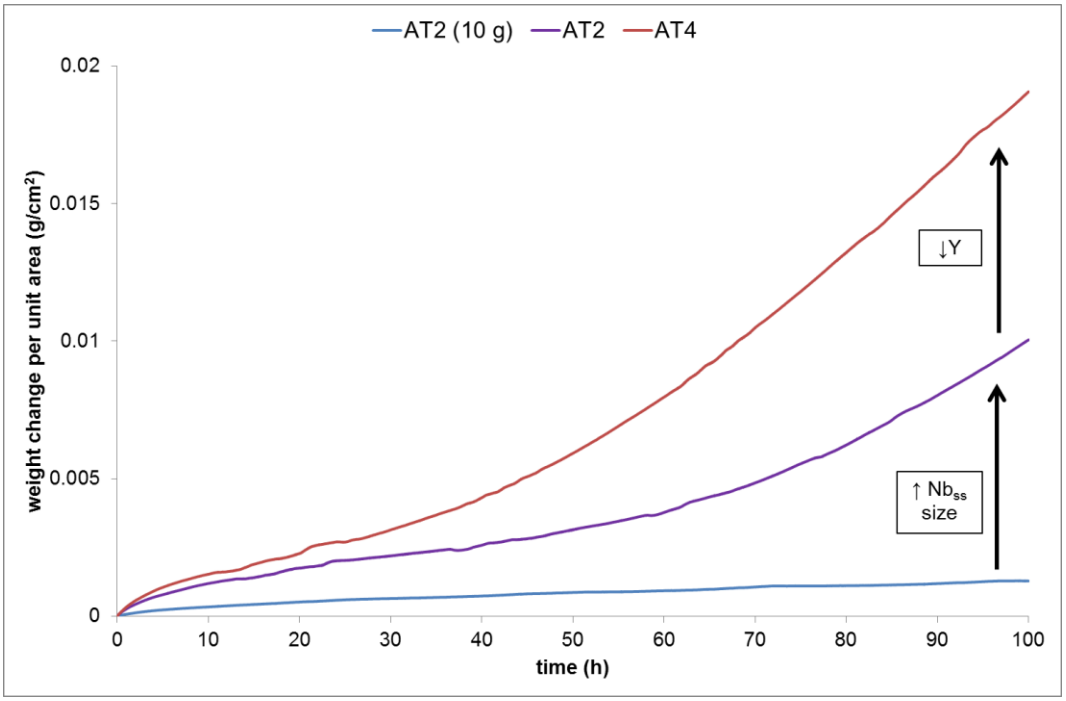

Figure 8.6 TG curves of alloys AT2 (made as 10 g and 600 g ingots) and AT4 oxidised at 800 ^{o}C for 100 h.

8.2.3.3 Oxidation at 1200 ^{o}C for 100 h

Figure 8.7 shows the specimens AT2 (10 g), AT2 (600 g) and AT4 after isothermal oxidation at 1200 ^{o}C for 100 h. The images show the oxide scales formed on AT2 (10 g) and AT2 (600 g) remained lightly adhered to the specimen during and after oxidation at 1200 ^{o}C, whilst the scale formed on AT4 was not adherent and had spalled off the substrate. The scale on all samples was not continuous as there were cracks at the edges and corners which undoubtedly contributed to the rapid, linear oxidation behaviour shown by the TG curves in Figure 8.8 and the data in Table 8.3. Table 8.3 shows that the 600 g ingots experienced an increase in the oxidation rate constant by two orders of magnitude from ~10^{-9} to ~10^{-7} g cm^{-2} s^{-1}. Also there was a dramatic increase in the overall weight gain/unit area from 3.3 mg cm^{-2} for alloy AT2 (10 g) to 58 and 56 mg cm^{-2} for AT2 and AT4 (600 g) ingots. The reduction in Y content had no significant effect on either the rate constant or the overall weight gain during oxidation.

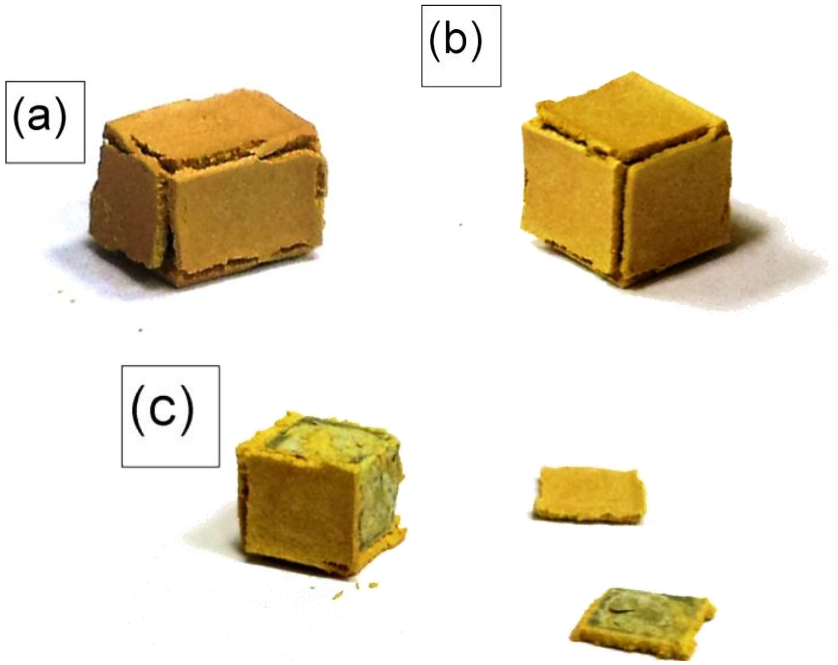

Figure 8.7 Images of samples (a) AT2 (10 g), (b) AT2 (600 g) and AT4 (600 g) after oxidation at 1200 ^{o}C for 100 h.

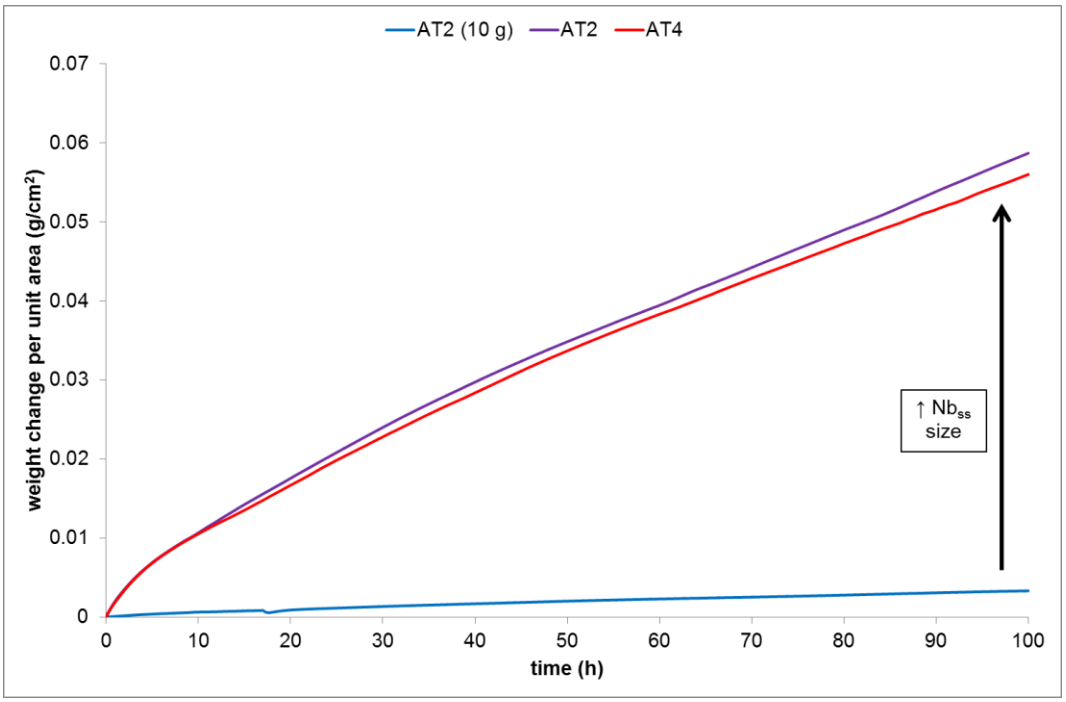

Figure 8.8 TG curves of alloys AT2 (made as 10 g and 600 g ingots) and AT4 oxidised at both (a) 800 ^{o}C and (b) 1200 ^{o}C for 100 h.

8.2.4 Microstructural observations of oxidation behaviour at 800 ^{o}C for 100 h

The oxidation behaviour of alloy AT2 (10 g) at 800 ^{o}C has been previously discussed in Chapter 7 and so will not be focused upon in this chapter, however, reference to the oxidation behaviour will be made in this chapter to make comparisons between the size of ingots made and the effects of microstructure on the oxidation behaviour.

8.2.4.1 Nb-24Ti-18Si-2Cr-5Al-3Ge-1Y (AT2 - 600 g)

Figure 8.9 shows (a) topographical features of the oxide scale, (b) cross sectional images of the substrate material and (c) oxide precipitation within the Nb_{ss} phase, as previously reported in Chapter 5 and 7 and in (Menon et al., 2004) . The topographical features observed are similar to those seen for alloy AT2 (10 g) also reported in Chapter 7. Firstly, there appears to be little oxidation damage to the βNb_5Si_3 phase as the Nb_{ss} is preferentially attacked at this temperature. Secondly, there is cracking of the scale at the $Nb_{ss}/\beta Nb_5Si_3$ interface and cracking of the oxide scale on the Nb_{ss} phase and thirdly, there is none of the 'whisker' like oxide formation as seen on alloy AT1 (Chapter 5). Cracking of the oxide scale is much more apparent with cracks going through both the oxide formed on the Nb_{ss} and the βNb_5Si_3 phase, which accounts for the lower oxidation resistance compared with AT2 (10 g) where the cracking was mainly located at the $Nb_{ss}/\beta Nb_5Si_3$ interface.

The cross sectional images (Figure 8.9(b) and (c)) again are similar to that reported for previous alloys at 800 ^{o}C. The ingress of oxidation is confined to the Nb_{ss} phase shown by the darker contrast of this phase at the substrate/scale interface creating a diffusion zone within the substrate. Due to the extensive damage of the substrate material, an exact value of the diffusion distance is difficult to achieve however the value is likely in the region of 30 – 50 µm. Also, there is cracking of the substrate parallel to the surface of the specimen. Unlike alloy AT2

(10 g) where cracking was mainly confined to the βNb_5Si_3 phase and cracks were arrested by the Nb_{ss} phase, in AT2 (600 g) cracking is no longer arrested by the Nb_{ss} phase close to the substrate/scale interface and cracking now proceeds through both phases. Cracking of the oxide scale and the substrate material below is undoubtedly the reason for the increased oxidation damage and overall weight gain of the alloy compared with AT2 (10 g). Figure 8.9(c) shows characteristic oxide precipitation within the Nb_{ss} during oxidation at 800 ^{o}C. This oxide precipitation is mainly TiO_2. This leads to strain hardening of the Nb_{ss} phase and the substrate material allowing crack propagation to be much easier.

As Figure 8.5 shows, the alloy exhibited partial pesting behaviour which allowed for part of the oxide scale to be removed and studied using powder XRD rather than glancing angle XRD. The data in Figure 8.11 shows the presence of Nb_2O_5, TiO_2, $Ti_2Nb_{10}O_{29}$ and $Nb_2O_5.GeO_2$. The first three were observed in the glancing angle patterns of the oxide scale produced on AT2 (10 g), the latter was not, however, SiO_2 and GeO_2 were. Since SiO_2 and GeO_2 can possess the same crystal structure, it can prove difficult to distinguish them in an XRD pattern. Also, powder XRD has eliminated most if not all possible texture and therefore signals from oxides that are present in glancing angle may not be present or may be completely overlapped in a powder XRD pattern.

8.2.4.2 Nb-24Ti-18Si-2Cr-5Al-3Ge-0.05Y (AT4)

Figure 8.10 shows similar images of alloy AT4 (600 g) oxidised at 800 ^{o}C for 100 h. The images show the topographical and cross sectional features of the oxide scale and the substrate material. The topographical features of the oxide scale are almost identical to that produced on AT2 (600 g). The βNb_5Si_3 phase is barely attacked during oxidation at 800 ^{o}C with most of the damage confined to the Nb_{ss} phase. There is extensive cracking of the oxide scale both at the $Nb_{ss}/\beta Nb_5Si_3$ interface and more large scale cracking through both parts of the oxide scale.

Again, there is no evidence of any ‘whisker’ type feature present on the oxide surface.

The cross sectional images (Figure 8.10(b) and (c)) show again that the oxygen ingress is mainly confined to the Nb_{ss} phase with a diffusion distance of ~30 – 50 μm and similarly cracking of the substrate material parallel to the surface of the oxidised specimen. Characteristically, there is precipitation of TiO_2 within the Nb_{ss} phase. Similar to AT2 (600 g), the oxide scale could be removed and studied using powder XRD to reveal the oxides present within the scale. The XRD pattern in Figure 8.11(b) is almost identical to the pattern for the oxide scale produced on AT2 (600 g) suggesting that the same oxides have formed.

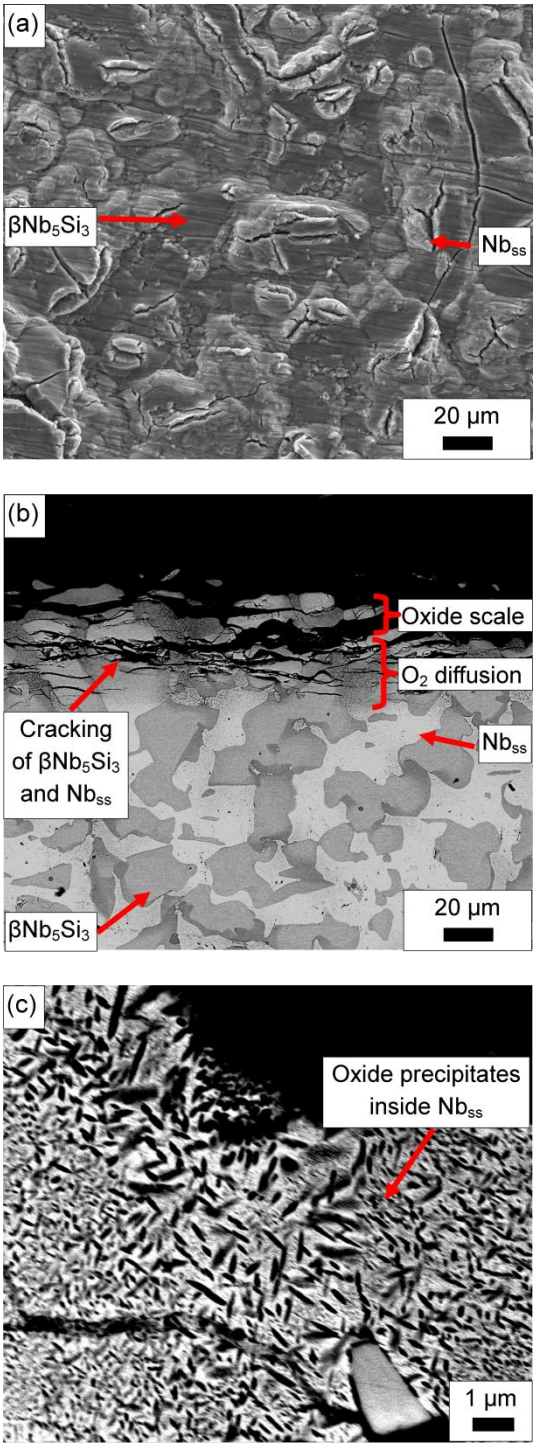

Figure 8.9 SEI and BSE images (taken in the FEI Inspect F microscope) of (a) topographical features and (b) cross section of alloy AT2 (600 g) oxidised at 800 ^{o}C for 100 h.

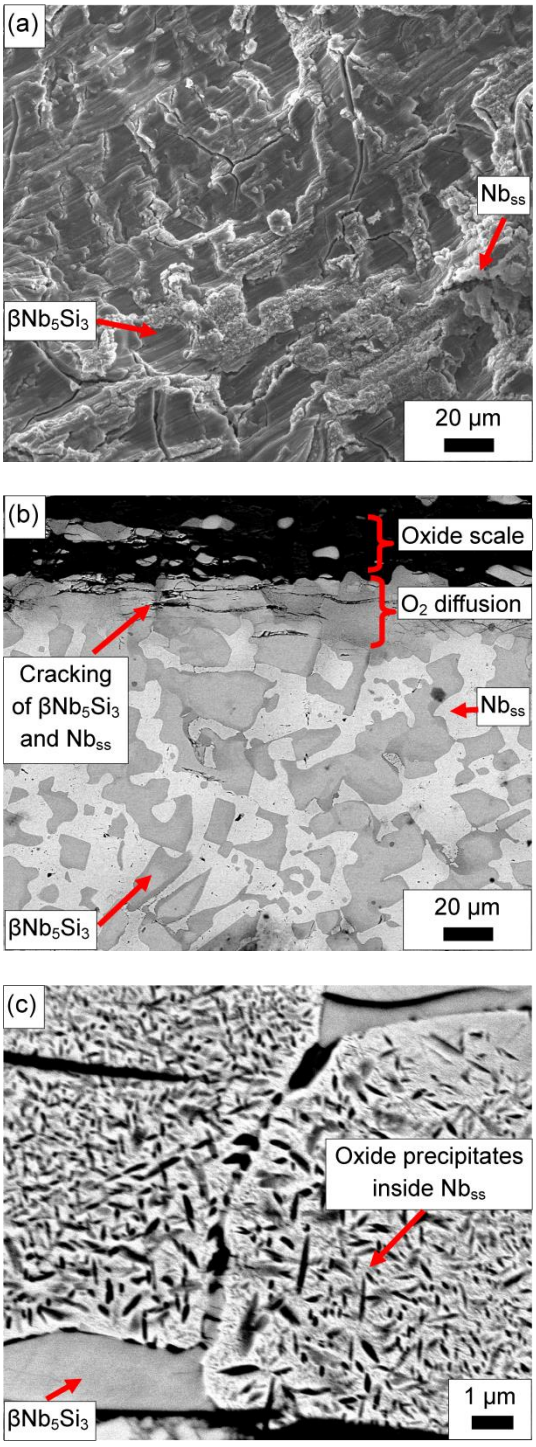

Figure 8.10 SEI and BSE images (taken in the FEI Inspect F microscope) of (a) topographical features and (b) cross section of alloy AT4 (600 g) oxidised at 800 ^{o}C for 100 h.

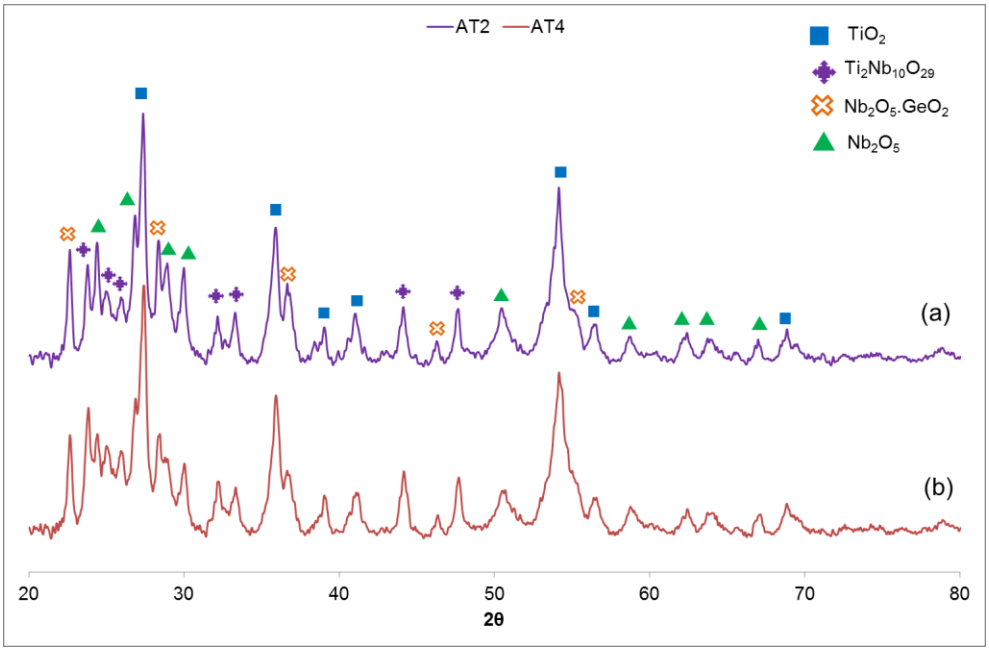

Figure 8.11 Powder XRD patterns of the oxide scale produced on (a) AT2 and (b) AT4 600 g ingots oxidised at 800 ^{o}C for 100 h.

8.2.5 Oxidation behaviour at 1200 ^{o}C for 100 h

8.2.5.1 Nb-24Ti-18Si-2Cr-5Al-3Ge-1Y (AT2 – 10 g)

Figure 8.12 shows the topographical features and cross sectional images of the oxide scale produced on AT2 (10 g) after isothermal oxidation at 1200 ^{o}C for 100 h. The features are very similar to those reported in Chapter 5 for the oxidation of alloy AT1 at 1200 ^{o}C for 100 h and similar to that reported by others in the literature (Geng et al., 2006c, Geng et al., 2007b). The topographical image (Figure 8.12(a)) shows once again that the Nb_{ss} phase is preferentially, but not exclusively, attacked during the oxidation process. The cross sectional images of the oxide scale reveal similar features and contrasts to those reported for alloy AT1. Even though no chemical analysis has been collected, it is reasonable to assume that similar oxides will form during the oxidation process compared with AT1, hence, the oxides present in the oxide scale are Nb_2O_5, Y_2O_3, $Ti_{0.6}Nb_{0.2}Cr_{0.2}O_2$, and SiO_2, which is confirmed by XRD (Figure 8.22) and corroborated by the TEM data presented in Chapter 5.

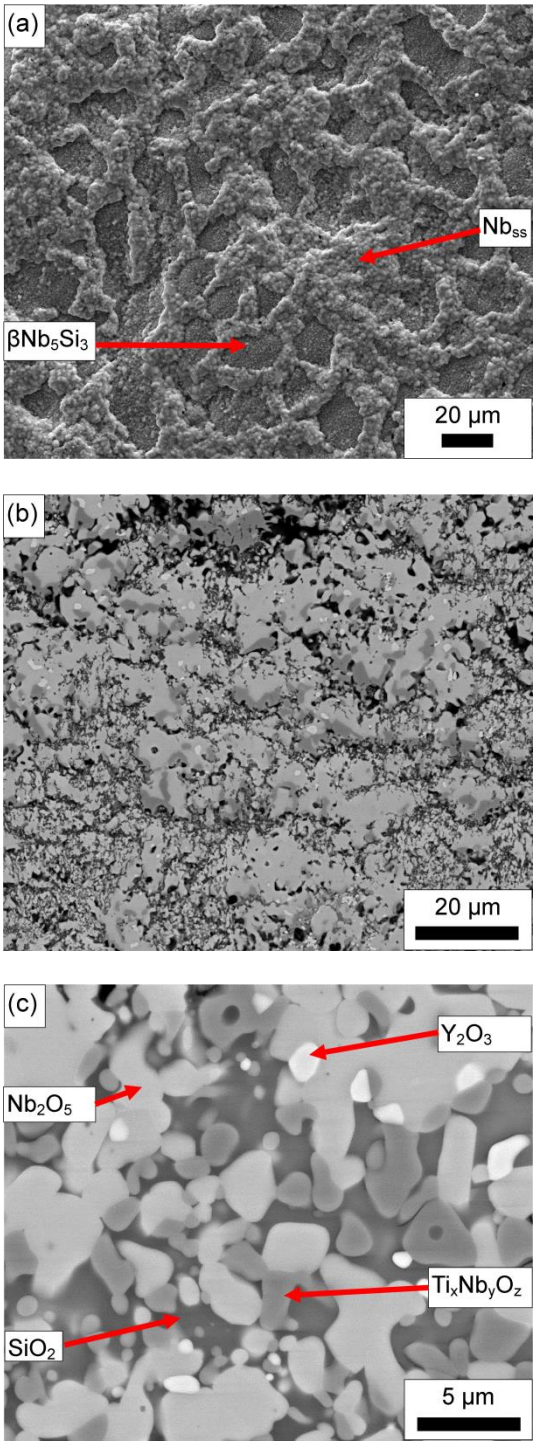

Figure 8.12 SEI and BSE images (taken in the FEI Inspect F microscope) of alloy AT2 (10 g) oxidised at 1200 ^{o}C for 100 h. Images show (a) SEI topographical features of the oxide scale, (b) low magnification BSE image of the oxide scale and (c) higher magnification BSE image of the oxide scale.

Figure 8.13 shows BSE cross sectional images of the substrate material at the substrate/oxide interface and images of the Nb_{ss} and βNb_5Si_3 phase after oxidation. Figure 8.13(a) shows substantial internal oxidation of the material mainly confined to the Nb_{ss} phase with less effect felt by the βNb_5Si_3 phase. Figure 8.13(b) shows a higher magnification BSE image of an area of Nb_{ss} and shows the formation of multiple oxides within the phase. The features are almost identical to those reported for alloy AT1 and qualitative x-ray maps (Figure 8.14 - Figure 8.17) show similar correlation of elements to specific features/oxides within the Nb_{ss} phase. Hence, the TEM data collected for AT1 is relevant to AT2 and therefore identification of the features/oxides can be achieved. The oxides formed within the Nb_{ss} include TiO_2, Al_2O_3 and a $Y_xAl_yO_z$ oxide. There are areas of Nb and Cr rich solid solution and residual Nb_{ss} and βNb_5Si_3 inside the oxides.

Figure 8.13(c) shows attack of the βNb_5Si_3 phase after oxidation and what is shown is similar to that reported for AT1. There is an inward attack of the silicide phase from the oxidation process and a similar effect has been reported by Mathieu et al., (2012). From the work presented in Chapter 5, the area of attack is comprised of Nb_5Ge_3, SiO_2 and $Ti_xNb_yO_z$. Again there is internal attack of the βNb_5Si_3 phase with dark spots intersecting a pathway of lighter contrast. These dark spots are identified as TiO_2 and the pathway of lighter contrast is a Ti depleted zone around a sub-grain boundary resulting from the recovery process within the silicide phase during the oxidation process.

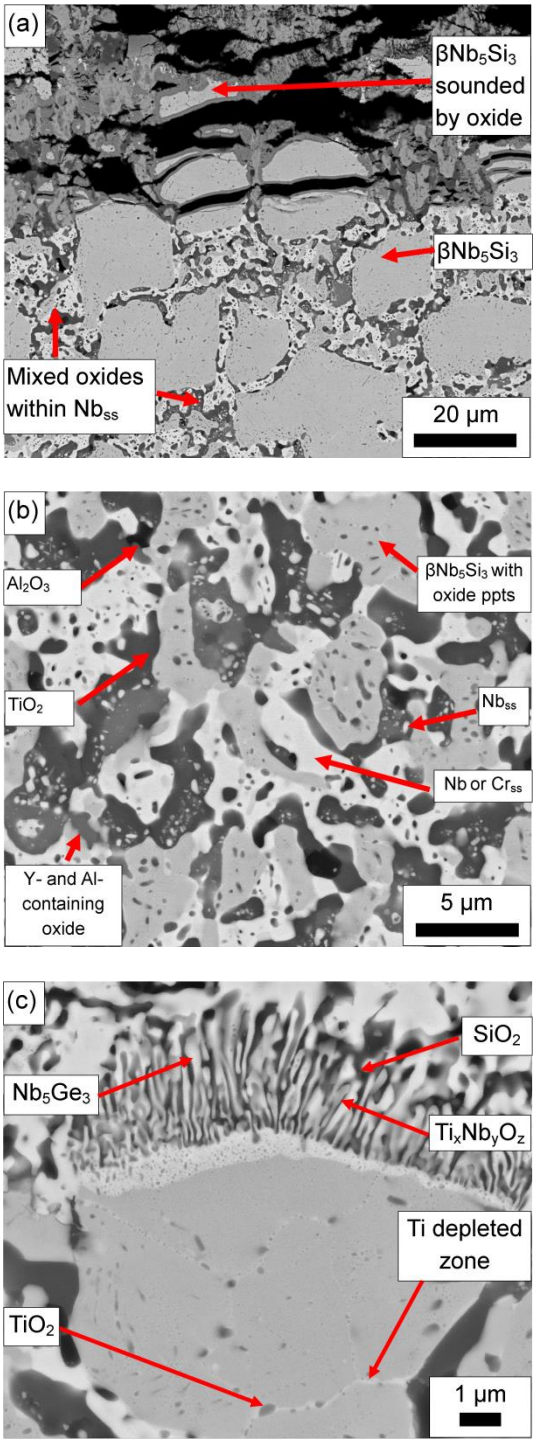

Figure 8.13 Cross sectional BSE images (taken in the FEI Inspect F microscope) of the susbtrate material from alloy AT2 oxidised at 1200 ^{o}C for 100 h. Images show (a) the substrate material showing oxidation of the Nb_{ss} phase, (b) oxidation attack of the βNb_5Si_3 and (c) higher magnification of the oxidised Nb_{ss} phase/βNb_5Si_3 interface.

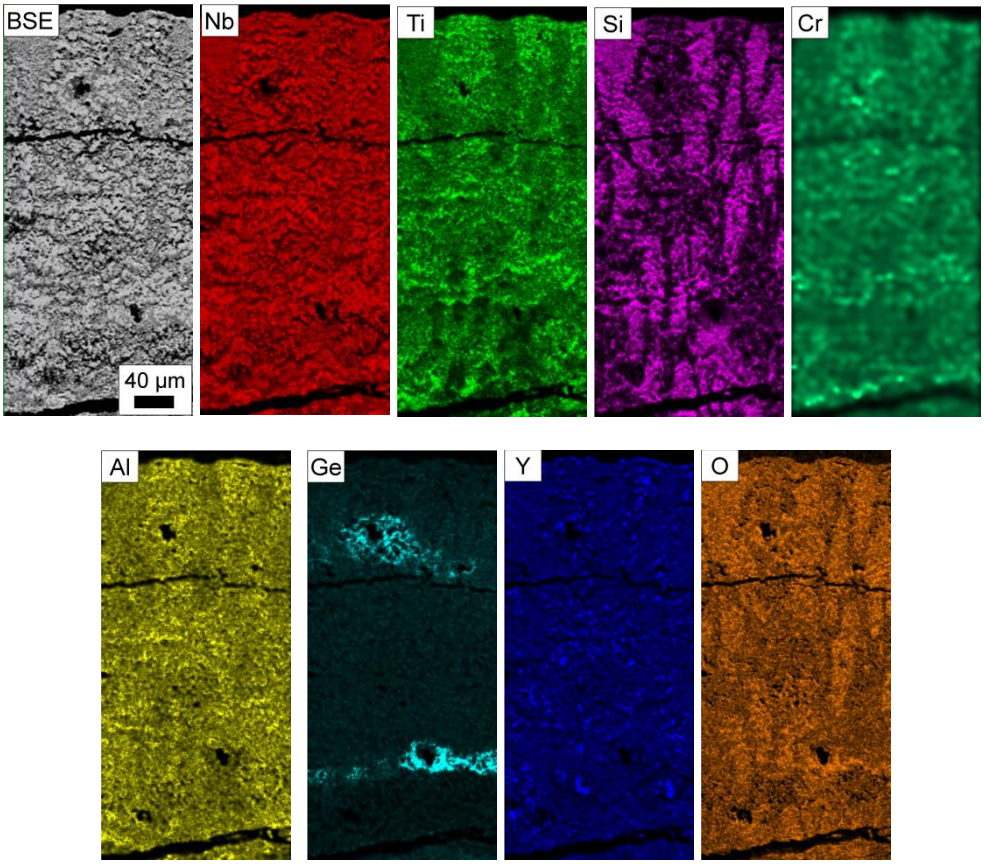

Figure 8.14 Elemental x-ray maps (collected on Phillips XL30 microscope) collected at low (250x) magnification of the oxide scale produced on alloy AT2(10 g) oxidised at 1200 ^{o}C for 100 h. Maps show the element distribution of Nb, Ti, Si, Cr, Al, Ge, Y, O.

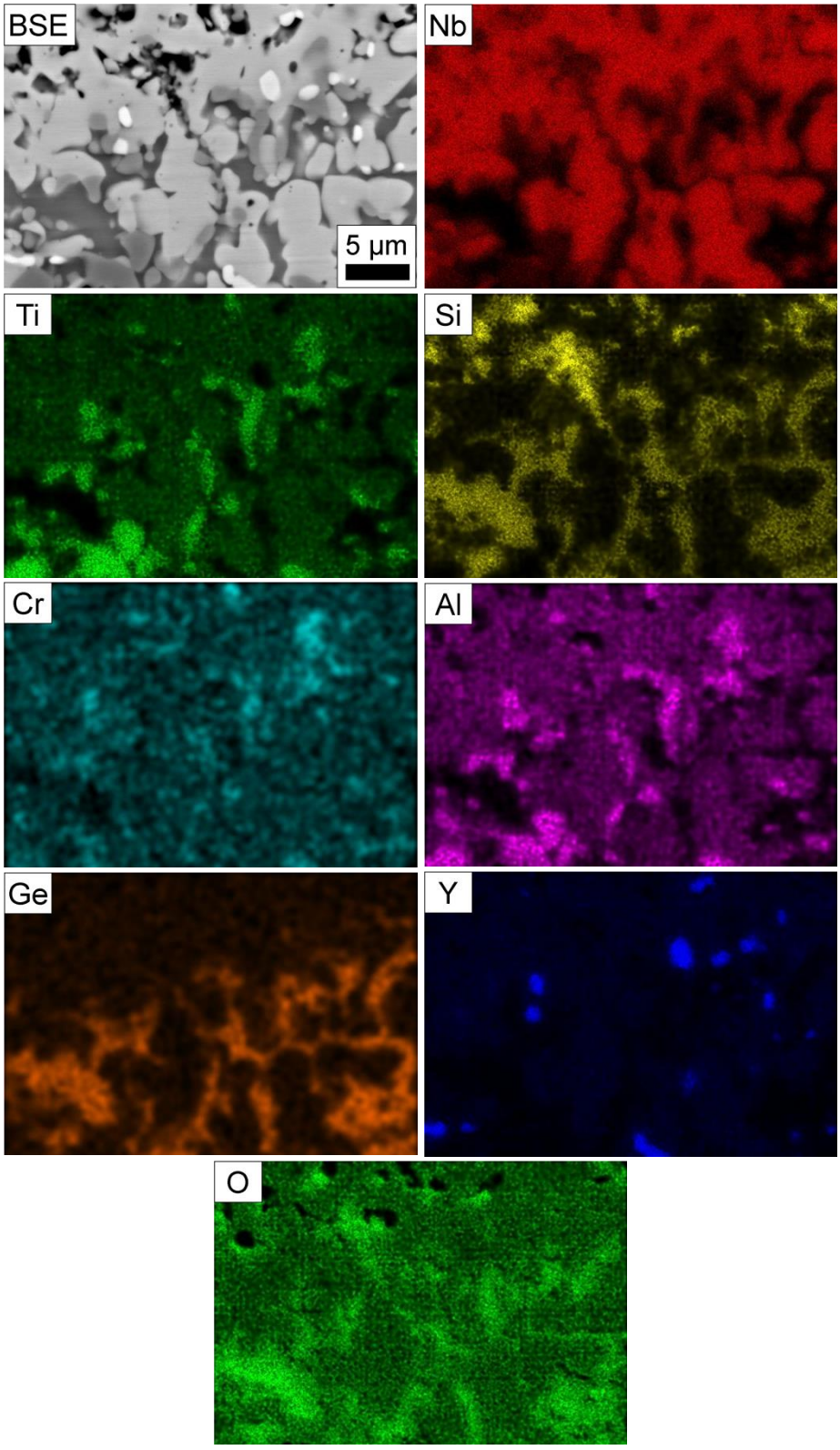

Figure 8.15 Elemental x-ray maps (collected on Phillips XL30 microscope) collected at high (x5000) magnification of the oxide scale produced on alloy AT2 (10 g) oxidised at 1200 ^{o}C for 100 h. Maps show the element distribution of Nb, Ti, Si, Cr, Al, Ge, Y, O.

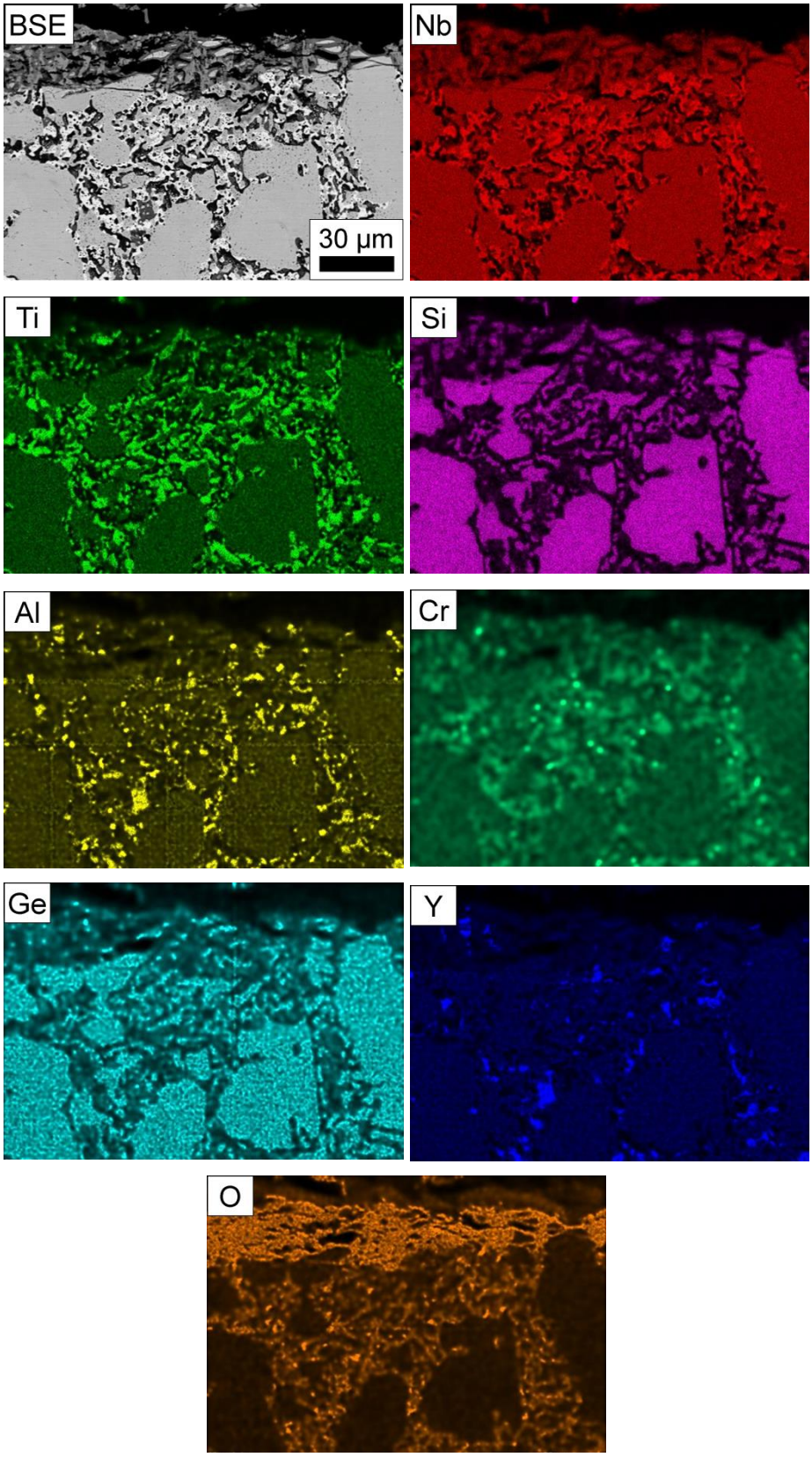

Figure 8.16 Elemental x-ray maps (collected on Phillips XL30 microscope) collected at low (x1000) magnification of the substrate alloy AT2 (10 g) oxidised at 1200 ^{o}C for 100 h. Maps show the element distribution of Nb, Ti, Si, Cr, Al, Ge, Y, O.

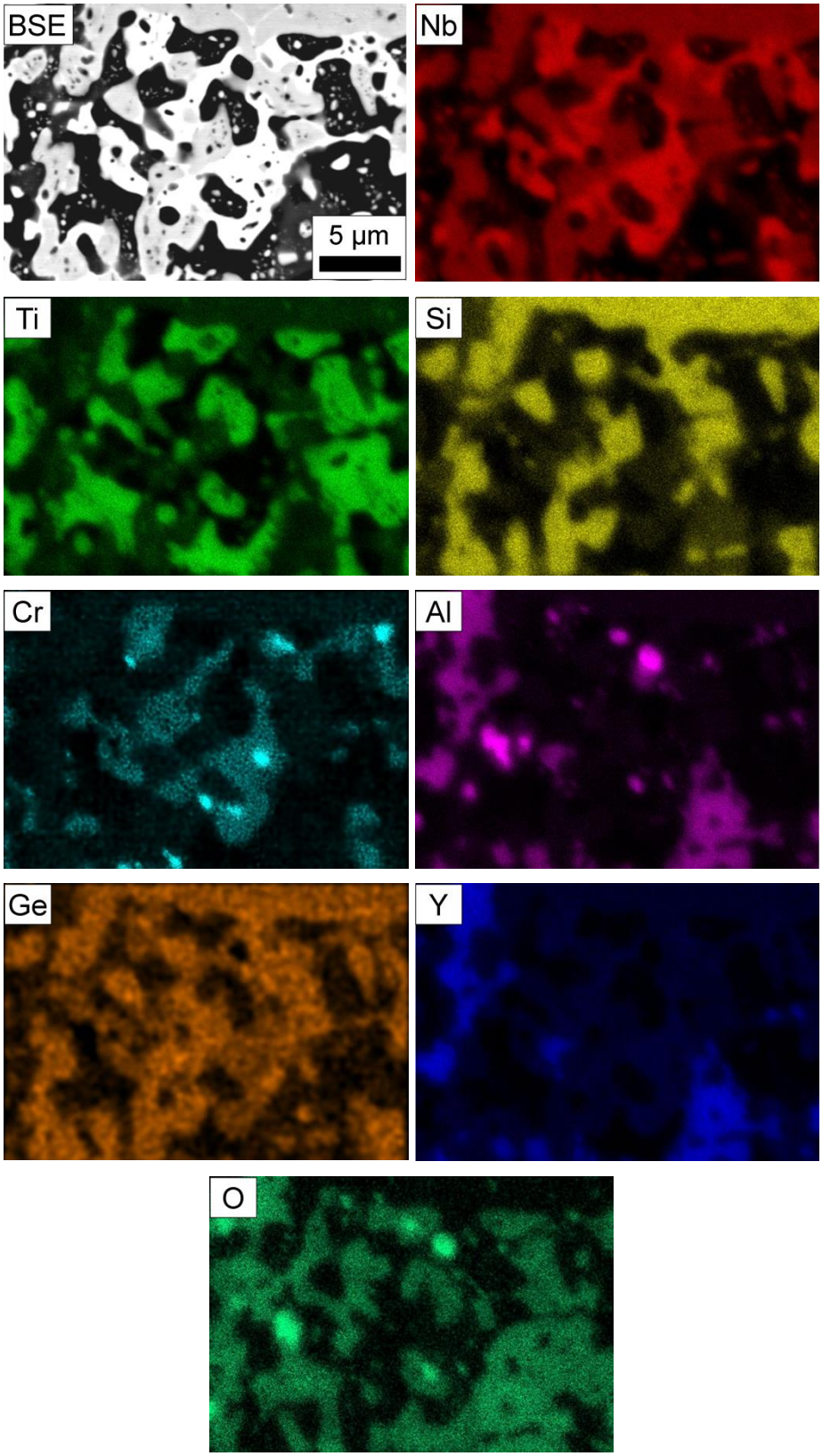

Figure 8.17 Elemental x-ray maps (collected on Phillips XL30 microscope) collected at high (6500x) magnification of the substrate alloy AT2 (10 g) oxidised at 1200 ^{o}C for 100 h. Maps show the element distribution of Nb, Ti, Si, Cr, Al, Ge, Y, O.

8.2.5.2 Nb-24Ti-18Si-2Cr-5Al-3Ge-1Y (AT2 – 600 g)

Figure 8.18, Figure 8.19 and the XRD pattern in Figure 8.22 show there are no significant differences to either scale morphology, phases present within the oxide scale or the effects on the substrate material when oxidising AT2 (600 g) compared with AT2 (10 g). Therefore, so as not to be repetitive no further comment will be made in this section.

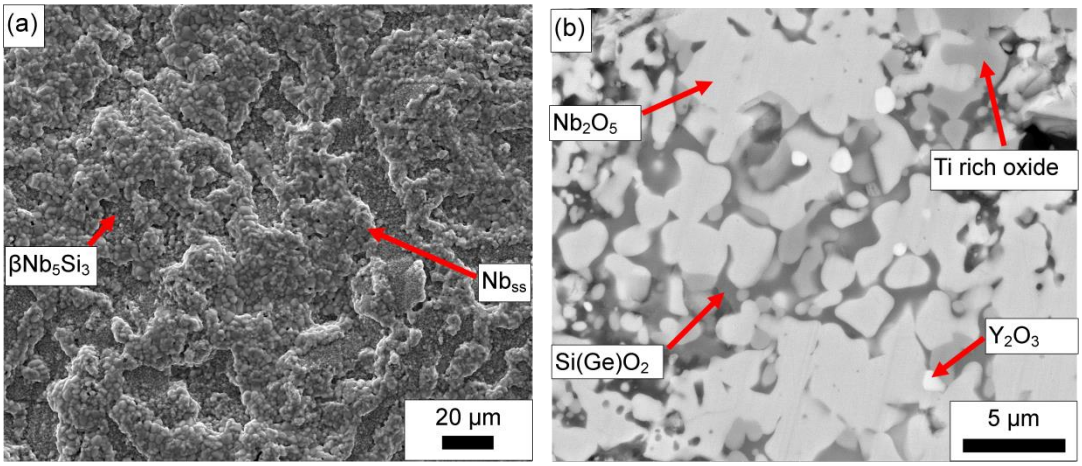

Figure 8.18 SEI and BSE images (taken in the FEI Inspect F microscope) of alloy AT2 (600 g) oxidised at 1200 ^{o}C for 100 h. Images show (a) SEI topographical features of the oxide scale, (b) higher magnification BSE image of the oxide scale.

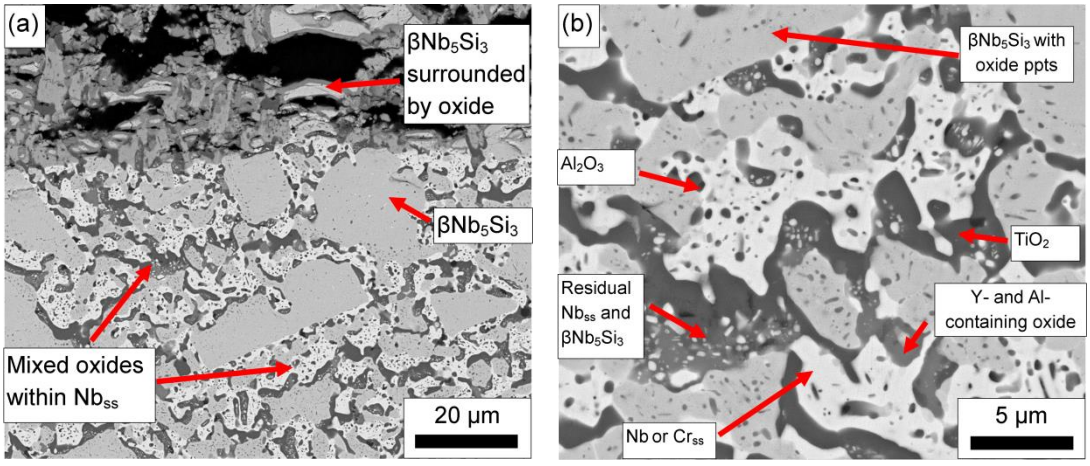

Figure 8.19 Cross sectional BSE images (taken in the FEI Inspect F microscope) of the susbtrate material from alloy AT2 (600 g) oxidised at 1200 ^{o}C for 100 h. Images show (a) the extent of oxygen penetration into the substrate material, (b) higher magnification of the oxidised Nb_{ss} phase/βNb_5Si_3 interface.

8.2.5.3 Nb-24Ti-18Si-2Cr-5Al-3Ge-0.05Y (AT4)

Similar images are shown in Figure 8.20 and Figure 8.21 for the features present after oxidation of alloy AT4 (600 g) at 1200 ^{o}C for 100 h. All features are almost identical to the previously reported features for alloy AT1, AT2 (10 and 600 g) with one exception. Now, as the Y content is very low, there is no evidence of Y_2O_3 within the oxide scale, which has allowed Nb_2O_5 to be ever more dominant within the oxide scale. The powder XRD pattern in Figure 8.22 shows that the oxides present within the oxide scale are identical to the previously reported alloys oxidised at 1200 ^{o}C for 100 h.

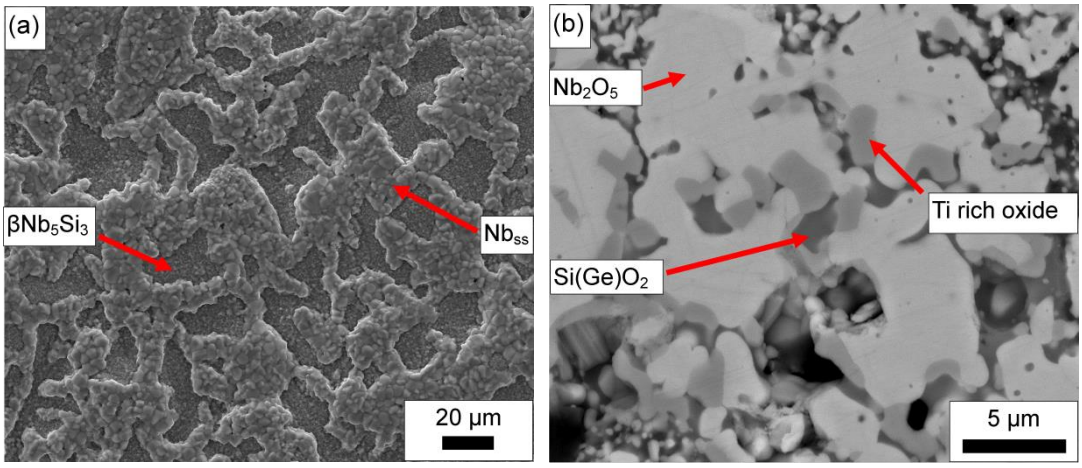

Figure 8.20 SEI and BSE images (taken in the FEI Inspect F microscope) of alloy AT4 (600 g) oxidised at 1200 ^{o}C for 100 h. Images show (a) SEI topographical features of the oxide scale, (b) low magnification BSE image of the oxide scale and (c) higher magnification BSE image of the oxide scale.

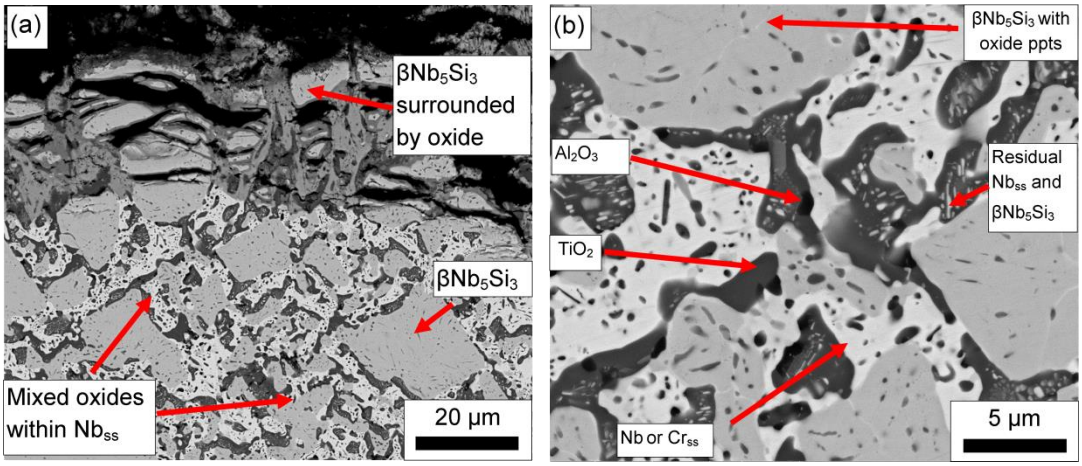

Figure 8.21 Cross sectional BSE images (taken in the FEI Inspect F microscope) of the susbtrate material from alloy AT4 (600 g) oxidised at 1200 ^{o}C for 100 h. Images show (a) the extent of oxygen penetration into the substrate material, (b) higher magnification of the oxidised Nb_{ss} phase/βNb_5Si_3 interface.

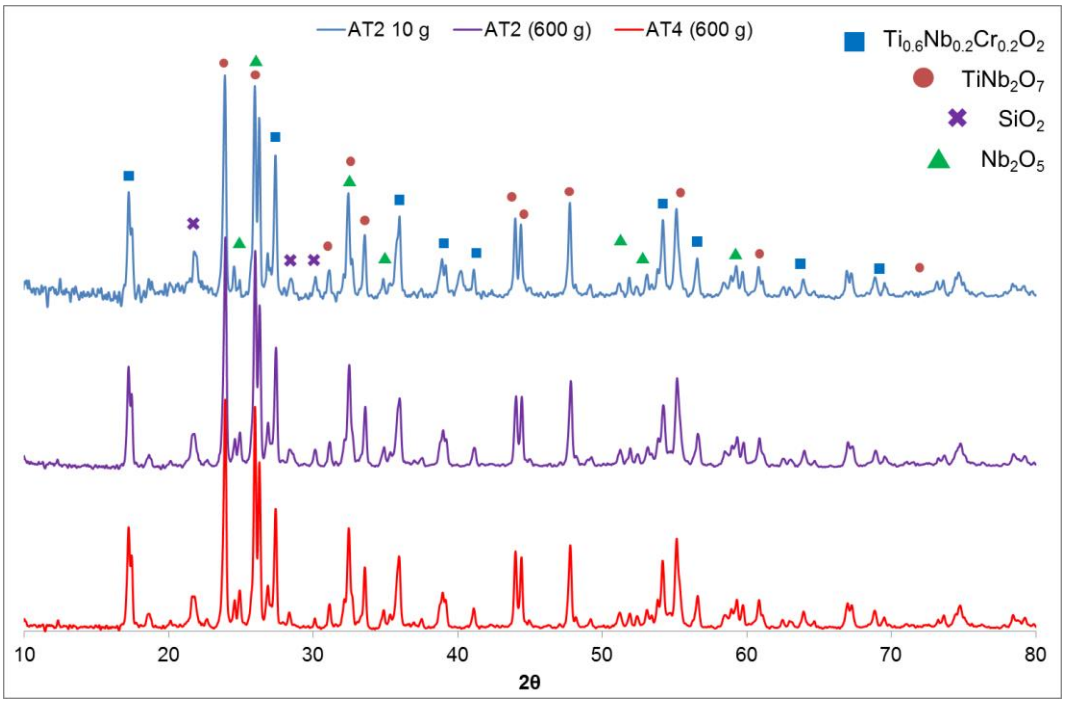

Figure 8.22 Powder XRD patterns of the oxide scale produced on alloys AT2 (10 and 600 g) and AT4 (600 g)

8.2.6 Oxidation tests of intermediate length (1, 10, 20 and 50 h)

In order to understand the oxidation process of these complex alloys better and in more detail, TGA tests were ran on samples of the 600 g ingots at shorter time scales. It was expected that the progression and development of the oxidation behaviour would become much more apparent and a more thorough oxidation mechanism can thus be proposed. There have been very few oxidation studies into Nb silicide alloys that have conducted TGA tests shorter than 100 h. Menon et al., (2001) ran TGA tests for 24 and 48 h and it would be helpful to confirm some of the observations that were made. Therefore, in this study, TGA tests on both the 600 g ingot of AT2 and AT4 were ran for 1, 10, 20 and 50 h giving a total of 5 TGA tests (including the 100 h).

8.2.6.1 Oxide scales

Figure 8.23 shows topographical and cross sectional images of the oxide scales produced on alloy AT2 during oxidation. Powder XRD patterns collected from the scales produced on the oxide sample of AT2 (600 g) from the isothermal 1200 ^{o}C tests for 1, 10, 20, 50 and 100 h are shown in Figure 8.24. The XRD patterns for all samples are almost identical and show some interesting features. Firstly the oxides that form are Nb_2O_5, TiO_2 (could easily be $Ti_{0.6}Nb_{0.2}Cr_{0.2}O_2$), SiO_2 and $TiNb_2O_7$ which are commonly found in these alloys. The patterns also show changes in intensities of some signals and slight shifting in 2θ position showing some changes and interaction of phases present within the oxide scale during the oxidation process.

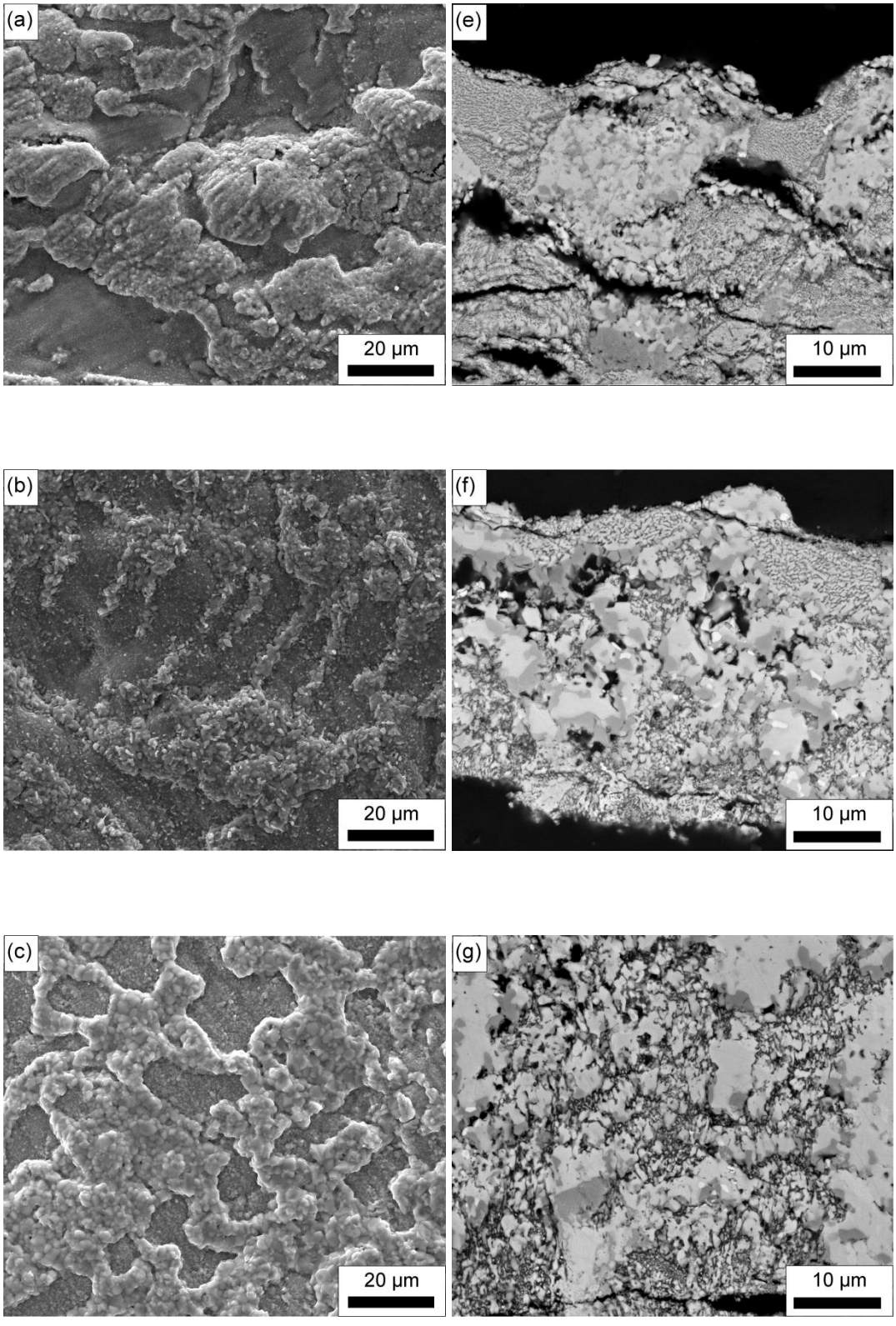
(a)
20 µm
(e)
10 µm
(b)
20 µm
(f)
10 µm
(c)
20 µm
(g)
10 µm

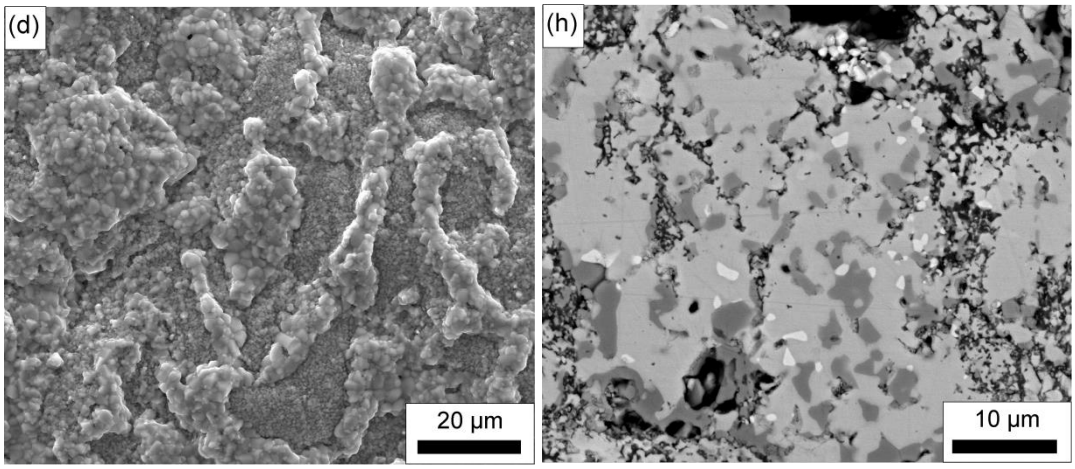

Figure 8.23 Topographical and cross sectional images (taken in the FEI Inspect F microscope) of the oxide scales produced on alloy AT2 (600 g) oxidised at 1200 ^{o}C for 1 h (a+e), 10 h (b+f), 20 h (c+g) and 50 h (d+h).

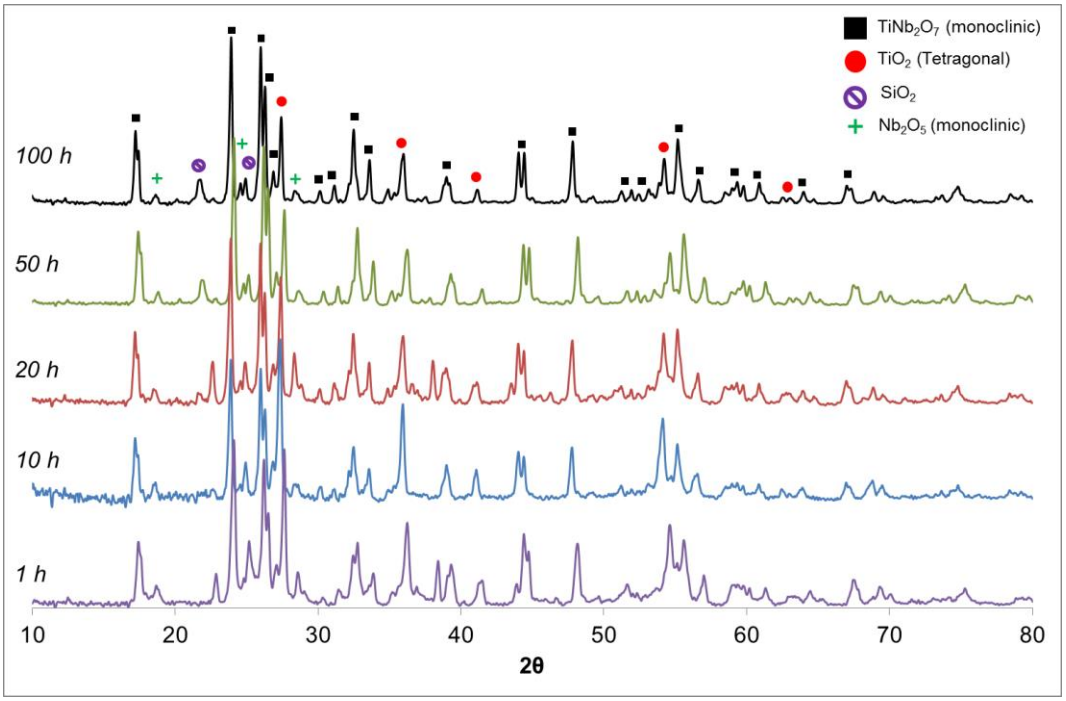

Figure 8.24 Powder XRD patterns of the oxide scale produced on AT2 (600 g) after oxidation at 1200 ^{o}C for 1, 10, 20, 50 and 100 h.

8.2.6.2 Substrate material

Figure 8.25 shows cross sectional BSE images of the AT2 (600 g) oxidised at 1200 ^{o}C for 1, 10, 20 and 50 h both showing the progression of the oxidation. The images show the progression of oxygen ingress into the substrate material and the effect that has on the phases present within the substrate and the oxides that form during the oxidation process. Firstly, it is shown that there is a diffusion distance of oxygen into the substrate defined by the appearance of black oxide phases and this diffusion distance increases over time, as shown by Figure 8.25(a-d). Figure 8.25(e-h) show close ups of the oxidation behaviour within and surrounding the phases present in the microstructure. The images show a progression of oxide formation at grain boundaries and inside the Nb_{ss} phase to growth and interaction of oxide phases over longer time periods (20 – 50 h). Figure 8.26 shows the relationship between the thickness of oxide scale produced and the depth of main oxygen penetration against time for alloy AT2 (600 g). This corroborates a linear behaviour of the oxidation behaviour and kinetics. Figure 8.27 shows that the precipitates that form early on during oxidation at 1200 ^{o}C (1–10 h) are mainly Ti based precipitates.

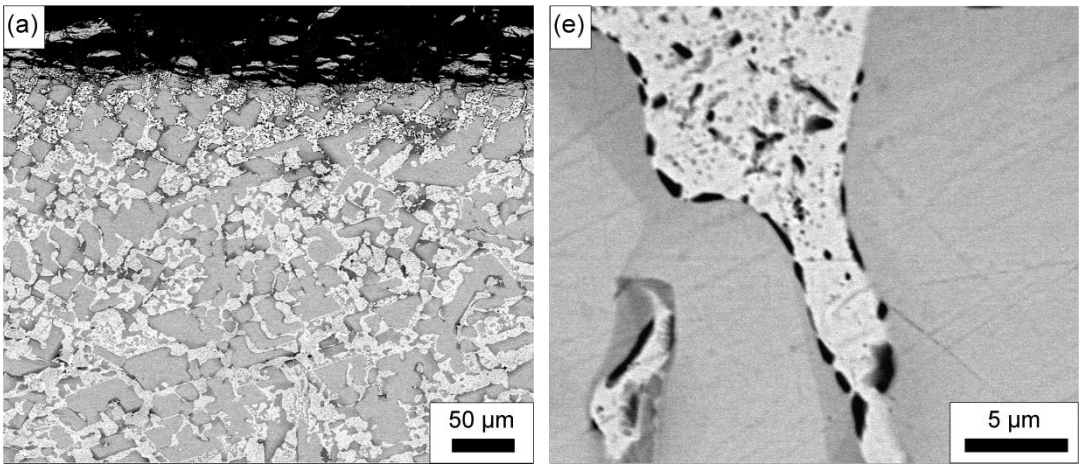

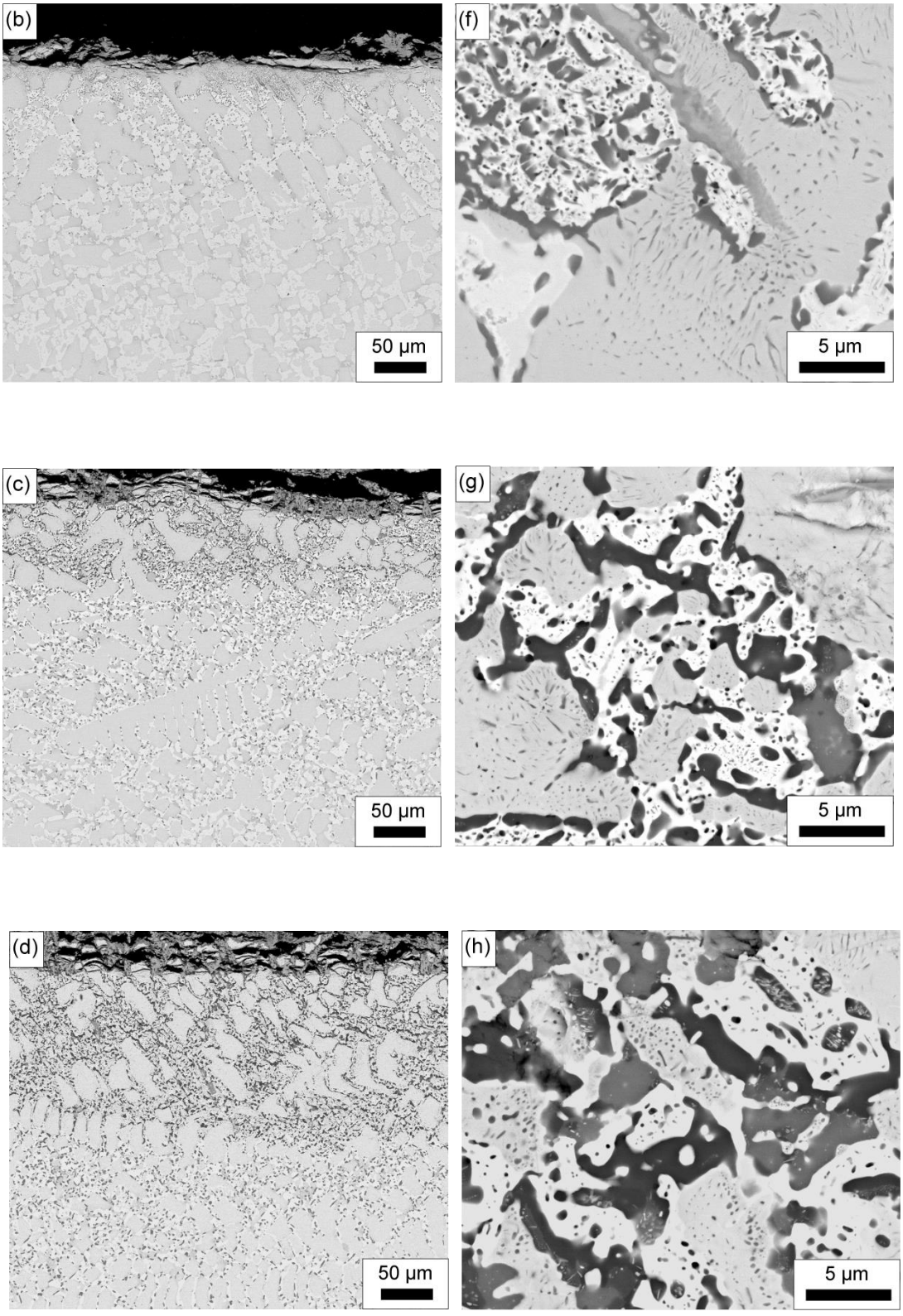

Figure 8.25 BSE cross section images (taken in the FEI Inspect F microscope) of alloy AT2 (600 g) oxidised at 1200 ^{o}C for 1 h (a+e), 10 h (b+f), 20 h (c+g) and 50 h (d+h).

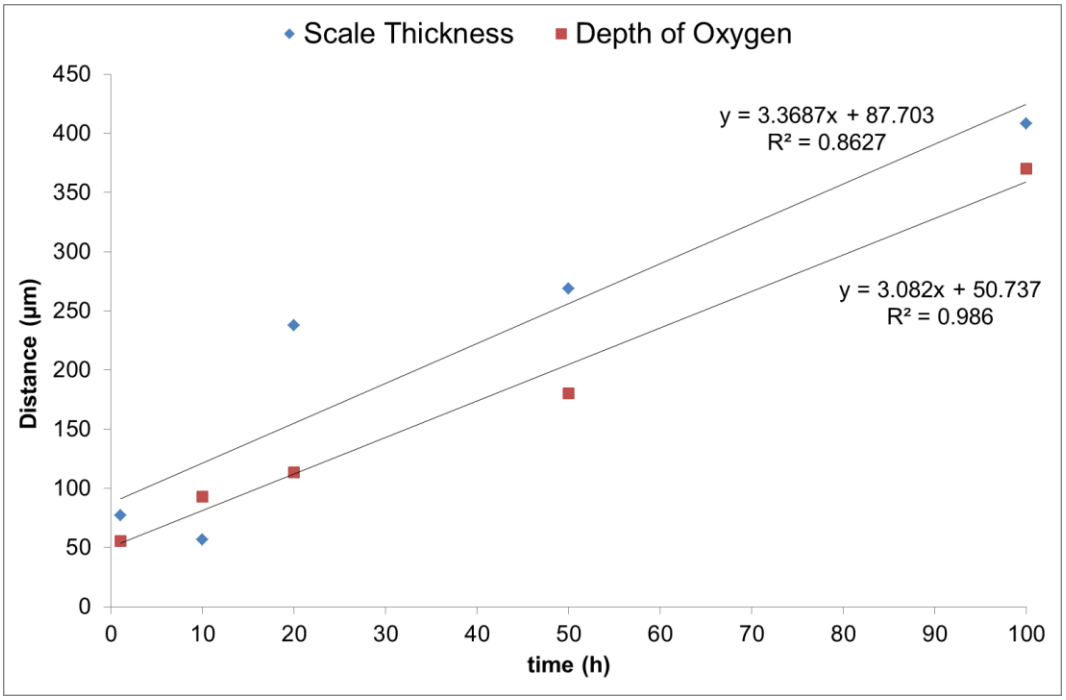

Figure 8.26 Showing the relationship between oxide scale thickness and depth of oxygen penetration into the substrate material and time of alloy AT2 (600 g).

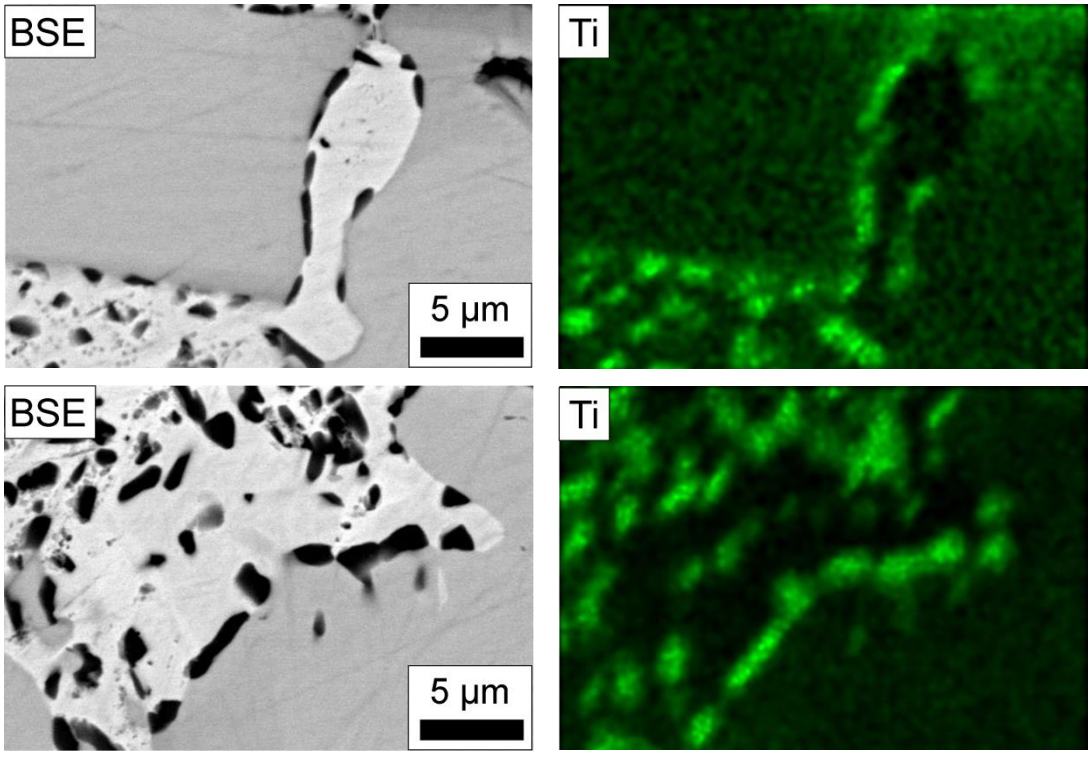

Figure 8.27 Elemental x-ray maps (collected on Phillips XL30 microscope) of Ti showing that the precipitates that form early in the oxidation process (at 1200 ^{o}C) are mostly Ti based.

8.3 Discussion

8.3.1 Microstructures

8.3.1.1 Nb-24Ti-18Si-2Cr-5Al-3Ge-1Y (AT2 10 g and 600 g)

The microstructure of AT2 (10 g) has been discussed in the previous chapter along with alloy AT3. Scaling up the size of the ingot from 10 g to 600 g has had little effect on the features and phases present within the microstructure. The solidification path proposed for AT2 (600 g) is $L \rightarrow L + \beta Nb_5Si_3 \rightarrow L + \beta Nb_5Si_3 + (Nb_{ss} + \beta Nb_5Si_3)_{eutectic} \rightarrow \beta Nb_5Si_3 + (Nb_{ss} + Nb_5Si_3)_{eutectic} + Nb_{ss}$.

8.3.1.2 Nb-24Ti-18Si-2Cr-5Al-3Ge-0.05Y (AT4)

8.3.1.2.1 As Cast

The microstructure of AT4 (600 g) is almost identical to that of AT2 (600 g) and therefore the solidification path is the same as proposed above. Reducing the Y content has had little effect on the morphology of the microstructure or the phases present within the microstructure. The phases therefore are the Nb_{ss} and the high temperature βNb_5Si_3. The intermetallic still possesses a high level of faceting due to the high entropy of fusion and kinetic attachment difficulties during solidification. The microstructure present at the bottom exhibits no evidence of the eutectic structure. The effect of supercooling on eutectic morphologies of binary alloys has been mentioned in this thesis and in the literature. The lack of eutectic structure near the chilled surface is attributed to the melt achieving an undercooling above some critical value. $\Delta T_{critical}$, leading the formation of anomalous eutectic structures. This has been explained in chapter 6 and in (Zifu and Tsakiropoulos, 2010, Li and Kuribayashi, 2003).

The top of the ingot experienced a higher cooling rate compared with the centre, but not as high as that experienced at the bottom of the ingot near the chilled surface. This cooling rate is enough to create a finer microstructure than the centre but still maintain a high level of eutectic.

8.3.1.2.2 Heat treated (1500 ^{o}C for 100 h)

Similar to alloy AT2, the microstructure of AT4 exhibited coarsening, the elimination of any eutectic type morphology and removal of darker areas of contrast within grains caused by the microsegregation of Ti. However, after heat treatment, there is no apparent evidence of γNb_5Si_3 (*hP16, Mn_5Si_3*) anywhere in the microstructure. The reduction in Y content has therefore inhibited the formation of the undesirable hexagonal phase. It has been discussed previously that Ti and Y along with Si and Ge form hexagonal crystal structures. The reduction in Y content to << 1 at.% is enough to destabilise the formation of γNb_5Si_3.

8.3.1.3 Structural Refinement

The results of the structural refinement are shown in Figure 8.28 and Table 8.4 and Table 8.5 for alloy AT4 (600 g) in both as cast and heat treated conditions and has been conducted using the same procedure that has been outlined in the previous chapters. It is shown that the site occupancy behaviour of Ti and Ge show no changes when solidifying a much larger ingot with Ti preferentially substituting for Nb on the more closed packed plane and Si preferentially substituting for Si on the less closed packed plane. Therefore, it is expected that this behaviour would occur regardless of manufacturing size.

Table 8.4 Structural refinement results showing the effect of element substitution on lattice parameters of Nb_{ss} and βNb_5Si_3.

			AT4	
		Reference	As cast	Heat treated
Nb_{ss}	a(Å)	3.3	3.26435(6)	3.27213(7)
	c(Å)	-	-	-
	V($Å^3$)	35.95	34.785	35.034(2)
	Volume fraction		0.44	0.37
βNb_5Si_3	a(Å)	10.02	10.05838(12)	10.06014(9)
	c(Å)	5.07	5.03451(11)	5.03187(8)
	c/a	0.506	0.501	0.500
	V($Å^3$)	509.03	509.349	509.259
	Volume fraction		0.56	0.63

Errors in brackets are those reported by GSAS. Errors are to the same number of decimal places as the value before it (e.g. 10.0566(17) = 10.0566 ± 0.0017).

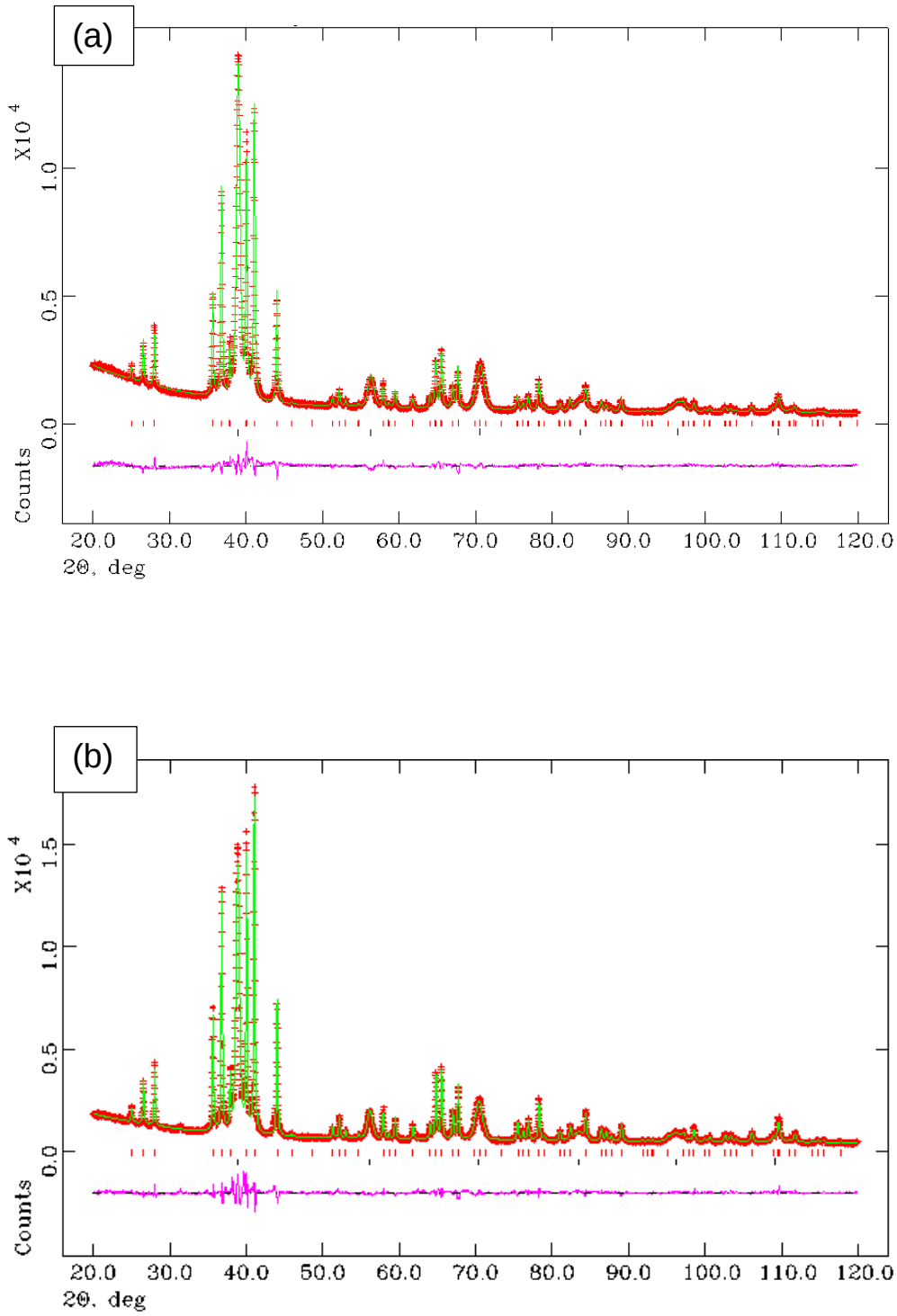

Figure 8.28 Calculated (solid green line), experimentally observed (red crosses) and difference (pink line underneath) diffraction profiles after the Rietveld refinement of AT4 (a) as cast and (b) heat treated.

Table 8.5 Results of structural refinement of crystal structure using XRD data for AT4 in the as cast and heat treated (1500 ^{o}C for 100 h) conditions. The reference values were generated from the crystallographic information file used for the refinement.

		AT4	
	Reference	As cast	Heat treated
χ^2	-	3.012	4.145
R_p (%)	-	4.2	4.5
R_{wp} (%)	-	5.2	6
Nb$_{ss}$			
x=y=z	0	0	
site occupancy	1.0Nb	0.55Nb/0.35Ti/0.1Al	0.6Nb/0.3Ti/0.1Al
Uiso (Å^2)	0.025	0.03276(4)	0.02830(4)
βNb$_5$Si$_3$			
atom site Nb(I)			
x	0	0	0
y	0.5	0.5	0.5
z	0.25	0.25	0.25
site occupancy	1.0Nb	0.5Nb/0.5Ti	0.5Nb/0.5Ti
Uiso (Å^2)	0.025	0.01751(7)	0.02208(6)
atom site Nb(II)			
x	0.074	0.07870(13)	0.07796(12)
y	0.223	0.21810(14)	0.21849(12)
z	0	0	0
site occupancy	1.0Nb	0.8Nb/0.2Ti	0.7Nb/0.3Ti
Uiso (Å^2)	0.025	0.03269(4)	0.02489(3)
atom site Si(I)			
x=y	0	0	0
z	0.25	0.25	0.25
site occupancy	1.0Si	1.0Si	1.0Si
Uiso (Å^2)	0.025	0.02527(17)	0.2534(15)
atom site Si(II)			
x	0.17	0.16475(26)	0.16305(24)
y	0.67	0.66475(26)	0.66305(24)
z	0	0	0
site occupancy	1.0Si	0.83Si/0.17Ge	0.85Si/0.15Ge
Uiso (Å^2)	0.025	0.02393(11)	0.02345(10)

Errors in brackets are those reported by GSAS. Errors are to the same number of decimal places as the value before it (e.g. 10.0566(17) = 10.0566 ± 0.0017).

8.3.2 Oxidation at 800 ^{o}C

The oxidation resistance of AT2 (10 g) has been reported in the previous chapter and a thorough discussion of its oxidation behaviour given. This section will discuss the oxidation resistance of the samples from the larger 600 g ingots discussing any observations and comparisons that can be made when scaling up manufacturing method.

8.3.2.1 Alloy AT2 (10 g and 600 g) and Alloy AT4 (600 g).

The oxide scale produced on alloy AT2 (10 g) was continuous and adherent, whilst the scale produced on AT2 (600 g) exhibited partial pesting, therefore the alloy composition is not to blame for this change in oxidation behaviour. The most observable change when solidifying larger ingots is a coarsening of the microstructure. Whilst coarsening of the microstructure has led to a reduction in the overall area fraction of grain boundaries and therefore should have reduced the overall diffusion distance of oxygen into the microstructure and aided the oxidation resistance, what it has changed is the grain size of the intermetallic phase. As it has been shown in previous chapters, grain boundary diffusion of oxygen into the sample leads to oxide formation at grain boundaries which, in turn, leads to a build-up of internal stress at 800 ^{o}C that is relieved by fracture of the intermetallic. In the 600 g ingot samples, there may be the same level of oxide formation at the grain boundaries; however, due to the presence of coarser Nb_5Si_3 grains, cracking of the intermetallic occurs over a larger distance before the crack is arrested by the Nb_{ss} phase; this may then be the cause of the pesting behaviour and further accelerated oxidation and the increased diffusion distance of oxygen into the microstructure.

It is also observed from the TGA curves that upon scaling up the ingot and microstructure size the oxidation kinetics no longer follow a parabolic behaviour throughout the test, but instead exhibit a transition from an initial parabolic behaviour to an accelerated oxidation behaviour. This is where, it is believed, the

other change to the microstructure renders its effect. It has been discussed previously (Chapter 3) that during oxidation of niobium, stresses can arise that affect the oxidation behaviour. With the PBR of Nb_2O_5 being 2.7 the oxide scale produced on Nb experiences a high compressive stress. Even though Nb_2O_5 is not exclusively formed during oxidation of these alloys, almost all oxide formation is accompanied by an increase in volume and therefore most oxide scales will experience a compressive stress. With a finer microstructure in alloy AT2 (10 g), this compressive stress is felt 'little and often' meaning that oxidation of individual areas of Nb_{ss} exposed at the edge of the sample experiencing the compressive stress are small, which is why most of the cracking of the oxide seen at the interface between the Nb_{ss} and the Nb_5Si_3. During oxidation of the much coarser microstructure, the compressive stress is felt over much larger (individual) areas. The oxide is therefore no longer free to expand over a much larger area. This has led to much greater cracking of the oxide scale. This, accompanied by the grain boundary oxidation mentioned previously, has led to the accelerated oxidation behaviour seen in the TGA curves.

8.3.3 Oxidation at 1200 ^oC

8.3.3.1 Nb-24Ti-18Si-2Cr-5Al-3Ge-1Y (AT2 – 10 g)

At 1200 ^oC, the TG curve and data presented in Table 8.3 show that there is a transition from an initial parabolic kinetic behaviour to a linear behaviour after 17 h. This transition has been seen by others in the literature (Li, 2012, Geng et al., 2007b). This transition, however, was not seen during the oxidation of alloy AT1 (Nb-24Ti-18Si-5Cr-5Al-5Ge-1Y) at 1200 ^oC for 100 h. It was discussed that the addition of Y had removed the early parabolic behaviour and that whilst there was no significant effect on the overall weight gain or the rate constant, Y had obviously inhibited any protective scale that formed early on. It seems that this parabolic behaviour can be re-instated with a reduction in Cr and Ge content.

It has been shown that the addition of 5 at.% Ge leads to a reduction in the overall weight gain from 64 mg/cm^2 to 39.9 mg/cm^2 (alloys KZ5 (Zelenitsas and Tsakiropoulos, 2006a) to ZF6 (Li, 2012)), a reduction of almost 38 %. Also the addition of 1 at.% Y causes a slight increased from 39.9 to 41.1 mg/cm^2 (Chapter 5). Following this, the reduction of Cr and Ge lead to a reduction in the overall weight gain from 41.1 to 3.3 mg/cm^2, a reduction of ~92 % (AT1 to AT2 from this work).

Internal attack of the substrate material occurred very similar to that previously reported for AT1, as the features observed are almost identical. For this reason the TEM data that is provided in Chapter 5 (that is data collected for AT1 oxidised at 1200 ^{o}C for 100 h) can be related to the oxidation of AT2 at 1200 ^{o}C for 100 h. Internal attack of the βNb_5Si_3 phase leads to the formation of Nb_5Ge_3, SiO_2 and $Ti_xNb_yO_z$. Oxidation of the intermetallic leads to the consumption of Si, which leaves the intermetallic now richer in Ge leading to the formation of Nb_5Ge_3. Attack within the bulk of the grain is characterised by the appearance of TiO_2 precipitates and as the TEM data suggests, either side of a sub-grain boundary. As discussed in Chapter 5, there is a recovery process occurring within the intermetallic during the oxidation of the substrate material. Oxide formation within the Nb_{ss} causes stress within the substrate material and now due to the high temperature, the intermetallic does not fracture, but instead experiences a recovery process to relieve the stress. This leads to the formation of sub-grain boundaries allowing oxygen to penetrate the intermetallic and form internal TiO_2 precipitates.

8.3.3.2 Alloy AT2 and Alloy AT4 (600 g) for 1, 10, 20, 50 and 100 h

All features and observations with the 600 g ingots are almost identical to those seen in AT2 (10 g) during oxidation at 1200 ^{o}C for 100 h and so the discussion made previously for AT2 (10 g) is valid for the larger cast ingots during oxidation at 1200 ^{o}C for 100 h. The most noticeable feature is from the TG curve with the much higher overall weight gain and therefore the much higher oxidation

rate constant. The larger ingots still possess an initial parabolic behaviour and transition to a linear behaviour after a certain time period. The parabolic behaviour lasted for 17 h in alloy AT2 (10 g) and for only 14 h in the 600g ingots. An increase in the size of the microstructure has therefore shortened this initial period. The rate constant has increased by two orders of magnitude from 10^{-11} to 10^{-9} g^2 cm^{-4} s^{-1} without an increase in the volume fraction of the Nb_{ss} phase. This increase of two orders of magnitude continues throughout the test with the linear sections increasing from 10^{-9} to 10^{-7} g cm^{-2} s^{-1}. This increase in the rate constant and weight gain cannot be attributed to any effect caused by chemistry or the volume fraction of the Nb_{ss} phase. The only observable feature is the size of the microstructure. As mentioned in the discussion for the oxidation behaviour at 800 ^{o}C, the area of the individual Nb_{ss} grains exposed at the surface of the sample is increased, therefore at 1200 ^{o}C, grain boundary and bulk diffusion of oxygen into the Nb_{ss} can occur and the effect felt over a much larger area. This means that the stresses are felt over a larger individual area which lead to spallation and cracking of the scale. The ingress of oxygen and then the formation of oxides will undoubtedly lead to a larger overall weight gain. Lowering the level of Y has had no effect on the overall weight gain and rate constant of the kinetics of the oxidation process.

The shorter TGA tests reveal interesting features about the oxidation mechanism and process. After 1 h, oxides can be seen clearly forming at the grain boundaries between the Nb_{ss} and the Nb_5Si_3 phase with the majority of these being Ti oxides (likely TiO_2) but there is also some diffusion into the bulk of the Nb_{ss} grains. After 10 h, the proportion of oxides within the Nb_{ss} is increased and now, oxide formations at the outer edges of the Nb_5Si_3 phase are seen where the Ti rich areas of the intermetallic reside. This shows that at 1200 ^{o}C, it takes <10 h for the intermetallic to be attacked by oxygen, and if the proposal of a recovery process taking place within the intermetallic is correct, this process has undoubtedly begun. Most of the oxides forming at this stage are likely binary oxides of Ti and Nb. After

20 h, catastrophic oxidation of the Nb_{ss} can be seen with the appearance of ternary oxides (likely $Y_xAl_yO_z$ and $Ti_xNb_yO_z$), so oxides within the substrate material are beginning to interact. Also, at this stage, we see areas of residual Nb_{ss} and the Nb_5Si_3 within oxides resulting from the consumption of Nb_{ss} and eutectic areas including the Nb_5Si_3. This process then continues for the 50 h and 100 h tests.

If the results are discussed in terms of oxide scale thickness and main oxygen diffusion zone within the substrate material, interesting analysis can be made. The graphs of these two parameters versus time shown in Figure 8.22 confirm the linear oxidation behaviour of the material during oxidation at 1200 ^oC and show a correlation between thickness over time. Scattering of the data for the oxide scale thickness is increased due to the nature of oxide scales formed on these materials. Oxide is inevitabley lost during TG testing and during sample preparation. The equations that come out of the data could hopefully aid any modelling of the oxidation process.

Powder XRD of the oxide scales produced on alloy AT2 (600 g) show that all oxides are formed after the first hour of isothermal oxidation. What is also interesting is that from 1 h to 100 h, the intensities of the peaks corresponding to Nb_2O_5 and TiO_2 decrease, whereas the peaks for $TiNb_2O_7$ increase in intensity. This data suggests, therefore, that over time, the two binary oxides can interact together and form the ternary oxide.

8.4 Conclusions

The microstructures of two alloys that were cast as 600 g ingots have been discussed and compared with the microstructure of alloy AT2 made as a 10 g button. The oxidation resistance of these alloys at 800 ^oC has been discussed and compared with other alloys including AT2 (10 g). The oxidation resistance of AT2 (10 g), AT2 (600 g) and AT4 (600 g) at 1200 ^oC has been discussed along with the

oxidation behaviour of alloy AT2 (600 g) investigated at 1, 10, 20, 50 h to determine the oxidation mechanism.

- AT2 (10 g) and AT2 (600 g) contained the same Nb_{ss} and βNb_5Si_3 phases in the microstructure along with the same overall microstructure morphology. Therefore, larger ingot manufacture had not altered the solidification behaviour or stability of phases.
- A reduction in the Y content from AT2 to AT4 (600 g) has had no effect on the stability of the phases present or on the microstructure morphology.
- A reduction in Y stabilises the formation of the tetragonal crystal structures of α and βNb_5Si_3.
- Structural refinement using the XRD patterns showed no change to the behaviour of occupancies of Nb/Ti and Si/Ge within the crystal structure of βNb_5Si_3. Therefore, these elements display the same site occupancy behaviour regardless of ingot manufacturing size.
- Reduction in the Cr and Ge levels reinstated the parabolic behaviour that exists early on during oxidation at 1200 ^oC leading to a much reduced overall weight gain and rate constant. Minor levels of Cr and Ge are beneficial for oxidation at 1200 ^oC.
- Manufacturing larger ingots (from 10 g to 600 g) has led to a drastic change in the oxidation behaviour. The oxidation behaviour of larger ingots is far worse than that of smaller ingot.
- The size of the Nb_{ss} is as important as the volume fraction. Larger areas of Nb_{ss} present at the surface of the sample during oxidation led to a higher level of cracking of the oxide scale and partial pesting behaviour at 800 ^oC.

- At 1200 ^{o}C, the oxidation behaviour remained linear in nature for the 10 and 600 g ingots however, the oxidation was much more rapid causing a higher weight gain and higher rate constant.
- The oxide scale produced at 1200 ^{o}C for all time scales suggested a possible interaction between TiO_2 and Nb_2O_5 to form $TiNb_2O_7$ within the oxide scale.
- The intermediate oxidation tests at 1200 ^{o}C showed the initial formation of TiN_x and TiO_y within the substrate material. Titanium based particles continue to form and grow over time with minor amounts of Y_2O_3 and Al_2O_3 forming. There is also an interaction between these two binary oxides to form a $Y_xAl_yO_z$ oxide within the substrate material.
- Consumption of the Nb_{ss} by the TiO_2 forming leads to residual Nb_{ss} (and βNb_5Si_3) being present within the oxides.

Chapter 9

Conclusions and a proposed mechanism of oxidation behaviour and suggestions for future work

9.1 Conclusions

This work has highlighted some of the gaps in knowledge and research that needed to be addressed in order to fully understand the microstructure and properties of these complex niobium silicide alloys; gaps that are required to be fully understood if they are ever to be used in an industrial application. The conclusions of this work are presented here followed by a proposed mechanism of oxidation of these alloys.

9.1.1 Alloy microstructure

1) The addition of 1 at.% Y to alloy ZF6 Nb-24Ti-18Si-5Cr-5Al-5Ge had no effect on destabilising the βNb_5Si_3 phase. There was no evidence of any transformation from $\beta Nb_5Si_3 \rightarrow \alpha Nb_5Si_3$ during heat treatment of alloy AT1.
2) Minor levels of Cr and Ge in conjunction with significant levels of Ti and the presence of Y destabilise βNb_5Si_3 and promote the formation of hexagonal γNb_5Si_3.
3) Lowering the Cr level had no effect of promoting the Nb_3Si phase within the alloy microstructure.
4) A reduction in Al stabilised the Nb_3Si phase and promoted the phase transformation of $\beta Nb_5Si_3 \rightarrow \alpha Nb_5Si_3$. Additions of Y led to the formation of Y_2O_3 particles within the heat treated microstructures.
5) The addition of 1 at.% Y inhibited the formation of Cr_2Nb Laves phase in the as cast alloy due to the large immiscibility of Y with the other elements present in the alloy. The last liquid was therefore rich in Y rather than Cr. This effect was present in all the alloys studied in this work.
6) Scaling up the ingot size from 10 g to 600 g for alloy AT2 had no effect on the phases present in the microstructure or the microstructure morphology, but the microstructure was far coarser.

9.1.2 Lattice parameters, volume fraction of phases and site occupancy during element substitution

1) Structural refinement has revealed that substitution of elements led to a contraction in the lattice parameter of the Nb_{ss} phase in the as cast ingots and after heat treatment there is a slight expansion in the lattice parameters.
2) Structural refinement also revealed an expansion in the *(a)* parameter and a contraction in the *(c)* parameter of the βNb_5Si_3 corroborating results from the literature.
3) Also, there is a slight contraction in both *(a)* and *(c)* parameters for the Nb_3Si phase.
4) Structural refinement revealed an increase in the volume fraction of the Nb_{ss} from 39 → 49 from alloy AT1 → AT3 via a reduction in *sp* elements Ge and Al. This increase in the volume fraction of Nb_{ss} had a dramatic effect on the oxidation resistance of these alloys.
5) Reduction in Ge and Al led to an increased volume fraction of the interdendritic eutectic with Al having a more dramatic effect. This had a dramatic effect on the oxidation resistance.
6) Rietveld refinement showed that Ti additions prefer to occupy Nb sites on the 'less closed packed plane' in the βNb_5Si_3 (but not exclusively) and after heat treatment, Ti will move from Nb sites on the more 'closed packed plane' to the 'less closed packed plane'. There is no preferential site occupancy of Ti within the Nb_3Si structure.
7) Germanium prefers to occupy the Si sites on the more closed packed plane in the βNb_5Si_3.

9.2 Oxidation behaviour

9.2.1 Oxidation behaviour at 800 ^{o}C

1) Pest oxidation behaviour was only present when the Al level was reduced from 5 at.% to 2 at.% due to an increased level of eutectic morphology in the microstructure and higher volume fraction of Nb_{ss} present within the microstructure.
2) On samples that did not pest, 'whisker' formation occurred on the surface of the oxidised sample. These whiskers are likely to be single crystals of monoclinic Nb_2O_5.
3) Oxidation occurs through oxygen ingress into the substrate material through the Nb_{ss} phase. The Nb_5Si_3 phase experiences little oxidation degradation.
4) Internal stress is relieved by cracking the Nb_5Si_3 phase.
5) The addition of Y improves the oxidation resistance at 800 ^{o}C, but does not eliminate the diffusion zone of oxygen into the substrate material.
6) Additions of Al are vital for reducing the overall diffusion distance of O into the substrate material. Additions of Cr and Ge are beneficial for reducing the internal diffusion zone in the substrate material.
7) Chromium is beneficial for oxidation resistance at 800 ^{o}C when it remains in solution and not in the presence of Cr_2Nb Laves phase.
8) Oxide precipitation occurs within the Nb_{ss} phase in the form of rod/needle precipitates. These are mainly TiO_2 oxide precipitates.
9) A coarser microstructure has reduced oxidation resistance and can lead to partial pesting behaviour.

9.2.2 Oxidation behaviour at 1200 ^{o}C

1) Additions of Y eliminate an early parabolic type oxidation behaviour and lead to a fully linear kinetic oxidation behaviour.
2) All oxide scales were cracked, possessed pores/voids and were spalled from the substrate material.
3) Lowering the Cr and Ge returned that early parabolic behaviour and led to an improved oxidation behaviour.
4) Additions of Cr are beneficial for oxidation but in the presence of Al and Ge, levels <5 at.% are more beneficial than levels ≥5 at.%.
5) Additions of Y are beneficial for reducing oxide scale thickness but not as beneficial as Hf for reducing the internal diffusion zone of O into the substrate material.
6) Oxides that form within the Nb_{ss} phase include TiO_2, Al_2O_3, Nb_2O_5, Y_2O_3 and a $Y_xAl_yO_z$ ternary oxide.
7) A recovery process within the Nb_5Si_3 phase occurs to relieve internal stress generated from oxide formation within the Nb_{ss} phase. The formation of sub-grain boundaries leads to internal formation of TiO_2 within the Nb_5Si_3 phase.
8) Inwards attack of the Nb_5Si_3 from the oxide/substrate interface leads to the formation of $Ti_xNb_yO_z$, SiO_2 and Nb_5Ge_3.

9.3 Proposed oxidation mechanism.

New information has been seen about the oxidation behaviour of these alloys and therefore a mechanism must be proposed. Others have reported oxidation mechanisms in the literature. The mechanism can be broken down into three sections, formation of oxide scale, internal oxidation of Nb_{ss} and internal

oxidation of Nb_5Si_3. This proposed mechanism for oxidation is related to that of oxidation at 1200 ^oC rather than at 800 ^oC.

9.3.1 Formation of oxide scale

1) Oxygen reacts at the surface with both phases.
2) As all elements are readily available at the surface, multiple and mixed oxides are formed immediately *(Chapter 8 – Figure 8.23 and Figure 8.24).*
3) The mixture of these oxides provide little (if any) protection from further oxidation *(linear oxidation behaviour, (Chapter 5 – Table 3, Figure 5.14; Chapter 8 – Table 3 and Figure 8.8).*
4) The massive volume expansion experienced (PBR Nb_2O_5 = 2.7) and the different volumes of the forming oxides lead to the formation of voids and cracking of the scale *(Chapter 5 – Figure 5.15; Chapter 8 – Figure 8.12, Figure 8.18, Figure 8.20 and Figure 8.23).*
5) The highly compressive nature of the scale leads to peeling of the scale at the edges to the sample.
6) Continuous attack of the material by oxygen is possible *(linear oxidation kinetics).*

9.3.2 Internal attack of the Nb_{ss}.

1) Oxygen can diffuse along grain boundaries and react to from simple, binary oxides such as TiO_2, NbO, Nb_2O_5, Al_2O_3, Y_2O_3 *(Chapter 5 – Figure 5.24 – Figure 5.27; Chapter 8 – Figure 8.25 and Figure 8.27)*
2) Over time, during growth of the major internal oxide TiO_2, Ti is being removed from the Nb_{ss} and leaves areas rich in Nb and Cr. Chromium seems to be providing a small measure of oxidation resistance *(Chapter 8 – Figures 25 and 27).*

3) Due to the high temperatures, oxides can grow and react together to form mixed oxides such as $Y_xAl_yO_z$ *(Chapter 5 – Figure 5.22; Chapter 8 – Figure 8.17 and Figure 8.25).*
4) Continued growth and formation of these oxides leads to residual Nb_{ss} being present within the oxides. Consumption of the Nb_{ss} starts at the grain boundary and continues into the grain leading to oxide formation *(Chapter 8 – Figure 8.25).*

9.3.3 Internal attack of the intermetallic

1) Oxygen can react with the surface of the intermetallic initially producing SiO_2 and $Ti_xNb_yO_z$ *(Chapter 5 – Figure 5.17(a), Figure 5.23 – Figure 5.27, Chapter 8 – Figure 8.13(c).*
2) This formation removes the Si from the intermetallic phase leaving it now richer in Ge and forming Nb_5Ge_3 *(Chapter 5 - Figure 5.24).*
3) As Nb_5Si_3 and Nb_5Ge_3 are isomorphous, little energy is required for the formation of Nb_5Ge_3 after the removal of Si from Nb_5Si_3 *(Chapter 1 – Table 1.15).*
4) The stress imposed by both this attack and the formation of oxides within the Nb_{ss} phase produce stress through the volume changes experienced by the formation of oxides leads to a recovery process within the intermetallic and the formation of sub-grains/boundaries. *(Chapter 5 – Figure 5.17(a) and Figure 5.25; Chapter 8 – Figure 8.13(c))*
5) These sub-grain boundaries allow for enhanced diffusion within the intermetallic. Therefore, oxygen is able to enter the intermetallic and react with Ti forming internal TiO_2 precipitates. This leads to a Ti depleted zone along the sub-grain boundaries *(Chapter 5 – Figure 5.17(a) and Figure 5.25;, Chapter 8 – Figure 8.13(c)).*

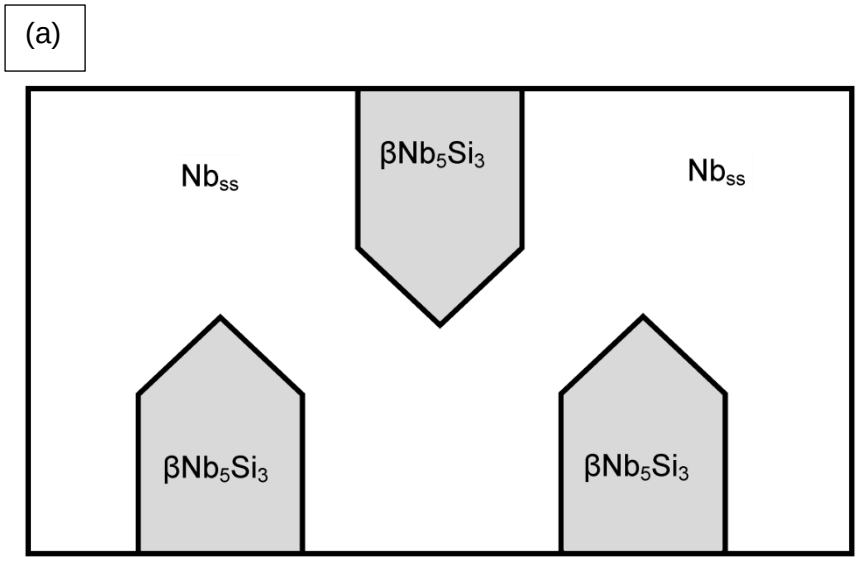

(a) Microstructure of hypereutectic Nb-Si alloy containing Nb_{ss} and Nb_5Si_3 phases. The Nb_{ss} phase is the continuous phase surrounding faceted grains of Nb_5Si_3.

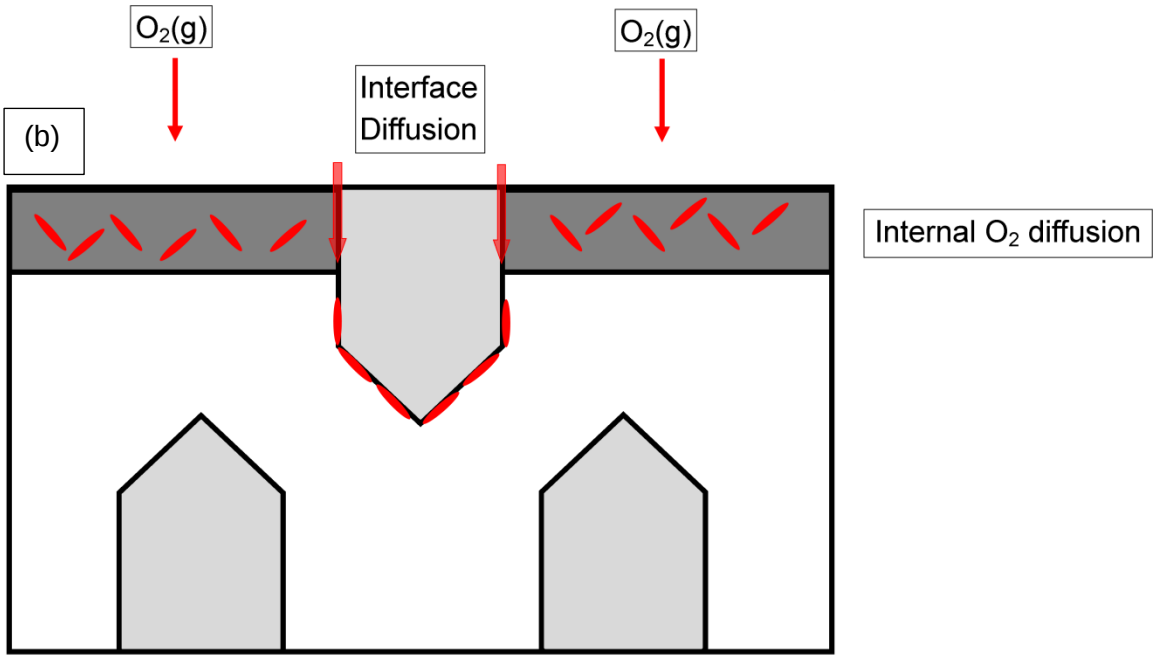

(b) Diffusion of O into the Nb_{ss} and down the interface of the Nb_{ss} and Nb_5Si_3 phases creates an internal diffusion zone. Oxygen penetrating down the interfaces will diffuse further and faster into the bulk microstructure. Diffusion into the Nb_{ss} phase leads to oxide formation.

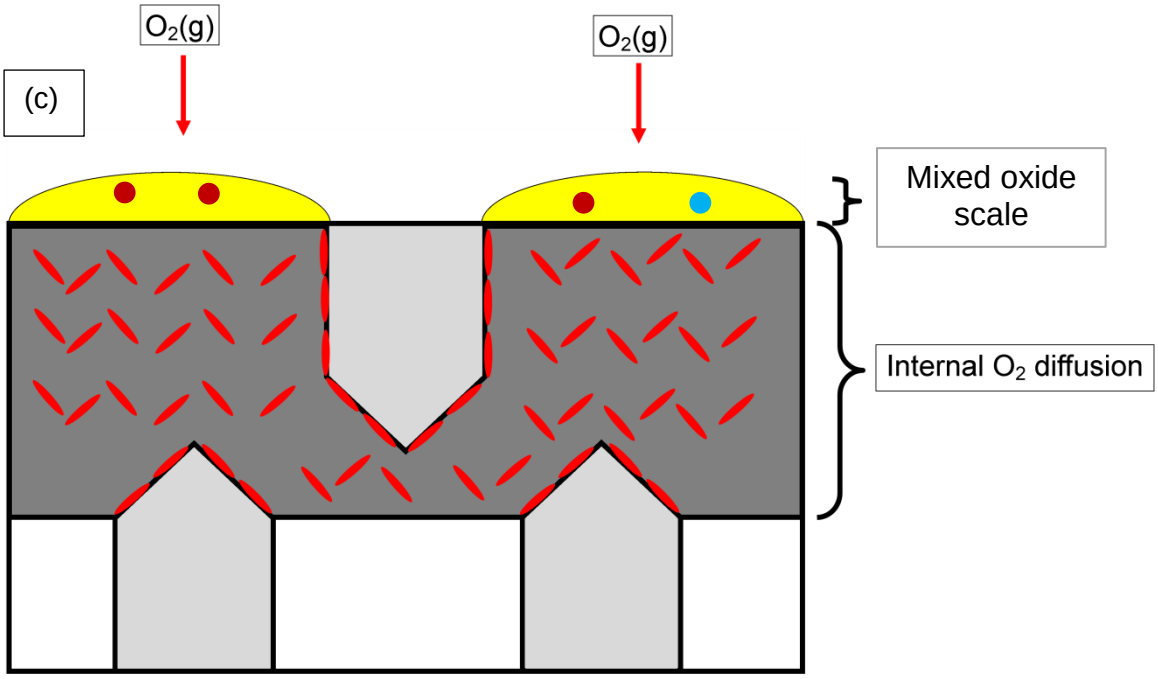

(c) Continued attack by O leads to an increased internal diffusion zone and the formation of an oxide scale which is uneven in height and topographical feature due to the rapid oxidation of the Nb_{ss} phase and slower oxidation of the Nb_5Si_3.

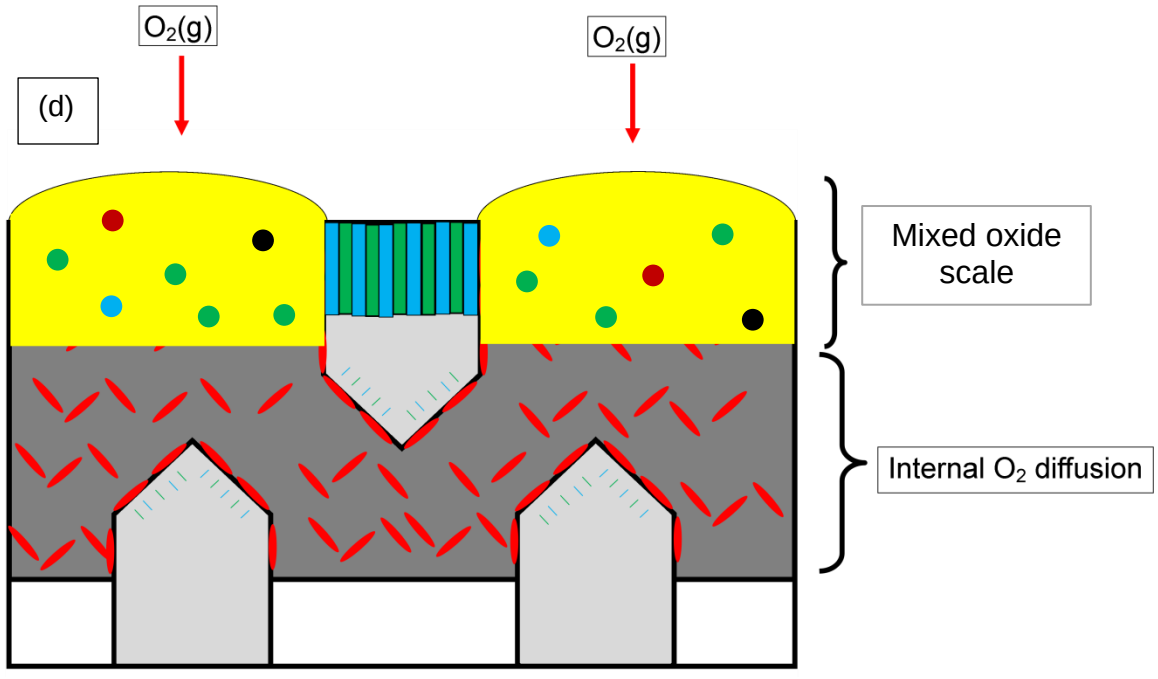

(d) Attack of the intermetallic phase occurs shortly aftwerwards leading to an inward attack at the grain/oxide interface and the formation of SiO_2, Nb_5Ge_3 and $Ti_xNb_yO_z$.

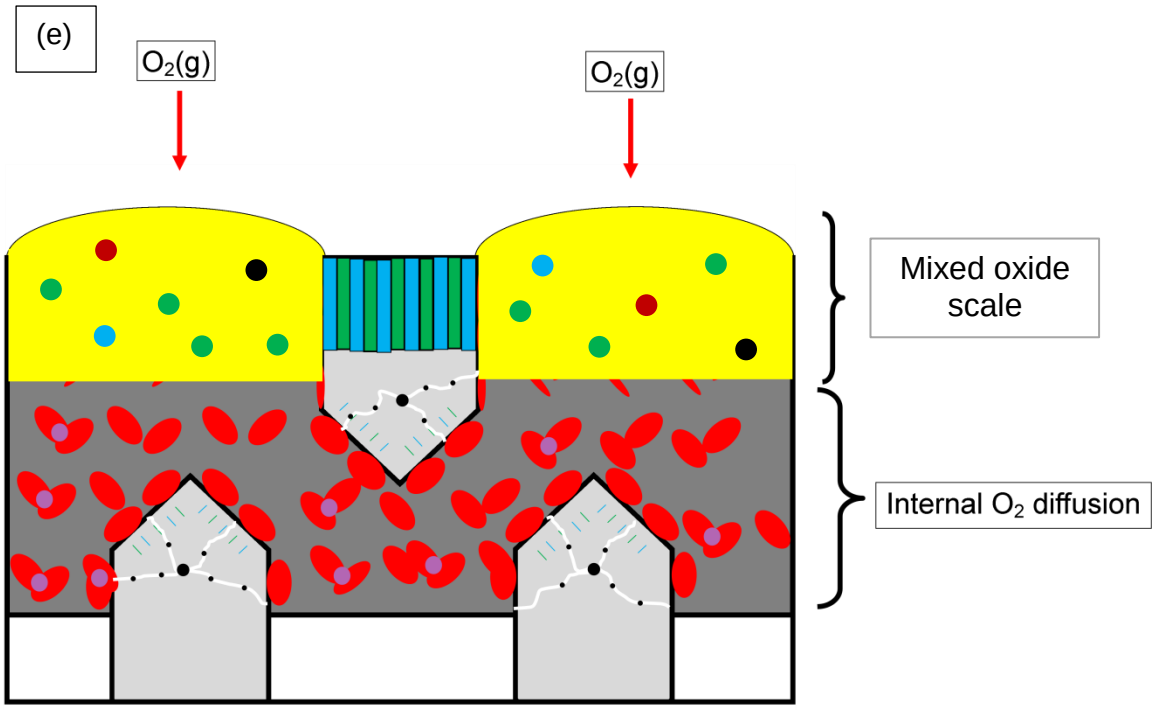

(e) Coarsneing of the oxides already present and the formation of more oxides within the Nb_{ss} and along the Nb_{ss}/Nb_5Si_3interface lead to recovery process within the Nb_5Si_3. This leads to an internal attack of the intermetallic and the formation of TiO_2 within the grain.

Figure 9.1 Schematic of the oxidation process of Nb-Si alloys at oxidised at 1200 ^{o}C. Progression of the oxidation behaviour occurs from (a) – (e).

9.4 Suggestions for future work

With the mechanical properties of Nb silicide alloys improving, the oxidation resistance is not developing nor improving as quickly with spallation of oxide scales, porous and cracked oxide scales and substantial internal oxidation of the Nb_{ss} and now even internal attack of the Nb_5Si_3 phase, further research is needed to improve the oxidation resistance.

1) Within our research group and within the literature, several elements are standing out as beneficial for oxidation resistance such as Al, Ge, Sn, B and Hf. It would be interesting to see how these elements aid oxidation resistance when combined all together. It is likely recognised that the standard alloy chemistry includes Nb-Ti-Si-Cr-Al-Hf. To add to this Ge-Mo-Sn-W-B-Y. This would make 12 elements in the alloy with minor additions (0 – 5 at%).

2) It has been shown that a coarser microstructure has worse oxidation performance than a finer microstructure. As these ingots grow in size, it will be necessary to control microstructure size and investigate a way of controlling the size of phases during solidification and heat treatment processes.

3) One major problem with these alloys is contamination of the ingot by O and N during solidification and heat treatment processes forming Ti_xN_y and Y_2O_3. It is vital that this contamination be eradicated if they are to ever be manufactured on an industrial scale.

4) A suitable coating system needs to be investigated that could be used for these alloys. The substrate/coating system needs to be developed in conjunction with each other and not rely upon the so called ‘band aid’ approach.

References

Abbaschian, R. and Lipschutz, M. D. 1997. Eutectic solidification processing via bulk melt undercooling. Materials Science and Engineering A*,* 226-228**,** 13-21.

Balsone, J. S., Bewlay, B. P., Jackson, M. R., Subramanian, P. R., Zhao, J. C., Chatterjee, A. and Heffernan, T. M. 2001. Materials Beyond Superalloys: Exploiting High-Temperature Composites. Technical Information Series. General Electric Research and Development.

Begley, R. T. Columbium alloy development at Westinghouse. In*:* Dalder, E. N. C., Grobenstein, T. & Olsen, C. S. (eds.) *Evolution of Refractory Metals and Alloys.* TMS, Warrendal, PA.1994

Bendersky, L., Biancaniello, F. S., Boettinger, W. J. and Perepezko, J. H. 1987. Microstructural characterization of rapidly solidified Nb-Si alloys. Materials Science and Engineering*,* 89**,** 151-159.

Bertero, G., Hofmeister, W., Robinson, M. and Bayuzick, R. 1991. Containerless processing and rapid solidification of Nb-Si alloys of hypereutectic composition. Metallurgical and Materials Transactions A*,* 22**,** 2723-2732.

Bewlay, B. P., Briant, C. L., Davis, A. W. and Jackson, M. R. 2001a. The effect of silicide volume fraction on the creep behaviour of Nb-silicide based in-situ composites. Materials Research Society Symposium Proceedings*,* 646**,** N 2.7.1 - N 2.7.6.

Bewlay, B. P., Briant, C. L., Sylven, E. T., Jackson, M. R. and Xiao, G. 2001b. Creep studies of monolithic phases in Nb-silicide based in-situ composites. Materials Research Society Symposium Proceedings*,* 646**,** N 2.6.1 - N 2.6.6.

Bewlay, B. P. and Jackson, M. R. High-temperature In Situ Composites: Processing and Properties. In*:* Anthony, K. & Carl, Z. (eds.) *Comprehensive Composite Materials.* Oxford: Pergamon.2000

Bewlay, B. P., Jackson, M. R. and Bishop, R. R. 1998. The Nb-Ti-Si ternary phase diagram: Determination of solid-state phase equilibria in Nb- and Ti-rich alloys. Journal of Phase Equilibria*,* 19**,** 577-586.

Bewlay, B. P., Jackson, M. R. and Gigliotti, M. F. X. Niobium Silicide High Temperature In Situ Composites. *Intermetallic Compounds: Principles and Practice, Vol. 3.* John Wiley and Sons.2002

Bewlay, B. P., Jackson, M. R. and Lipsitt, H. A. 1996. The balance of mechanical and environmental properties of a multielement niobium-niobium silicide-based In Situ composite. Metallurgical and Materials Transactions A*,* 27**,** 3801-3808.

Bewlay, B. P., Jackson, M. R. and Lipsitt, H. A. 1997. The Nb-Ti-Si ternary phase diagram: Evaluation of liquid- solid phase equilibria in Nb-and Ti-rich alloys. Journal of Phase Equilibria*,* 18**,** 264-278.

Bewlay, B. P., Jackson, M. R. and Subramanian, P. R. 1999. Processing high-temperature refractory-metal silicide in-situ composites. JOM (Journal of the Minerals Metals and Materials Society)*,* 51**,** 32-36.

Bewlay, B. P., Jackson, M. R., Subramanian, P. R. and Zhao, J. C. 2003. A review of very-high-temperature Nb-silicide-based composites. Metallurgical and Materials Transactions A*,* 34**,** 2043-2052.

Bewlay, B. P., Yang, Y., Casey, R. L., Jackson, M. R. and Chang, Y. A. 2009. Experimental study of the liquid-solid phase equilibria at the metal-rich region of the Nb-Cr-Si system. Intermetallics*,* 17**,** 120-127.

Brukl, C., Nowotny, H. and Benesovsky, F. 1961. Untersuchungen in den Dreistoffsystemen: V—Al—Si, Nb—Al—Si, Cr—Al—Si, Mo—Al—Si bzw. Cr(Mo)—Al—Si. Monatshefte für Chemie / Chemical Monthly*,* 92**,** 967-980.

Chan, K. and Davidson, D. 1999. Effects of Ti addition on cleavage fracture in Nb-Cr-Ti solid-solution alloys. Metallurgical and Materials Transactions A*,* 30**,** 925-939.

Chan, K. and Davidson, D. 2001. Delineating brittle-phase embrittlement and ductile-phase toughening in Nb-based in-situ composites. Metallurgical and Materials Transactions A*,* 32**,** 2717-2727.

Chan, K. S. 2002. Alloying effects on fracture mechanisms in Nb-based intermetallic in-situ composites. Materials Science and Engineering A*,* 329-331**,** 513-522.

Chan, K. S. 2004. Cyclic-Oxidation Resistance of Niobium-Base in situ Composites: Modeling and Experimentation. Oxidation of Metals*,* 61**,** 165-194.

Chan, K. S. 2005. Alloying effects on the fracture toughness of Nb-based silicides and Laves phases. Materials Science and Engineering A*,* 409**,** 257-269.

Chen, Y., Hu, Q.-M. and Yang, R. 2011. Energetic effects of dopants on the eutectoid decomposition of Nb–Si in situ composites. Philosophical Magazine Letters*,* 91**,** 640-647.

Chen, Y., Shang, J. X. and Zhang, Y. 2007a. Bonding characteristics and site occupancies of alloying elements in different Nb_5Si_3 phases from first principles. Physical Review B*,* 76**,** 184204.

Chen, Y., Shang, J. X. and Zhang, Y. 2007b. Effects of alloying element Ti on alpha-Nb_5Si_3 and Nb_3Al from first principles. Journal of Physics: Condensed Matter*,* 19**,** 1-8.

Cullity, B. D. 1978. *Elements of X-ray diffraction,* London, Addison-Wesley.

Davidson, D. and Chan, K. 1999. The fatigue and fracture resistance of a Nb-Cr-Ti-Al alloy. Metallurgical and Materials Transactions A*,* 30**,** 2007-2018.

Davidson, D., Chan, K. and Anton, D. 1996. The effects on fracture toughness of ductile-phase composition and morphology in Nb-Cr-Ti and Nb-Si in situ composites. Metallurgical and Materials Transactions A*,* 27**,** 3007-3018.

Deal, A., Heward, W., Ellis, D., Cournoyer, J., Dovidenko, K. and Bewlay, B. 2007. Phase Identification in Nb-Cr-Si Alloys. Microscopy and Microanalysis*,* 13**,** 90-91.

Dicks, R., Wang, F. and Wu, X. 2009. The manufacture of a niobium/niobium-silicide-based alloy using direct laser fabrication. Journal of Materials Processing Technology*,* 209**,** 1752-1757.

Dimiduk, D. M., Subramanian, P. and Mendiratta, M. G. 1995. Exploration of Nb-based advanced intermetallic materials. Acta Metallurgica Sinca, 8**,** 11.

Ehrman, S. H., Friedlander, S. K. and Zachariah, M. R. 1999. Phase segregation in binary SiO_2/TiO_2 and $SiO_2/Fe2O_3$ nanoparticle aerosols formed in a premixed flame. Journal of Materials Research, 14**,** 4551-4561.

Geng, J., Shao, G. and Tsakiropoulos, P. 2006a. Study of three-phase equilibrium in the Nb-rich corner of Nb-Si-Cr system. Intermetallics, 14**,** 832-837.

Geng, J. and Tsakiropoulos, P. 2007. A study of the microstructures and oxidation of Nb-Si-Cr-Al-Mo in situ composites alloyed with Ti, Hf and Sn. Intermetallics, 15**,** 382-395.

Geng, J., Tsakiropoulos, P. and Shao, G. 2006b. The effects of Ti and Mo additions on the microstructure of Nb-silicide based in situ composites. Intermetallics, 14**,** 227-235.

Geng, J., Tsakiropoulos, P. and Shao, G. 2006c. Oxidation of Nb-Si-Cr-Al in situ composites with Mo, Ti and Hf additions. Materials Science and Engineering A, 441**,** 26-38.

Geng, J., Tsakiropoulos, P. and Shao, G. 2007a. A study of the effects of Hf and Sn additions on the microstructure of Nb_{ss}/Nb_5Si_3 based in situ composites. Intermetallics, 15**,** 69-76.

Geng, J., Tsakiropoulos, P. and Shao, G. 2007b. A thermo-gravimetric and microstructural study of the oxidation of Nb_{ss}/Nb_5Si_3-based in situ composites with Sn addition. Intermetallics, 15**,** 270-281.

Geng, T., Li, C., Bao, J., Zhao, X., Du, Z. and Guo, C. 2009. Thermodynamic assessment of the Nb-Si-Ti system. Intermetallics, 17**,** 343-357.

Geng, T., Li, C., Du, Z., Guo, C., Zhao, X. and Xu, H. 2011. Thermodynamic assessment of the Nb–Ge system. Journal of Alloys and Compounds, 509**,** 3080-3088.

Gesmundo, F., Viani, F., Niu, Y. and Douglass, D. L. 1993. Further aspects of the oxidation of binary two-phase alloys. Oxidation of Metals, 39**,** 197-209.

Gokhale, A. B., 1990a, *Cr-Si Phase Diagram,* ASM Alloy Phase Diagram Centre, P. Villars, editor in chief; H. Okamoto and K. Cenzual, section editors; , http://www1.asminternational.org/AsmEnterprise/APD, ASM International, Materials Park, OH, 2006.

Gokhale, A. B., 1990b, *Ge-Y Phase Diagram,* ASM Alloy Phase Diagram Centre, P. Villars, editor in chief; H. Okamoto and K. Cenzual, section editors; , http://www1.asminternational.org/AsmEnterprise/APD, ASM International, Materials Park, OH, 2006.

Gokhale, A. B., Sarkar, G., Abbaschian, G. J., Haygarth, J. C., Wojcik, C. and Lewis, R. E. 1988. Supercooling effects in faceted eutectic Nb-Si alloys. Solidification Processing of Eutectic Alloys**,** 177-197.

Goldschmidt, H. J. and Brand, J. A. 1961. The constitution of the chromium-niobium-silicon system. Journal of the Less Common Metals, 3, 34-43.

Gramme, S., 1991, *Al-Cr-Nb Phase Diagram,* ASM Alloy Phase Diagram Centre, P. Villars, editor in chief; H. Okamoto and K. Cenzual, section editors; , http://www1.asminternational.org/AsmEnterprise/APD, ASM International, Materials Park, OH, 2006.

Grammenos, I. and Tsakiropoulos, P. 2010. Study of the role of Al, Cr and Ti additions in the microstructure of Nb-18Si-5Hf base alloys. Intermetallics, 18, 242-253.

Grill, R. and Gnadenberger, A. 2006. Niobium as mint metal: Production-properties-processing. International Journal of Refractory Metals and Hard Materials, 24, 275-282.

Henshall, G. A., Strum, M. J., Subramanian, P. R. and Mendiratta, M. G. 1995. Simulations of Creep in Ductile-Phase Toughened Nb_5Si_3/Nb in-situ composites. Mat. Res. Soc. Symp. Proc., 364, 937-942.

Hou, P. Y. and Stringer, J. 1995. The effect of reactive element additions on the selective oxidation, growth and adhesion of chromia scales. Materials Science and Engineering: A, 202, 1-10.

Hunt, C. R. J. and Raman, A. 1968. Alloy chemistry of sigma(betaU)-related phases. I. extension of mu- and occurence of mu'-phases in the ternary systems Nb (Ta)--X--Al (Z = Fe, Co, Ni, Cu, Cr, Mo). Z. Metallk 59, 701-707.

Hurlen, T. 1961. Oxidation of Niobium. Journal of the Institute of Metals, 89, 273-80.

Ibrahim, M. and Bright, N. F. H. 1962. The Binary System Nb_2O_5— SiO_2. Journal of the American Ceramic Society, 45, 221-222.

Jackson, M. R., Bewlay, B. P., Rowe, R. G., Skelly, D. W. and Lipsitt, H. A. 1996. High-Temperature Refractory Metal-Intermetallic Composites. JOM (Journal of the Minerals Metals and Materials Society), 48, 39-44.

Jéhanno, P., Kestler, H., Venskutonis, A., Böning, M., Heilmaier, M., Bewlay, B. and Jackson, M. 2005. Assessment of a powder metallurgical processing route for refractory metal silicide alloys. Metallurgical and Materials Transactions A, 36, 515-523.

Jing, B., Qiang, H., Liang, T., Tai, G., Xinqing, Z. and Chaoli, M. 2008. Liquid-Solid Phase Equilibria of Nb-Si-Ti Ternary Alloys. Chinese Journal of Aeronautics, 21, 275-280.

Jorda, J. L., Flükiger, R. and Müller, J. 1978. The phase diagram of the niobium-germanium system. Journal of the Less Common Metals, 62, 25-37.

Kang, Y., Han, Y., Qu, S. and Song, J. 2009. Effects of Alloying Elements Ti, Cr, Al, and Hf on β-Nb_5Si_3 from First-principles Calculations. Chinese Journal of Aeronautics, 22, 206-210.

Kattner, U. R., 1990, *Al-Nb Phase Diagram,* ASM Alloy Phase Diagram Centre, P. Villars, editor in chief; H. Okamoto and K. Cenzual, section editors; , http://www1.asminternational.org/AsmEnterprise/APD, ASM International, Materials Park, OH, 2006.

Kim, W.-Y., Tanaka, H. and Hanada, S. 2002. Microstructure and high temperature strength at 1773 K of Nb_{ss}/Nb_5Si_3 composites alloyed with molybdenum. Intermetallics*,* 10**,** 625-634.

Kim, W.-Y., Tanaka, H., Kasama, A. and Hanada, S. 2001. Microstructure and room temperature fracture toughness of Nb_{ss}/Nb_5Si_3 in situ composites. Intermetallics*,* 9**,** 827-834.

Kofstad, P. and Kjollesdal, H. 1961. Oxidation of Niobium (Columbium) in the temperature range 500 to 1200 ^{o}C. Transactions of the Metallurgical Society of AIME*,* 221**,** 248-294.

Kubaschewski, O. and Hopkins, B. E. 1960. Oxidation mechanisms of niobium, tantalum, molybdenum and tungsten. Journal of the Less Common Metals*,* 2**,** 172-180.

Kurz, W. and Fisher, D. J. 1979. Dendrite growth in eutectic alloys: the coupled zone. International Metals Reviews*,* 24**,** 177-204.

Larson, A. C. and Dreele, R. B. V. 2000. General Structure and Analysis Systems (GSAS). Los Alamos National Laboratory Report LAUR 86-748.

Levin, E. M. 1966. Phase Equilibria in the System Niobium Pentoxide - Germanium Dioxide. Journal of Research of the National Bureau of Standards - A. Physics and Chemistry*,* 70A**,** 5-10.

Li, M. and Kuribayashi, K. 2003. Nucleation-controlled microstructures and anomalous eutectic formation in undercooled Co-Sn and Ni-Si eutectic melts. Metallurgical and Materials Transactions A*,* 34**,** 2999-3008.

Li, M., Nagashio, K. and Kuribayashi, K. 2002. Reexamination of the solidification behavior of undercooled Ni–Sn eutectic melts. Acta Materialia*,* 50**,** 3241-3252.

Li, Z. 2012. *The effect of Germanium additions in Microstructure and Properties of Niobium Silicide alloys.* PhD Thesis, University of Sheffield.

Li, Z. and Peng, L. M. 2007. Microstructural and mechanical characterization of Nb-based in situ composites from Nb–Si–Ti ternary system. Acta Materialia*,* 55**,** 6573-6585.

Li, Z. and Tsakiropoulos, P. 2013. The microstructures of Nb–18Si–5Ge–5Al and Nb–24Ti–18Si–5Ge–5Al in situ composites. Journal of Alloys and Compounds*,* 550**,** 553-560.

Ma, L., Tang, X., Wang, B., Jia, L., Yuan, S. and Zhang, H. 2012a. Purification in the interaction between yttria mould and Nb-silicide-based alloy during directional solidification: A novel effect of yttrium. Scripta Materialia*,* 67**,** 233-236.

Ma, L. M., Tang, X. X., Jia, L. N., Yuan, S. N., Ge, J. R. and Zhang, H. 2012b. Influence of Hf contents on interactions between Nb-silicide based alloys and yttria moulds during directional solidification. International Journal of Refractory Metals and Hard Materials, 33, 87-92.

Ma, L. M., Yuan, S. N., Cui, R. J., Tang, X. X., Li, Y. L., Gao, M. and Zhang, H. 2012c. Interactions between Nb-silicide based alloy and yttria mould during directional solidification. International Journal of Refractory Metals and Hard Materials, 30, 96-101.

Massalski, T. B. 1986. *Binary alloy phase diagrams*, ASM.

Mataga, P. A. 1989. Deformation of crack-bridging ductile reinforcements in toughened brittle materials. Acta Metallurgica, 37, 3349-3359.

Mathieu, S., Knittel, S., Berthod, P. and Vilasi, M. 2012. On the oxidation mechanism of niobium-base in situ composites. Corrosion Science, 60, 181-192.

Medraj, M., Hammond, R., Parvez, M. A., Drew, R. a. L. and Thompson, W. T. 2006. High temperature neutron diffraction study of the Al_2O_3–Y_2O_3 system. Journal of the European Ceramic Society, 26, 3515-3524.

Mendiratta, M. and Dimiduk, D. 1993. Strength and toughness of a Nb/Nb_5Si_3 composite. Metallurgical and Materials Transactions A, 24, 501-504.

Mendiratta, M., Lewandowski, J. and Dimiduk, D. 1991. Strength and ductile-phase toughening in the two-phase Nb/Nb_5Si_3 alloys. Metallurgical and Materials Transactions A, 22, 1573-1583.

Mendiratta, M. G. and Dimiduk, D. M. 1991. Phase relations and transformation kinetics in the high Nb region of the Nb-Si system. Scripta Metallurgica et Materialia, 25, 237-242.

Menon, E., Parthasarathy, T. and Mendiratta, M. Microstructural Effects and Kinetics of High Temperature Oxidation in Nb-Si Base Alloys. *Metallic Materials with High Structural Efficiency.* 2004

Menon, E. S. K., Mendiratta, M. G. and Dimiduk, D. M. 2001. Oxidation behaviour of complex Niobium based alloys. Niobium; Science & Technology. Niobium 2001 Limited.

Murakami, T., Sasaki, S., Ichikawa, K. and Kitahara, A. 2001. Microstructure, mechanical properties and oxidation behavior of Nb-Si-Al and Nb-Si-N powder compacts prepared by spark plasma sintering. Intermetallics, 9, 621-627.

Murray, J. L., 1990, *Si-Ti Phase Diagram,* ASM Alloy Phase Diagram Centre, P. Villars, editor in chief; H. Okamoto and K. Cenzual, section editors; , http://www1.asminternational.org/AsmEnterprise/APD, ASM International, Materials Park, OH, 2006.

Nijdam, T. J., Jeurgens, L. P. H. and Sloof, W. G. 2003. Modelling the thermal oxidation of ternary alloys--compositional changes in the alloy and the development of oxide phases. Acta Materialia, 51, 5295-5307.

Nijdam, T. J. and Sloof, W. G. 2008. Modelling of composition and phase changes in multiphase alloys due to growth of an oxide layer. Acta Materialia, 56, 4972-4983.

Okamoto, H., 1990a, *Ge-Nb Phase Diagram,* ASM Alloy Phase Diagram Centre, P. Villars, editor in chief; H. Okamoto and K. Cenzual, section editors; , http://www1.asminternational.org/AsmEnterprise/APD, ASM International, Materials Park, OH, 2006.

Okamoto, H., 1990b, *Nb-O Phase Diagram,* ASM Alloy Phase Diagram Centre, P. Villars, editor in chief; H. Okamoto and K. Cenzual, section editors; , http://www1.asminternational.org/AsmEnterprise/APD, ASM International, Materials Park, OH, 2006.

Okamoto, H., 1991, *Si-Y Phase Diagram,* ASM Alloy Phase Diagram Centre, P. Villars, editor in chief; H. Okamoto and K. Cenzual, section editors; , http://www1.asminternational.org/AsmEnterprise/APD, ASM International, Materials Park, OH, 2006.

Okamoto, H. 1997. Cr-Si (Chromium-Silicon). Journal of Phase Equilibria, 18, 222-222.

Palenzona, A., 1990, *Nb-Y Phase Diagram,* ASM Alloy Phase Diagram Centre, P. Villars, editor in chief; H. Okamoto and K. Cenzual, section editors; , http://www1.asminternational.org/AsmEnterprise/APD, ASM International, Materials Park, OH, 2006.

Pan, V. M., 1982, *Ge-Nb-Si Phase Diagram,* ASM Alloy Phase Diagram Centre, P. Villars, editor in chief; H. Okamoto and K. Cenzual, section editors; , http://www1.asminternational.org/AsmEnterprise/APD, ASM International, Materials Park, OH, 2006.

Pan, V. M., Latysheva, V. I., Kulik, O. G. and Popov, A. G. 1982. Influence of alloying with Germanium and Copper on the conditions of formation of the superconducting compound Nb3Si. Russian Metallurgy, 167-171.

Pan, V. M., Latysheva, V. I., Kulik, O. G., Popov, A. G. and N., L. E. 1984. Phase diagram for Nb-Nb_3Al-Nb_5Si_3. Izuvestiya Akademii Nauk SSSR, Metally, 225.

Pan, V. M., Latysheva, V. I. and Shishkin, E. A. Phase Diagram of the Nb—Ge System. In: Savitskii, E. M. & Baron, V. V. (eds.) *Physics and Metallurgy of Superconductors / Metallovedenie, Fiziko-Khimiya I Metallozipika Sverkhprovodnikov / Металловедение Физико-Химип и Металлофизика Сверхпроводников.* Springer US.1995

Park, J.-H. 1989. Role of yttrium in enhanced adhesion of chromia scale to chromium. Materials Letters, 8, 405-408.

Pawel, R. E. and Campbell, J. J. 1966. Stress measurements during the oxidation of tantalum and niobium. Acta Metallurgica, 14, 1827-1833.

Perepezko, J. H. 2009. The Hotter the Engine, the better. Science Magazine. AAAS.

Pint, B. A. 1996. Experimental observations in support of the dynamic-segregation theory to explain the reactive-element effect. Oxidation of Metals, 45, 1-37.

Ramanarayanan, T. A., Ayer, R., Petkovic-Luton, R. and Leta, D. P. 1988. The influence of yttrium on oxide scale growth and adherence. Oxidation of Metals, 29, 445-472.

Reich, C. M., Kaiser, A. and Irvine, J. T. S. 2001. Niobia Based Rutile Materials as SOFC Anodes. Fuel Cells, 1, 249-255.

Rietveld, H. 1967. Line profiles of neutron powder-diffraction peaks for structure refinement. Acta Crystallographica, 22, 151-152.

Rietveld, H. 1969. A profile refinement method for nuclear and magnetic structures. Journal of Applied Crystallography, 2, 65-71.

Saito, Y. and Önay, B. 1990. Improvements of scale adherence on heat-resisting alloys and coatings by rare earth additions. Surface and Coatings Technology, 43–44, Part 1, 336-346.

Schlesinger, M., Okamoto, H., Gokhale, A. and Abbaschian, R. 1993. The Nb-Si (Niobium-Silicon) system. Journal of Phase Equilibria, 14, 502-509.

Shao, G. 2005. Thermodynamic modelling of the Cr-Nb-Si system. Intermetallics, 13, 69-78.

Smialek, J. 2000a. Maintaining adhesion of protective Al_2O_3 scales. JOM, 52, 22-25.

Smialek, J. 2000b. Maintaining adhesion of protective Al_2O_3 scales. JOM Journal of the Minerals, Metals and Materials Society, 52, 22-25.

Subramanian, P. R., Mendiratta, M. G., Dimiduk, D. M. and Stucke, M. A. 1997. Advanced intermetallic alloys--beyond gamma titanium aluminides. Materials Science and Engineering A, 239-240, 1-13.

Subramanian, P. R., Parthasarathy, T. A., Mendiratta, M. G. and Dimiduk, D. M. 1995. Compressive creep behavior of Nb_5Si_3. Scripta Metallurgica et Materialia, 32, 1227-1232.

Thandorn, T. and Tsakiropoulos, P. 2010. Study of the role of B addition on the microstructure of the Nb-24Ti-18Si-8B alloy. Intermetallics, 18, 1033-1038.

Thoma, D. J. and Perepezko, J. H. 1992. An experimental evaluation of the phase relationships and solubilities in the Nb---Cr system. Materials Science and Engineering A, 156, 97-108.

Tian, X. and Guo, X. 2009. Structure and oxidation behavior of Si-Y co-deposition coatings on an Nb silicide based ultrahigh temperature alloy prepared by pack cementation technique. Surface and Coatings Technology, 204, 313-318.

Toby, B. H. 2001. EXPGUI, a graphical user interface for GSAS. Journal of Applied Crystallography, 34, 210 - 213.

Vellios, N. and Tsakiropoulos, P. 2007. The role of Sn and Ti additions in the microstructure of Nb-18Si base alloys. Intermetallics, 15, 1518-1528.

Vellios, N. and Tsakiropoulos, P. 2010. Study of the role of Fe and Sn additions in the microstructure of Nb-24Ti-18Si-5Cr silicide based alloys. Intermetallics, In Press, Corrected Proof.

Venkatraman, M. and Neumann, J. P. 1986. The Cr−Nb (Chromium-Niobium) system. Bulletin of Alloy Phase Diagrams, 7, 462-466.

Wang, G., Gleeson, B. and Douglass, D. L. 1991a. A diffusional analysis of the oxidation of binary multiphase alloys. Oxidation of Metals, 35, 333-348.

Wang, G., Gleeson, B. and Douglass, D. L. 1991b. An extension of Wagner's analysis of competing scale formation. Oxidation of Metals, 35, 317-332.

Wang, X. L., Wang, G. and Zhang, K. F. 2010a. Microstructure and room temperature mechanical properties of hot-pressed Nb–Si–Ti–Fe alloys. Journal of Alloys and Compounds, 502, 310-318.

Wang, X. L., Wang, G. F. and Zhang, K. F. 2010b. Effect of mechanical alloying on microstructure and mechanical properties of hot-pressed Nb–16Si alloys. Materials Science and Engineering: A, 527, 3253-3258.

Wang, X. L. and Zhang, K. F. 2010. Mechanical alloying, microstructure and properties of Nb–16Si alloy. Journal of Alloys and Compounds, 490, 677-683.

Wei, B., Herlach, D. M. and Sommer, F. 1993. Rapid eutectic growth of undercooled metallic alloys. Journal of Materials Science Letters, 12, 1774-1777.

Westbrook, J. H. and Wood, D. L. 1964. "PEST" degradation in beryllides, silicides, aluminides, and related compounds. Journal of Nuclear Materials, 12, 208-215.

Yao, D., Cai, R., Zhou, C., Sha, J. and Jiang, H. 2009a. Experimental study and modeling of high temperature oxidation of Nb-base in situ composites. Corrosion Science, 51, 364-370.

Yao, D., Zhou, C., Yang, J. and Chen, H. 2009b. Experimental studies and modeling of the oxidation of multiphase niobium-base alloys. Corrosion Science, 51, 2619-2627.

Zarembo, S., 2000, *Ge-Ti Phase Diagram,* ASM Alloy Phase Diagram Centre, P. Villars, editor in chief; H. Okamoto and K. Cenzual, section editors; , http://www1.asminternational.org/AsmEnterprise/APD, ASM International, Materials Park, OH, 2006.

Zelenitsas, K. and Tsakiropoulos, P. 2005. Study of the role of Al and Cr additions in the microstructure of Nb-Ti-Si in situ composites. Intermetallics, 13, 1079-1095.

Zelenitsas, K. and Tsakiropoulos, P. 2006a. Effect of Al, Cr and Ta additions on the oxidation behaviour of Nb-Ti-Si in situ composites at 800 °C. Materials Science and Engineering A, 416, 269-280.

Zelenitsas, K. and Tsakiropoulos, P. 2006b. Study of the role of Ta and Cr additions in the microstructure of Nb-Ti-Si-Al in situ composites. Intermetallics, 14, 639-659.

Zhao, J. C., Jackson, M. R. and Peluso, L. A. 2003a. Determination of the Nb-Cr-Si phase diagram using diffusion multiples. Acta Materialia, 51, 6395-6405.

Zhao, J. C., Jackson, M. R. and Peluso, L. A. 2004. Mapping of the Nb-Ti-Si phase diagram using diffusion multiples. Materials Science and Engineering A*,* 372**,** 21-27.

Zhao, J. C., Peluso, L. A., Jackson, M. R. and Tan, L. 2003b. Phase diagram of the Nb-Al-Si ternary system. Journal of Alloys and Compounds*,* 360**,** 183-188.

Zhao, L. L., Li, G. Y., Zhang, L. Q., Lin, J. P., Song, X. P., Ye, F. and Chen, G. L. 2010. Influence of Y addition on the long time oxidation behaviors of high Nb containing TiAl alloys at 900 °C. Intermetallics*,* 18**,** 1586-1596.

Zifu, L. I. and Tsakiropoulos, P. 2010. Study of the effects of Ge addition on the microstructure of Nb-18Si in situ composites. Intermetallics*,* 18**,** 1072-1078.